CAVITY-QED STUDIES OF COMPOSITE SEMICONDUCTOR NANOSTRUCTURE AND DIELECTRIC MICROSPHERE SYSTEMS

by

XUDONG FAN

A DISSERTATION

Presented to the Department of Physics
and the Graduate School of the University of Oregon
in partial fulfillment of the requirements
for the degree of
Doctor of Philosophy

December 2000

"Cavity-QED Studies of Composite Semiconductor Nanostructure and Dielectric Microsphere Systems," a dissertation prepared by Xudong Fan in partial fulfillment of the requirements for the Doctor of Philosophy degree in the Department of Physics. This dissertation has been approved and accepted by:

Dr. Hailin Wang, Chair of the Examining Committee

Date

Committee in charge:
Dr. Hailin Wang, Chair
Dr. Michael Raymer
Dr. Howard Carmichael
Dr. Raymond Frey
Dr. Mark Lonergan

Accepted by:

Dean of the Graduate School

An Abstract of the Dissertation of

Xudong Fan for the degree of Doctor of Philosophy

in the Department of Physics to be taken December 2000

Title: CAVITY-QED STUDIES OF COMPOSITE SEMICONDUCTOR NANOSTRUCTURE AND DIELECTRIC MICROSPHERE SYSTEMS

Approved: _____

Dr. Hailin Wang

Spontaneous emission, which reflects fundamental dynamical interactions between matter and vacuum, can be controlled by using optical microcavities with dimensions of optical wavelength. This dissertation presents experimental studies aimed at controlling the spontaneous emission process in semiconductor quantum dots by coupling colloidal core/shell CdSe/ZnS nanocrystals to whispering gallery modes of a dielectric microsphere. Extensive cavity-QED studies are carried out in both the low-Q regime where the spontaneous emission features modified decay rate and the high-Q regime where dynamics of the cavity is sensitive to absorption occurring in a single nanocrystal.

For studies in the low-Q regime, we have embedded CdSe/ZnS nanocrystals in the interior surface of a polystyrene sphere. We have demonstrated pronounced enhancement in spontaneous emission rates when the nanocrystals are resonant with a whispering gallery mode. The manifestation of these cavity-QED effects depends sensitively on temperature and especially on nanocrystal sizes, providing

a unique probe to the underlying radiative dynamics. We show that emissions from the lowest dipole-allowed transition represent a predominant contribution to the photoluminescence. Comparison between the theoretically expected Purcell factor and the observed enhancement in the photoluminescence decay rate also indicates that quantum yield for the lowest dipole-allowed transition in large nanocrystals (D $>$ 6 nm) is near unity, which reflects the high surface quality of core/shell nanocrystals and is also important for using these nanocrystals as artificial atoms for applications in photonics and quantum optics.

For studies in the high-Q regime, we have deposited nanocrystals to the surface of a fused silica microsphere. We have demonstrated that the Q-factor of this composite nanocrystal-microcavity system can exceed 10^8, four orders of magnitude greater than Q-factors of other monolithic semiconductor microcavities. We find that the Q-factor is primarily limited by surface adsorption of chloroform solution used in the deposition process. The extremely high Q-factor puts us in a regime where cavity-QED at the level of a single nanocrystal can be pursued. This composite nanocrystal-fused silica microsphere system should open up a new avenue to a variety of physical phenomena including single-quantum-dot lasers, vacuum Rabi oscillation of nanocrystals, and nanocrystal-based quantum information processing.

CURRICULUM VITA

NAME OF AUTHOR: Xudong Fan

PLACE OF BIRTH: Xi'an, Shaanxi Province, People's Republic of China

DATE OF BIRTH: February 01, 1969

GRADUATE AND UNDERGRADUATE SCHOOLS ATTENDED:

University of Oregon
Peking University

DEGREES AWARDED:

Doctor of Philosophy in Physics, 2000,
University of Oregon
Master of Science in Physics, 1999,
University of Oregon
Master of Science in Physics, 1994,
Peking University
Bachelor of Science in Physics, 1991,
Peking University

AREAS OF SPECIAL INTEREST:

Quantum Optics and Cavity-QED of Semiconductors
Nonlinear Optical Spectroscopy of Semiconductor Nanostructures
Ultrafast Dynamics in Semiconductor Quantum Wells and Dots
Fabrication of CdSe Semiconductor Nanocrystals

PROFESSIONAL EXPERIENCE:

Research Assistant, Department of Physics,
University of Oregon, Eugene, Oregon, 1996-2000

Teaching Assistant, Department of Physics,
University of Oregon, Eugene, Oregon, 1995-1996

Research Assistant, Department of Physics,
Peking University, Beijing, People's Republic of China, 1991-1994

AWARDS AND HONORS:

Travel Grants Award from Division of Laser Science of the American Physical Society, 2000
New Focus Student Travel Grants Award, 1999
Travel Grants Award from Division of Laser Science of the American Physical Society, 1999
Graduate Research Award from Graduate School of the University of Oregon, 1999
Travel Grants Award from Division of Laser Science of the American Physical Society, 1998
New Focus Student Travel Grants Award, 1997
Travel Grants Award from Division of Laser Science of the American Physical Society, 1997
Graduate Research Award from Graduate School of the University of Oregon, 1997
First Prize Winner in Ph. D Qualification Exam, 1996
First Prize Winner in Master's Degree Qualification Exam, 1996
Highest Honor with the Full Scholarship Award from Peking University, 1992-1993
Excellence Award for the Academic Achievement from Peking University, 1992
Excellence Award for the Academic Achievement from Peking University, 1988

PUBLICATIONS:

Fan, X., Doran, A., and Wang, H., "High-Q whispering gallery modes from a composite system of GaAs quantum well and fused silica microsphere," Appl. Phys. Lett. **73**, 3190 (1998).

Fan, X. and Gu, B., "Quantum percolation and ballistic conductance in a system of double-coupled chains," ACTA Physica SINICA (Overseas Edition), Vol. **3**, No. X (1994).

Fan, X., Gu, B., Yang, G., and Lin, T., "Effects of various obstacles on oscillatory magnetoconductance of quantum double-coupled channels," J. Appl. Phys. **75**, 2466 (1994).

Fan, X., Lacey, S., Palinginis, P., and Wang, H., "Coupling semiconductor nanocrystals to a fused silica microsphere: A quantum-dot microcavity with extremely high-Q factors," Opt. Lett. **25**, 1600 (2000).

Fan, X., Lacey, S., and Wang, H., "Microcavities combining a semiconductor nanostructure with a fused silica microsphere," Opt. Lett. **24**, 771 (1999).

Fan, X., Lonergan, M. C., Zhang, Y., Sercel, P. C., and Wang, H. "Probing radiative dynamics in semiconductor nanocrystals with cavity QED," Phys. Rev. B (in press).

Fan, X., Takagahara, T., Cunningham, J. E., and Wang, H., "Pure dephasing induced by exciton-phonon interactions in lower dimensional semiconductors," Solid State Commun. **108**, 857 (1998).

Fan, X., Wang, H., Hou, H. Q., and Hammons, B. E., "Biexcitonic effects in the nonperturbative regime of semiconductor microcavities," Phys. Rev. B **57**, R9451 (1998).

Fan, X., Wang, H., Hou, H. Q., and Hammons, B. E., "Laser emission from semiconductor microcavities: transition from nonperturbative to perturbative regimes," Phys. Rev. B **56**, 15256 (1997a).

Fan, X., Wang, H., Hou, H. Q., and Hammons, B. E., "Laser emission from semiconductor microcavities: the role of cavity-polaritons," Phys. Rev. A, **56**, 3233 (1997b).

Gu, B. and Fan X., "Oscillatory magnetoconductance of narrow quantum waveguides in the presence of inhomogeneous magnetic fields", Zeitschrift für Physik B **4**, 527 (1996).

Wang, H., Fan, X., Hou, H. Q., and Hammons, B. E., "Stimulated emission from GaAs quantum well microcavities: toward laser emission from a few excitons," Proceeding of SPIE **3283**, 221 (1998).

ACKNOWLEDGEMENTS

Foremost, I would like to express my sincere appreciation to Dr. Hailin Wang for his guidance, support, and encouragement throughout my graduate work. His extensive knowledge, scientific expertise, and critical thinking have been the most valuable resources for my study and led me into the door of semiconductor optics. I also appreciate the opportunities that he has provided to attend many conferences from which I have greatly benefited.

I deeply thank Dr. Mark Lonergan for his help in nanocrystal synthesis, Dr. Michael Raymer for his creative and challenging questions, and Dr. Howard Carmichael for his stimulating discussion on cavity-QED theory. Special thanks also go to Dr. David Alavi for his assistance in laser set up, to Dr. Peter Sercel for lending me the devices to do time-correlated single photon measurement, to Dr. Yuzhong Zhang from Molecular Probes, Inc. for doping nanocrystals into polystyrene spheres, and to Ms. Colleen McKillip, Office Coordinator at Oregon Center for Optics, for her wonderful work and kind help. I would also like to thank Scott Lacey, Mark Phillips, Ethan Blansett, and Sasha Tavenner for proofreading the dissertation manuscript.

During five years of research at the University of Oregon, I am grateful to have obtained very generous help and invaluable suggestions from my colleagues Dr. Weidong Yang, Dr. Hao Lee, Dr. Xin Zhou, Dr. Dan McAlister, Dr. Wolfram Arnold, Scott Lacey, Mark Phillips, Phedon Palinginis, Ethan Blansett, and Andy Doran. Discussion with them is always enjoyable and their friendship will be

cherished forever. Particularly, I would like to thank Sasha Tavenner, Scott Lacey, and Phedon Palinginis for the respective contribution of Figure 12, Figure 64, and Figure 65 in this dissertation.

My thanks also go to Paul and Julie Thomas, my host parents in Eugene, for their love that has made Eugene my second hometown.

A particular gratitude is dedicated to Ms. Yin Xia. Without her continuing care and love, the completion of this dissertation would be impossible.

Finally, I give my deepest appreciation to my parents and sister for their everlasting support, love, and understanding.

DEDICATION

To my parents Zaibin Fan and Jiaoe Cheng, my sister Xufang Fan,

and

Yin Xia,

for their constant love, understanding, and support

TABLE OF CONTENTS

Chapter Page

I. INTRODUCTION 1

Atomic Cavity-QED 2
Cavity-QED in Semiconductors 3
Outline of Dissertation 11

II. THEORETICAL BACKGROUND OF CAVITY-QED 15

Introduction 15
Cavity-QED 15
Summary 24

III. WHISPERING GALLERY MODES IN A DIELECTRIC MICROSPHERE 25

Fabrication of a Fused Silica Microsphere 25
Theory of Whispering Gallery Modes 26
Characterization of Whispering Gallery Modes 38
Summary 47

IV. COMPOSITE SYSTEM OF GaAs QUANTUM WELL AND FUSED SILICA MICROSPHERE 49

Introduction 49
Photoluminescence From the Composite Quantum Well and Microsphere System 52
Measurement of the Q-Factor of the Composite Quantum Well and Microsphere System 59
Probing the Interaction Between Exciton and the Whispering Gallery Modes 63
Conclusion 69

V. SYNTHESIS OF ZnS-CAPPED CdSe SEMICONDUCTOR NANOCRYSTALS 71

Introduction 71
Properties of CdSe Nanocrystals 74
Fabrication and Characterization of ZnS-Capped CdSe Nanocrystals 79
Conclusion 95

Page

VI. CAVITY-QED STUDIES OF COMPOSITE NANOCRYSTAL AND MICROSPHERE SYSTEM IN THE LOW-Q REGIME 96

Introduction 96
Energy Structure of CdSe Nanocrystals 100
Experimental Results for CdSe/ZnS Nanocrystals in Free Space . 107
Cavity-QED Studies of CdSe/ZnS Nanocrystals 118
Discussion 132
Conclusion 141

VII. CAVITY-QED STUDIES OF COMPOSITE NANOCRYSTAL AND MICROSPHERE SYSTEM IN THE HIGH-Q REGIME 142

Introduction 142
Photoluminescence From the Composite System 144
Q-Factor of the Composite System 147
Discussion 151
Summary 155

VIII. SUMMARY AND FUTURE WORK 157

Summary 157
Future Work 159

APPENDIX

A. LASER EMISSION FROM SEMICONDUCTOR MICROCAVITIES: THE ROLE OF CAVITY POLARITONS 162

B. LASER EMISSION FROM SEMICONDUCTOR MICROCAVITIES: TRANSITION FROM NONPERTURBATIVE TO PERTURBATIVE REGIMES 167

C. BIEXCITONIC EFFECTS IN THE NONPERTURBATIVE REGIME OF SEMICONDUCTOR MICROCAVITIES 173

D. PURE DEPHASING INDUCED BY EXCITON-PHONON INTERACTIONS IN NARROW GaAs QUANTUM WELLS . . . 178

Page

BIBLIOGRAPHY 184

LIST OF FIGURES

Figure Page

1. Various Types of Semiconductor Microcavities 6
2. A Photonic Crystal 7
3. Composite Systems Based on Dielectric Microspheres 11
4. Spontaneous Emission 16
5. Coupled Atom-Cavity System 17
6. Enhanced Spontaneous Emission 20
7. Strong Coupling Regime 23
8. Fabrication of a Fused Silica Microsphere 26
9. Formation and the Electric Field of Whispering Gallery Modes 27
10. Effective Potential for a Sphere with a Constant Refractive Index . . 30
11. Normalized TE-Mode Electric Field of Whispering Gallery Modes . . 34
12. AFM Surface Image of a Fused Silica Microsphere 37
13. Confocal Microscope Image of a Polystyrene Sphere 38
14. Setup for Excitation and Collection of Whispering Gallery Modes (I) 39
15. Spectrum of Whispering Gallery Modes 40
16. Setup for Excitation and Collection of Whispering Gallery Modes (II) 41
17. Setup for Excitation and Collection of Whispering Gallery Modes (III) 43
18. Whispering Gallery Mode Structure 44
19. Measurement of the Intrinsic Q-Factor of Whispering Gallery Modes 46
20. Exciton Energy Structure 50
21. GaAs/AlGaAs Quantum Well and Its Energy Structure 51

Page

22. Experimental Setup of Composite Quantum Well and Microsphere System for Photoluminescence Measurement 54

23. Photoluminescence Spectrum of the Composite Quantum Well and Microsphere System 56

24. Photoluminescence Spectrum of the Composite Quantum Well and Microsphere System 58

25. Mechanisms for Q-spoiling of the Composite Quantum Well and Microsphere System 60

26. A Portion of the Coupled Photoluminescence Spectrum 61

27. Experimental Setup for Resonant Light Scattering 62

28. Resonant Scattering Spectra of Composite Quantum Well and Microsphere System 64

29. Measurement of the Interaction Between Exciton in Quantum Well and Resonant Whispering Gallery Mode 66

30. Exciton in a Bulk Crystal and in a Nanocrystal 72

31. Structure of CdSe Nanocrystals 75

32. Energy Structures of CdSe (a) and CdSe/ZnS Nanocrystals (b) . . . 76

33. Fabrication Setup and Apparatus 81

34. Evolution of Size and Size Distribution of CdSe Nanocrystals 89

35. Absorption and Photoluminescence Spectra of CdSe/ZnS Nanocrystals 91

36. Pictures of CdSe/ZnS Nanocrystal Under UV Illumination 92

37. (a): TEM Image of CdSe/ZnS Nanocrystals 94

38. Comparison of Time-Resolved Photoluminescence From CdSe and CdSe/ZnS Nanocrystals 99

39. Diagram of the Band Structure of a Bulk Semiconductor with a Direct Gap and Cubic Lattice Structure 101

40. Band Edge Structure of the Exciton in a Spherical CdSe Nanocrystal 105

Page

41. Relative Oscillator Strength of the Bright Excitonic States of a Spherical CdSe Nanocrystal 106

42. (a): The Setup Diagram for Time-Correlated Single Photon Counting Measurement 109

43. Excitation and Aging Dependence of Time-Resolved Photoluminescence of CdSe/ZnS Nanocrystals 110

44. Wavelength Dependence of Time-Resolved Photoluminescence of 5.4 nm Diameter CdSe/ZnS Nanocrystals (NC2) at T = 10 K 111

45. The First 150 ns of Time-Resolved Photoluminescence From NC2 CdSe/ZnS Nanocrystals in Free Space 113

46. Wavelength Dependence of Time-Resolved Photoluminescence of 5.4 nm Diameter CdSe/ZnS Nanocrystals (NC2) at Room Temperature 114

47. Temperature Dependence of Time-Resolved Photoluminescence in 1 μs Scale 116

48. Temperature Dependence of Time-Resolved Photoluminescence of CdSe/ZnS Nanocrystals for the First 100 ns 117

49. The Image of a Typical Nanocrystal-Doped Polystyrene Microsphere 119

50. Photoluminescence Spectrum of CdSe/ZnS Nanocrystal Doped in the Interior Surface of a Polystyrene Sphere 120

51. Enhanced Spontaneous Emission From 4.0 nm Diameter CdSe/ZnS Nanocrystals 123

52. Enhanced Spontaneous Emission From 5.4 nm Diameter CdSe/ZnS Nanocrystals 124

53. Enhanced Spontaneous Emission From 9.0 nm Diameter CdSe/ZnS Nanocrystals 125

54. Cavity-QED Component of Time-Resolved Photoluminescence From 5.4 nm Diameter CdSe/ZnS Nanocrystals 128

55. Enhanced Spontaneous Emission From CdSe/ZnS Nanocrystals at Elevated Temperature 130

Page

56. Enhanced Spontaneous Emission From CdSe/ZnS Nanocrystals at the Center of Photoluminescence Spectrum 131

57. Decay Dynamics of the Exciton in CdSe Nanocrystals 133

58. Spatial and Spectral Distribution of the Purcell Factor 137

59. Effects of Spatial and Spectral Distribution of the Purcell Factor on Time-Resolved Photoluminescence 139

60. (a): Composite Nanocrystal and Fused Silica Microsphere System . . 143

61. Experimental Setup for Cavity-QED Studies of a Composite Nanocrystal and Fused Silica Microsphere System 145

62. Photoluminescence from a Composite Nanocrystal and Fused Silica Microsphere System 146

63. Resonant Scattering Spectrum of Composite Nanocrystal and Fused Silica Microsphere System 148

64. Measurement of Photon Lifetime in a Whispering Gallery Mode . . . 150

65. Q-Spoiling Effects of Nanocrystal Absorption 154

LIST OF TABLES

Table Page

1. Q-factor and Effective Mode Volume for Various Semiconductor Microcavities 8
2. Evolution from One-Atom System to Bulk Crystal System 71
3. Decay Times of 5.4 nm Diameter CdSe/ZnS Nanocrystals at 10 K . . 127
4. Decay Times of 5.4 nm Diameter CdSe/ZnS Nanocrystals at 20 K . . 127
5. Decay Times of 9.0 nm Diameter CdSe/ZnS Nanocrystals at 10 K . . 127
6. Decay Times of 9.0 nm Diameter CdSe/ZnS Nanocrystals at 20 K . . 129

CHAPTER I

INTRODUCTION

The central subject of cavity-QED (cavity quantum electrodynamics) is the study of the interaction between the optical dipole in matter and the electric field of a cavity mode when the effective mode volume of the cavity is comparable to λ^3. Contrary to what was believed, that the spontaneous emission is an intrinsic property associated with an optical dipole, the radiative characteristics of the dipole can be drastically changed in the presence of a cavity, or even a metallic or dielectric boundary due to the modification of the local vacuum electric field. Consequently, the dipole and the cavity mode must be treated as a coupled dipole-cavity (or cavity-QED) system rather than two isolated systems [1, 2].

The dynamics of this cavity-QED system is determined by three parameters, the dipole coupling rate between the dipole and the cavity mode g, the cavity electric field decay rate κ, and the dipole decay rate γ. Depending on their relative strength, the cavity-QED system displays two very distinct types of behavior. When the dipole coupling is weak compared with the relevant decay rates, *i.e.*, $g < (\kappa, \gamma)$, the system is in the weak coupling regime. In this regime, both the spontaneous emission of the dipole and the cavity electric field feature exponential decay with the modified decay rates. On the other hand, when $g \gg (\kappa, \gamma)$, the system enters the strong coupling regime. In this regime, the dipole coupling rate is so large that the emitted photon can be reabsorbed before it leaks out of the

cavity, leading to the coherent energy exchange between the cavity electric field and the dipole. As a consequence, the spontaneous emission of the dipole becomes reversible and exhibits oscillatory structure. Moreover, as opposed to a classical system where many dipoles and photons are involved, the dynamics of a cavity-QED system in this strong coupling regime can be affected by the addition of even a single photon or a single dipole.

In this chapter, I will briefly review cavity-QED studies in atomic systems and in semiconductors, followed by the outline of the results in each chapter of this dissertation.

Atomic Cavity-QED

The theoretical exploration of the cavity-QED effects was originally applied to atomic systems and started half a century ago [3, 4]. However, it took the atomic community decades to present experimental evidence showing such effects. The first confirmation of modification of fluorescence of organic dye molecules dates back to the 1970s [5], followed by the demonstration of the inhibition of the spontaneous emission from Rydberg states of Cesium atoms in 1985 [6]. The strong coupling regime was realized in the late 1980s when high finesse ($F \sim 10^6$) mirrors became available. This soon led to the observation of vacuum Rabi splitting at the level of a single atom [1, 7, 8] and the clear demonstration of the higher excited states of the cavity-atom system [9].

In addition to fundamental studies of some interesting aspects of quantum mechanics such as controlled spontaneous emission mentioned above and quantum nondemolition measurements [10], cavity-QED has also created a new class of

applications that are not accessible to classical systems. One-atom lasers and one-atom masers [11, 12, 13, 14, 15] have been demonstrated with the mean intracavity atom number of order one. More recently, quantum logic gates and quantum computation using atom-cavity systems have been proposed and experimentally explored [16, 17, 18, 19, 20].

Cavity-QED in Semiconductors

Despite the tremendous progress made in atomic systems, cavity-QED studies on semiconductors are still in their early stages with only ten years of history. In semiconductors the optical properties at the fundamental band edge are determined by excitons [21]. An exciton is the bound state of an electron-hole pair due to the attractive Coulomb interaction. Like atoms, excitons feature discrete energy structures. The crystal ground state and the lowest excitonic state can be viewed as a two-level system analogous to an atomic system. Correspondingly, the main subject of the cavity-QED studies in semiconductors becomes the coupled exciton-cavity system.

Although in cavity-QED studies of semiconductors many concepts and terminologies are directly borrowed from cavity-QED of atomic systems, semiconductor cavity-QED features a number of interesting differences. First, semiconductor nanostructures such as quantum wells and quantum dots are easily fixed in resonators and therefore can be repeatedly accessed. This is a distinct advantage over atomic systems where atoms or ions are flying into and out of the resonator due to thermal motion, making it extremely difficult to address a particular particle. Secondly, unlike atoms, the energy level of quantum nanostructures can be artifi-

cially tuned to accommodate various applications using state-of-the-art techniques such as molecular beam epitaxy (MBE), metalorganic chemical vapor deposition (MOCVD), and high temperature organometallic synthesis. Furthermore, due to the nature of these semiconductor nanostructures and the successful fabrication of semiconductor devices, it becomes possible to incorporate these nanostructures with other devices.

There are also important differences between excitonic systems and atomic systems in terms of physics. Crystal momentum conservation due to the translational symmetry can lead to the formation of exciton polariton, which drastically change the optical properties of excitons in semiconductor nanostructures such as quantum wells. In addition, exciton-exciton interaction in semiconductor nanostructures including semiconductor quantum dots can lead to different optical properties, especially nonlinear optical properties, from those of atomic systems.

Recently, cavity-QED studies of semiconductor nanostructures have attracted much attention in the semiconductor community. First of all, they enable us to probe the fundamental processes in semiconductors by manipulating the interaction between the photon and excitons [22]. The presence of a cavity not only modifies the interaction of an exciton with the photon, but also has significant effects on the exciton-exciton scattering rate and exciton-phonon scattering rate. Cavity-QED studies also provide very useful spectroscopic tools to probe the dynamics of excitons in semiconductor nanostructures. Secondly, from an application point of view, cavity-QED studies of these semiconductor nanostructures can lead to novel photonic devices such as low-threshold lasers and high-efficiency LEDs. With extremely high finesse cavities, a laser operating at the level of a single quantum

dot can be constructed, featuring entirely different dynamics from conventional lasers. Recently, quantum logic gates and quantum computation using semiconductor quantum dots or nanocrystals have also been proposed and are currently under intensive investigation [23, 24, 25].

Parallel to the success in engineering electronic confinement using various semiconductor nanostructures such as quantum wells, quantum wires, and quantum dots, optical confinement has been achieved either with semiconductor microcavities, microdisks, and micropillars since the 1980s. Currently typical semiconductor microcavities are fabricated using MBE or MOCVD. Figure 1 shows the three most commonly used microcavities, planar microcavities, microdisks, and micropillars where semiconductor quantum wells, or quantum dots are placed at the center of the cavity. Micropillars are variants of planar microcavities, achieved by chemically etching the sidewalls to further reduce the mode volume. In planar microcavities and micropillars, optical resonators are formed by a stack of alternating quarter-wave dielectric layers with different refractive indices as drawn in Figures 1(a) and (c), whereas in microdisks, the resonator is formed through the total internal reflection along the curved boundary as shown in Figure 1(b).

Recently, another type of semiconductor cavity utilizing so-called photonic crystals has also drawn much attention [26]. In these photonic crystals, different dielectric spheres or rods are periodically placed as schematically shown in Figure 2(a). In analogy to real crystals where the electronic bandgap emerges as a result of constructive and destructive interference of electron waves, a photonic bandgap occurs as shown in Figure 2(b) due to the interference of electromagnetic waves scattered off the dielectric materials. When a defect is introduced in a photonic

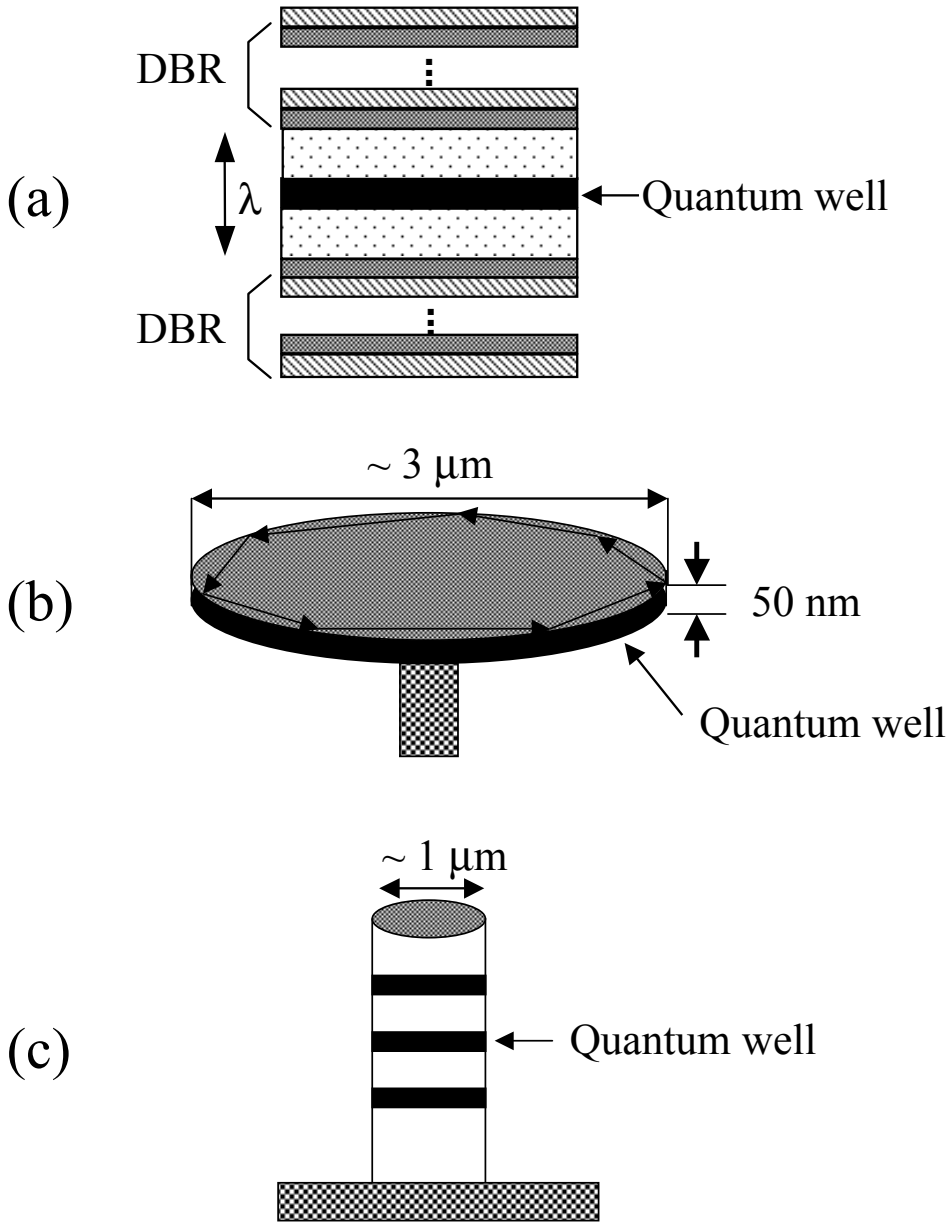

FIGURE 1. Various types of semiconductor microcavities. (a): Planar microcavity. (b): Microdisk. (c): Micropillar. Distributed Bragg reflector (DBR) is formed by a stack of alternating quarter-wave dielectric layers.

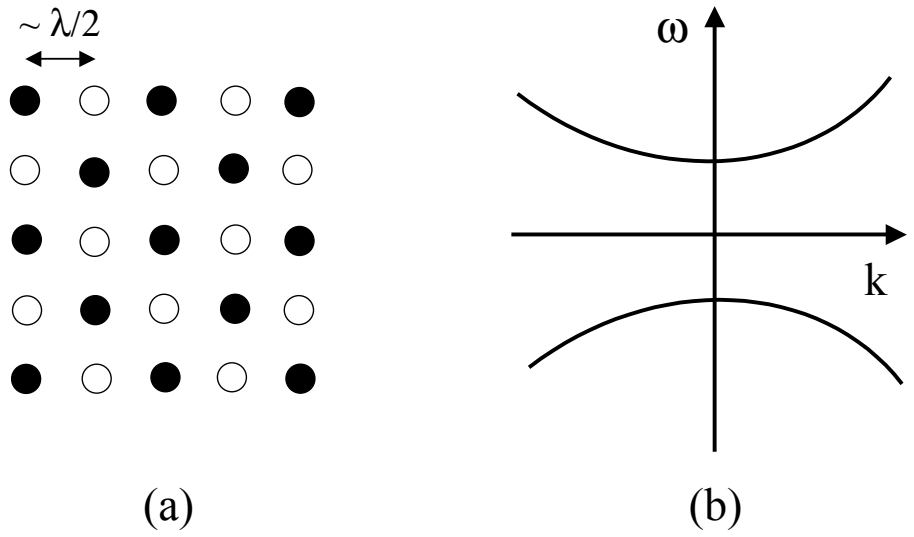

FIGURE 2. A photonic crystal. (a): Spatial configuration of a photonic crystal. (b): Photonic bandgap structure.

crystal, the photonic crystal traps the light, effectively forming a cavity.

Table 1 gives the Q-factor and the effective mode volume for the cavity configurations described above. For semiconductor microcavities the Q-factor is typically of order 10^4, limited by the leakage through the sidewalls and surface roughness of the sidewalls and also by the finite number of quarter-wave layers. Furthermore, both the electronic and optical confinement is integrated in the same semiconductor nanostructures. Any modification of the electronic confinement will eventually impose a significant impact on the optical confinement or vice versa, making the fine-tuning of either one of the confinements difficult. For photonic crystals, a Q-factor of only a few hundred has been achieved due to the difficulty in arrangement and the finite number of the dielectric spheres or rods.

Using these microcavities, a number of cavity-QED studies on semiconductor

TABLE 1. Q-factor and effective mode volume for various semiconductor microcavities

Microcavity type	**Q-factor**	**Effective Mode Volume**
Planar microcavity	$10^3 \sim 10^4$	$\sim 10\ \mu\text{m}^3$
Microdisk	$10^2 \sim 10^3$	$1 \sim 10\ \mu\text{m}^3$
Micropillar	$10^3 \sim 10^4$	$1 \sim 10\ \mu\text{m}^3$
Photonic crystal	$10^2 \sim 10^3$	$\sim 1\ \mu\text{m}^3$
d = 15 μm fused silica microsphere	$10^8 \sim 10^9$	$35\ \mu\text{m}^3$
d = 15 μm Polystyrene microsphere	$10^3 \sim 10^4$	$35\ \mu\text{m}^3$

nanostructures have been performed. Normal mode splitting and excitonic Rabi oscillations have been observed in semiconductor microcavities when the collective coherent energy exchange rate between the excitons in the quantum wells and the photons in the semiconductor microcavity is large compared with the relevant decay rates [27, 28]. Semiconductor microlasers in the form of disk, pillar, and Fabry-Perot configurations have also been achieved with extremely low threshold [29]. Enhanced spontaneous emission rates of InAs quantum dots with Purcell factors up to 5 have been observed when InAs quantum dots are placed in the core of GaAs/AlAs micropillar resonators [30].

One of the primary challenges in semiconductor cavity-QED is the realization of the strong coupling regime where the dipole coupling rate g between an exciton and a photon in a cavity exceeds the exciton dephasing rate γ and cavity decay rate κ. While the decay rate of an excitonic dipole is primarily determined by the semiconductor nanostructures, the cavity decay rate and the dipole coupling rate are related to the cavity Q-factor and the cavity effective mode volume through $\kappa \propto 1/Q$ and $E \propto 1/\sqrt{V_{eff}}$, respectively. Despite the small cavity effective mode volume achieved in the existing monolithic semiconductor microcavities,

the Q-factors of these resonators are far too low for many cavity-QED studies and applications. In order to further pursue the cavity-QED studies in semiconductor nanostructures, a cavity with much higher Q-factor is desired.

Dielectric microspheres are a promising optical resonator in this regard. In a dielectric microsphere, whispering gallery modes form through total internal reflection along the curved boundary. Whispering gallery modes confined within a wavelength of the sphere surface can feature both high Q-factor and small mode volume. Both parameters are critical for achieving strong light-matter coupling as discussed above. For fused silica microspheres, Q-factors can approach 10^9 as shown in Table 1, whereas the maximum vacuum field strength can exceed 60V/cm at $\lambda = 800$ nm for spheres with a diameter of 50 μm [31, 32].

Extensive research efforts have aimed at taking advantage of these unique properties of microspheres for cavity-QED studies and for possible applications. In atomic physics, whispering gallery modes are used as an alternative to the conventional Fabry-Perot type cavities [31, 33, 34]. Experimental results have shown that the atoms in the vicinity of the microsphere surface are strongly coupled into the whispering gallery modes, leading to a splitting in the absorption spectrum [34]. Single molecule spectroscopy using a fused silica microsphere has also been under investigation [35]. In addition, enhanced stimulated Raman scattering and enhanced Rayleigh scattering have been observed in earlier studies in liquid droplets [36, 37].

The research presented in this dissertation is focused on controlling the spontaneous emission process in semiconductor quantum dots. In order to achieve this goal, we have developed a new composite microcavity system by coupling colloidal

core/shell CdSe/ZnS nanocrystals to the whispering gallery modes of a dielectric microsphere. We have also carried out cavity-QED studies on this type of composite system in the weak coupling regime as a first step towards the final realization of the strong coupling between the cavity electric field and the exciton in the semiconductor nanostructures.

The composite semiconductor nanostructure and dielectric microsphere system can be constructed by placing semiconductor nanostructures such as quantum wells (Figure 3(a)) and nanocrystals (Figure 3(b)) in the electric field of the whispering gallery modes of a dielectric microsphere. The dynamics of excitons in these semiconductor nanostructures can thus be controlled by coupling the excitons in semiconductor nanostructures to the whispering gallery modes. This system takes advantage of the high Q-factor and small mode volume of the whispering gallery modes, as shown in Table 1 and allows for separate engineering of the electronic and photonic confinement. The electronic confinement is given by various semiconductor nanostructures whereas three-dimensional photonic confinement is provided by the microsphere. Compared with the conventional semiconductor microcavities, dielectric microspheres can be conveniently fabricated without using complicated techniques such as MBE or MOCVD. Furthermore, the resonance of the whispering gallery mode can be easily tuned over the whole spectral range without spoiling the Q-factor by using a thermal or mechanical tuning scheme [32, 38]. Therefore, this composite system represents an excellent model system for cavity-QED studies of different linear and nonlinear optical processes in semiconductors and for potential applications such as microlasers and quantum computation.

In the following section, I will give an outline of this dissertation.

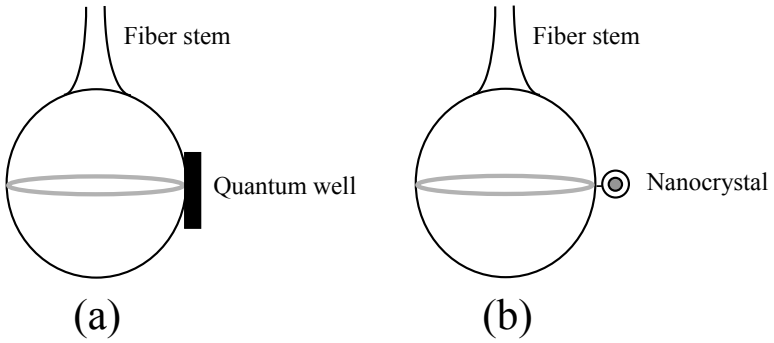

FIGURE 3. Composite systems based on dielectric microspheres. (a): Composite system of semiconductor quantum well and fused silica microsphere. (b): Composite system of semiconductor nanocrystal and fused silica microsphere.

Outline of Dissertation

In Chapter II, we introduce the basic concepts and terminologies of cavity-QED in atomic systems, which can be extended to cavity-QED in semiconductors.

In Chapter III, we give a detailed description of the properties of the whispering gallery modes of a dielectric microsphere. The mode structure, mode volume, and Q-factor will be discussed. We investigate two types of dielectric microspheres. Polystyrene microspheres feature a Q-factor of 10^3 and can be used for cavity-QED studies in the low-Q regime, whereas fused silica microspheres, with a Q-factor of 10^8 achieved, are used for cavity-QED studies in the high-Q regime. In addition, we present in this chapter the experimental setup used for mode characterization and the cavity-QED studies in later chapters.

As our first attempt in cavity-QED studies of the composite semiconductor nanostructure and dielectric microsphere system, we discuss in Chapter IV a composite system where an epitaxially grown semiconductor sample is placed in the vicinity of a fused silica microsphere. We have demonstrated that the photolumi-

nescence from quantum wells can be efficiently coupled into the whispering gallery modes. This combined system features a Q-factor of 2×10^5, two orders of magnitude higher than conventional monolithic semiconductor microcavities. However, further development of this composite epitaxially grown nanostructure and fused silica microsphere system is hindered by two problems. Large Q-spoiling occurs at the contact area arising from the output coupling loss through the dielectric capping layers. This sets the upper limit of the Q-factor to $10^5 \sim 10^6$, as measured in the above experiments. In addition, since a capping layer of a few tens of nanometers is needed to avoid surface effects, the dipole coupling strength between the exciton in the quantum wells and the electric field in the whispering gallery modes is too weak to achieve any significant modification in optical properties of the excitons in semiconductor samples.

In order to avoid these problems and bring the excitons as close as possible to the dielectric microsphere surface, we incorporate semiconductor nanocrystals with a dielectric microsphere. Semiconductor nanocrystals such as CdSe, ZnSe, and CdS are fabricated in colloid using high temperature organometallic synthesis. The size of the nanocrystals ranges from 1 nm to 10 nm in diameter. The nanocrystal surface is passivated by another semiconductor with a larger bandgap, leading to a quantum yield of over 50%. The capping layer is approximately 1 nm thick, thus bringing the excitons in nanocrystals much closer to the microsphere surface than epitaxially grown quantum wells or quantum dots. In addition, the output coupling loss through the dielectric capping layer no longer exists and the surface scattering loss due to a single nanocrystal is expected to be negligibly small. Therefore, high Q-factor can be achieved in the composite system based on semiconductor

nanocrystals. The properties, synthesis, and characterization of semiconductor core/shell CdSe/ZnS nanocrystals will be presented in Chapter V.

Extensive cavity-QED studies are carried out in this type of nanocrystal-based composite system in both the low-Q (Chapter VI) and the high-Q regimes (Chapter VII), depending on the microsphere used.

For cavity-QED studies of the composite system based on semiconductor nanocrystals and for the applications such as quantum logic gate using semiconductor nanocrystals, it is crucial to understand the radiative recombination processes in semiconductor nanocrystals, since these processes reflect the fundamental dynamical interactions between the matter and the vacuum electric field. However, in semiconductor nanocrystals, the decay dynamics feature multiple exponential components due to various complicated nonradiative decay processes. In order to investigate the radiative processes, and therefore, to control the spontaneous emission from the nanocrystals, we have developed in Chapter VI an experimental approach based on the cavity-QED that only radiative processes are directly affected by modifications in vacuum fluctuations. We dope the nanocrystals in the interior surface of a polystyrene microsphere with a Q-factor of a few thousand. In this low-Q regime (or bad cavity limit) where $\kappa \gg \gamma$, we have demonstrated pronounced enhancement in the spontaneous emission rate when the nanocrystals are resonant with a whispering gallery mode. Furthermore, by comparing the time-resolved photoluminescence resonant with and off-resonant with the relevant whispering gallery mode, we are able to single out the radiative decay component from the complex decay dynamics. This radiative component is attributed to the optical emission from the lowest dipole-allowed transition in nanocrystals. The

decay time measured is of order 10 ns, in agreement with the theoretical expectation. We also study the dependence of the enhanced spontaneous emission on the nanocrystal size. It is found that in the large nanocrystals (D $>$ 6 nm) the lowest dipole-allowed transition is predominantly radiative, which is crucial for many cavity-QED phenomena and applications.

For studies in the high-Q regime where $\kappa \ll \gamma$, we have deposited nanocrystals to the surface of a fused silica microsphere. Our experimental results show that the Q-factor of this composite system exceeds 10^8. The Q-factor is four orders of magnitude higher than Q-factors of other monolithic semiconductor microcavities and is primarily limited by surface adsorption of chloroform solutions used in the deposition process. In addition, we have achieved for the first time in a semiconductor system the "critical atom number" smaller than one, thus making the composite microcavity system a model system for cavity-QED studies at the level of a single nanocrystal.

As mentioned previously, cavity-QED in semiconductor nanostructures is still at its early stage. In the final chapter, I will briefly discuss some interesting topics in terms of future direction in this area.

My research work on semiconductor microcavity lasing, biexcitonic effects on semiconductor microcavities, and ultrafast dynamics of semiconductor quantum wells will be presented in the appendices.

CHAPTER II

THEORETICAL BACKGROUND OF CAVITY-QED

Introduction

It has long been known that spontaneous emission is not an intrinsic property associated with an atom, but rather it is one of the results of the dipole interaction between the atom and the vacuum electric field. In the presence of a cavity, this dipole coupling is changed due to the modification of the local vacuum electric field. Therefore, the atom and the cavity must be treated as a coupled system. The study of such a coupled atom-cavity system is called cavity-QED.

The objective of this chapter is to provide a theoretical background for cavity-QED studies of composite nanostructure and dielectric microsphere systems in the later chapters. For simplicity, we use an atomic system as an example to elucidate the basic concepts of cavity-QED. These concepts can be extended to semiconductor excitonic systems. Note that the effects of polaritons and exciton-exciton interaction on the dynamics of the coupled exciton-cavity system will be discussed in more detail in the Appendix.

Cavity-QED

Consider the two-level atomic system shown in Figure 4. Upon absorption of a photon, the atom undergoes a transition from the ground state to the excited state. After a certain amount of time in the excited state, the atom makes a

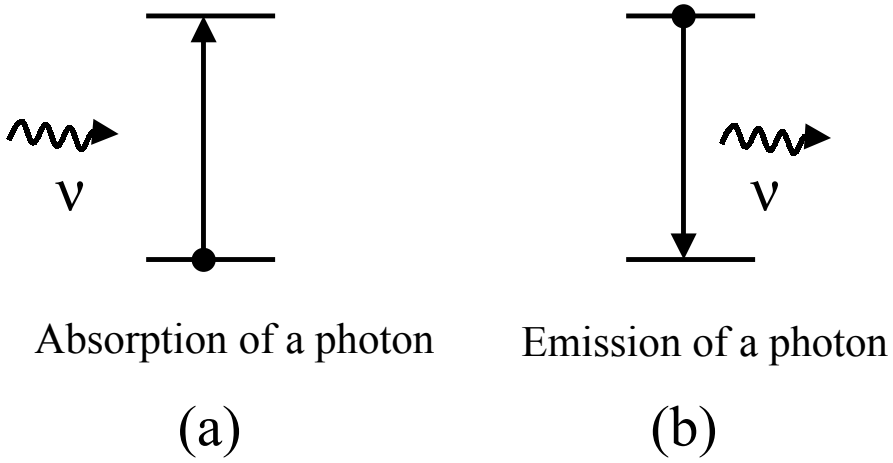

FIGURE 4. Spontaneous emission. (a): An atom undergoes a transition from ground state to excited state upon absorption of a photon. (b): A photon is emitted due to the dipole coupling with the local vacuum electric field.

transition back to the ground state and emits a photon. This is spontaneous emission. Einstein phenomenologically introduced the so-called A coefficient to describe this process. Spontaneous emission can be understood within the frame of quantum electrodynamics. The atom interacts with the continuum states of the local vacuum electric field via dipole coupling. It is the dipole coupling strength and the final density of states of the emitted photon that determines the lifetime of the excited atom.

The local vacuum electric field changes under different boundary conditions. Consequently, the radiative characteristics of an atom such as the radiative lifetime and radiation pattern will be modified in the presence of a cavity, or metallic or dielectric boundary.

Consider the ideal case where an atom is positioned inside a cavity and coupled with a single mode of the cavity, as schematically shown in Figure 5.

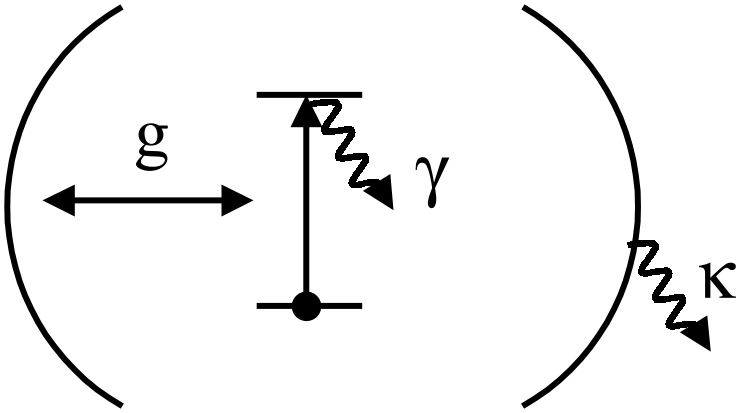

FIGURE 5. Coupled atom-cavity system.

Within the rotating wave approximation, the dynamics of this atom-cavity system is governed by the Jaynes-Cummings Hamiltonian [4]:

$$\widehat{H} = \frac{1}{2}\hbar\omega_A\hat{\sigma}^z + \hbar\omega_C\hat{a}^\dagger\hat{a} + \hbar\left[g\hat{a}^\dagger\hat{\sigma}^- + g\hat{a}\hat{\sigma}^+\right] \tag{2.1}$$

where the operators $\hat{a}$ and $\hat{a}^\dagger$ are the annihilation and creation operators for the single mode cavity of interest. $\hat{\sigma}^z$ is the Pauli operator for the atomic inversion. $\hat{\sigma}^-$ takes an atom in the upper state into the lower state whereas $\hat{\sigma}^+$ takes an atom in the lower state into the upper state. In matrix notation, $\hat{\sigma}^z$, $\hat{\sigma}^-$, and $\hat{\sigma}^+$ have the form:

$$\hat{\sigma}^z = \begin{pmatrix} 1 & 0 \\ 0 & -1 \end{pmatrix}, \hat{\sigma}^- = \begin{pmatrix} 0 & 0 \\ 1 & 0 \end{pmatrix}, \hat{\sigma}^+ = \begin{pmatrix} 0 & 1 \\ 0 & 0 \end{pmatrix}. \tag{2.2}$$

In the above Hamiltonian, the first two terms describe the noninteracting atom

and cavity mode, respectively. The third term arises from the dipole interaction between the atom and the cavity electric field. ω_A and ω_C are the atomic and cavity resonance frequencies, respectively. For simplicity, we assume the system under consideration is on resonance, so that $\omega_A = \omega_C$. The dipole coupling between the atomic transition and the vacuum electric field is given by

$$g = \left(\frac{\mu^2 \omega}{2\hbar\varepsilon_0 V_{eff}} \right)^{1/2} \tag{2.3}$$

where μ is the atomic dipole moment and V_{eff} is the effective mode volume of the cavity [1]. We have assumed here that the dipole moment is parallel to the electric field.

In the Heisenberg picture, the equations of motion for $\hat{a}$ and $\hat{\sigma}^{\pm}$ are given by

$$d\hat{a}(t)/dt = \frac{1}{i\hbar}[\hat{a}, H] = -i\omega\hat{a} - ig\hat{\sigma}^{-} \tag{2.4}$$

$$d\hat{\sigma}^{-}(t)/dt = \frac{1}{i\hbar}\left[\hat{\sigma}^{-}, H\right] = -i\omega\hat{\sigma}^{-} + ig\hat{\sigma}^{z}\hat{a}. \tag{2.5}$$

Therefore the equation of motion for the expectation value of the electric field of the cavity mode and the atomic polarization is given by:

$$d\alpha(t)/dt = -igp \tag{2.6}$$

$$dp(t)/dt = -ig\alpha \tag{2.7}$$

---

[1] V_{eff} is defined as

$$\sqrt{1/V_{eff}} \equiv u(\mathbf{r}_{atom})$$

where

$$\int |u(\mathbf{r}_{atom})|^2 d^3\mathbf{r} = 1.$$

where $\alpha(t) =< (\widehat{a})(t) > e^{i\omega t}$ and $p(t) =< \widehat{\sigma}^{-}(t) > e^{i\omega t}$ represent the expectation values of the electric field in the cavity and the atomic polarization, respectively. Here we have used $< \widehat{\sigma}^{z} >= -1$ for weak excitation.

So far, we have assumed that there is no damping of the cavity field, namely, Q $\longrightarrow \infty$ and the atom is coupled only with the single cavity mode. For a more practical treatment, we need to consider a leaky cavity with an electric field decay rate of κ where κ is related to Q by equation:

$$Q = \omega/2\kappa. \tag{2.8}$$

Furthermore, apart from the single cavity mode under consideration, the atom is also coupled with the leaky modes and the continuum states of the local vacuum electric field. The dissipation of the spontaneous emission into all electric field modes other than the cavity mode of interest is represented by 2γ. Accordingly, the dynamics of the electric field and the polarization is given by the modified equations:

$$\begin{aligned} d\alpha(t)/dt &= -\kappa\alpha - igp \\ dp(t)/dt &= -\gamma p - ig\alpha. \end{aligned} \tag{2.9}$$

Assuming that $\alpha(t)$ and $p(t)$ have the form of $e^{\lambda t}$, we arrive at two eigenvalues for Equation (2.9):

$$\lambda_{\pm} = -(\frac{\kappa+\gamma}{2}) \pm \left[(\frac{\kappa-\gamma}{2})^2 - g^2\right]^{1/2}. \tag{2.10}$$

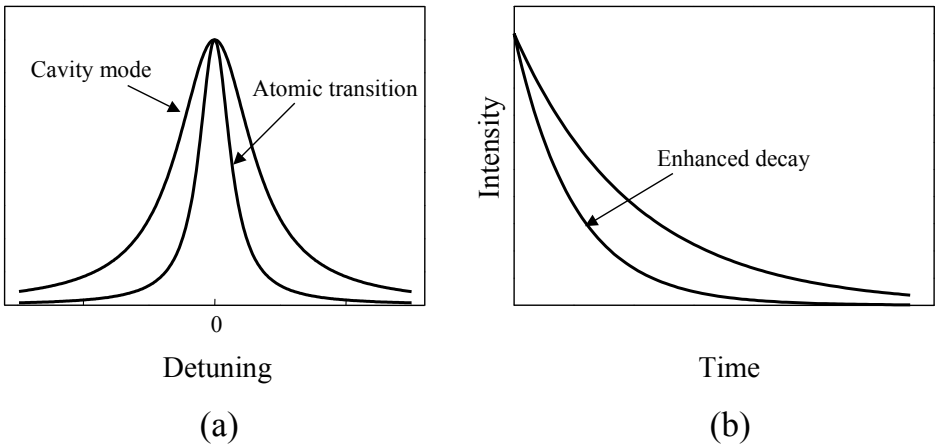

FIGURE 6. Enhanced spontaneous emission. (a): Bad cavity limit where $\kappa \gg \gamma$. (b): Spontaneous emission is enhanced due to the presence of a resonant cavity.

The dynamics of the coupled atom-cavity system is thus determined by these three parameters, the dipole coupling rate between the atom and the electric field g, the cavity decay rate κ, and the atomic dipole decay rate γ. Depending on their relative strength, we have two fundamentally different regimes as discussed below.

(1) Weak coupling regime

When $g < (\gamma, \kappa)$, we enter the weak coupling regime. In this regime, the dynamics of the cavity and the atomic dipole still features exponential decay, but with the modified decay rates. In particular, we have two interesting regimes when we consider two extreme cases where $\kappa \gg \gamma$ and $\kappa \ll \gamma$.

In the low-Q regime (or bad cavity limit), *i.e.*, $\kappa \gg g^2/\kappa \gg \gamma$, as illustrated in Figure 6(a), the decay rate for the atomic dipole can be simplified as:

$$\lambda = -(\gamma + \frac{g^2}{\kappa}). \tag{2.11}$$

From Equation (2.11), it is easy to see that the dipole decay rate is enhanced. In addition to the original decay rate γ, we have an extra decay rate g^2/κ resulting from the presence of a resonant cavity. In the time domain, this enhancement is manifested as a shorter lifetime for an atom as illustrated in Figure 6(b).

In 1946, Purcell introduced the Purcell factor F_p to describe this cavity enhanced spontaneous emission [3]. The Purcell factor F_p is defined as the ratio of the dipole decay rate into the cavity mode to the dipole decay rate in free space:

$$F_p = \frac{g^2/\kappa}{A/2} = \frac{3}{4\pi^2} Q \frac{\lambda^3}{V_{eff}} \tag{2.12}$$

where A is the Einstein A coefficient. λ is the wavelength of the emitted photon and V_{eff} is the cavity effective mode volume.

In order to achieve significant enhancement effects, we need a cavity with a good Q-factor and small mode volume.

On the other hand, in the high-Q regime (or good cavity limit) where $\gamma \gg g^2/\gamma \gg \kappa$, the cavity decay rate will be enhanced due to the absorption occurring in an atom. Mathematically, this Q-spoiling effect can be expressed as:

$$\kappa' = (\kappa + \frac{g^2}{\gamma}). \tag{2.13}$$

In this case, the cavity linewidth in the frequency domain is broadened due to the Q-spoiling effects.

It should be noted that in the above discussion, we have assumed that only a single atom is interacting with the cavity mode. However, the results can be easily extended when more than one atom involved. In this case, the Q-spoiling effect

will be expressed as:

$$\kappa' = (\kappa + \frac{g^2 N}{\gamma}) \tag{2.14}$$

where N is the number of atoms interacting with the cavity mode.

(2) Strong coupling regime

Another important regime is the strong coupling regime where $g \gg (\gamma, \kappa)$. In this regime, the emitted photon can be reabsorbed before it leaks out of the cavity. The eigenvalues for Equation (2.9) become:

$$\lambda_{\pm} = -\frac{(\kappa + \gamma)}{2} \pm i\Omega_{Rabi} \tag{2.15}$$

where $\Omega_{Rabi} = [g^2 - ((\kappa - \gamma)/2)^2]^{1/2}$ is the vacuum Rabi splitting. In the frequency domain, the coupled cavity-atom system has two well-resolved resonances separated by $2\Omega_{Rabi}$ as shown in Figure 7(a). The dynamics of the atom no longer features irreversible exponential decay as in the weak coupling regime, but rather, it exhibits oscillatory behavior. Figure 7(b) shows schematically the coherent energy exchange between the atomic dipole and the cavity photon in the time domain, corresponding to the spectrum shown in Figure 7(a).

Using the parameters g, γ, and κ, we can define two important dimensionless parameters that specify the role of a single atom and a single photon, respectively. The first parameter, the "critical atom number", is defined as:

$$N_0 = \frac{2\kappa\gamma}{g^2}, \tag{2.16}$$

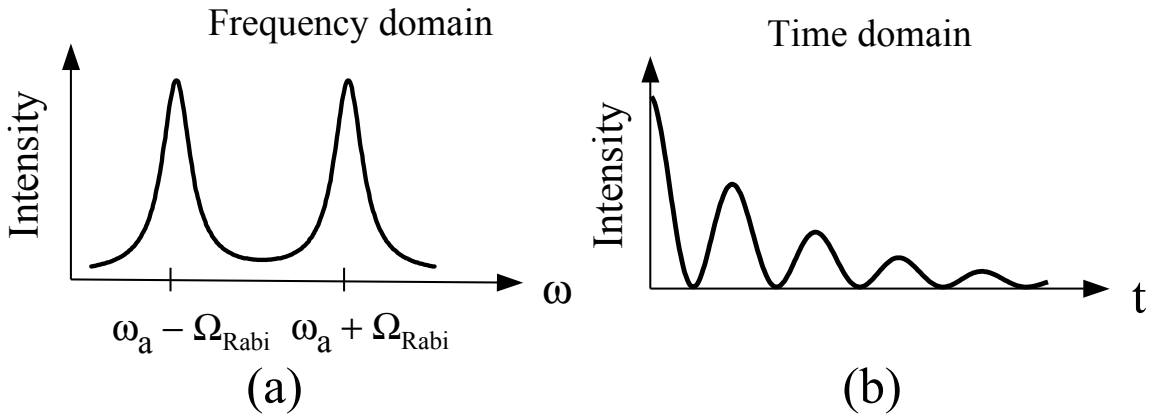

FIGURE 7. Strong coupling regime is manifested in (a): Frequency domain. (b): Time domain.

which indicates the number of atoms needed to have significant effects on the lifetime of the cavity electric field. The other parameter is the "saturation photon number" defined as:

$$n_{sat} = \frac{\gamma^2}{2g^2}, \tag{2.17}$$

which gives the average number of photons needed to saturate the atomic transition.

In the regime where $g \ll (\gamma, \kappa)$, $(N_0, n_{sat}) \gg 1$. Consequently the effect of a single atom or a single photon is negligible. In contrast, in the regime where $g \gg (\gamma, \kappa)$ and $(N_0, n_{sat}) < 1$, the dynamics of the coupled cavity-atom system can be considerably affected by the addition of even a single atom or a single photon.

Summary

In this chapter we have discussed the dynamics of the coupled cavity-atom system which is characterized by three parameters, g, γ, and κ. Depending on their relative strength, we have the weak coupling and strong coupling regimes. In the weak coupling regime, we have discussed two extreme cases. In the bad cavity limit, the spontaneous emission from an atom is modified due to the presence of a cavity whereas in the good cavity limit, the cavity Q-factor is spoiled due to the loss through the atomic absorption.

Recently the strong coupling regime of cavity-QED has received a lot of attention. In this regime, a single atom can coherently exchange its energy with the cavity photon, resulting in the vacuum Rabi splitting in the frequency domain and the vacuum Rabi oscillation in the time domain. In addition, the coupled system is operated with $(N_0, n_{sat}) < 1$ where a single photon or a single atom has a significant impact on the dynamics of the cavity-atom system. In order to achieve the strong coupling regime, a cavity with a small mode volume and a high Q-factor is desired to increase the dipole coupling and to reduce the cavity loss, as stated in Equation (2.3) and (2.8).

The concepts of cavity-QED in atomic systems can be extended to semiconductor quantum dots. In this dissertation, we present the experimental results of cavity-QED studies on composite semiconductor quantum dot and dielectric microsphere system in the weak coupling regime in both the low-Q regime (see Chapter VI) and the high-Q regime (see Chapter VII).

CHAPTER III

WHISPERING GALLERY MODES IN A DIELECTRIC MICROSPHERE

In this section we discuss the properties of whispering gallery modes of a dielectric microsphere. We also present the experimental characterization of these whispering gallery modes for later cavity-QED studies. Two types of microspheres are used in this dissertation. Polystyrene microspheres used for low-Q cavity-QED studies are commercially available whereas fused silica microspheres for high-Q cavity-QED studies are fabricated in our laboratory.

Fabrication of a Fused Silica Microsphere

Fused silica microspheres can be easily fabricated by heating the end of a tapered optical fiber using a CO_2 laser, as illustrated in Figure 8(a). In this setup, multi-mode or single-mode fiber is used, depending on the desired size. In some cases, microspheres are also prepared using rare earth doped fiber for laser emission studies. A small weight is attached to the bottom of the fiber and pulls the fiber during slow heating process to form the stem. Once the desired size of the stem is achieved, the laser is moved down with the increased power to break the fiber and then to melt the lower end of the fiber. A microsphere forms due to surface tension and its size grows as more glass is fed into the laser beam. Figure 8(b) shows a picture of a fused silica microsphere. Typical diameters of such microspheres can range from 10 μm to 200 μm with a stem size approximately a third or a quarter

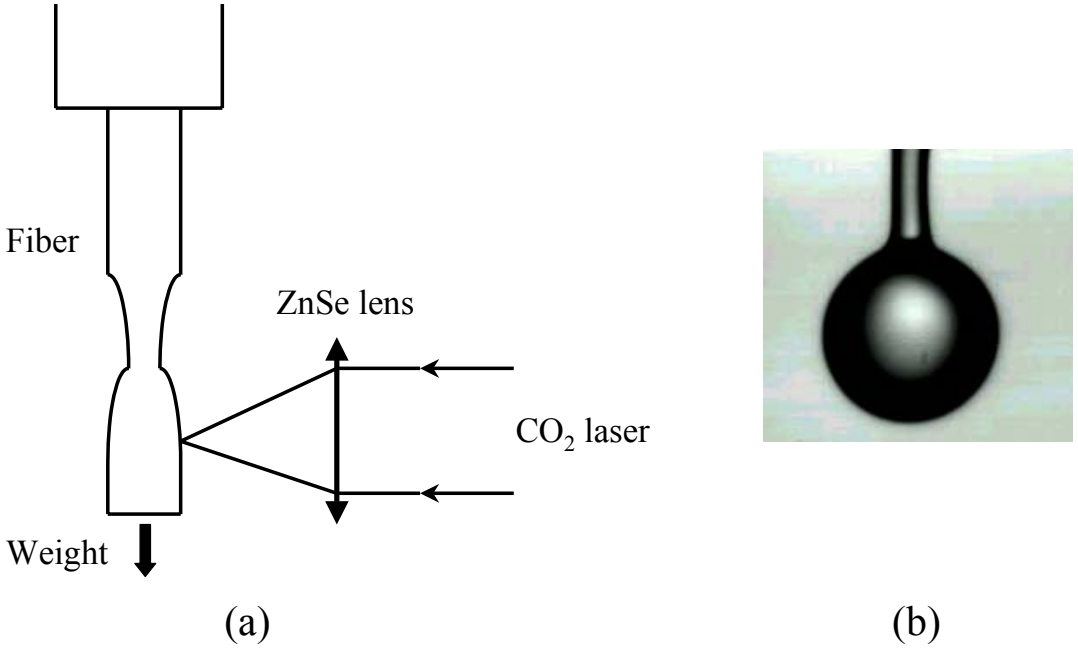

FIGURE 8. Fabrication of a fused silica microsphere. (a): The setup for fabrication of fused silica microspheres using CO_2. (b): A picture of a fused silica microsphere with a stem.

of the sphere diameter. When a sphere larger than 1 mm is needed, a glass rod instead of an optical fiber is used and in this case a microtorch serves better than a CO_2 laser [39, 40]. Although the actual microsphere prepared this way is elongated along the stem direction with ellipticity of a few percent, due to the gravity, the equator perpendicular to the stem is still very circular.

Theory of Whispering Gallery Modes

A microsphere serves as an optical resonator. Among all resonances supported by such a microsphere, of particular interest are a group of resonances called whispering gallery modes formed via total internal reflection along the sphere

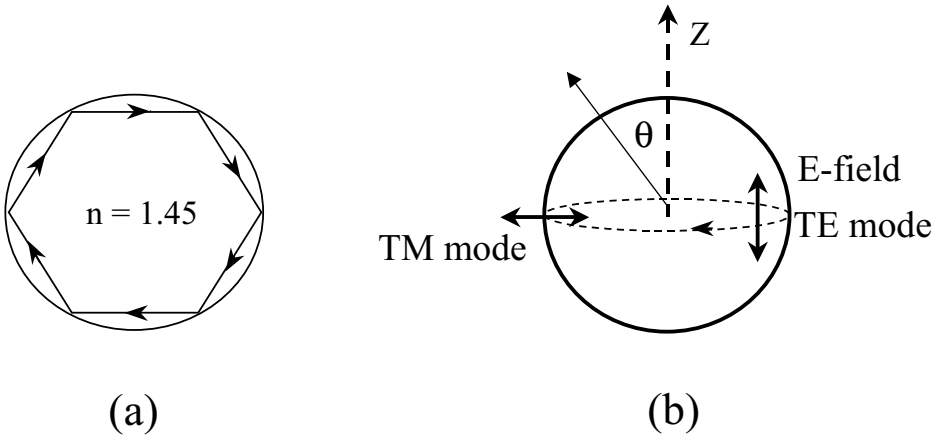

FIGURE 9. Formation and the electric field of whispering gallery modes. (a): Whispering gallery modes in a dielectric microsphere can form via total internal reflection along the curved boundary. (b): The electric field is perpendicular to the propagation plane in TE-modes whereas the electric field lies in the propagation plane in TM-modes. The electric field in both modes is normal to the propagation direction.

boundary, as shown in Figure 9(a). Whispering gallery modes were first observed by G. Mie in 1908 in a number of experiments where light was scattered off a dielectric sphere and analyzed quantitatively by Rayleigh, in 1914, when he was studying the analogous problem in acoustics [41, 42]. Whispering gallery modes are also referred to as "Mie resonances" after their discoverer or "Morphology-dependent resonance" because of their shape dependence.

Whispering gallery modes in a dielectric sphere can be precisely computed from the Helmholtz equation given below:

$$-\nabla^2\mathbf{E} - k^2n^2(r)\mathbf{E} = 0 \tag{3.18}$$

where $\mathbf{E}$ is the electric field, $k = 2\pi/\lambda$ is the magnitude of the wavevector in vacuum

and n is the refractive index of the sphere. The electric field of the whispering gallery modes is typically decomposed into TE-modes and TM-modes, as shown in Figure 9(b). In a TE-mode, the electric field is perpendicular to the propagation plane that is defined as the plane contains the circle formed by the whispering gallery mode, as illustrated in Figure 9(b). In a TM-mode, the electric field lies in the propagation plane. For simplicity, we discuss only the TE-mode to elucidate the basic properties of the whispering gallery modes.

The TE-mode solution to Equation (3.18) is given by:

$$\begin{aligned} \mathbf{E}_{l,m}(r,\theta,\phi) &\sim \frac{1}{sin\theta}\frac{S_l(r)}{kr}\mathbf{Y}_{l,m}(\theta,\phi) \\ S_l(r) &= krj_l(kr) \end{aligned} \tag{3.19}$$

where $j_l(kr)$ and $\mathbf{Y}_{l,m}(\theta,\phi)$ are spherical Bessel and harmonic functions with the mode number l and m, respectively. The resonances can be obtained when solving the differential equations for $S_l(r)$ under the appropriate boundary conditions at the origin and the sphere surface [37, 43, 44, 45].

For experimentalists, it is more intuitive to rewrite Equation (3.18) in a form similar to the Schrödinger equation in quantum mechanics, which describes a particle in the effective potential well due to the discontinuity of the refractive index at the sphere surface [46]:

$$-\nabla^2\mathbf{E} + k^2(1-n^2(r))\mathbf{E} = k^2\mathbf{E}. \tag{3.20}$$

This analogy between the whispering gallery modes and atomic wave function

provides a simple way to understand whispering gallery modes in the framework of quantum mechanics. In this analogy, **E** is regarded as a wavefunction and k^2 is the total energy. The resulting differential equation for the radial direction is therefore given by [1]:

$$-\frac{d^2 S_l(r)}{d^2 r} + V_l(r) S_l(r) = k^2 S_l(r) \tag{3.21}$$

where the effective potential $V_l(r)$ is the sum of potential function describing the discontinuity of the refractive index and centrifugal potential and is dependent on energy k^2:

$$V_l(r) = k^2(1 - n^2(r)) + \frac{l(l+1)}{r^2}. \tag{3.22}$$

For the sphere with a constant refractive index, the effective potential becomes

$$\begin{aligned} V_l(r) &= k^2(1 - n^2(r)) + l(l+1)/r^2, \ r < a \\ V_l(r) &= l(l+1)/r^2, \ r \geq a \end{aligned} \tag{3.23}$$

and is schematically shown in Figure 10.

The classical turning points are defined by the intersection of the energy line, *i.e.*, k^2 and the effective potential well:

$$k^2 n^2(r) = \frac{l(l+1)}{r^2}. \tag{3.24}$$

[1] Valid only when $n(r)$ is constant or piece-wise constant inside the sphere.

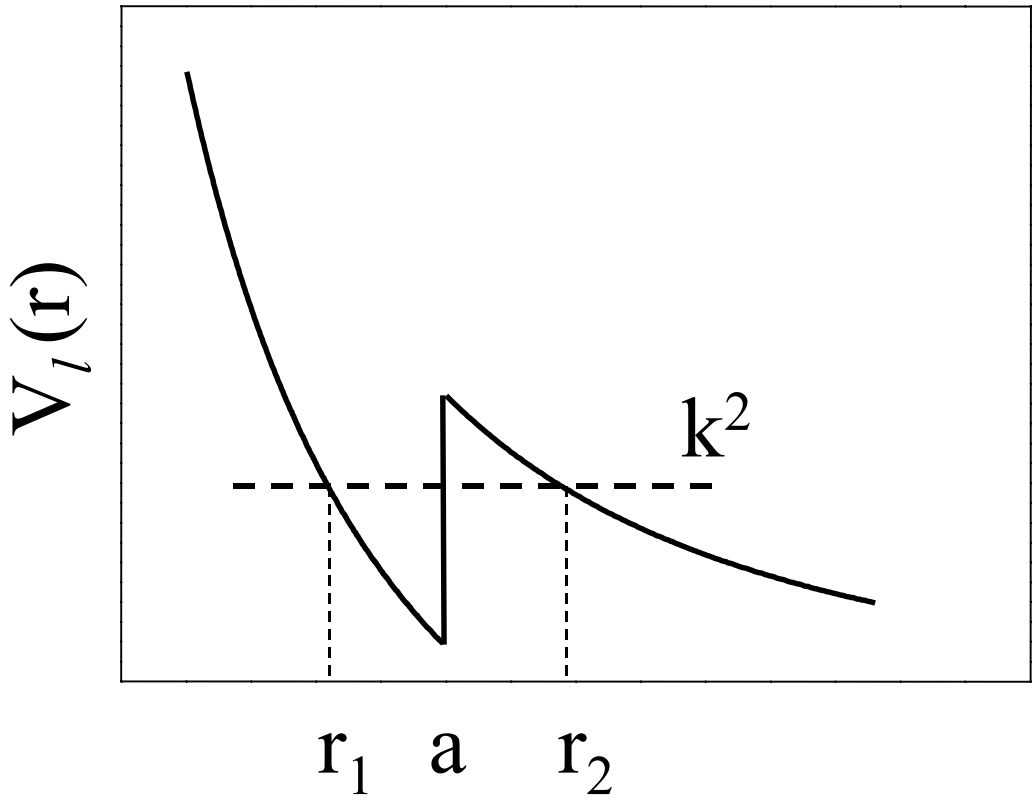

FIGURE 10. Effective potential for a sphere with a constant refractive index. The parameters are chosen as $l = 40$, $k/a = 33$, refractive index $n = 1.47$. $r_1 < r < a$ and $r > r_2$ define two classically allowed regions.

As a result, the two turning points are located at

$$\begin{aligned} r_1 &= (l+1/2)/kn \\ r_2 &= (l+1/2)/k. \end{aligned} \tag{3.25}$$

where we have replaced $[l(l+1)]^{1/2}$ with $l+1/2$.

Unlike the potential well in quantum mechanics, the potential well here is k-dependent. For a given l, only a few discrete resonant states can be trapped in the well, or in other words, can form whispering gallery modes. The range of these resonances is given by $k_B < k < k_T$ where k_B and k_T are the wavenumbers when k^2 hits the bottom and the top of the potential well at the surface ($r = a$). Solving Equation (3.25) gives $k_B = (l+1/2)/na$ and $k_T = (l+1/2)/a$. For the discussion in the remainder of this chapter, it is useful to use a dimensionless size parameter defined as $x = ka$. The range of resonances can then be expressed in terms of size parameter:

$$x_B < x < x_T \tag{3.26}$$

$$x_B = (l+1/2)/n \tag{3.27}$$

$$x_T = (l+1/2). \tag{3.28}$$

Although the wavefunction for whispering gallery modes features different characteristics from their counterparts in quantum mechanics, they can still be described by three mode numbers, p, l, m analogous to the denotation used in quantum mechanics. The radial quantum number p obtained by solving the radial Equation (3.21) denotes the radial modes with $p-1$ nodes inside the sphere.

The angular dependence of whispering gallery modes is described by the spherical harmonic $Y_{l,m}$, as given in Equation (3.19). While l represents the total angular momentum of the electric field, different azimuthal modes are labeled by m with a θ-direction extension of $\theta \approx \pi/2 \pm arccos(m/l)$. The $m = l$ mode lies in the equator with the narrowest θ spread. For large spheres and $p = 1$ mode, l can be approximately expressed as $l \approx n \times x$. Thus the mode number l is nearly equal to the number of wavelengths, λ/n, circulating along the sphere circumference. The spacing between two adjacent l modes with the same radial mode number, known as the free spectral range (FSR), is given by

$$\Delta x = x_{l+1}^p - x_l^p = c/\pi n D \tag{3.29}$$

where c is the speed of light in vacuum. D and n are the diameter and the refractive index of the sphere, respectively.

For an ideal microsphere, different azimuthal modes are degenerate. Slight deformation of the sphere leads to the removal of such degeneracy and is treated as shape perturbation on the otherwise degenerate modes. The resulting splitting of azimuthal modes can be expressed in terms of ellipticity:

$$\omega(m) = \omega_0 \left\{ 1 - \frac{e}{6} \left[1 - \frac{3m^2}{n(n+1)} \right] \right\} \tag{3.30}$$

where ω_0 is the frequency of the degenerate whispering gallery mode for a sphere. $e = (r_p - r_e)/r$ is the ellipticity of the sphere expressed in terms of the polar, equatorial and volume-averaged radii ($r = (r_p r_e^2)^{1/3}$) [47, 48]. For the lowest radial modes, *i.e.* $p = 1$ modes, where $l \approx n \times x = \pi n D/\lambda$, the spacing between two

adjacent azimuthal modes has an even simpler expression:

$$\delta\lambda/\lambda = e/l \tag{3.31}$$

where $\delta\lambda$ is the wavelength separation of the two adjacent m-modes.

Figure 11 shows, as an illustration, the TE-mode electric field distribution along the radial direction for the first two lowest radial modes ($p = 1, 2$) for $l = 40$ and the first order radial mode for $l = 400$. The potential well for $l = 40$ supports three TE modes as well as three TM modes within the range of $x_B = 27.5 < x < x_T = 40.5$. The resonances for TE modes can be accurately calculated with appropriate boundary conditions. They are located at $x_{40}^1 = 31.058854$, $x_{40}^2 = 34.611195$, and $x_{40}^3 = 37.908035$, respectively. For $l = 400$, the first radial mode is located at $x_{400}^1 = 282.51101$. For the first order radial mode shown in Figure 11(a) and (b), the maximum of the electric field is within a wavelength of the sphere surface. Both feature nearly exponential decay outside the sphere with a slightly oscillatory structure. From the figure, it is easily seen that the $l = 400$ mode decays much faster than the $l = 40$ mode, meaning that the diffraction loss for the $l = 400$ mode is much smaller than that of the $l = 40$ mode. For the $p = 2, l = 40$ mode shown in Figure 11(c), the peak of electric field shifts towards the origin. Furthermore, the mode is more spread inside the sphere and decays more slowly than the $p = 1$ mode. As a consequence, $p = 2$ modes feature larger effective mode volume and higher diffraction loss.

For cavity-QED studies, effective mode volume and Q-factor of a cavity are two critical parameters, since the cavity effective mode volume determines the electric field per photon in that mode through the equation $|\mathbf{E}| = \sqrt{\hbar\omega/2\varepsilon_0 V_{eff}}$,

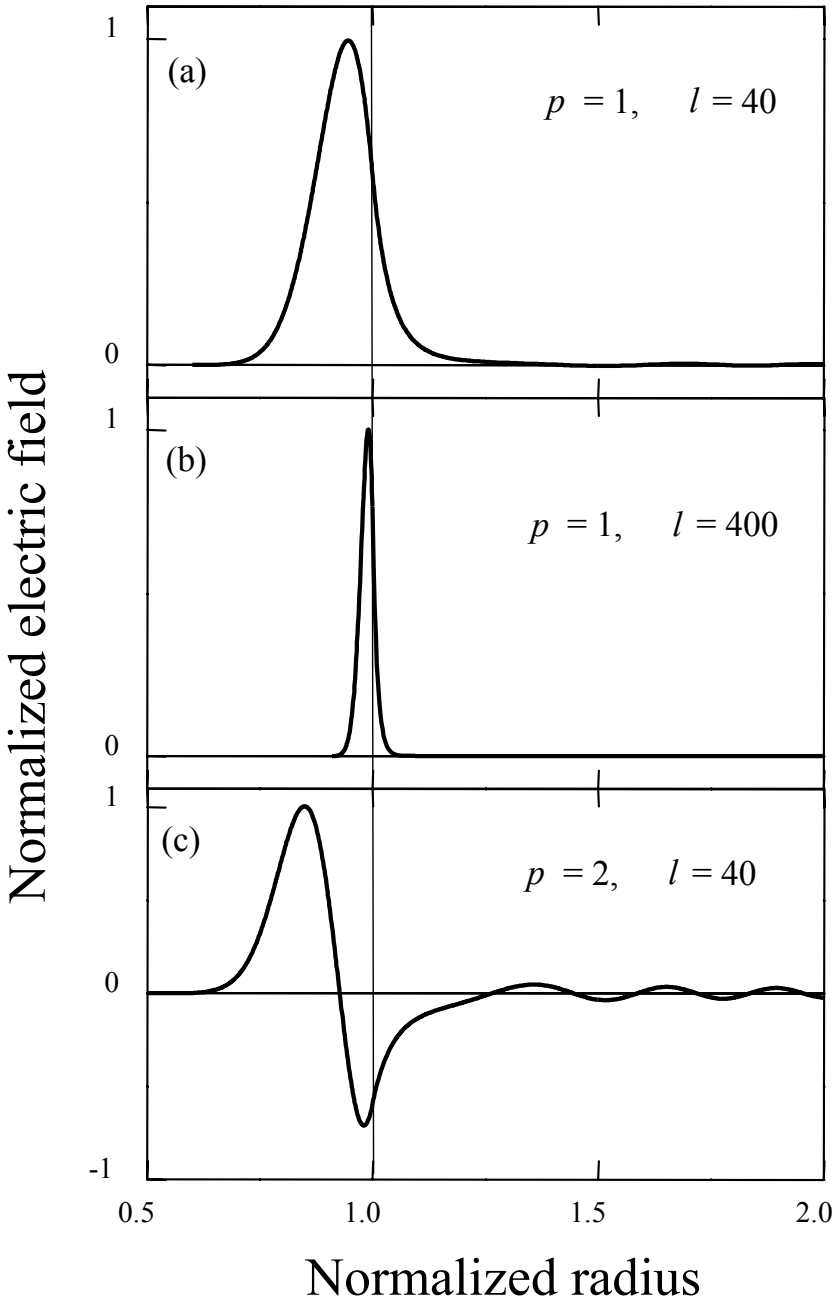

FIGURE 11. Normalized TE-mode electric field of whispering gallery modes with (a): $p = 1,\ l = 40$. (b): $p = 1,\ l = 400$. (c): $p = 2,\ l = 40$. The resonances locate at the size parameter (a): $x_{40}^1 = 31.058854$. (b): $x_{400}^1 = 282.51101$. (c): $x_{40}^2 = 34.611195$. The refractive index of the sphere is 1.47.

while the Q-factor determines how long a photon can be stored in the cavity. As discussed previously, the whispering gallery mode is a surface mode. The effective mode volume is expected to be much smaller than that of the sphere itself. Comparison between Figure 11(a) and Figure 11(c) shows that lower radial modes are more concentrated along the sphere surface, thus featuring smaller mode volume. A theoretical calculation of the effective mode volume for the lowest radial modes with $l = m$ shows that [32]:

$$V_{eff} \approx x^2\lambda^3/60 \tag{3.32}$$

for the atoms at the peak of the electric field.

For a given wavelength λ, the mode volume is approximately proportional to l^2 (proportional to diameter squared), while the sphere volume increases with l^3. For the azimuthal modes with $m < l$, the mode volume scales as $\sqrt{l-m+1}$ [31]. According to the equation, the smallest mode volume is achieved for $l = m$ resulting from the narrowest θ distribution. As a result, the mode with $l = m$ and the lowest radial mode number features the smallest effective mode volume.

The Q-factor of a dielectric sphere is determined by a number of factors. In addition to diffraction loss, Rayleigh scattering and self-absorption, surface roughness, and surface contaminants can also cause Q-spoiling. The overall Q-factor of a microsphere can thus be formulated as:

$$Q^{-1} = Q^{-1}_{intrinsic} + Q^{-1}_{s.s.} + Q^{-1}_{s.c.} \tag{3.33}$$

where $Q_{s.s.}$ and $Q_{s.c.}$ are related to surface scattering and surface contaminants,

respectively. $Q^{-1}_{intrinsic}$ can be further decomposed into

$$Q^{-1}_{intrinsic} = Q^{-1}_{diffraction} + Q^{-1}_{Rayleigh} + Q^{-1}_{absorption}. \tag{3.34}$$

According to the previous discussion, the electric field decays extremely fast outside the sphere. A theoretical calculation shows that for relative large spheres ($D/\lambda \geq 15$), $Q_{diffraction}$ exceeds 10^{11} [44, 49, 50, 51].

The Q-factor for Rayleigh scattering and self-absorption is determined by

$$Q^{-1}_{Rayleigh} + Q^{-1}_{absorption} = \frac{\alpha\lambda}{2\pi n} \tag{3.35}$$

where α is the optical attenuation including both Rayleigh scattering and the absorption loss. For a fused silica microsphere, optical attenuation at $\lambda = 633$ nm is approximately 7dB/km, with 5 dB/km from Rayleigh scattering and 2 dB/km from self-absorption, while at $\lambda = 1.55$ μm, Rayleigh scattering loss and self-absorption loss are reduced to 0.15 dB/km and 0.2 dB/km, respectively. Therefore, in the red or infrared regime, the Q-factor due to Rayleigh scattering and self-absorption is nearly 10^{10} for a fused silica microsphere.

The Q-factor due to the surface roughness or surface scattering is given by [49]:

$$Q^{-1}_{s.s} = \frac{2\pi^2\sigma^2 B}{\lambda^2 D} \tag{3.36}$$

where σ and B are the root-mean-square (rms) of the surface fluctuation and the correlation length of surface inhomogeneities. For a 100 μm diameter fused silica

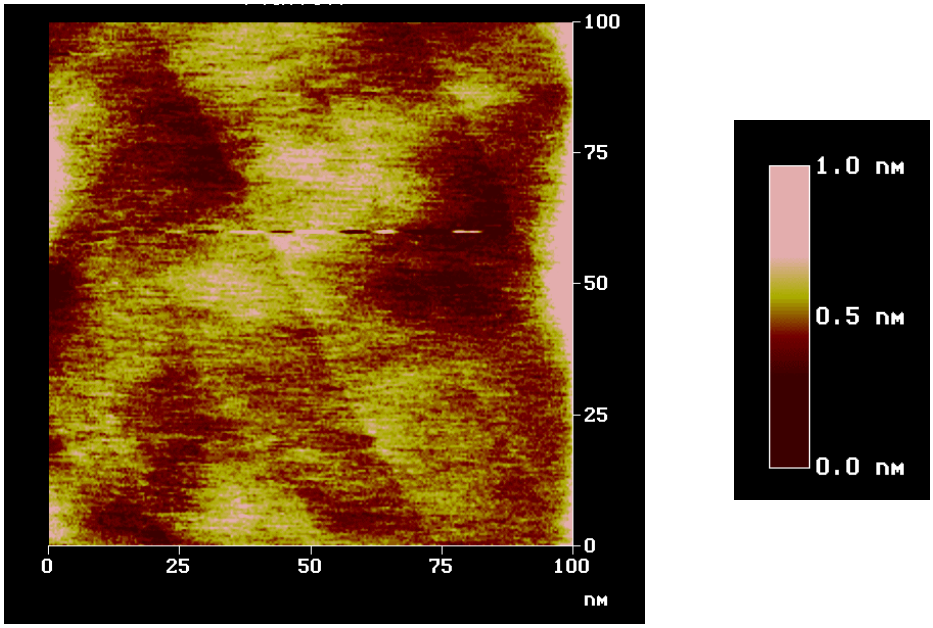

FIGURE 12. AFM surface image of a fused silica microsphere surface. The diameter of the sphere is approximately 100 μm. The correlation length of surface inhomogeneities is $\sim$ 20 nm and the root-mean-square of the surface fluctuation is of order 0.3 nm, corresponding to a $Q_{s.s.}$ of 10^9 at 633 nm.

microsphere σ is typically 0.3 nm and B $\sim$ 20 nm as shown in Figure 12, leading to a $Q_{s.s}$ of 10^9 at $\lambda = 633$ nm. For a polystyrene microsphere, as shown in a confocal microscopy image in Figure 13, the overall Q-factor is dominated by $Q_{s.s.}$ due to the pronounced surface roughness ($\sigma \sim 0.5$ μm). For this type of microspheres the Q-factor is in the range of $10^3 \sim 10^4$.

Surface contamination is another important factor that limits the Q-factor of the whispering gallery mode. Studies show that adsorption of water vapor onto a fresh SiO_2 (fused silica microsphere) surface not only leads to surface scattering and absorption of light, but also works as a substrate for further deposition of microparticles [52]. It is found that the Q-factor drops by a factor of five from

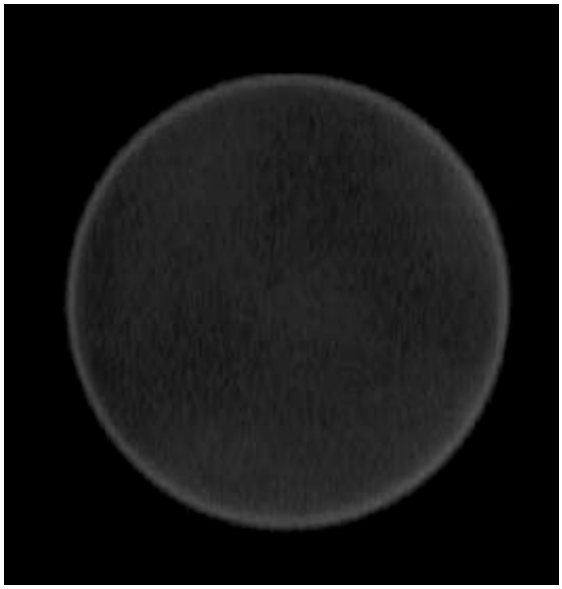

FIGURE 13. Confocal microscope image of a polystyrene sphere with a 100 μm diameter reveals the surface roughness.

9×10^9 in fresh fused silica microspheres in the first five minutes, and stays at 10^9 for ten hours. The original Q-factor is resumed after the water-contaminated spheres are baked at 400 °C for 30 seconds [49].

Taken together, for a fused silica microspheres, the overall Q-factor is of order 10^9, limited by the combined effects of Rayleigh scattering, self-absorption, surface roughness, and surface contaminants. However, for a polystyrene sphere the overall Q-factor is determined by the overwhelming surface scattering due to the nature of the polymer, resulting in a Q-factor of order 10^3 to 10^4.

Characterization of Whispering Gallery Modes

Whispering gallery modes can be launched and collected in many ways. To efficiently launch a whispering gallery mode, not only should the laser frequency or

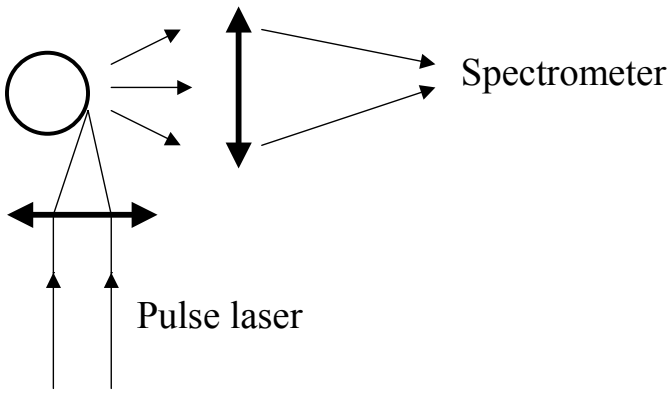

FIGURE 14. Setup for excitation and collection of whispering gallery modes (I). A broad band pulsed laser is focused onto the edge of a sphere and the scattered light is collected at 90° off the incident direction.

wavelength be on resonance, but also the mode matching between the excitation laser beam and the mode to be excited is important.

In the simplest setup shown in Figure 14, a broad band pulsed laser is focused onto the edge of the sphere where the light is coupled into the whispering gallery modes at a glancing angle. The scattered light is collected and sent to a spectrometer at an angle of 90° from the incident direction. A typical scattered light spectrum is given in Figure 15, where only TE-modes are excited due to the polarization of the Ti:Sapphire pulsed laser used. Since the laser has finite angular spread, in addition to the first order radial modes that have the best mode matching, the second order radial modes can also be excited, leading to the doublets observed in the spectrum. Sphere diameter can be easily determined from the free spectral range using $\Delta\lambda = \lambda^2/n\pi D$, providing a convenient way to measure the sphere size. However, in the spectrum given in Figure 15, the fine resonance struc-

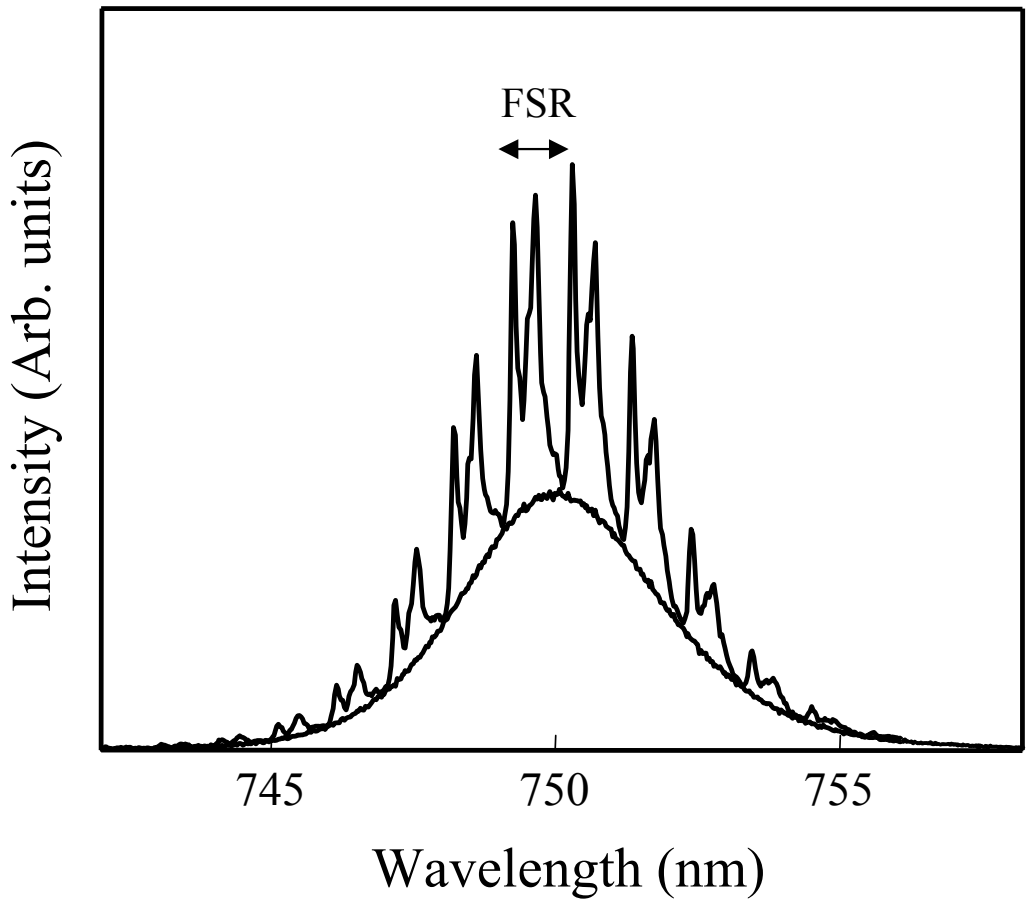

FIGURE 15. Spectrum of whispering gallery modes is obtained by collecting the laser light scattered off the edge of a 118 μm diameter fused silica microsphere. In this case, only TE modes are excited due to the laser polarization. Doublets arise from the first and the second radial modes. Laser spectrum is also shown for a reference.

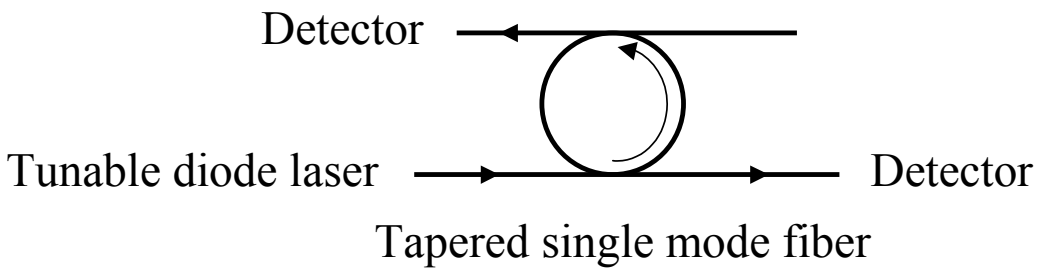

FIGURE 16. Setup for excitation and collection of whispering gallery modes (II). A polished and tapered single-mode fiber is placed against the equatorial region of a sphere. Whispering gallery modes are launched and collected through the fiber via evanescent coupling.

ture in whispering gallery modes is lost due to the inadequate spectral resolution.

In the second setup, the microsphere is placed in the evanescent field of a polished single mode fiber as shown in Figure 16. The fiber is tapered at the contact region with the transverse dimension of a few microns for better coupling [53, 54]. The whispering gallery modes can be launched by a tunable diode laser propagating through the fiber and can be coupled out via either the same fiber or another single mode fiber at the other side of the sphere. In this setup, only the first order radial modes are excited due to nearly perfect mode matching. Nearly 100% energy transfer from the fiber to the whispering gallery mode on resonance has been reported recently [54]. Due to its simplicity in alignment, this setup is a very promising candidate for optoelectronics and integrated optics applications. Applications of this setup can also be found in add/drop switches in telecommunications [54] and a recently proposed experiment in quantum entanglement using microspheres [24].

A third setup, which we will use throughout the dissertation unless otherwise stated, differs slightly from the second setup in that a high refractive index prism instead of single mode fiber is used as an optical coupler to launch the whispering gallery modes, as illustrated in Figure 17. Excitation can be provided by focusing the laser beam onto the inner surface of the prism. The gap between the microsphere and the prism can be adjusted by a piezoelectric translation stage. With the laser reflected off the prism at the critical angle between the microsphere and the prism, the first order radial modes are mostly excited due to their strongest mode matching. 80% coupling efficiency is reported when the sphere is in contact with the prism [31]. When the whispering gallery modes are launched at an incident angle smaller than the critical angel, higher order radial modes that lie deeper inside the sphere can also be preferentially excited. On the other hand, when the angle is larger than the critical angle, the lowest order radial modes are still excited, but with lower coupling efficiency.

In this setup, two approaches are suitable to collect the resonant emission from the whispering gallery modes. The first and simpler approach is to send the scattered light off the microsphere to the detector. In this case, however, the signal is extremely weak for high-Q microspheres due to the weak surface scattering. Furthermore, the leakage of the pumping light into the detector results in a strong background and sometimes even causes interference between the pumping light and the emission. To avoid the problems mentioned above, a more sophisticated method is employed where we make use of so-called precession modes for the collection of the resonant emission [55, 56]. As shown in Figure 17(b), the laser beam is inclined with respect to the equatorial plane to excite the whispering

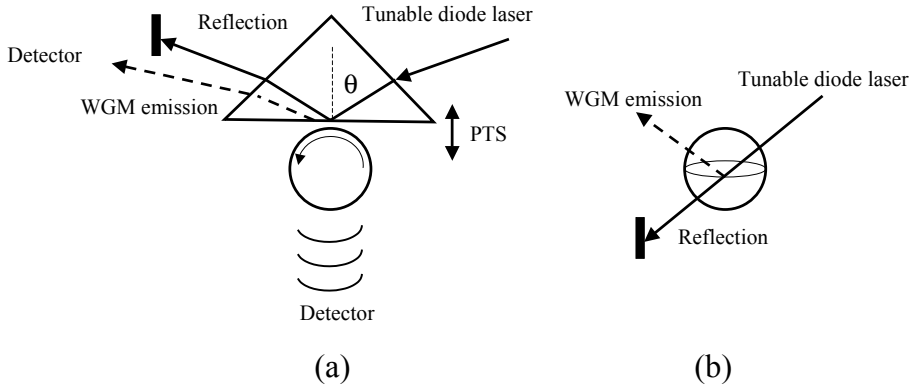

FIGURE 17. Setup for excitation and collection of whispering gallery modes (III). (a): Top view of the setup. A prism on piezoelectric translation stage is placed close to the sphere. The whispering gallery modes are excited by a tunable diode laser via frustrated total internal reflection. The whispering gallery modes can be detected either by the emission through the prism or by the scattered light off the sphere. (b): Side view. The emission of whispering gallery modes can be collected at the direction symmetric with the reflection beam.

gallery modes. The resonant emission is coupled out by the prism and collected in the direction symmetric to the reflection beam. Typically 5° inclination is enough to well separate the pumping beam and the emission. Therefore, $m \sim l$ modes that lie in the vicinity of the equatorial plane can still be efficiently excited.

Figure 18 shows the typical whispering gallery mode structure in a fused silica microsphere when excited at the critical angle. The diameter of the sphere is 140 μm, corresponding to a free spectral range of 1 nm at $\lambda = 800$ nm. The doublets in the large spectral scale are from the first two radial modes. When we expand a portion of one of the resonances using finer laser scanning step size, a series of azimuthal modes emerge as a result of removal of m-mode degeneracy. The spacing between two adjacent azimuthal modes is 0.004 nm, corresponding to

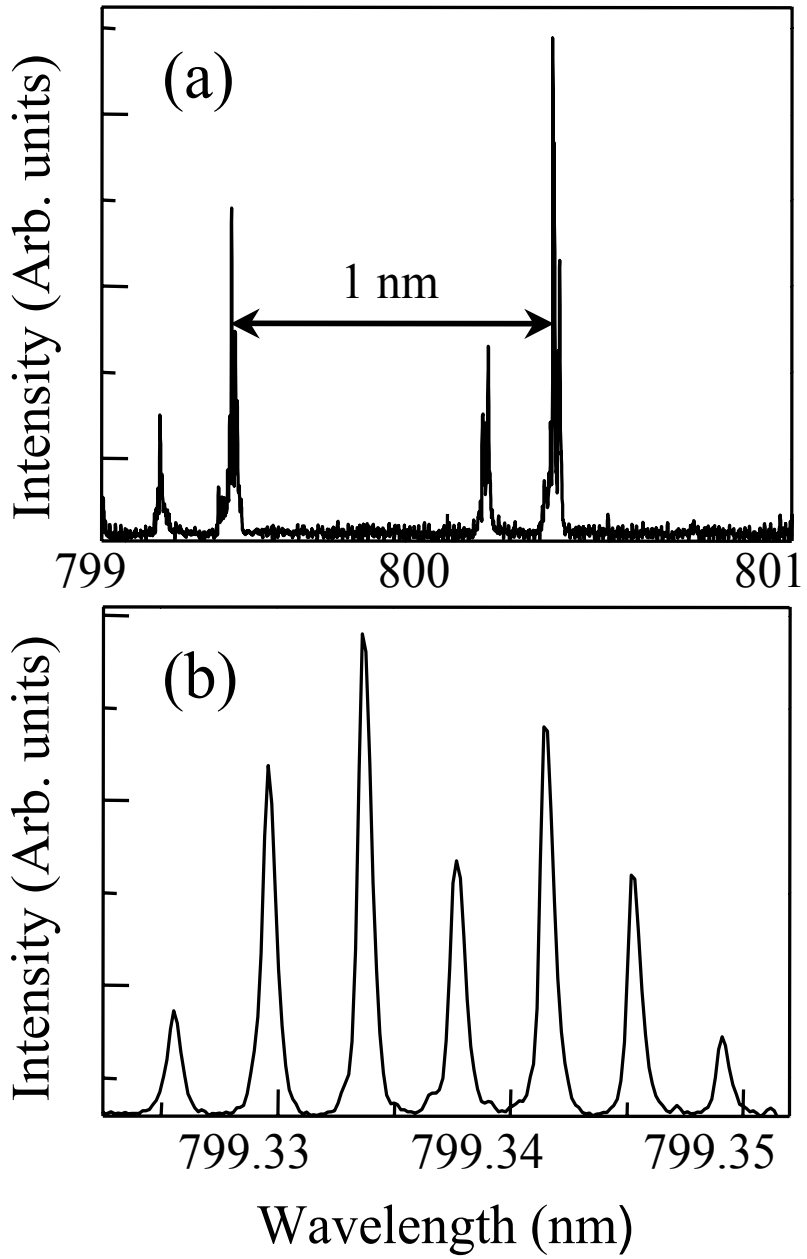

FIGURE 18. Whispering gallery mode structure of a 140 μm diameter fused silica microsphere. (a): Free spectral range and two lowest radial modes. (b): Expanded portion of one of peaks in (a). A series of azimuthal modes emerge due to the deformation of the sphere. The spacing between two adjacent azimuthal modes is approximately 0.004 nm, corresponding to an ellipticity of 0.4%.

an ellipticity of $e \approx 0.4\%$, assuming that $l \approx 800$ for a D = 140 μm silica sphere at $\lambda = 800$ nm. Typically, the ellipticity of the microspheres prepared under our laboratory conditions is less than a few percent.

In order to measure the Q-factor of the microsphere, the prism is pulled away from the sphere to reduce the loading effects from the prism and the corresponding resonant scattering spectra are given in Figure 19(a). From top to bottom, the sphere undergoes a transition from overloaded to underloaded regimes when the gap increases. During this process, different m-modes experience nearly the same output coupling loss through the prism, leading to the similar Q-factor in all these m-modes in each spectrum. The sharpest resonances are obtained in Figure 19(b) where the gap $l_{gap} \gg \lambda/2\pi$, corresponding to a Q-factor of order 10^7. It should be noted that the Q-factor obtained here is still limited by the laser scanning step size. Further studies in the time domain using ring-down spectroscopy reveals that the Q-factor exceeds 7×10^8. A detailed discussion of time-domain ring-down spectroscopy will be provided in Chapter VII.

In cavity-QED studies, the whispering gallery modes should match the atomic or excitonic transition for a resonant coupling. It has been shown that the frequency of a whispering gallery mode is dependent upon the temperature at the rate of $\Delta\nu/\nu = -5 \times 10^{-6}/\Delta T$, which gives a frequency shift of 2.5 GHz/K at $\lambda = 600$ nm [32]. Therefore, a thermo-electric plate can be used for fine adjustment of the frequency. Alternatively, we can also implement a tuning scheme by mechanically squeezing the sphere. The resonance frequency is tuned as a result of the strain-induced change in the refractive index and the circumference of the microsphere. Earlier studies have demonstrated that the Q-factor of the sphere

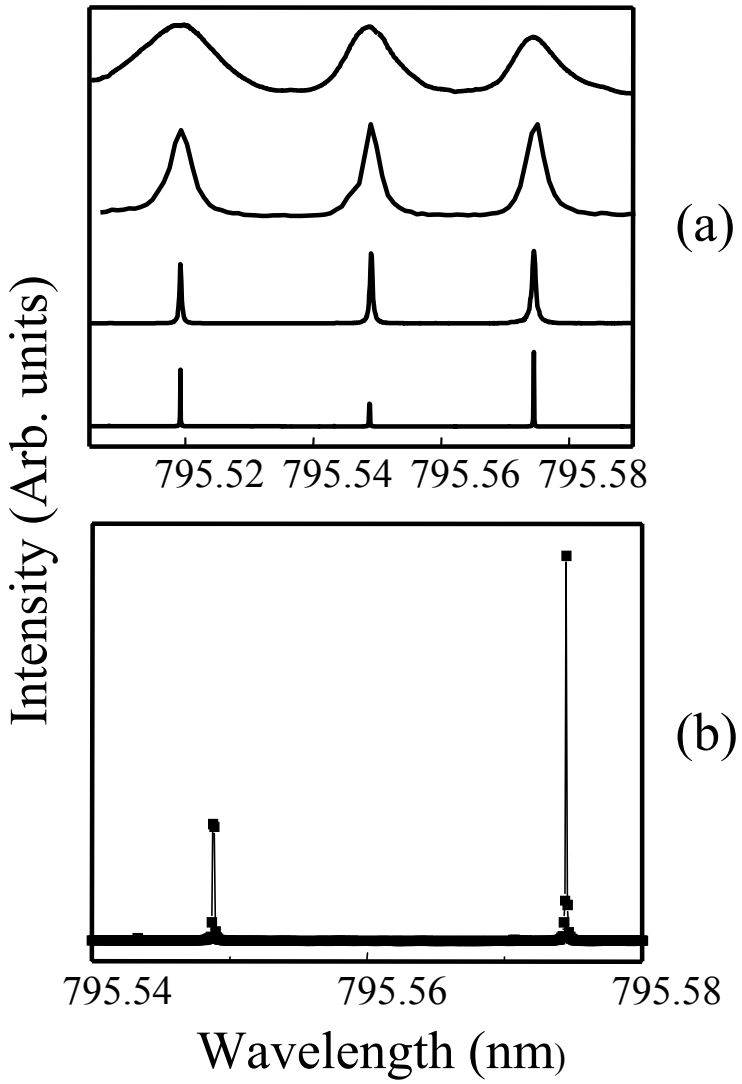

FIGURE 19. Measurement of the intrinsic Q-factor of whispering gallery modes. (a): Resonant scattering spectra of whispering gallery modes shown from top to bottom are obtained when the prism is pulled away from the microsphere . (b): Intrinsic Q-factor $\geq 8\times10^6$ is obtained when loading effects from the prism becomes negligible. Note the Q-factor is still limited by laser scanning step size.

can be maintained at 10^8, while the frequency varies over the whole free spectral range [38].

As discussed above, a typical microsphere made in our laboratory is elongated along the stem direction during fabrication due to the presence of gravity. However, at the cross section through the equator (perpendicular to the stem), the whispering gallery modes still see the circular shape. Consequently, the emission from this type of microsphere is isotropic. Recently, theoretical calculation and experimental results have shown that the whispering gallery modes feature highly directional emission in a so-called deformed sphere [57, 58], with the deformation occurring at the equatorial plane. Recent experiments by Scott Lacey in our group show that the Q-factor and directional emission is very sensitive to ellipticity compared with the conventional microspheres. With 0.7% ellipticity, the deformed microsphere features highly directional emission [59].

Summary

In this chapter, we have presented the characterization of the whispering gallery modes in a dielectric microsphere in order to develop an optical resonator for future cavity-QED studies. We have also shown the experimental approaches to excite and couple out the whispering gallery modes in such a dielectric microsphere which will be used in this dissertation. Various factors affecting the Q-factor of the whispering gallery modes are discussed along with the experiments. With a fused silica microsphere, we have achieved a resolution-limited Q-factor approaching 10^7 (7×10^8 is achieved as demonstrated later in this dissertation), making it a very promising candidate for cavity-QED studies in the high-Q regime. With a

polystyrene sphere, on the other hand, a Q-factor of a few thousand is achieved due to the dominant surface scattering. Therefore, it is more suitable to use this type of microsphere for cavity-QED studies in the low-Q regime.

CHAPTER IV

COMPOSITE SYSTEM OF GaAs QUANTUM WELL AND FUSED SILICA MICROSPHERE

Introduction

The optical properties of a semiconductor at the fundamental band edge are determined by excitons. The exciton is a bound state of an electron-hole pair due to the attractive Coulomb interaction. Figure 20 shows the energy structure of the exciton. In semiconductor nanostructures such as semiconductor quantum wells and quantum dots, excitons are confined by a semiconductor with a larger bandgap. The sketch in Figure 21 gives as an example a 13 nm GaAs/AlGaAs multiple quantum well structure and its energy structure. The alternating AlGaAs and GaAs layers are grown on the GaAs substrate. A GaAs capping layer is used to passivate the AlGaAs surface. This electronic confinement changes the energy structure and the density of states of the exciton and can also lead to an improved electronic performance of solid-state devices. For instance, lower threshold and larger modulation bandwidth are theoretically predicted and experimentally realized in semiconductor quantum well lasers or quantum dot lasers [60, 61].

In addition to the electronic confinement, optical confinement can be achieved by incorporating semiconductor nanostructures such as quantum wells and quantum dots in a semiconductor microcavity. The semiconductor microcavity typically consists of a stack of alternating quarter-wave dielectric layers with different

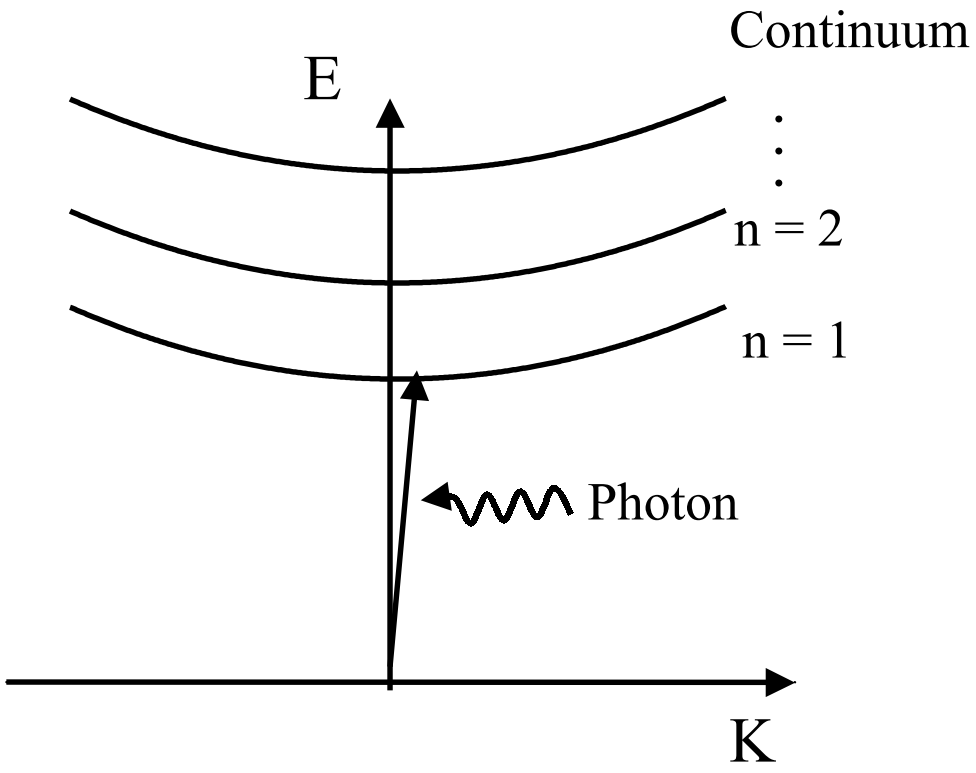

FIGURE 20. Exciton energy structure. Excitons form via Coulomb interaction between electrons and holes. Upon absorption of a photon, exciton undergoes a transition from ground state to excited state. At low density, the crystal ground state and the lowest excitonic state can be viewed as a two-level system analogous to an atomic system.

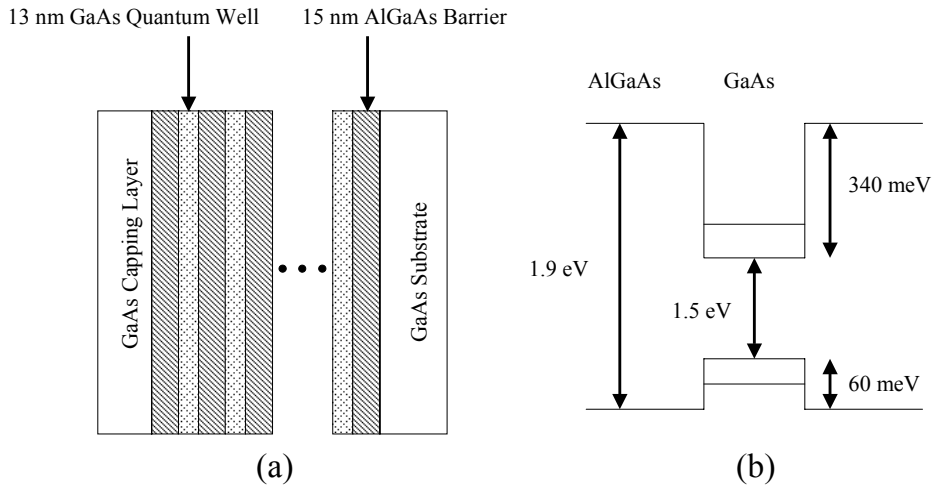

FIGURE 21. GaAs/AlGaAs quantum well and its energy structure. (a): 13 nm GaAs/AlGaAs multiple quantum wells structure. The quantum wells are grown on the GaAs substrate and capped by a GaAs capping layer. (b): Energy Structure of GaAs/AlGaAs quantum well.

refractive indices as described in Chapter I. Typical Q-factors of the above semiconductor microcavities are in the range of 10^3 to 10^4. In order to enter the strong coupling regime where the dynamics of the cavity-exciton system is qualitatively changed by the addition of even a single photon or a single exciton, a much higher Q-factor is required.

As discussed in Chapter III, dielectric microspheres are unique and versatile optical microresonators. In a dielectric microsphere, whispering gallery modes form through total internal reflection along the curved boundary. Whispering gallery modes confined within a wavelength of the sphere surface can feature both high Q-factor and small mode volume.

To use dielectric microspheres for cavity-QED studies, one can place a semiconductor nanostructure sample, such as a semiconductor quantum well or quan-

tum dot, in the evanescent field of the whispering gallery mode of the microsphere, as shown in Figure 22. Effectively, we place the exciton in the electric field of the whispering gallery mode. This particular scheme not only takes advantage of the high Q-factor and small mode volume of whispering gallery modes, but also allows for separate engineering of the optical and electronic confinements. In this setup, whispering gallery modes provide a three dimensional photonic confinement, whereas electronic confinement is given by the semiconductor nanostructure. In particular, this scheme allows one to incorporate almost all different types of nanostructures, as shown later. In this chapter, we will focus on studies of the composite system of GaAs/AlGaAs quantum wells and whispering gallery modes in a fused silica microsphere. The composite nanocrystal and polystyrene microsphere in the low-Q regime will be discussed in Chapter VI, followed by the composite nanocrystal and fused silica microsphere in the high-Q regime.

In order to characterize this composite system, the following issues should be addressed. 1. How is the spontaneous emission coupled into the whispering gallery modes? 2. What is the intrinsic Q-factor of the composite system? 3. How strong is the dipole interaction between the exciton in a quantum well and the electric field in whispering gallery modes? 4. What are the limitations of the composite system?

Photoluminescence From the Composite Quantum Well and Microsphere System

Our first experiment is designed to investigate the photoluminescence from the composite system.

The basic experimental setup for the photoluminescence measurement is

shown in Figure 22. In its simplest geometry, the composite system consists of a microsphere in contact with a quantum well sample. We also place a high index prism on the other side of the microsphere for output coupling of whispering gallery modes. A piezoelectric translation stage is used to vary the gap between the prism and the microsphere to avoid any strain on the quantum well samples and to minimize the output coupling loss through the prism. The composite system can be excited by launching whispering gallery modes on the equator of the sphere via frustrated total internal reflection from the prism or can be excited by directly creating electron-hole pairs or excitons in the quantum well sample. Photoluminescence coupled into whispering gallery modes of the composite system is collected from the side of the prism. Conventional photoluminescence that is not coupled into whispering gallery modes can also be collected from the side of the prism. The uncoupled photoluminescence, however, is along a slightly different direction as indicated in Figure 22. The whole setup is attached to the cold finger of a cryostat. All measurements are performed at 10 K unless otherwise specified. To elucidate mode structures of the composite quantum well-microsphere system and to demonstrate evanescent coupling between excitons and relevant whispering gallery modes, we present here results obtained from a system that uses a 110 μm diameter sphere and a GaAs quantum well sample (shown in Figure 21) that exhibits strong inhomogeneous broadening at low temperature. The sample is grown by MOCVD and contains 8 periods of GaAs/AlGaAs quantum wells with well width of 13 nm and barrier width of 15 nm. The first quantum well is located 100 nm from the sample surface. The sample also contains a bulk GaAs substrate layer 870 nm beneath the sample surface. In this first experiment, the prism is in

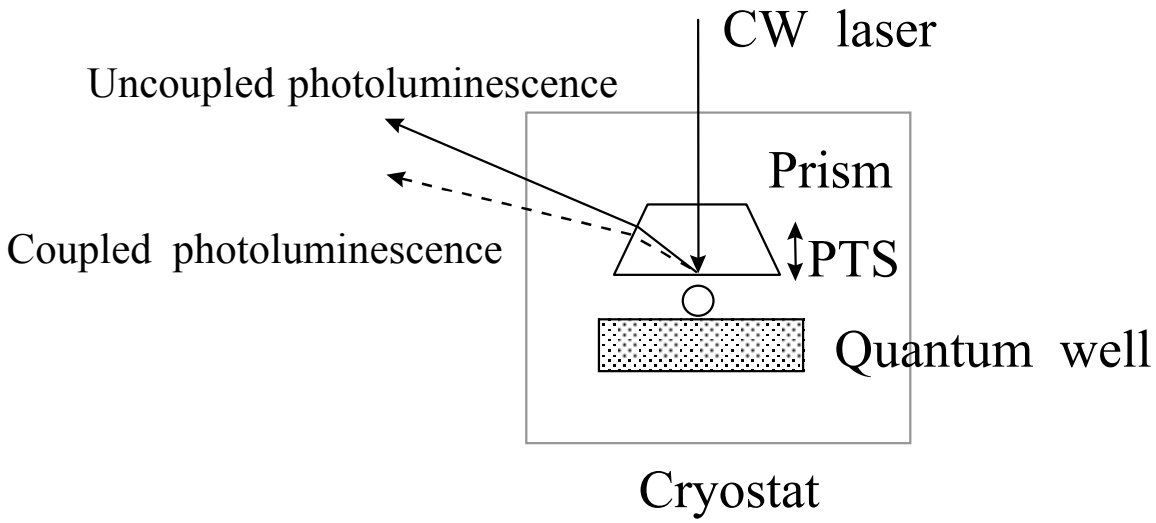

FIGURE 22. Experimental setup of composite quantum well and microsphere system for photoluminescence measurement. The system is excited by a continuous wave (CW) laser. The solid line represents photoluminescence coupled into the whispering gallery modes and then coupled out through prism. The dotted line represents photoluminescence that is not coupled into the whispering gallery modes. The gap between the sphere and the prism is controlled by a piezoelectric translation stage (PTS).

contact with the microsphere to obtain maximum coupling efficiency.

Figure 23 shows photoluminescence spectra collected from one side of the prism. For these measurements, the composite system is excited with a continuous wave Ti:Sapphire laser at 740 nm and with an intensity of order 5 W/cm^2. Figure 23(a) is the spectrum of photoluminescence that is not coupled with whispering gallery modes (referred to as uncoupled photoluminescence). Figure 23(b) is the spectrum of photoluminescence that is coupled with relevant whispering gallery modes (referred to as coupled photoluminescence). Similar results are also obtained at much lower excitation intensities.

The spectrum of uncoupled photoluminescence shown in Figure 23(a) exhibits two resonances. The resonance at 805 nm is from heavy hole excitons in the quantum well and the resonance at 818 nm is from excitons in the bulk GaAs. The photoluminescence spectrum in Figure 23(a) is also identical to the photoluminescence spectrum obtained in the absence of the microsphere. In addition, separate absorption measurements show a Stokes shift of 2 nm between the absorption and photoluminescence resonance for heavy hole excitons in the quantum well.

In comparison, the spectrum of coupled photoluminescence shown in Figure 23(b) shows a dominant contribution from heavy hole excitons in the quantum well and nearly negligible contribution from excitons in the bulk GaAs. The coupled photoluminescence also exhibits a pronounced periodic doublet mode structure with the mode spacing determined approximately by the free spectral range of the sphere. An analysis of the polarization of the coupled photoluminescence shows that the higher energy resonance in the doublet structure is TM-polarized while the lower energy resonance is predominantly TE-polarized. It should be noted that

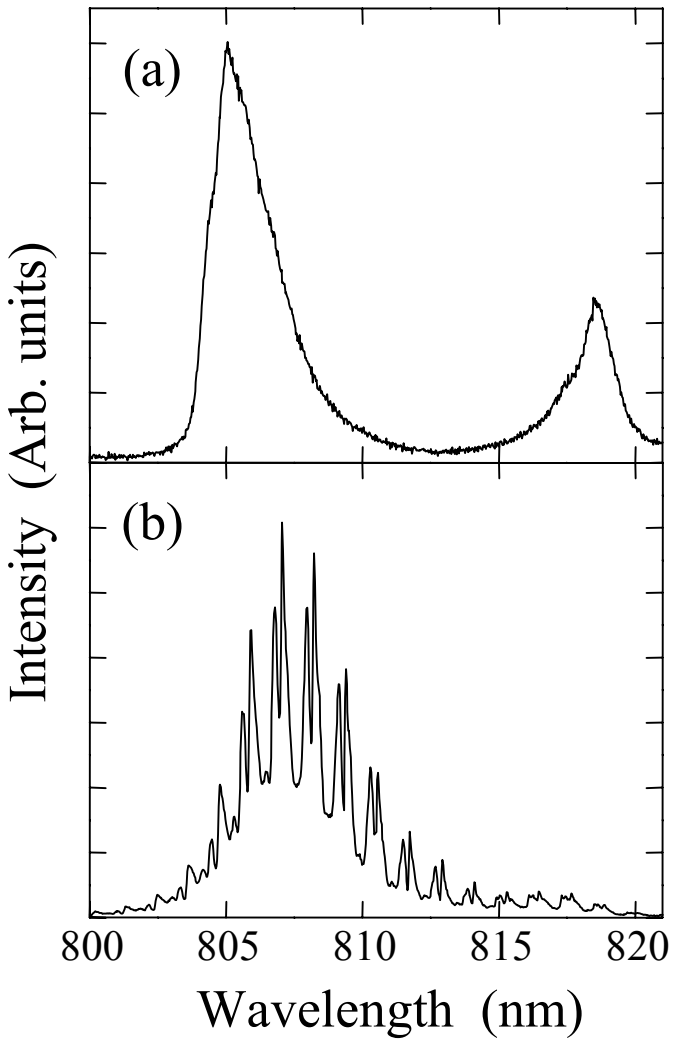

FIGURE 23. Photoluminescence spectrum of the composite quantum well and microsphere system at 10 K. The prism is in contact with the microsphere. (a): Photoluminescence not coupled into the whispering gallery modes. (b): Photoluminescence coupled into the whispering gallery modes. Whispering gallery modes are not fully resolved due to the limited spectral resolution of the spectrometer used.

during the measurement, the prism is in contact with the quantum well sample. While the background is completely eliminated when the prism is pulled away from the microsphere, the large background observed in Figure 23(b) is due to the scattered light off the contact region.

The absence of the photoluminescence from bulk GaAs layer shows that the coupling efficiency into the whispering gallery modes is depth dependent. To estimate the capture depth of whispering gallery modes in the contact region, we have used a number of single quantum well samples and have also used chemical etching to vary the distance between the quantum well layer and the sample surface [62]. Efficient coupling between whispering gallery modes and heavy hole excitons in a single GaAs quantum is observed when the quantum layer is even 300 nm away from the sample surface, suggesting that the capture depth can be as large as a few hundred nanometers in the contact region. This result is further confirmed by a later theoretical calculation [63].

During the experiment, it is found that the strain induced by the prism causes spectral broadening in photoluminescence and sometimes even damages the whole sample. To avoid these problems, our later experiments are performed using an improved setup where a piezoelectric translation stage is employed to adjust the small gap between the prism and the microsphere.

Figure 24 shows spectra of both uncoupled and coupled photoluminescence using the improved setup. The quantum well sample is identical to the one used in the previous experiment. In sharp contrast, the background or uncoupled photoluminescence emerging in Figure 23(b) completely disappears. The coupled photoluminescence spectra with TE and TM polarization feature periodic mode structures

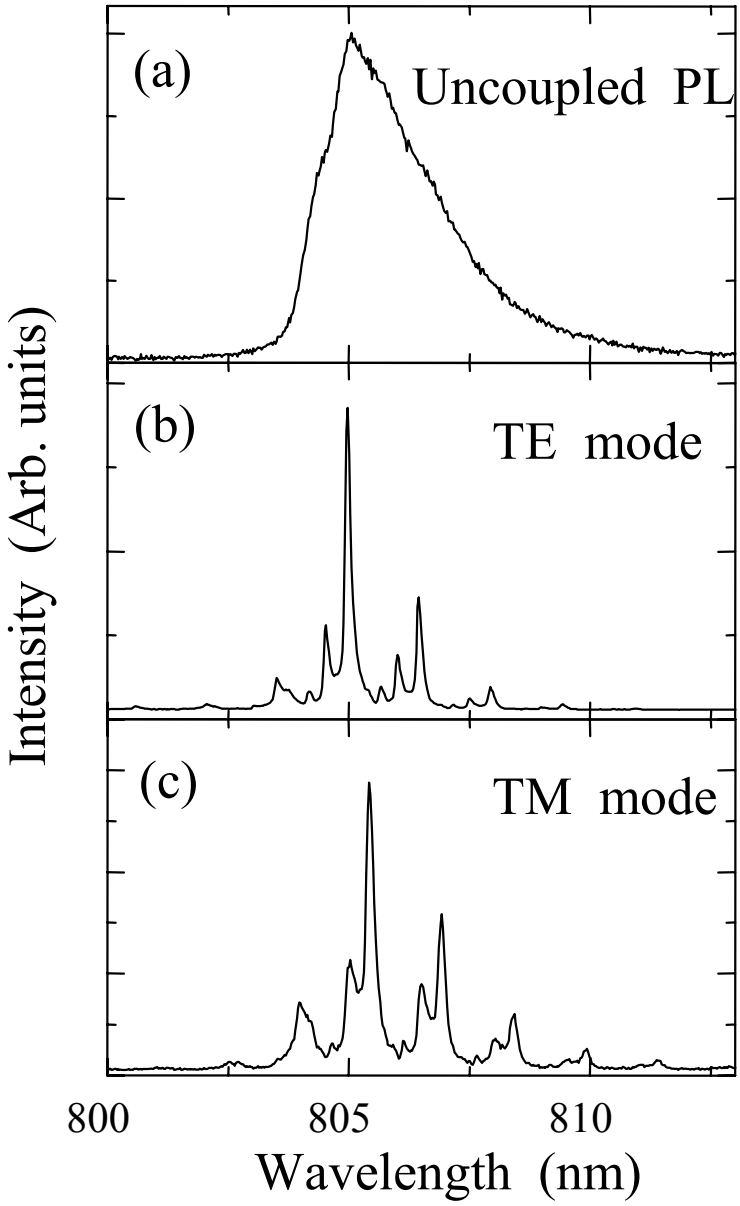

FIGURE 24. Photoluminescence spectrum of the composite quantum well and microsphere system at 10 K. A piezoelectric translation stage is used to generate a gap between the prism and the microsphere. (a): Photoluminescence not coupled into the whispering gallery modes. (b): Photoluminescence coupled into the whispering gallery modes with TE polarization. (c): Photoluminescence coupled into the whispering gallery modes with TM polarization.

with a free spectral range (FSR) of 1.5 nm, determined by the diameter of the microsphere.

It should be pointed out that the spectral linewidth (0.2 nm) of the mode structures shown in Figure 23(b) and Figure 24(b), (c) does not determine the Q-factor of the composite system. Data shown in Figures 23 and 24 are obtained by using a CCD detector, which limits spectral resolution to 0.08 nm.

Measurement of the Q-Factor of the Composite Quantum Well and Microsphere System

Our second experiment is designed to measure the intrinsic Q-factor of the composite system. The Q-factor can be spoiled either by the refractive loss through the prism or quantum well sample, or by the loss due to the exciton absorption, as illustrated in Figure 25. The overall Q-factor of the system can be described by:

$$Q^{-1} = Q^{-1}_{refractive} + Q^{-1}_{absorption} + Q^{-1}_{intrinsic} \tag{4.37}$$

where $Q^{-1}_{refractive}$ corresponds to the output coupling loss through the prism and the quantum well sample, and $Q^{-1}_{absorption}$ is determined by the loss due to the exciton absorption.

Figure 26 shows a small portion of the coupled-photoluminescence spectrum in Figure 23. A photo-multiplier tube instead of a CCD is used to improve the spectral resolution. The sphere in this case is in contact with the sample. As shown by Figure 26, each resonance in Figure 24(b) and (c) can contain many whispering gallery modes due to the removal of spherical degeneracy discussed in Chapter III. Although the spectral linewidth of 0.01 nm shown in Figure 26 is still limited by the spectrometer resolution, the measurements indicate that the

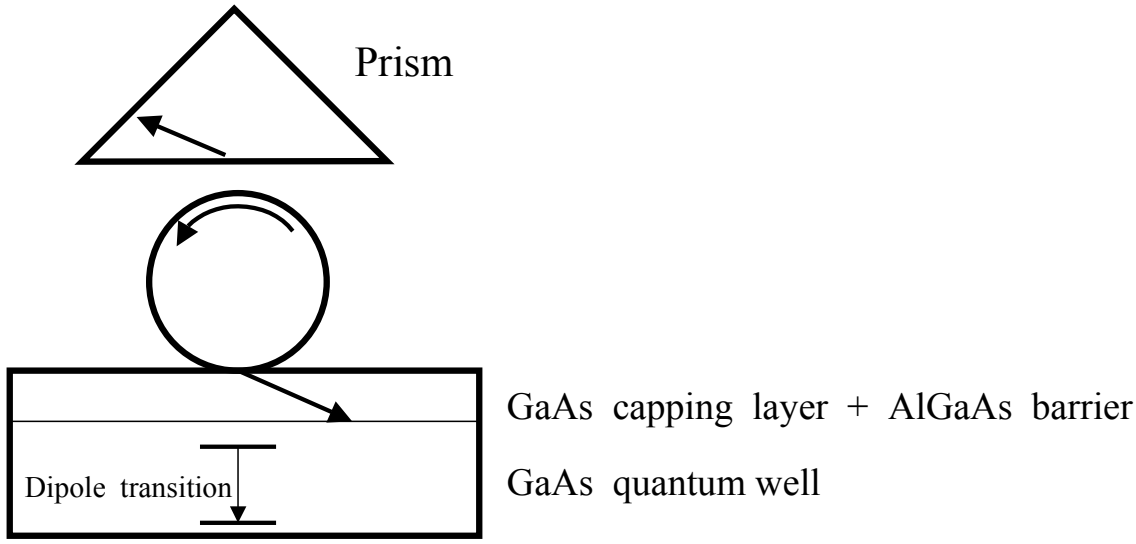

FIGURE 25. Mechanisms for Q-spoiling of the composite quantum well and microsphere system. Q-factor of the composite quantum well and microsphere system can be spoiled either by the refractive loss through prism or quantum well sample, or by exciton absorption via dipole coupling.

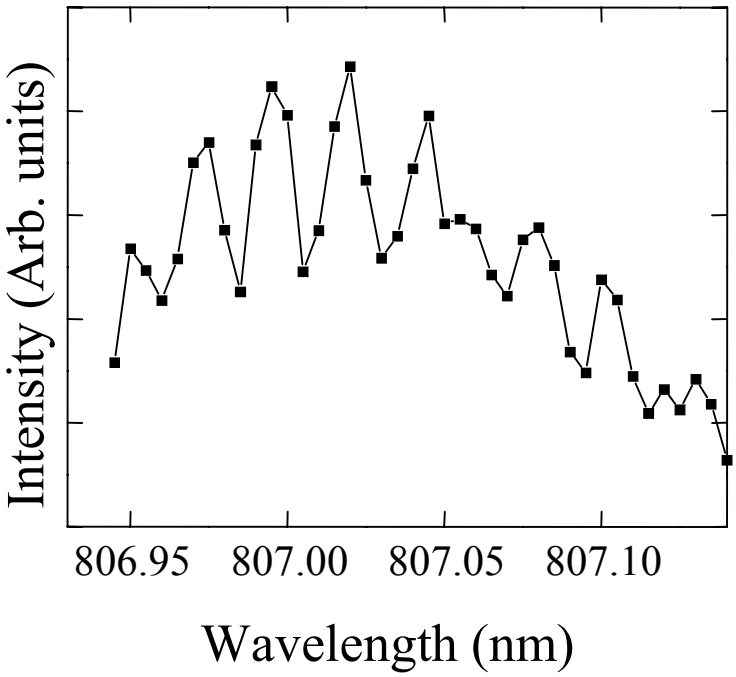

FIGURE 26. A portion of the coupled photoluminescence spectrum obtained with a much higher spectral resolution shows that the Q-factor of the composite system is 8×10^4.

Q-factor of the composite system exceeds 8×10^4. In the limit that scattering and absorption loss is negligible, we expect the Q-factor to be limited by over-coupling loss of the whispering gallery modes, which can in principle be reduced by a small gap between the sample and the sphere and also between the prism and the sphere.

To achieve adequate spectral resolution to determine the Q-factor of the composite system, we have used a resonant light scattering technique described in Chapter III. As shown in Figure 27, a tunable diode laser is used to launch whispering gallery modes near the equator of the microsphere via frustrated total internal reflection in the high refractive index prism. During the measurement,

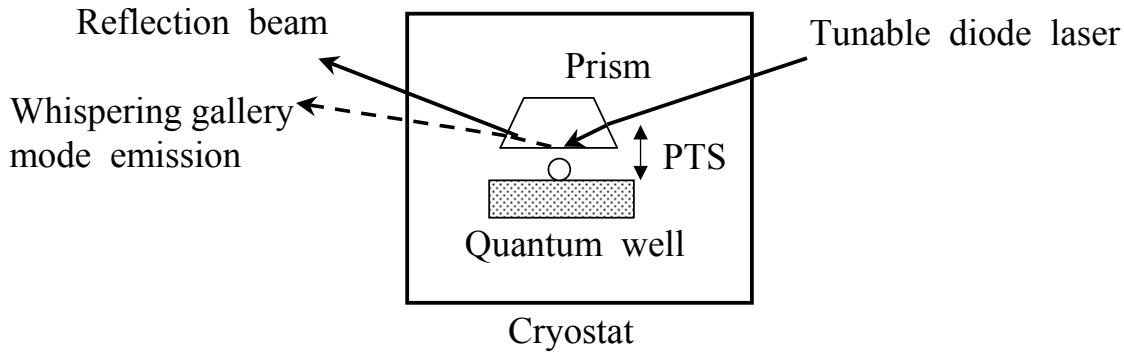

FIGURE 27. Experimental setup for resonant light scattering. A tunable diode laser is used to launch the whispering gallery modes via the frustrated total internal reflection through the prism. Emission is observed from the whispering gallery modes when the laser is on resonance with one of the modes. PTS=Piezoelectric Translation Stage.

the gap between the microsphere and the prism is maintained as large as possible to minimize the output coupling loss through the prism. Emissions from these whispering gallery modes are collected away from the reflection direction of the incident laser beam.

Figure 28 shows the emission spectra (TE polarization) as a function of the laser frequency in the absence and presence of a quantum well sample, respectively. The quantum well sample used contains a 17 nm GaAs well approximately 32 nm beneath the sample surface. The measurement is performed at room temperature. Whispering gallery modes with lowest radial mode numbers are preferentially excited by using a launch angle near the critical angle. The resonances in Figure 28 correspond to whispering gallery modes that have the same l and p but different m.

In the absence of the sample, the spectral linewidth of the whispering gallery

mode resonances shown in Figure 28 is 0.0003 nm, corresponding to a Q-factor of 2.7×10^6, and is limited by the output coupling loss through the high index prism. In comparison, when the sample is placed in contact with the sphere, the linewidth of the whispering gallery modes increases to 0.004 nm. This corresponds to a Q-factor of 2×10^5, in agreement with the later theoretical calculation [63]. The Q-spoiling results from output coupling and scattering loss occurring in the contact area between the sample and the sphere. Note that excitonic and band-to-band absorption processes in the quantum well sample does not contribute to the Q-spoiling shown in Figure 28 since similar Q-factors are also obtained at 10 K and at wavelengths below the exciton absorption resonance, as we will discuss later.

Probing the Interaction Between Exciton and the Whispering Gallery Modes

While in the previous section $Q_{intrinsic}$ of the composite system is measured, our next experiment is aimed at probing how exciton absorption in the quantum well sample affects the Q-factor of the combined semiconductor-microsphere system, and at determining the dipole coupling rate between excitons in the quantum well and resonant whispering gallery modes in the microsphere. For this experiment, we have selected microspheres that have whispering gallery modes resonant with the heavy hole exciton in the single quantum well sample discussed earlier. Since the evanescent field of the whispering gallery modes decays rapidly away from the sphere surface, we have chemically etched the GaAs capping layer of the sample down to approximately 25 nm thick to position the GaAs quantum well nearly 32 nm away from the sphere surface (there is also a 7 nm AlGaAs barrier

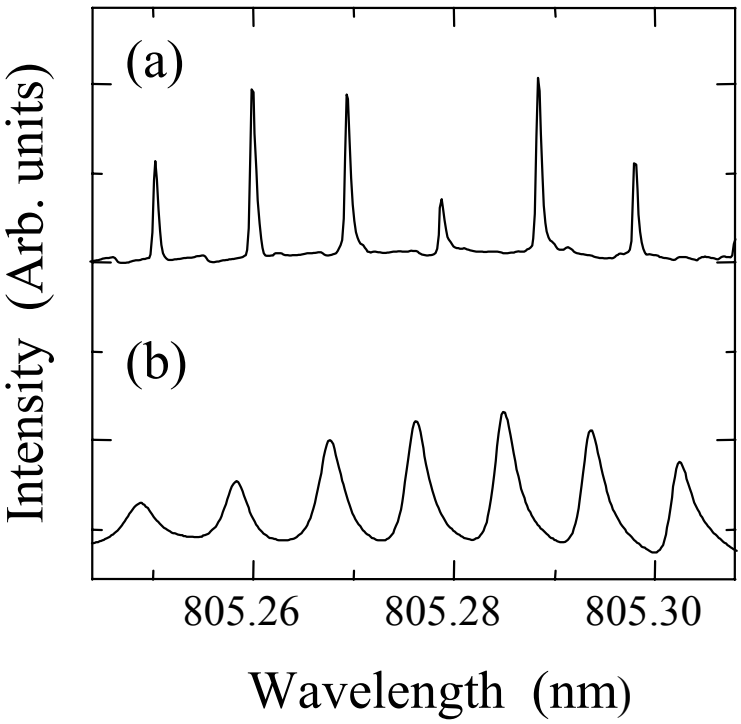

FIGURE 28. Resonant scattering spectra of composite quantum well and microsphere system at room temperature in the absence (a) and presence (b) of a quantum well sample.

between the GaAs cap and the 17 nm GaAs well). Figure 29(a) shows the reflection spectrum of the heavy hole exciton resonance at 10 K with an exciton linewidth of 0.3 nm. Note that further etching of the GaAs capping layer results in a drastic spectral broadening of the exciton resonance due to non-radiative surface effects. To avoid significant surface effects, the GaAs well needs to be at least 25 to 40 nm beneath the sample surface [64].

Figure 29(b) shows the emission spectrum of whispering gallery modes (TE polarization) near the heavy hole exciton resonance. The experimental configuration used is the same as that of Figure 27 and the diameter of the microsphere used is 120 μm. The spectral linewidth of the whispering gallery mode resonances shown in Figure 10(b) is 0.004 nm. Similar linewidths are also observed when the incident laser is tuned to a few nm above or below the heavy hole exciton resonance. The absence of any significant effect of exciton absorption on the Q-factor of the combined system indicates that absorption loss due to dipole coupling between the exciton resonance and the resonant whispering gallery mode is small compared with output coupling and scattering loss occurring in the contact area.

To describe interactions between excitons in the quantum well and resonant whispering gallery modes in the microsphere, and to estimate Q-spoiling due to the dipole coupling between the exciton and the whispering gallery modes, we have used the equations presented in Chapter II. In the limit of $\kappa \ll \gamma$ (the good cavity limit) where κ and γ are the bare-cavity decay rate and exciton dephasing rate, respectively, the increase in the cavity decay rate due to exciton absorption is given by g^2/γ where g is the collective dipole coupling rate between the exciton and the resonant cavity mode. If we assume that evanescent fields of whispering

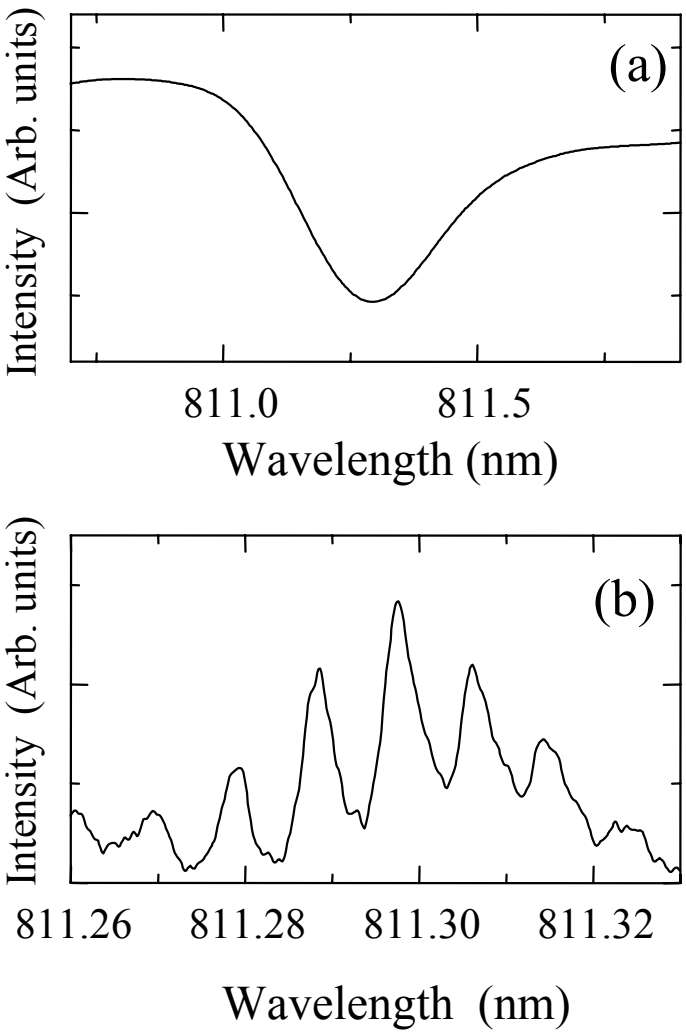

FIGURE 29. Measurement of the interaction between exciton in quantum well and resonant whispering gallery mode. (a): Reflection spectrum of a single GaAs quantum well at 10 K. (b): Resonant light scattering spectrum of the composite quantum well and microsphere system when the whispering gallery modes are on resonance with the exciton resonance in the quantum well.

gallery modes decay exponentially in the sample with a characteristic length r_0, the dipole coupling rate can be written as

$$g = \sqrt{\frac{e^2 S f}{4m\varepsilon V}} \times e^{-r/r_0} \tag{4.38}$$

where e and m are electron charge and mass, respectively, ε is the dielectric constant of the microsphere, f is the exciton oscillator strength per unit area in the quantum well, S is the effective coupling area between the sphere and the sample, V is the effective mode volume, and r is the effective distance of the quantum well away from the microsphere surface. Note that while the above result is intended for a homogeneously broadened system, the result can provide a good description for an inhomogeneously broadened system if we take γ as the inhomogeneous absorption linewidth of the excitonic transition.

For a 120 μm diameter microsphere and for whispering gallery modes with $p = 1$ and $l = m$, S is of order 10^{-8} cm^2 and V is of order 10^{-8} cm^3. The dipole coupling rate is then estimated to be 5 GHz for a quantum well right at the microsphere surface (r =0) where we have used $f = 3.5 \times 10^{12}/\text{cm}^2$ for the single quantum well [65]. This dipole coupling rate can lead to an increase of 0.0013 nm in the whispering gallery mode linewidth of the combined system, or an increase of 30% in the whispering gallery mode linewidth.

The dipole coupling rate in the actual composite semiconductor-microsphere system, however, is considerably smaller because the quantum well sample is at the tail instead of the peak of the evanescent field. For the sample used in our measurement, the distance between the center of the quantum well and the sample surface is nearly 40 nm. For a microsphere in the vacuum and for whispering gallery

modes that are near glancing incidence, the field penetration depth into the vacuum is given by $\lambda/2\pi\sqrt{n^2-1}$ where λ is the wavelength in the vacuum and n=1.45 is the index of refraction of the microsphere. While the actual penetration depth of evanescent waves in the combined system requires a detailed calculation of spatial field distributions of whispering gallery modes when a sphere is in contact with the sample, for a simple estimate we take the penetration depth in the sample to be $\lambda_S/2\pi\sqrt{n^2-1}$, where λ_S is the wavelength in the sample (the index of refraction of the sample is 3.5). At $\lambda = 800$ nm this yields a penetration depth of $r_0 = 35$ nm. Using r=40 nm, we arrived at an estimated dipole coupling rate of 1.5 GHz, which can lead to an increase of 1.2×10^{-4} nm in the spectral linewidth of the relevant whispering gallery modes, or only 3% of the overall linewidth. This small increase is within the experimental error of our current linewidth measurements.

In our experiment, we also use a multiple quantum well sample with 30 periods of 18 nm GaAs well and with an exciton absorption linewidth of 0.25 nm to increase the total oscillator strength per area, *i.e.*, f. However, due to the finite penetration depth, only the first quantum well is important. Therefore, in this case, the results obtained are similar to what we have measured in a single quantum well.

To further increase the dipole coupling between excitons and relevant whispering gallery modes, future studies need to use semiconductor nanostructures where the active medium such as a quantum well is positioned within a few nm from the microsphere surface. While for GaAs-based semiconductor nanostructures a capping layer with a thickness of 25 to 40 nm is necessary in order to avoid significant surface effects, surfaces of other semiconductors such as II-VI semicon-

ductor nanocrystals can be efficiently passivated by a capping layer of only 1 nm thick [66]. Finally, we note that while our current studies have been limited to GaAs-based nanostructures, these studies open the door for future experiments in which suitable semiconductor nanostructures can be used to take advantage of high-Q whispering gallery modes for cavity-QED studies of semiconductors and for applications in semiconductor lasers.

Conclusion

In this Chapter, we have developed and characterized the composite system of semiconductor quantum well and fused silica microsphere. We have demonstrated that the photoluminescence from a quantum well sample can be efficiently coupled into the whispering gallery mode with negligible background. The Q-factor of this composite system exceeds 10^5, at least two orders of magnitude higher than conventional monolithic semiconductor microcavities and microdisks [29].

Our experimental results also show the strong Q-spoiling effects arising from the output coupling loss through the high index sample, which determines the upper limit of the Q-factor for this type of composite system. In addition, the dipole interaction between the exciton in the quantum well and the whispering gallery modes is small due to the fact that the electric field of whispering gallery modes outside the sphere features an extremely fast exponential decay and the quantum well, on the other hand, is in excess of 40 nm beneath the sample surface.

In order to bring nanostructures as close to the microsphere surface as possible, we have developed another type of composite system where semiconductor nanocrystals are placed on the fused silica microsphere surface. The properties

and the applications in cavity-QED studies of such a composite system will be presented in the next few chapters.

CHAPTER V

SYNTHESIS OF ZnS-CAPPED CdSe SEMICONDUCTOR NANOCRYSTALS

Introduction

Semiconductor nanocrystals (also commonly referred to as free-standing quantum dots) exhibit very interesting size tunable optical properties due to the spatial confinement of electron-hole pair wavefunctions. In contrast to bulk band structure, these nanocrystals have discrete electronic states and thus can be analogously treated as "artificial atoms". The typical size of nanocrystals is a few nanometers, comparable to or smaller than the corresponding exciton Bohr radius as illustrated by Figure 30. The number of atoms in a nanocrystal is in the range of a few thousand, as listed in Table 2.

As discussed in the previous chapter, in order to solve the problems associated with epitaxially grown semiconductor quantum wells and quantum dots, semiconductor nanocrystals can be used to construct composite nanocrystal-microsphere systems. The thickness of the capping layer of the semiconductor nanocrystals is

TABLE 2. Evolution from one-atom system to bulk crystal system

	Number of atoms	**Dimension**
Atom	1	< 0.1 nm
Molecule	a few	$0.1 \sim 1$ nm
Cluster	~ 100	1 nm
Nanocrystals	$1000 \sim 10000$	$1 \sim 10$ nm
Bulk crystals	billions	> 1 μm

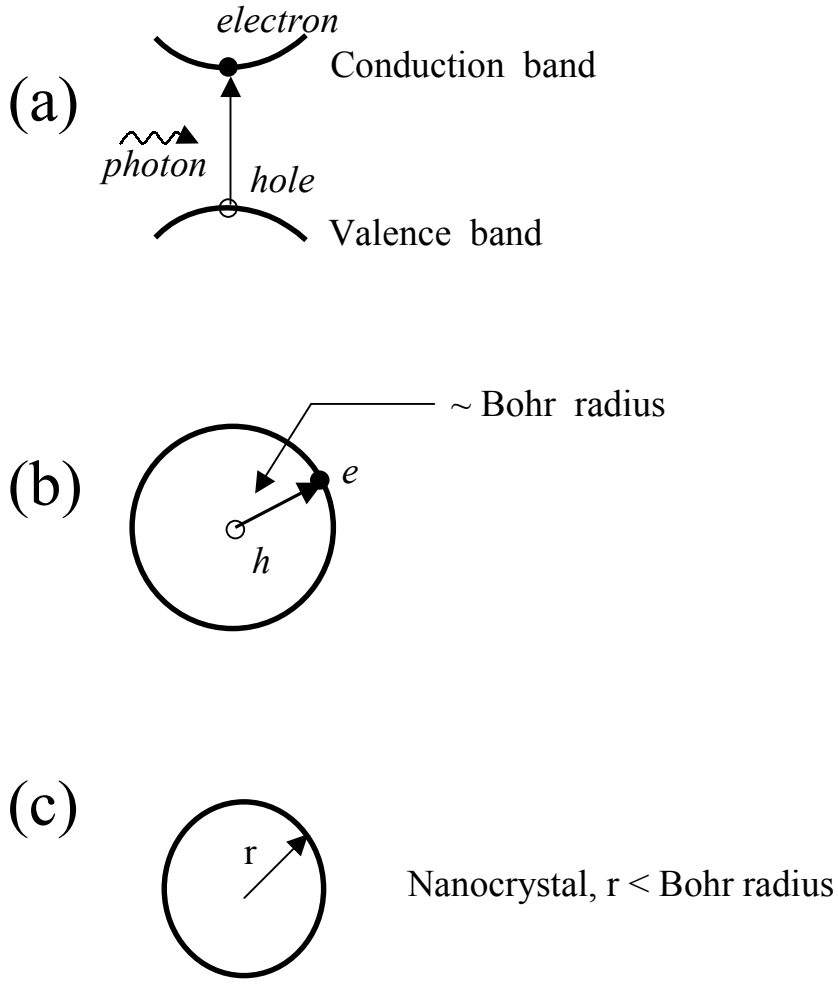

FIGURE 30. Exciton in a bulk crystal and in a nanocrystal. (a): Formation of the exciton upon absorption of a photon. (b): Exciton in a bulk crystal. (c): A nanocrystal whose radius is comparable to or smaller than the corresponding Bohr radius.

typically less than 1 nm. Thus the excitonic dipole can be brought very close to the maximum of the electric field of the whispering gallery modes.

In addition to their appealing use as artificial atoms, semiconductor nanocrystals also represent one of the very important stages when a system consisting of a few atoms evolves into a bulk crystal, as shown in Table 2, and thus serve as a model system to study the changes in chemical and optical properties in the course of the evolution [67].

From an application point of view, semiconductor nanocrystals are among the best luminescent materials due to their high quantum yield. Novel optical and electronic devices such as LEDs, lasers, and transistors based on nanocrystals have been either proposed or realized [68, 69]. The use of nanocrystals in place of conventional dyes in biological labeling has also been explored since the advent of high quality nanocrystals [70, 71].

Over the course of the last decade, much progress has been made in the synthesis and characterization of semiconductor nanocrystals for better understanding of size control, monodispersity, shape, surface composition, and surface passivation. Currently a wide variety of semiconductor nanocrystals can be synthesized, including CdSe [66, 72, 73, 74, 75, 76], Si [77, 78], GaAs [79], InP [80], and InAs [81]. In particular, the techniques used to fabricate inorganically capped CdSe nanocrystal have been greatly improved, leading to an excellent quantum yield (up to unity even at room temperature), narrow size distribution (less than 5% rms) and broad coverage of the visible spectrum [66, 74, 75, 76].

In this chapter, we will focus on the synthesis and characterization of ZnS-capped CdSe nanocrystals (also denoted as CdSe/ZnS) due to the fact that ZnS-

capped CdSe nanocrystals can be used to demonstrate the synthesis of a series of inorganically capped nanocrystals such as CdS and ZnSe nanocrystals and that these CdSe/ZnS nanocrystals will be used in cavity-QED studies discussed in Chapter VII and Chapter VI.

Properties of CdSe Nanocrystals

Figure 31 shows the structure of CdSe nanocrystals. Although the nanocrystals have only a few tens of lattice periods, they retain the crystal structure and lattice parameter of the corresponding bulk crystal [82]. At low pressure, CdSe nanocrystals feature hexagonal symmetry with wurzite lattice structure as shown in Figure 31. A structural transition occurs when the nanocrystals are subject to high pressure (9 GPa) at which a salt lattice structure has lower energy [83]. When fabricated at low monomer concentration, CdSe nanocrystals grow isotropically, namely, all facets grow at the same rate. Consequently, the resulting nanocrystals features nearly spherical shape. At much higher monomer concentration, however, the growth rate along c-axis, which is normal to the plane shown in the figure, is faster than that in the hexagonal plane, leading to the formation of so-called nanorods with the ratio of nearly 100:1 [84, 85].

The boundary of nanocrystals determines the electronic confinement of electrons and holes, leading to an increase in bandgap with decreasing size. Figure 32 shows schematically the energy structures of bare CdSe nanocrystals and ZnS-capped CdSe nanocrystals with the lowest transition arising from the lowest electron and hole states. The energies of the electron and hole in ZnS-capped CdSe nanocrystals differ slightly from those in bare CdSe nanocrystals due to the pen-

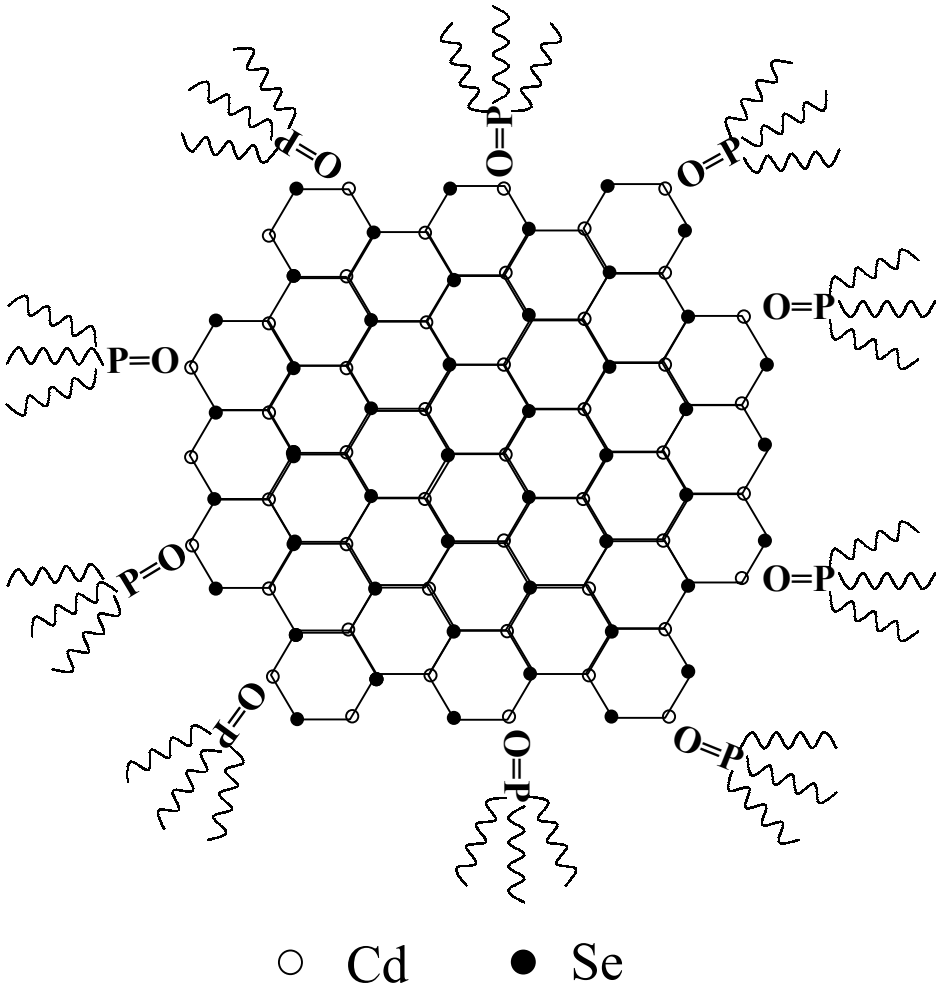

FIGURE 31. Structure of CdSe nanocrystals. At low pressure (< 9 GPa), CdSe nanocrystals have hexagonal symmetry with wurzite lattice structure. Cadmium atoms are bonded to oxygen atoms from Tri-n-octylphosphine oxide. C-axis is normal to the hexagonal plane.

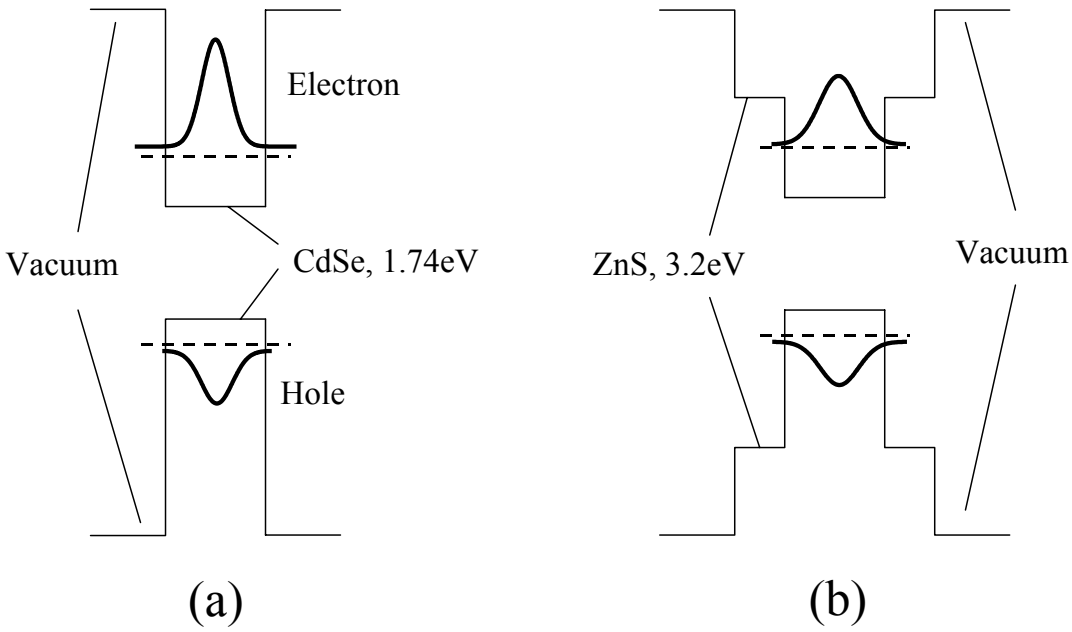

FIGURE 32. Energy structures of CdSe (a) and CdSe/ZnS Nanocrystals (b).

etration of the electron and hole wavefunctions into the ZnS capping layer. For 4 nm diameter CdSe nanocrystals with a 0.4 nm (1.3 monolayers) ZnS capping layer, the wavefunction penetration causes 30 meV red shift in the absorption spectrum relative to bare CdSe nanocrystals [74].

In bulk semiconductors, the surface has negligible effect on semiconductor optical properties. However, the surface of semiconductor nanocrystals plays a critical role in almost all optical properties, including quantum yield, Stokes shift in photoluminescence, and decay dynamics due to large surface to volume ratio. For instance, for a 4 nm diameter CdSe nanocrystal, over 20% of the cadmium and selenium atoms in the whole nanocrystal are on the surface. A large number

of surface dangling bonds trap the electrons or holes, resulting in a total quantum yield of less than 1%, very large red shift in photoluminescence, and chemical and photo instability. An extremely slow decay time (~ 1 μs) is also observed due to surface state recombination [86], in sharp contrast to the 1 ns decay time in bulk CdSe crystal [87]. Passivation is needed to eliminate trap states, and consequently, to improve the surface quality.

From the early 1980s to 1995, CdSe nanocrystals were synthesized in different coordinating solvents at high temperature [88]. The resulting nanocrystal surface is therefore passivated with organic materials among which TOPO (Tri-n-octylphosphine oxide) is most commonly used. As shown in Figure 31, cadmium atoms in CdSe nanocrystals are bonded to oxygen from the surface ligand TOPO while selenium atoms are left almost unbonded. Experimental studies show that overall coverage of cadmium atoms ranges from 30% for large nanocrystals to 60% for small nanocrystals [89], leading to an improved quantum yield of a few percent at room temperature [88, 90]. However, due to the unsaturated selenium and cadmium atoms on the surface, TOPO-capped nanocrystals are very sensitive to oxygen and light. Degradation has been observed with the formation of SeO_2 surface film in CdSe nanocrystals [89]. Decay times are still extremely long (a few hundreds of nanoseconds to several microseconds). Furthermore, depending on the surface passivation, a large red shift arising from surface state recombination still exists from sample to sample.

Starting from 1995, inorganically capped nanocrystals (also referred to as core/shell structure nanocrystals) came into the central stage. Thanks to the pioneer work by the groups of Guyot-Sionnest at the University of Chicago, Bawendi

at MIT, and Alivisatos at UC Berkeley [66, 74, 75, 76], inorganically capped CdSe nanocrystals have now achieved nearly perfect passivation of the core surface which is otherwise capped by TOPO. The basic idea of inorganic capping is to epitaxially grow onto the CdSe facets a few monolayers of inorganic materials with a larger bandgap. Capping materials can be chosen according to their optical properties, lattice constants and bandgaps. For CdSe nanocrystals, ZnS and CdS are two common choices for capping layers with the respective lattice mismatch of 12% and 3%.

The energy structure of a CdSe/ZnS nanocrystal is shown in Figure 32(b). Although the capping process has slight effects on the absorption properties due to the very weak penetration of the electron/hole wavefunction into the capping layer (the bandgap offset is nearly 1.5 eV), it dramatically changes the quantum yield, photoluminescence and decay dynamics. A quantum yield of 50% at room temperature has easily been obtained using the approaches provided by the above groups. Unity quantum yield at room temperature with CdS-capped CdSe nanocrystals is also reported [76]. The decay times are shortened by a factor of 10 to 100, accompanied by the disappearance of the very large red shift in photoluminescence. In addition, the ZnS capping layer prevents the CdSe cores from photon-assisted oxidation and/or contamination by other chemicals, which usually deteriorate the overall quantum yield. Consequently, CdSe/ZnS nanocrystals have excellent chemical and photo stability compared with organically capped nanocrystals.

The exterior surface of CdSe/ZnS nanocrystals is still covered with TOPO to avoid aggregation. As a result, the entire CdSe/ZnS nanocrystals still exhibit similar surface reactivity as TOPO-capped CdSe nanocrystals. This scheme allows

us to modify the CdSe/ZnS nanocrystal surface or to exchange surface ligands with little effect on the optical properties of the nanocrystals [91]. This not only proves to be particularly useful in biological labeling but also provides a promising approach to attach CdSe/ZnS nanocrystals to the surface of a fused silica microsphere using bifunctional chemical links for cavity-QED studies in our lab.

Fabrication and Characterization of ZnS-Capped CdSe Nanocrystals

CdSe/ZnS nanocrystals were synthesized by a variant of the approach presented in the paper by Hines [66]. After a number of times of trial-and-errors, we have developed our own recipe with high reproducibility in CdSe/ZnS nanocrystal fabrication.

Tri-n-octylphosphine oxide (TOPO) with 99% purity, Tri-n-octylphosphine (TOP) with 90% purity, 1 M dimethylzinc (Me_2Zn) in heptane were purchased from Aldrich. Bis(trimethylsilyl) sulfide ($(TMS)_2S$) and dimethylcadmium (Me_2Cd) were purchased from Fluka. Anhydrous methanol and anhydrous chloroform were prepared in the laboratory.

Preparation of CdSe Stock Solution: Under the protection of nitrogen, selenium (0.2 g, 0.0025 mol) was dissolved in 4.5 mL TOP (Tri-n-octylphosphine) using an ultrasonic device. Me_2Cd (0.25 mL, 0.0035 mol) was then added to the TOP/Se solution and diluted with 19.5 mL of TOP. The resulting stock solution was clear and light yellow. When the stock solution was stored for a long time, a small amount of precipitation was observed, indicating the formation of CdSe nanocrystals and/or other unknown decomposition products.

It should be noted that in the stock solution described above, the molar ratio of Cd to Se is 1.4:1. In order to fabricate larger sizes of CdSe nanocrystals, the ratio can be raised to 1.9:1 to avoid the defocusing in size distribution over a long growth time, as discussed later in this chapter.

Preparation of ZnS Stock Solution: $(TMS)_2S$ (0.52 mL, 0.0025 mol) was prepared in 4.5 mL of TOP, to which Me_2Zn (3.5 mL, 0.0035 mol) was added. The final solution was then diluted with 16 mL of TOP. Upon the initial preparation, slight fuming was observed and disappeared in ten minutes. The resulting stock solution was clear and slightly pink. After one day or so, the stock solution turned colorless. After a long storage time, small ZnS nanocrystals and/or other unknown products form and precipitate.

Apparatus and Setup: The basic fabrication setup is shown in Figure 33. Nitrogen and vacuum are provided through a Schlenk-line. Syringes are used to add stock solution and to take out aliquots through a rubber septum. A heating mantle in conjunction with a thermometer can be brought up and down to obtain desired temperature. The glassware was flame-dried and backfilled with Nitrogen before the addition of TOPO [1].

Fabrication: Nanocrystals were fabricated using high temperature organometallic synthesis. A TOPO/TOP solvent coordinates the nanocrystals' surface and provides a kinetic barrier, allowing steady growth and easy control of nanocrys-

[1]It is found that even slight contamination from grease will totally destroy the whole fabrication. Therefore, grease should be added with great caution.

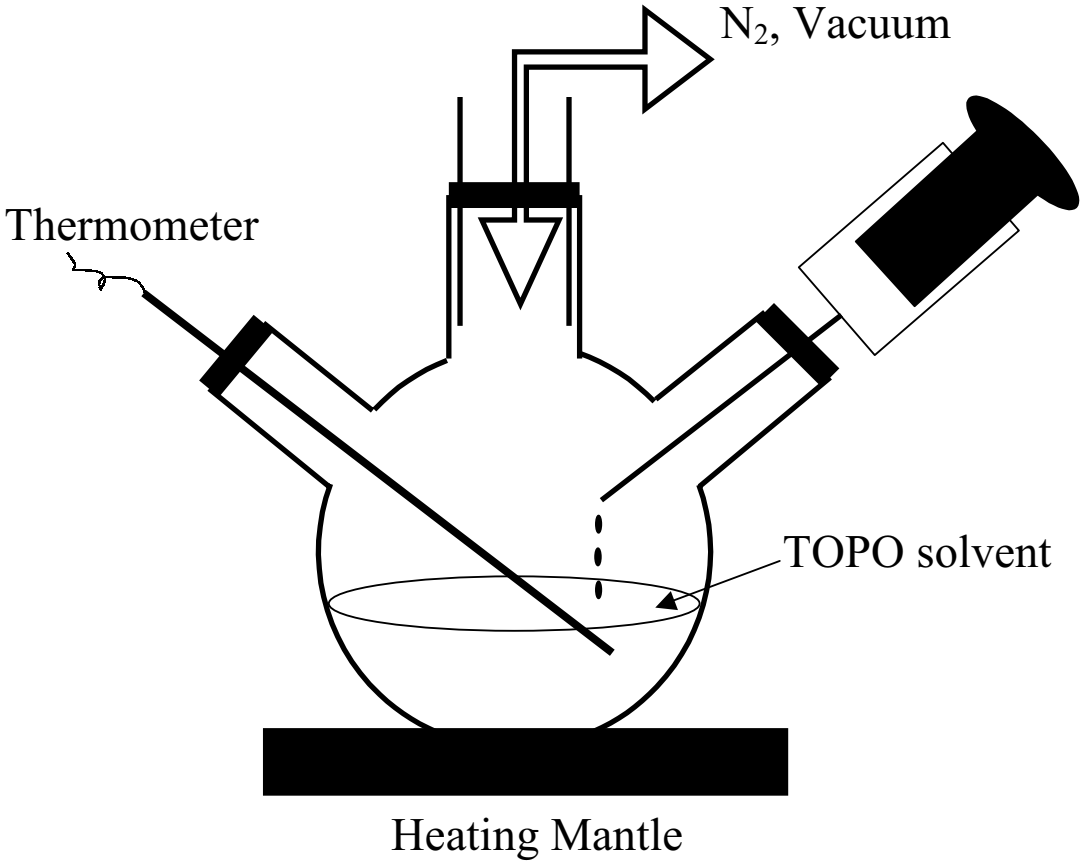

FIGURE 33. Fabrication setup and apparatus

tals at a temperature above 280 °C. In the following section, we will present the procedure to fabricate relatively small nanocrystals (D $\sim 3-4$ nm), followed by a discussion of the fabrication of larger nanocrystals (D > 4 nm).

(1) Degassing and Refluxing

The TOPO (12.5 g) was dried and degassed by refluxing at 210 °C under vacuum for a minimum of 90 minutes. During this period, the solvent should be colorless and clear. Any yellowish or brownish color is the precursor of failure of later fabrication due to either contamination of grease or impurities in TOPO.

(2) Injection, growth and capping

After the degassing and drying, the temperature was raised to and stabilized at 350 °C under approximately 1 atmosphere of nitrogen. At T = 350 °C, Cd/Se/TOP stock solution (0.7 mL) was injected through an 18G needle into the reaction flask in one quick shot. Upon the initial injection, the temperature dropped down to 330 °C, fuming was observed and the color changed from light yellow to orange, light red and red progressively in a minute or so, indicating the increasing nanocrystal size. A small aliquot was taken out from time to time and diluted with t-butanol in order to monitor the nanocrystal size with a UV-Vis spectrum analyzer. Once the desired size was reached, Zn/S/TOP stock solution (2.75 mL) was added at 300 °C either dropwise in the course of 5 minutes or in 5 injections with an interval of 20 seconds. The heating mantle was then lowered and the reaction mixture was stirred at 100 °C for at least 1 hour for thermal annealing. Finally, anhydrous methanol was added at T = 65 °C upon the removal

of the heating mantle. After 12 hours, a red precipitate was observed at the reaction flask bottom. Under UV illumination, the precipitate emitted green or yellow light depending on the size achieved while the supernatant exhibited a bluish green color, meaning that the small sized nanocrystals were still suspended in the solvent.

(3) Washing and Size Selection

The powder-like nanocrystals were isolated and washed by the addition of anhydrous methanol, which caused aggregation among nanocrystals via van der Waals force. The precipitate was subsequently collected by centrifuging. Two or three cycles were sufficient to get rid of residual TOPO and unreacted reagents. The final nanocrystal powder was then redispersed in anhydrous chloroform and saved in a storage tube under the protection of nitrogen.

The resulting nanocrystals typically have inhomogeneous linewidth of 50nm in photoluminescence. The size distribution can be further narrowed by selective precipitation from chloroform by the addition of a polar solvent such as methanol. Larger nanocrystals are easier to precipitate due to clustering, resulting in larger average size and narrower distribution.

Discussion: The final nanocrystals are typically characterized by size, size distribution, quantum yield, and shape. These four parameters are highly dependent upon the growth temperature, monomer concentration, quality of capping layer, and the way that stock solutions are injected. These parameters should be closely monitored during the fabrication in order to obtain the desired nanocrystals. It should be noted that the recipe provided in this section is for the fabrication

of spherical or nearly spherical CdSe nanocrystals where the crystals growth rate along the c-axis is the same as that in the hexagonal plane. For the fabrication of nanorods, much higher monomer concentration should be used [84, 85]. In the following section, we will discuss the control of the remaining three parameters followed by an example obtained during a real fabrication process for illustration.

(1) Size

The recipe given above shows how to make CdSe nanocrystals ranging from 3 to 4 nm in diameter. Rapid injection of cold Cd/Se/TOP stock solution into the superheated TOPO solvent results in the supersaturation of cadmium and selenium monomers with respect to the precipitation of CdSe, which subsequently triggers the formation of initial seeds with a diameter of approximately 1 nm [88]. Starting with these initial seeds, CdSe nanocrystals grow epitaxially.

The dynamics of the whole process can be formulated as follows:

$$\text{Cd (monomer)} + \text{Se (monomer)} \Longleftrightarrow \text{CdSe (nanocrystal)}$$

Cadmium and selenium atoms dynamically exchange with CdSe nanocrystals in the TOPO solvent. When the monomer concentration is high, the nanocrystal growth rate is positive and the size of the nanocrystals increases. On the other hand, when monomer concentration is low, the growth rate becomes negative. As a result, some nanocrystals are dissolved back to monomer to balance the monomer concentration.

At the initial fast growth when the monomer concentration is high, CdSe nanocrystals grow very rapidly. For the recipe given above, it takes a few minutes

for the average size of the nanocrystals to increase from 1 nm to 3 nm in diameter. However, after 10 minutes or so the system gradually enters the so-called Ostwald ripening regime [92]. During ripening, large nanocrystals still continue to grow, but at a much lower rate due to the depletion of monomers. In the meantime, small nanocrystals become unstable because of high surface free energy with respect to large nanocrystals and are dissolved back to monomers, which effectively leads to the broadening of the size distribution.

During fabrication, the temperature should be maintained above 230 °C in order to overcome the potential barrier to form nanocrystals. Removal of the heating mantle will stop the growth. On the other hand, if the temperature is too high, then the initial nearly homogeneous size distribution will be lost. Therefore, during fabrication, temperature should be carefully monitored. Growth will be accelerated by simply raising the temperature. Conversely, when size distribution defocuses, the temperature should drop.

The above recipe works very well to grow small nanocrystals ($3 - 4$ nm in diameter). The growth time is less than 10 minutes before the removal of the heating mantle. However, it takes nearly 6 hours to obtain a relatively large size of nanocrystals (> 5 nm) due to the fact that the growth rate is extremely low in the Ostwald ripening regime. Additionally the size distribution becomes worse due to the dissolution of small nanocrystals. Some modifications to the original recipe are given as follows to speed up the growth while maintaining a good size distribution:

(a) Increase in monomer concentration in the TOPO solvent delays the occurrence of Ostwald ripening and speeds up the growth rate. During fabrication of

large nanocrystals, we used 8 g rather than 12.5 g of TOPO with the same amount of CdSe stock solution [81].

(b) Increase monomer concentration ratio. Studies have shown that an increase in the ratio of cadmium to selenium from 1.4:1 to 1.9:1 extends the defocusing time from 22 minutes to a few hours. As a result, the temperature can be kept as high as possible without causing degradation in the size distribution during the first few hours, thus effectively increasing the growth rate [81].

(c) Lowering the temperature is another way to shorten the total growth time since injection at lower temperature ($\sim$ 300 °C) results in a decrease in the number of initial seeds that are to be fed by cadmium and selenium monomers [93].

(d) Initial injection is also an important place where the growth time can be greatly reduced. Instead of rapid injection in a burst, slow injection makes cadmium and selenium monomers arriving in the solution later overcoat on the existing nanocrystal seeds rather than form nanocrystals themselves [66, 93].

(e) Multiple injections during the course of fabrication to overcoat existing nanocrystals with cadmium and selenium monomer (see the discussion later in this chapter).

(2) Size distribution

Upon the initial injection, the size distribution is nearly homogeneous with an average size of 1 nm in diameter. However, when the nanocrystals continue to grow, the size distribution starts to defocus due to Ostwald ripening. Retention of the initial size distribution is determined by a combination of temperature and

monomer concentration ratio. Lowering the temperature during fabrication causes nanocrystals to refocus at the expense of growth rate. Higher monomer concentration ratio at initial injection delays the time at which nanocrystals start to defocus. In order to achieve a good size distribution without sacrificing the growth, multiple injections during fabrication have proven to be a good choice. It not only drastically increases the average size by overcoating the existing nanocrystals rather than forming new nanocrystals, but also increases the monomer concentration in the solvent to accelerate the growth. In the meantime, at high monomer concentration smaller nanocrystals catch up with larger nanocrystals as a consequence of faster growth rate, effectively narrowing the size distribution.

Size distribution can be further narrowed after the synthesis. Alternate addition of polar and nonpolar solvents such as methanol/chloroform causes the larger nanocrystals to precipitate more than the smaller nanocrystals, leading to a narrower size distribution as well as larger average size.

(3) Quantum yield and inorganical capping

Excellent surface passivation and high quantum yield can be achieved by epitaxially growing ZnS or CdS onto CdSe nanocrystal surface. Both ZnS and CdS have a larger bandgap than CdSe. While the lattice mismatch between ZnS and CdSe is approximately 12%, it differs by only 3% between CdS and CdSe. This suggests that CdS may be a better candidate for a capping layer [76]; however this has yet to be experimentally tested. At relatively high temperature ($\sim$ 260 °C), thermal energy activates TOPO that is weakly bonded to the nanocrystal surface. ZnS or CdS monomers with stronger bonds replace TOPO through thermody-

namic exchange. It is found that the quantum yield varies as the monolayers grow. The highest quantum yield of 50% is obtained when ZnS or CdS is two to three monolayers thick [74, 76]. Addition of monolayers causes strain to build up along the interface between the core and the capping layer and eventually the relaxation of strain leads to faults and cracks in the nanocrystal surface. During fabrication, the amount of ZnS to be injected is calculated according to the desired CdSe nanocrystal size to ensure only two or three capping layers. ZnS stock solution is injected dropwise or in five portions with an interval of 20 seconds. This allows for epitaxial growth of ZnS onto the CdSe surface and in the meantime prevents ZnS from forming nanocrystals themselves. The annealing process as a final step, at T $\sim$ 100 °C, is also important since it allows ZnS to slightly relocate along the surface to release the strain.

(4) Example

To demonstrate the evolution of size and size distribution, a series of photoluminescence spectra of CdSe nanocrystals were taken during fabrication and are presented in Figure 34. The CdSe stock solution was prepared as stated in the above recipe and the TOPO solvent was heated to 350 °C after 1 hour of drying and degassing. The aliquots were taken out from hot reaction flask during the fabrication and dispersed in a UV cuvette filled with t-butanol to avoid solidifying. The photoluminescence spectra were obtained using a Hitachi F-4500 fluorescence spectrophotometer with the excitation wavelength at 350 nm.

The initial fast growth and progressive size defocusing are well represented through Figure 34(a)-(c). As shown in (a), within two minutes the initial nanocrys-

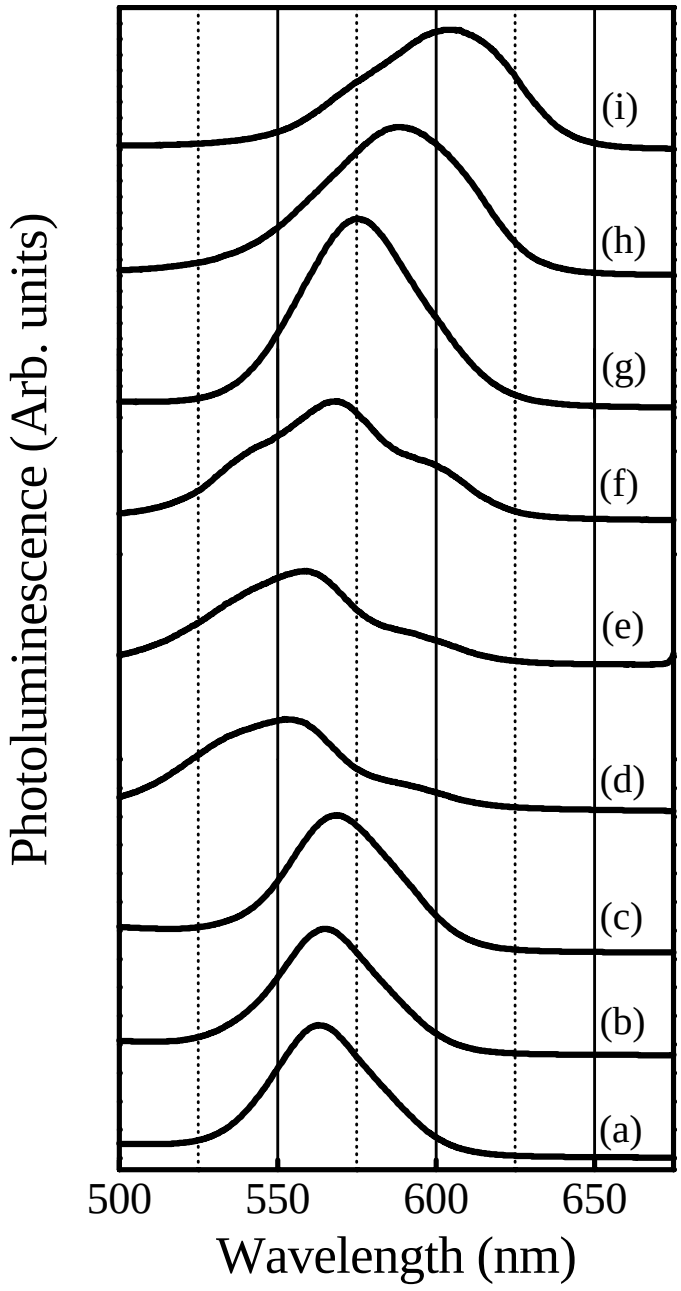

FIGURE 34. Evolution of size and size distribution of CdSe nanocrystals. Photoluminescence is taken at (a): 2 min. (b): 10 min. (c): 20 min. (d): 27 min. (e): 35 min. (f): 50 min. (g): 80 min. (h): 100 min. (i): 150 min. Second injection is added at t = 25 min.

tal seeds grow from 1 nm to 4 nm in diameter. The narrowest size distribution is achieved in (b), 10 minutes after the initial injection. During the course of growth between 10 and 20 minutes, Ostwald ripening gradually takes place, leading to the broadened size distribution as evidenced by the broader photoluminescence spectrum in (c).

A second injection of CdSe stock solution at t = 25 min has two immediate consequences. It increases the size of the existing nanocrystals through epitaxial growth, as represented by the right-most resonance at $\lambda = 600$ nm in Figure 34(d). In addition, some leftover CdSe monomers form small nanocrystals themselves, as seen in the peak at 530 nm and 560 nm.

As time goes by, the average size increases and the size distribution undergoes refocusing. This is well illustrated by the photoluminescence spectra in Figure 34(e)-(g) with the narrowest size distribution achieved in Figure 34(g) at t = 80 min. After that, as shown in Figure 34(h) and (i), Ostwald ripening becomes dominant again and the size increases at the expense of size distribution.

Characterization

Figure 35 shows a series of absorption and photoluminescence spectra of various sizes of CdSe/ZnS nanocrystals at room temperature. The corresponding samples under UV illumination are shown in Figure 36. The nanocrystals are fabricated, capped and washed using the methods discussed previously. Multiple resonances representing different optical transitions emerge in the absorption spectrum, indicative of a narrow size distribution. The inhomogeneous linewidth also gives a measure of size distribution. At room temperature, the full-width-

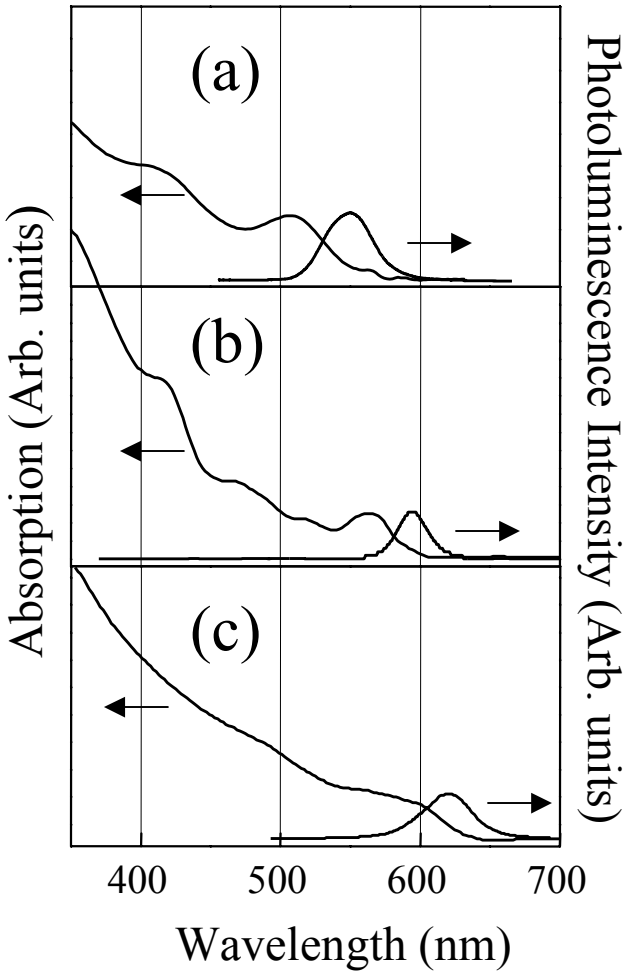

FIGURE 35. Absorption and photoluminescence spectra of CdSe/ZnS nanocrystals at room temperature. The mean diameters are (a): 3.0 nm. (b): 4.0 nm. (c): 5.4 nm. In addition to lowest optical transition, higher optical transitions can also be observed in absorption spectra.

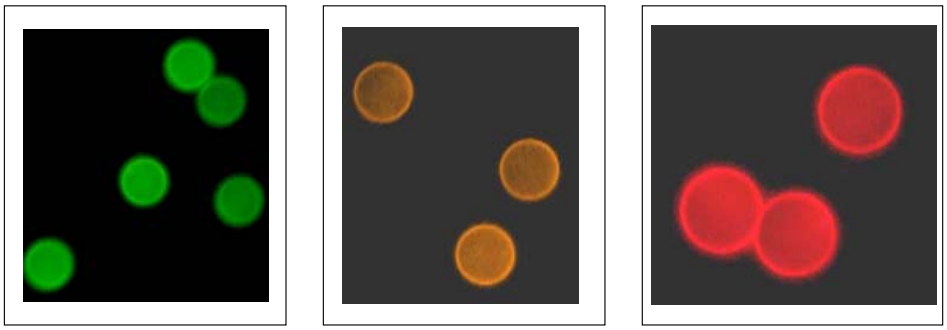

FIGURE 36. Pictures of CdSe/ZnS nanocrystal samples under UV illumination show the coverage of the visible spectrum. The samples are doped in polystyrene spheres. The corresponding spectra are given in Figure 35.

at-half-maximum is less than 50 nm, which is another indication of a narrow size distribution. The photoluminescence is Stokes-shifted towards red with respect to absorption spectrum. The Stokes shift ranges from 7 nm to 20 nm. In contrast to the photoluminescence from some TOPO capped nanocrystals, the emission at longer wavelength arising from the surface states completely disappears, exhibiting greatly improved surface passivation.

At low temperature, both absorption and photoluminescence spectra shift to blue due to the increase in the bandgap. The full-width-at-half-maximum is reduced down to 26 nm, which primarily arises from the decrease in the homogenous linewidth of CdSe/ZnS nanocrystals. Since surface passivation can annihilate some dephasing channels, homogenous linewidth measurement provides another indirect approach to check the surface quality. Recently our preliminary experimental results obtained using spectral hole burning at T = 4 K shows that the homogeneous linewidth of CdSe/ZnS nanocrystal is below 0.02 nm [94]. A further experiment

is under way to study the temperature and size dependent of the homogenous broadening in CdSe/ZnS nanocrystals.

Quantum yield is measured against Rhodamine 6G which has nearly unity quantum yield [95, 96, 97]. The excitation wavelength is set on the blue side of the lowest absorption resonance. Rhodamine 6G is diluted using chloroform to have the same optical density as the nanocrystals at this particular wavelength. The quantum yield of the nanocrystals is defined as the ratio between the integrated photoluminescence spectrum of the nanocrystals and Rhodamine 6G. Quantum yield varies from sample to sample, with a typical value ranging from 40% to over 50% in our samples. With such high quantum yield, the samples appear to glow with a green or yellow color even under room light.

As discussed previously, nanocrystals should retain their crystal properties, with the same lattice constant as bulk crystals. However, during the fabrication any contaminants or any fluctuation in temperature or in monomer concentration can result in degraded crystallization. A representative high resolution TEM image of nanocrystals of 5.4 nm in diameter is given in Figure 37, corresponding to the absorption and photoluminescence spectrum in Figure 35(c). The sharp contrast fringes reveal that the nanocrystals have crystal lattice structure. The nanocrystals are faceted, indicative of epitaxial growth of the ZnS capping layer.

Decay times are measured using time-correlated photon counting techniques. In contrast to TOPO-capped nanocrystals, over 90% of the photons emitted are within the first 150 ns, indicative of much improved surface quality. We will present more detailed discussion of the decay dynamics in CdSe nanocrystals in Chapter VI.

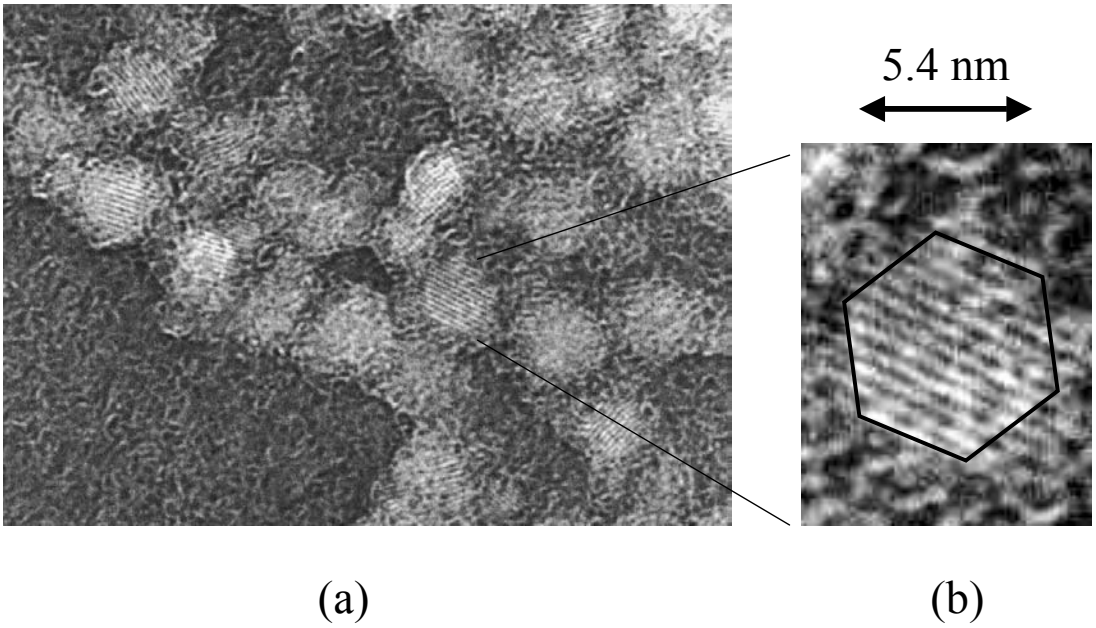

FIGURE 37. (a): TEM image of CdSe/ZnS nanocrystals. (b): A zoomed-in image for a clear view. Nanocrystals feature hexagonal facets. Sharp fringes indicate good crystallization.

Conclusion

In this chapter, a detailed description of the fabrication of CdSe/ZnS nanocrystals was presented. The control of size, size distribution, and quantum yield was discussed along with the characterization of the nanocrystals by absorption/photoluminescence spectra, TEM imaging, and a quantum yield measurement. With the recipe and the approaches provided in this chapter, we have successfully obtained CdSe/ZnS nanocrystals with high quantum yield, excellent size distribution, good crystallization and broad coverage of the visible spectrum, which allows us to construct composite nanocrystal-microsphere systems as discussed in the next two chapters.

CHAPTER VI

CAVITY-QED STUDIES OF COMPOSITE NANOCRYSTAL AND MICROSPHERE SYSTEM IN THE LOW-Q REGIME

Introduction

In chapter IV, we presented our first attempt to develop a composite semiconductor nanostructure and microsphere system by placing a semiconductor quantum well in the evanescent field of the whispering gallery modes of a fused silica microsphere [98, 99]. Further development, however, has been hindered by two problems associated with these epitaxially grown semiconductor samples. The Q-factor of this composite system is limited by the output coupling loss occurring at the contact area between the microsphere and the sample. In addition, the excitons in the quantum well are far away from the sample surface compared with the penetration depth of the whispering gallery modes, resulting in a small dipole coupling between the exciton and the electric field in the whispering gallery modes.

In order to avoid these problems, we have developed a microcavity system by coupling semiconductor core/shell nanocrystals to the whispering gallery modes of a dielectric microsphere. As discussed in Chapter V, recent advances in colloidal chemistry have led to the synthesis of semiconductor nanocrystals. A nearly defect free semiconductor core, such as CdSe, is capped with a thin shell ($\sim$ 1 nm in thickness) of another semiconductor with a greater bandgap [66, 74, 75, 76, 88, 90]. These core/shell nanocrystals feature much improved core surface passivation.

Near unity quantum yield has been observed in core/shell CdSe/CdS nanocrystals even at room temperature [76]. Photoluminescence studies of single CdSe nanocrystals have also revealed extremely narrow linewidth [94, 100].

The physical nature of band edge optical emission from semiconductor nanocrystals, however, has been the subject of considerable debate for over a decade [101]. This is due in part to the very complicated energy structures and nonradiative relaxations in nanocrystals, such as Auger effects, phonon-assisted transitions, and the fluctuations of the surface electric field [102, 103]. Time-resolved photoluminescence has shown that the decay times may range from sub-nanoseconds to a few microseconds and the overall decay varies from sample to sample, depending on the quality of the surface passivation as well as the wavelength. As a consequence, the extraction of information on radiative dynamics by using regular time-resolved photoluminescence becomes very difficult, if not impossible.

While earlier studies on organically capped nanocrystals (often referred to as bare nanocrystals) have emphasized the contribution from dark (*i.e.*, nearly dipole-forbidden) excitonic states and attributed the unusually slow ($\sim 1\ \mu$s) decay component to optical emission of dark states [75, 101, 104], the role of dipole-allowed excitonic transitions is still an open question. The need to address this question has been made more urgent by recent advances in synthesis of core/shell nanocrystals, such as CdSe/ZnS nanocrystals, with an extremely high quantum yield. The quantum yield can be simply estimated as:

$$\eta = \frac{\tau_n}{\tau_n + \tau_r} \tag{6.39}$$

where τ_n and τ_r are decay times for non-radiative and radiative recombination,

respectively. For CdSe nanocrystals, τ_n ranges from 1 ns to 100 ns. While it is reasonable that τ_r is of order 1 μs for organically capped nanocrystals with a quantum yield of a few percent, radiative recombination time τ_r in inorganically capped nanocrystals with a quantum yield exceeding 50% should be much shorter. Additionally, the direct comparison of the time-resolved photoluminescence between bare CdSe and CdSe/ZnS nanocrystals in Figure 38 shows a qualitative difference in the decay dynamics. Compared with less than 50% emission within the first 150 ns in CdSe nanocrystals, over 90% of the total number of photons emitted are from the first 150 ns in CdSe/ZnS nanocrystals, with decay times shorter than 50 ns, suggesting a different origin of the optical emission from that in bare CdSe nanocrystals.

To investigate the radiative dynamics, and consequently, demonstrate the modified spontaneous emission in these inorganically capped semiconductor nanocrystals, we have developed an experimental approach using a polystyrene microsphere with a relatively low Q-factor of a few thousand. The system is in the low-Q regime or bad cavity limit. The nanocrystals are doped in the interior surface of the sphere to ensure good spatial overlap with the lowest radial mode. We have observed the enhanced spontaneous emission from the nanocrystals resonant with the relevant whispering gallery modes. Comparison between the time-resolved photoluminescence resonant with and off-resonant with the whispering gallery mode also allows us to single out the radiative decay component from the complicated decay dynamics and to determine the radiative decay rate in these nanocrystals. In addition, we have shown that the manifestation of cavity-QED effects depends strongly on the size of the nanocrystals, thus providing unique and valuable information on

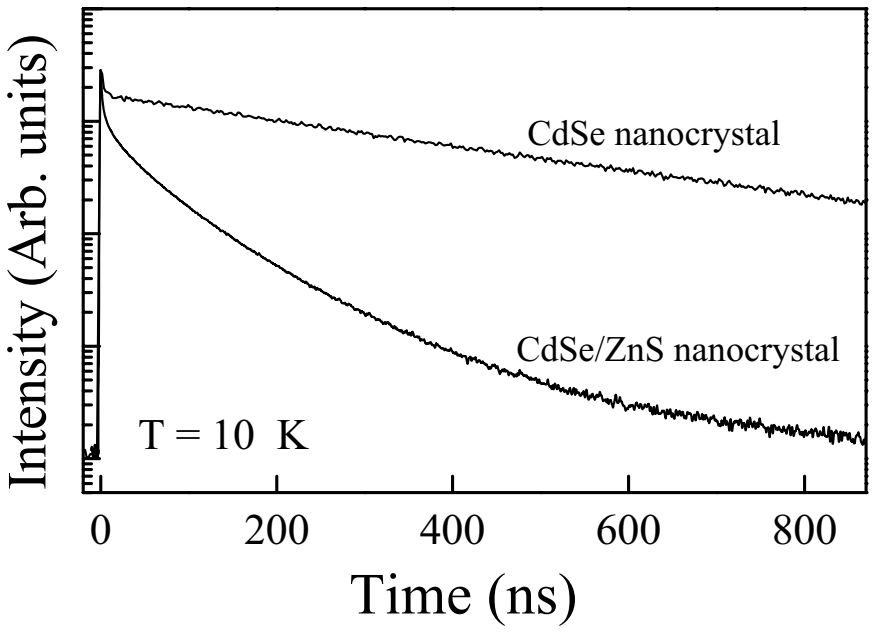

FIGURE 38. Comparison of time-resolved photoluminescence between CdSe and CdSe/ZnS nanocrystals reveals qualitative differences in nanocrystal decay dynamics. Optical emission from the first 150 ns accounts for 46% and over 90% of the total photoluminescence in bare CdSe and CdSe/ZnS nanocrystals, respectively. The decay times for bare CdSe nanocrystals are $\sim$ 200 ns while they are less than 50 ns for CdSe/ZnS nanocrystals.

the underlying optical transitions in these nanocrystals. For large nanocrystals (D $>$ 6 nm), the lowest dipole-allowed transition is predominantly radiative in origin, which is crucial for using these nanocrystals as artificial atoms in future cavity-QED studies.

In the remainder of this chapter, we will first briefly discuss the energy structure of the exciton in CdSe nanocrystals, followed by the time-resolved photoluminescence of CdSe/ZnS nanocrystals in free space and the cavity-QED studies of the composite nanocrystal-polystyrene microsphere system.

Energy Structure of CdSe Nanocrystals

In this section, we briefly discuss the energy structure of the exciton in CdSe nanocrystals to provide the necessary theoretical background for the discussion in the later sections [101, 105].

The band structure of a bulk semiconductor with a direct bandgap and cubic lattice structure is schematically shown in Figure 39. The conduction and valence bands arise from s-like and p-like atomic orbitals, respectively. At the band edge, *i.e.*, the Γ point of the Brillouin zone, the electron state is doubly degenerate with the total angular momentum of $J_e = \frac{1}{2}$ whereas the valence band is sixfold degenerate. When the spin-orbit coupling is taken into account, the valence band is further split into a fourfold degenerate subband with the total angular momentum of $J_h = \frac{3}{2}$ and a split-off subband with the total angular momentum of $J_h = \frac{1}{2}$. This fourfold degenerate valence subband consists of heavy hole and light hole bands with the azimuthal angular momentum of $M_h = \pm 3/2, \pm 1/2$, respectively.

For a spherical semiconductor nanocrystal with the size smaller than the

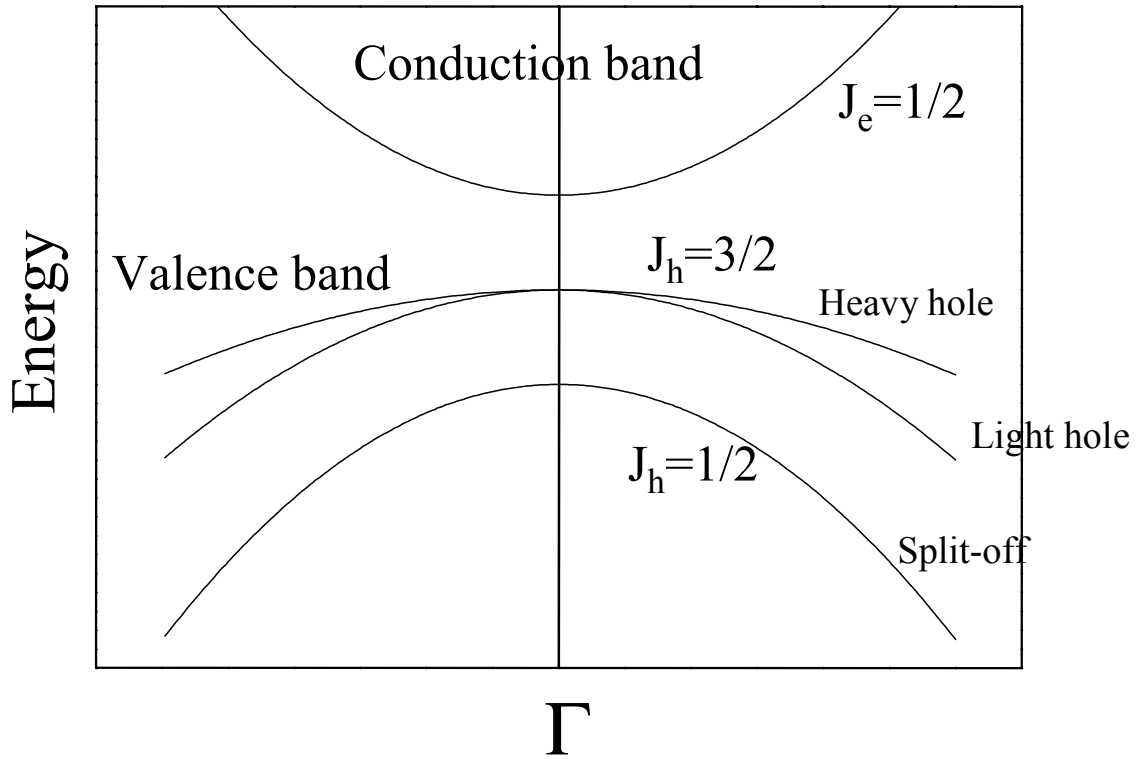

FIGURE 39. Diagram of the band structure of a bulk semiconductor with a direct gap and cubic lattice structure.

relevant Bohr radius, the energy spectrum and the wavefunctions of electron-hole pairs can be approximately obtained in the framework of the multiband Effective Mass Approximation (EMA) where the electron and hole are independently quantized and separately treated as individual particles confined in a spherical quantum well [106]. The electron and hole envelop wavefunction can thus be expressed as the product of a spherical harmonic and a spherical Bessel function and labeled by its orbital angular momentum (L_e, L_h) and radial quantum number (n_e, n_h). For a spherical nanocrystal with a cubic lattice structure, the first electron state $1S_{1/2}$ is doubly degenerate at the Γ point with $J_e = \frac{1}{2}$ whereas the first hole state $1S_{3/2}$ is fourfold degenerate with $J_h = \frac{3}{2}$ and the azimuthal angular momentum of $M_h = \pm 3/2, \pm 1/2$. Both the electron and hole have the s-like ($L_e = L_h = 0$) envelop wavefunction with the first radial quantum number ($n_e = n_h = 1$). The relevant energies of the electron and hole are given as:

$$E_{1S_{1/2}} = \frac{\hbar^2 \pi^2}{2 m_e a^2} \tag{6.40}$$

$$E_{1S_{3/2}}(\beta) = \frac{\hbar^2 \varphi^2(\beta)}{2 m_{hh} a^2} \tag{6.41}$$

where m_e and m_{hh} are the electron and heavy hole effective mass, respectively. a is the radius of the nanocrystal. $\beta = m_{lh}/m_{hh}$ is the ratio of the light hole to heavy hole effective masses. $\varphi(\beta)$ is the first root of the equation:

$$j_0(\varphi) j_2(\sqrt{\beta}\varphi) + j_2(\varphi) j_0(\sqrt{\beta}\varphi) = 0 \tag{6.42}$$

where j_n are spherical Bessel functions. Correspondingly, the first excited excitonic state for this type of nanocrystal $1S_{3/2}1S_{1/2}$ is made up of the lowest electron state

and the lowest hole state and is eightfold degenerate. However, this degeneracy will be lifted due to the effects of nanocrystal shape, internal crystal structure anisotropy and electron-hole exchange interaction. We will show that these effects not only qualitatively change the exciton energy structure at the band edge, but also redistribute the oscillator strength among all the eight excitonic states.

As discussed in Chapter V, under low pressure (< 9 GPa), CdSe nanocrystals feature hexagonal lattice structure. This intrinsic asymmetry of the crystal splits the fourfold degenerate hole states into two twofold degenerate states with $M_h = \pm 1/2$ and $M_h = \pm 3/2$, respectively. The corresponding exciton energy splitting is:

$$\Delta_{int} = \Delta_{cr} v(\beta) \tag{6.43}$$

where Δ_{cr} is the crystal field splitting in bulk crystal with a hexagonal lattice structure and the dimensionless function $v(\beta)$ describes the dependence of the energy splitting on the ratio of light hole to heavy hole masses.

The effect of nonsphericity of the nanocrystals also splits the fourfold degenerate hole states into two twofold degenerate states with $M_h = \pm 1/2$ and $M_h = \pm 3/2$, respectively. The energy splitting due to nonsphericity is given by:

$$\Delta_{shape} = 2\mu u(\beta) E_{3/2}(\beta) \tag{6.44}$$

where $\mu = c/b - 1$ is determined by the ratio of the major to minor axes of the ellipsoid nanocrystal. $E_{3/2}(\beta)$ is the energy of the $1S_{3/2}$ states in a spherical nanocrystal with the radius of $a = (b^2 c)^{1/3}$. The dimensionless function $u(\beta)$ is associated with the energy splitting due to the nonsphericity of the nanocrystals.

The degeneracy of the exciton is further lifted by the electron-hole exchange interaction that mixes different electron and hole states. The effect of the electron-hole exchange interaction on the energy splitting can be described by:

$$\eta = (a_B/a)^3 \hbar \omega_{ST} \chi(\beta) \tag{6.45}$$

where $a_B = 5.6$ nm and a are the Bohr radius and actual radius of the CdSe nanocrystal, respectively. ω_{ST} is the splitting due to the exchange interaction in bulk CdSe crystals. The dimensionless function $\chi(\beta)$ is associated with the energy splitting due the electron-hole exchange interaction. As a consequence of this electron-hole mixing, $J_{h,e}$ and $M_{h,e}$ are no longer conserved. The total angular momentum $F = J_h + J_e$ and azimuthal angular momentum $F_m = M_h + M_e$ become the only two good quantum numbers and therefore can be used to label the exciton states.

Taken together, the hexagonal lattice structure, nonsphericity of the nanocrystals, and the electron-hole exchange interaction lift the eight-fold degenerate exciton ground states into five energy levels labeled by the azimuthal angular momentum of the exciton F_m, where $F_m = \pm 2$, $F_m = \pm 1^U$, $F_m = \pm 1^L$ are doubly degenerate and $F_m = 0^U$ and $F_m = 0^L$ are singlets, as plotted in Figure 40. In addition, the oscillator strength also undergoes redistribution among these states. The oscillator strengths of $F_m = \pm 2$ and 0^L states are identically zero. For this reason, the excitonic states $F_m = \pm 2$ and $F_m = 0^L$ are called dark states. The other five states are optically active. As shown in Figure 41, while it remains the same for $F_m = 0^U$ state, the relative oscillator strength of $\pm 1^U$ and $\pm 1^L$ states feature interesting size dependence. When the nanocrystal size increases, the os-

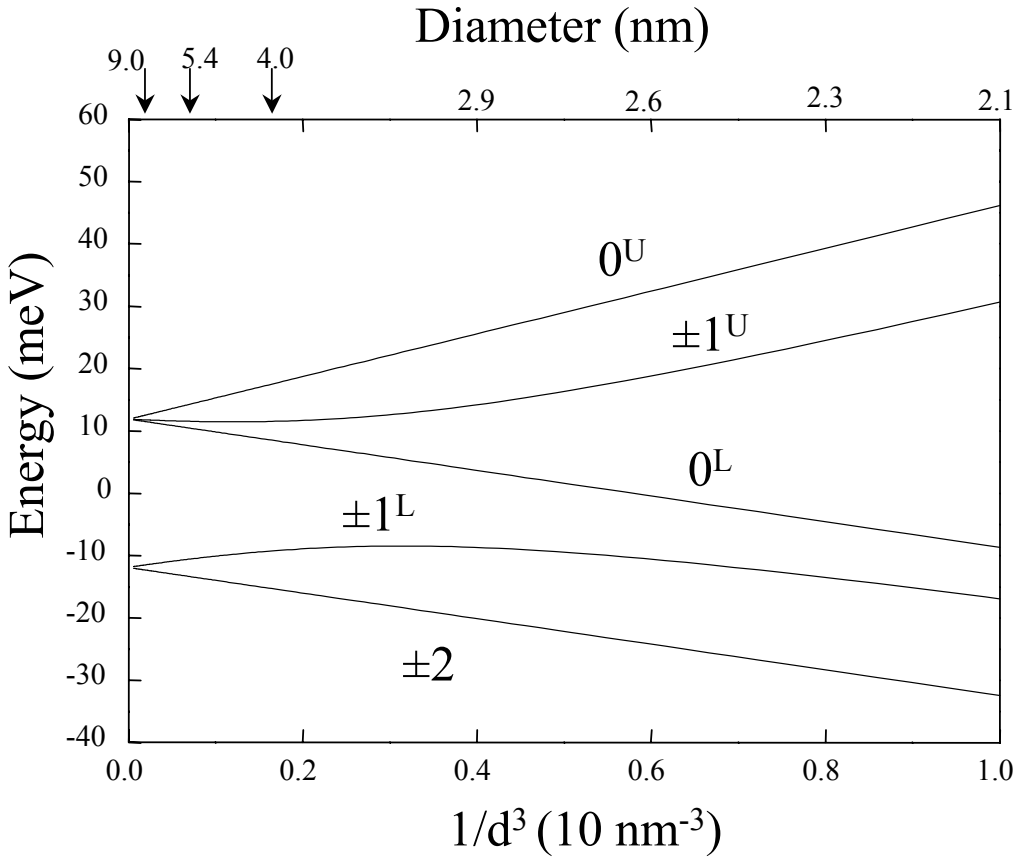

FIGURE 40. Band edge structure of the exciton in a spherical CdSe nanocrystal with hexagonal lattice structure. Arrows indicate the size of NC1, NC2, and NC3 used in the experiments. The ratio of light hole to heavy hole masses, *i.e.*, β, is 0.28 for the CdSe crystal. (Based on the results obtained in Ref [101]).

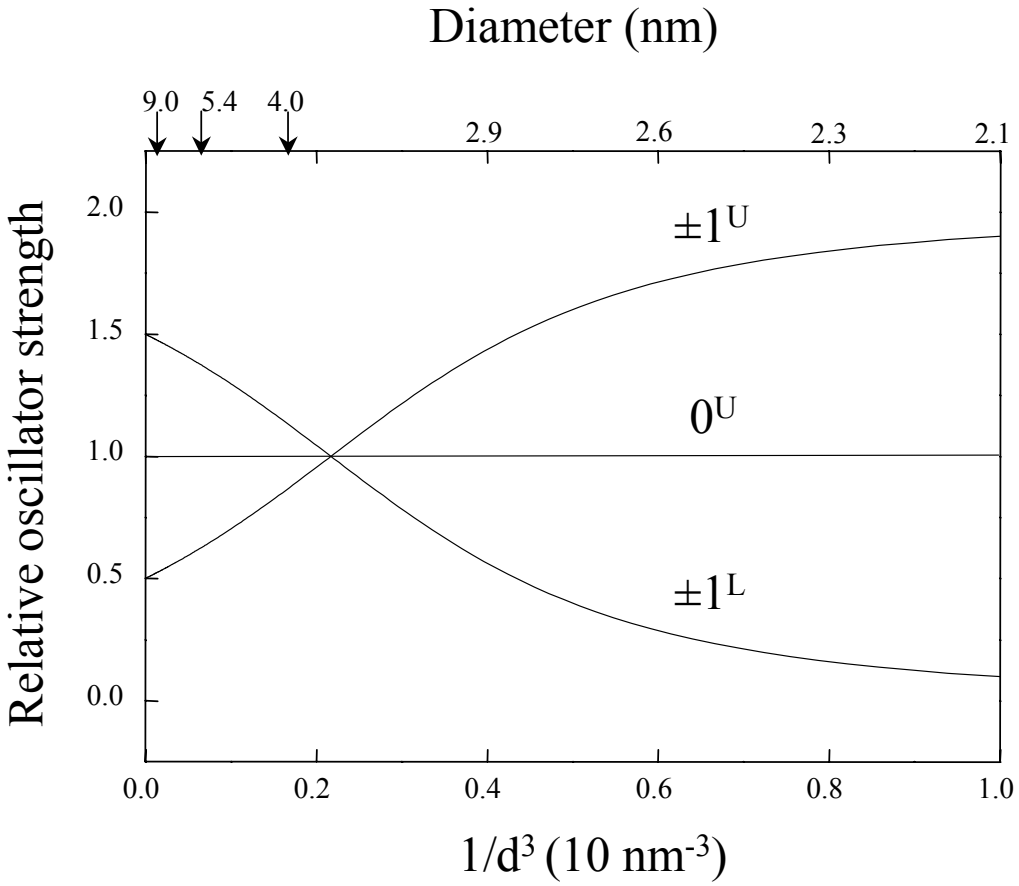

FIGURE 41. Relative oscillator strength of the bright excitonic states of a spherical CdSe nanocrystal with respect to 0^U state. Arrows indicate the size of NC1, NC2, and NC3 used in the experiments. The ratio of light hole to heavy hole masses, *i.e.*, β, is 0.28 for the CdSe crystal. (Based on the results obtained in Ref [101])
.

cillator strength of $\pm 1^L$ overtakes the oscillator strength of $\pm 1^U$. For instance, the ratio of the oscillator strength of $\pm 1^L$ to that of $\pm 1^U$ changes from 1.4 to nearly 3 when the nanocrystal diameter increases from 4.0 nm to 9.0 nm. Detailed studies of the oscillator strength of $\pm 1^{U,L}$ using size dependent ellipticity show an even more remarkable change in ratio from 0.6 to nearly 3 [101].

Although the actual shape and hence the oscillator strength may vary slightly from sample to sample, the energy structure and relative oscillator strengths of the excitons in CdSe nanocrystals plotted in Figures 40 and 41 still provide insight into the underlying physics for the discussion in the remaining chapter. Note that in the above figures we have assumed that the nanocrystals are spherical, since under the current fabrication conditions the shape of the CdSe nanocrystals is spherical or nearly spherical, as confirmed by small-angle x-ray scattering and transmission electron microscopy [88]. In this case, $F_m = \pm 2$, *i.e.*, the dark states, are the lowest lying excitonic states [1].

Experimental Results for CdSe/ZnS Nanocrystals in Free Space

We first perform time-resolved photoluminescence measurements on the CdSe/ZnS nanocrystals in free space to understand the temporal behavior of these nanocrystals.

In our experiments, three groups of core/shell CdSe/ZnS nanocrystals with respective average core diameters of 4.0 nm, 5.4 nm, and 9.0 nm (referred to as NC1, NC2, and NC3) are used. The nanocrystals are fabricated using high temper-

[1]Further theoretical calculation has shown that for oblate shaped CdSe nanocrystals, the $F_m = \pm 2$ states are still the lowest lying excitonic states. For prolate shape CdSe nanocrystals, the lowest lying excitonic state changes to the $F_m = 0^L$ state. However, this does not affect the general discussion presented later in the chapter since the $F_m = 0^L$ state is also a dark state.

ature organometallic synthesis as discussed in Chapter V. A typical quantum yield measured at room temperature is $40\% - 50\%$. In addition to optical absorption and photoluminescence, transmission electron microscopy is also used for sample characterization. Details are also provided in Chapter V.

For the time-resolved photoluminescence measurement, we use a time-correlated single photon counting system, as depicted in Figure 42(a). The excitation pulses, obtained by frequency doubling a mode-locked Ti:Sapphire laser, are centered at $\lambda = 400$ nm. An adjustable external pulse picker is used to reduce the repetition rate to 500 KHz. A spectrometer is used to spectrally choose the photoluminescence from the strongly inhomogeneously broadened nanocrystals. During the experiment, a photo-multiplier tube (PMT) is used with a time resolution of 1.5 ns, as shown in Figure 42(b).

For the low temperature experiment, the CdSe/ZnS nanocrystals suspended in chloroform are directly dispersed on a sapphire disk held to a cold finger. After the chloroform vaporizes, the powder-like nanocrystals are left on the sapphire disk.

It is known that CdSe nanocrystals, especially organically capped CdSe nanocrystals, are susceptible to oxygen and ultraviolet (UV) radiation [89]. An exposure to air or UV light can lead to surface oxidation, thus totally damaging the sample. Our first concern is therefore the effect of excitation and aging on the temporal behavior of these inorganically capped nanocrystals. Figure 43 gives the time-resolved photoluminescence from the CdSe/ZnS sample at room temperature. Curve (a) shows the decay of photoluminescence immediately after the nanocrystals are taken out from the storage tube. Curve (b) is taken after the sample

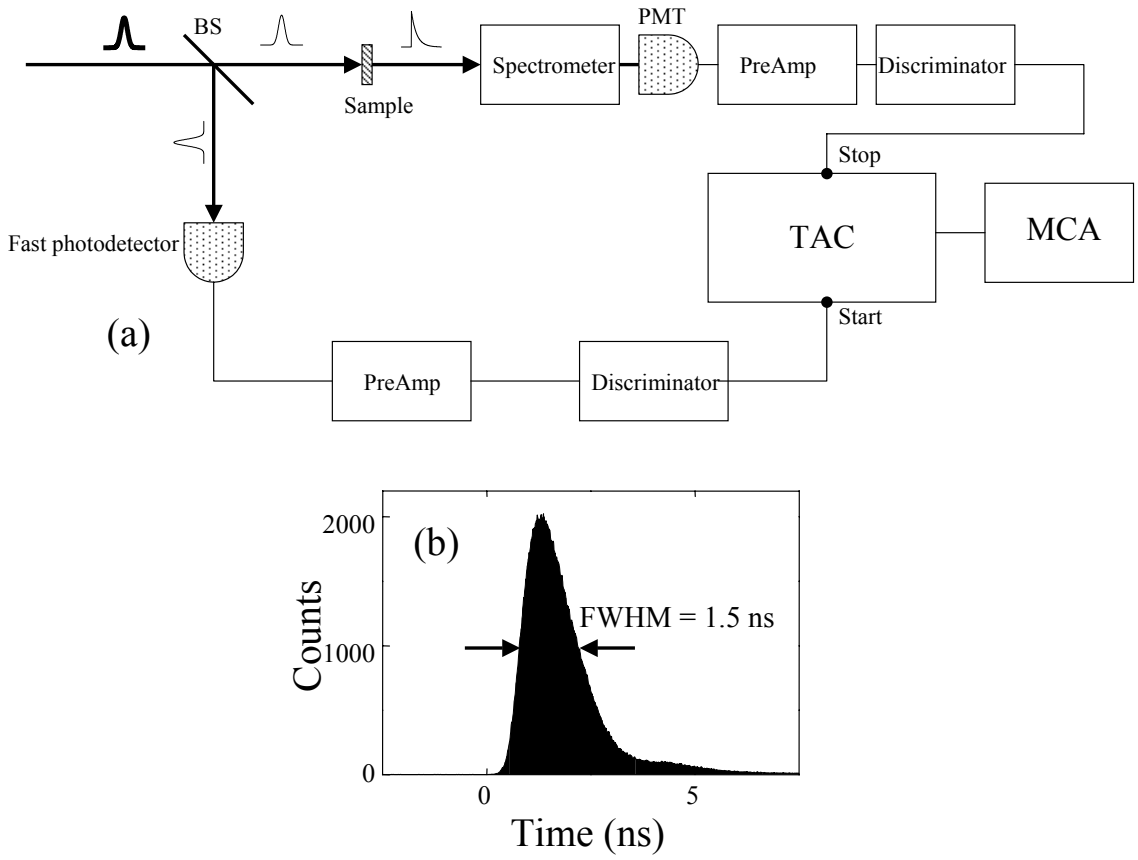

FIGURE 42. (a): The setup for the time-correlated single photon counting measurement. BS=Beam Splitter, TAC=Time-to-Amplitude Converter, MCA=Multiple Channel Analyzer. (b): A time resolution of 1.5 ns is achieved with a photo-multiplier tube (PMT).

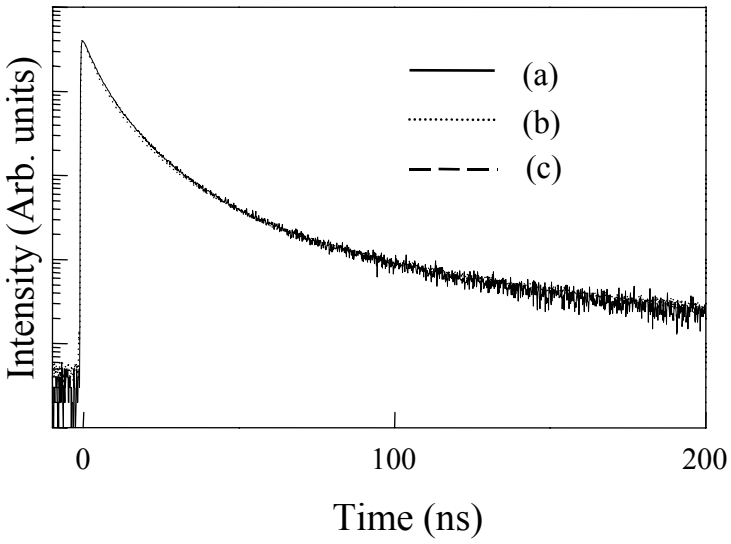

FIGURE 43. Excitation and aging dependence of time-resolved photoluminescence of CdSe/ZnS nanocrystals. (a): Sample is measured immediately after taken out from the storage tube. (b): After four hours of UV illumination and at the power level increased by a factor of two. (c): Two days exposure to air. Same power as in (a). Three nearly identical curves show that power and aging have negligible effects on time-resolved photoluminescence of the nanocrystals.

is exposed to UV illumination for four hours and at twice the power level as in curve (a). Curve (c) is taken from the same sample after being exposed to air for two days. The negligible difference among these three curves indicates that the CdSe/ZnS nanocrystals are highly stable at the excitation level that we use and over the period of two days. For experiments performed at low temperature in the vacuum cryostat, the CdSe/ZnS nanocrystals should exhibit even higher excitation and aging stability.

Figure 44(b) shows the typical time-resolved photoluminescence from NC2 at T = 10 K. Qualitatively the same results have also been obtained by another group [107]. The decay times range from nearly 1 ns for the fastest component

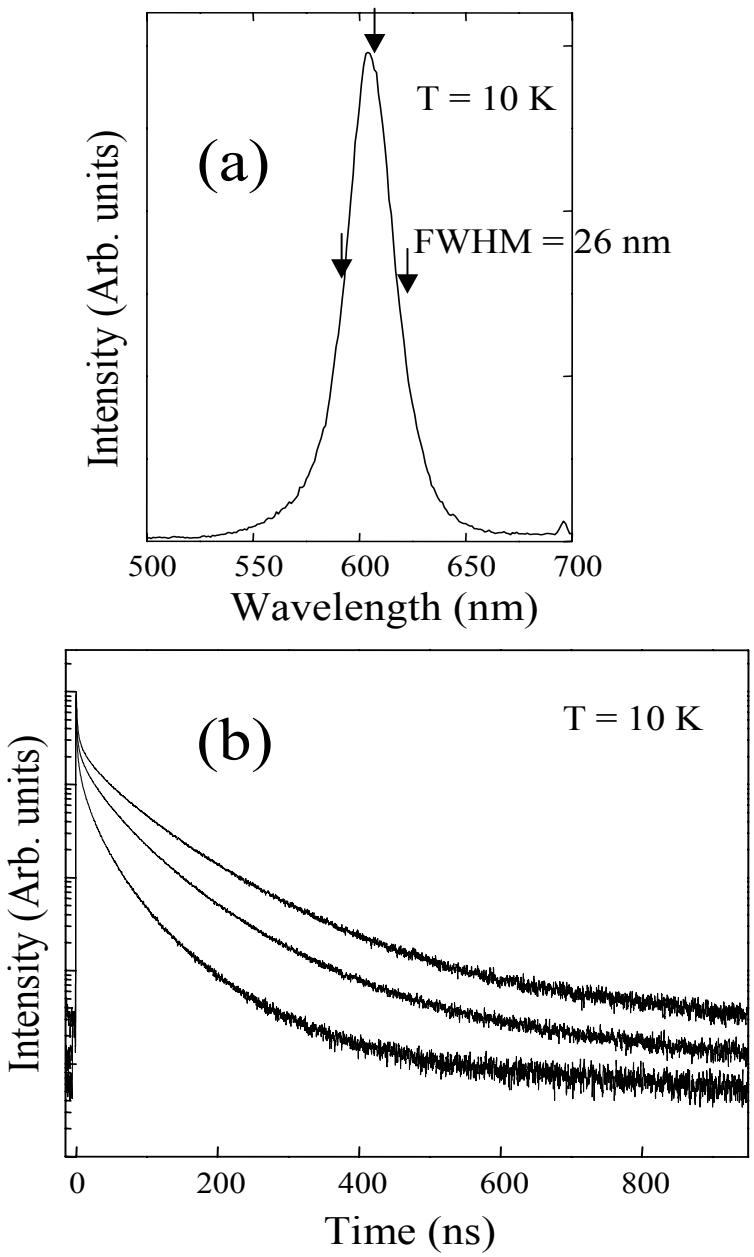

FIGURE 44. Wavelength dependence of time-resolved photoluminescence of 5.4 nm diameter CdSe/ZnS nanocrystals (NC2) at T = 10 K. From top to bottom, the wavelength is centered at 620 nm, 605 nm, and 590 nm as indicated by arrows in (a). Data are obtained with an avalanche photodiode with a time resolution of 200 ps.

to a few hundred ns for the slowest component. These decay times reflect the relevant lifetimes of various electronic states in nanocrystals and can be due to a variety of radiative and nonradiative processes. While it is difficult to determine the physical nature of the photoluminescence from these measurements, Figure 44(b) shows that optical emission in the first 150 ns accounts for nearly 90% of the overall photoluminescence. Additional measurements at room temperature (Figure 46(b)) show that optical emission in the first 100 ns can account for more than 95% of the overall photoluminescence, as was also pointed out in an earlier study [66]. As discussed later, at low temperature the time-resolved photoluminescence of the first 150 ns can be characterized by three components. Figure 45 gives the curve fit for NC2 using three exponential decay components with respective decay times of 1.35 ns, 13.3 ns, and 42.0 ns. In sharp contrast, studies of organically capped CdSe nanocrystals at 10 K, as given in Figure 38, shows that the time-resolved photoluminescence is dominated by a decay component with a decay time of a few hundred nanoseconds. The optical emission in the first 150 ns accounts for less than 50% of the total photoluminescence, in agreement with earlier studies [104].

Figure 44(b) also shows the evolution of the nanocrystal temporal behavior at T = 10 K as the wavelength changes from the red edge to the blue edge of the inhomogeneously broadened photoluminescence spectrum. For a collection of nanocrystals with an extremely large inhomogeneous spectral linewidth, apart from the direct radiative recombination, phonon-assisted optical transitions, as shown by LO-phonon progressions in fluorescence line narrowing studies [75], can also contribute to photoluminescence measured at a given wavelength. In principle, each transition can lead to a single or to multiple decay components in the time-

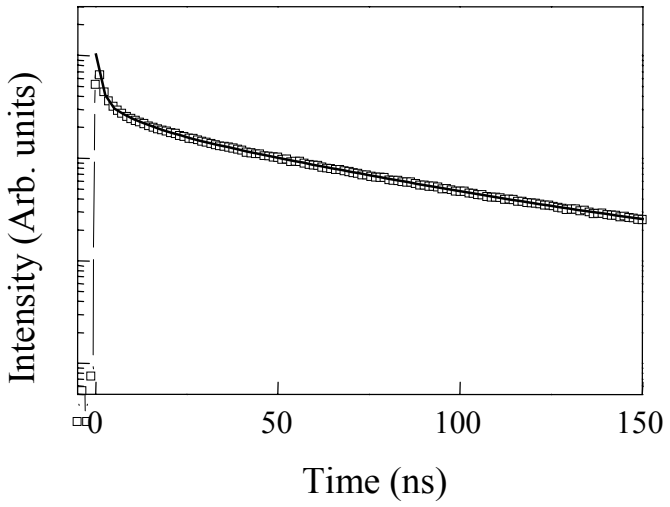

FIGURE 45. The first 150 ns of time-resolved photoluminescence from NC2 CdSe/ZnS nanocrystals in free space obtained at T=10 K and at $\lambda = 620$ nm can be fit with three exponential decay components with decay times of 1.35 ns, 13.3 ns, and 42.0 ns, respectively. For clarity, the experimental data are shown every ten data points as open squares.

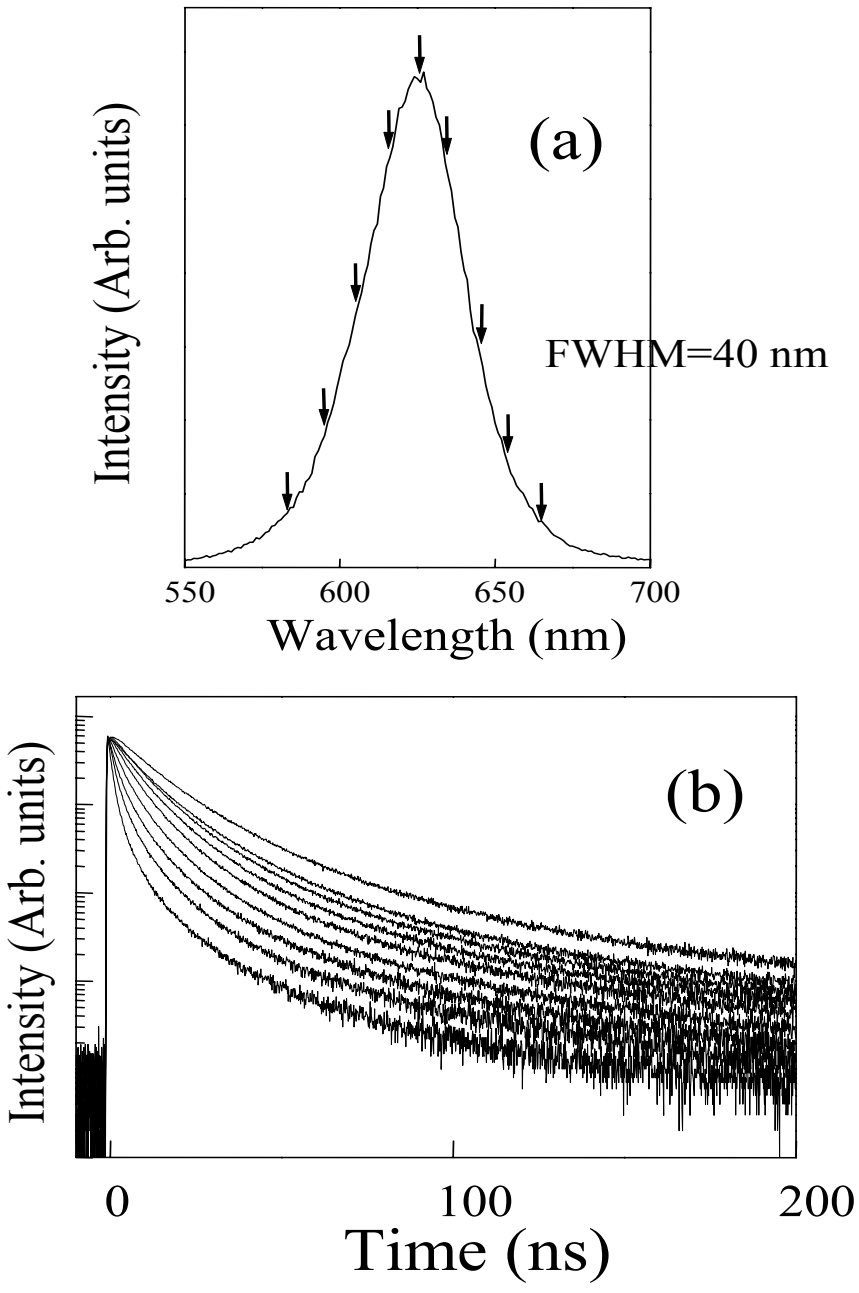

FIGURE 46. Wavelength dependence of time-resolved photoluminescence of 5.4 nm diameter CdSe/ZnS nanocrystals (NC2) at room temperature. (a): Photoluminescence spectrum of CdSe/ZnS nanocrystals at room temperature. Arrows show the spectral positions where time-resolved photoluminescence are measured. (b): Time-resolved photoluminescence at room temperature is taken at the positions marked by arrows in (a). From top to bottom, the wavelength shifts from red to blue successively.

resolved photoluminescence, resulting in complex decay dynamics. Therefore, the decay times exhibit strong wavelength dependence due to size dependence, spectral relaxation, and contributions from the higher excited states. In particular, at the blue side of the photoluminescence spectrum, the time-resolved photoluminescence picks up more contributions of the relaxation from the higher excited states, thus featuring faster decay. This is further confirmed by Figure 46 where the time-resolved photoluminescence obtained at room temperature. In order to reduce the contribution from the higher excited states, the time-resolved photoluminescence studies presented in this paper are carried out at the lower energy end of the photoluminescence spectrum (red side) unless otherwise stated.

In addition to the spectral dependence, the overall decay also exhibits pronounced temperature dependence due to strong temperature dependent nonradiative relaxation such as electron-phonon interaction. As shown in Figure 46(b) the decay times become much faster at room temperature than at helium temperature. This trend becomes more obvious if we plot in Figure 47 the temperature dependence of time-resolved photoluminescence obtained at the spectral positions a half-width higher than the respective photoluminescence center. Note that the direct comparison between two different temperatures is valid only when the temperature is below 50 K where the overall photoluminescence spectrum does not change. However, at higher temperatures, along with the broadened spectral width, the photoluminescence spectrum center shifts to a lower energy due to the decreased bandgap, making the direct comparison at two different temperatures difficult.

A closer look at the first 150 ns shown in Figure 48 reveals more details

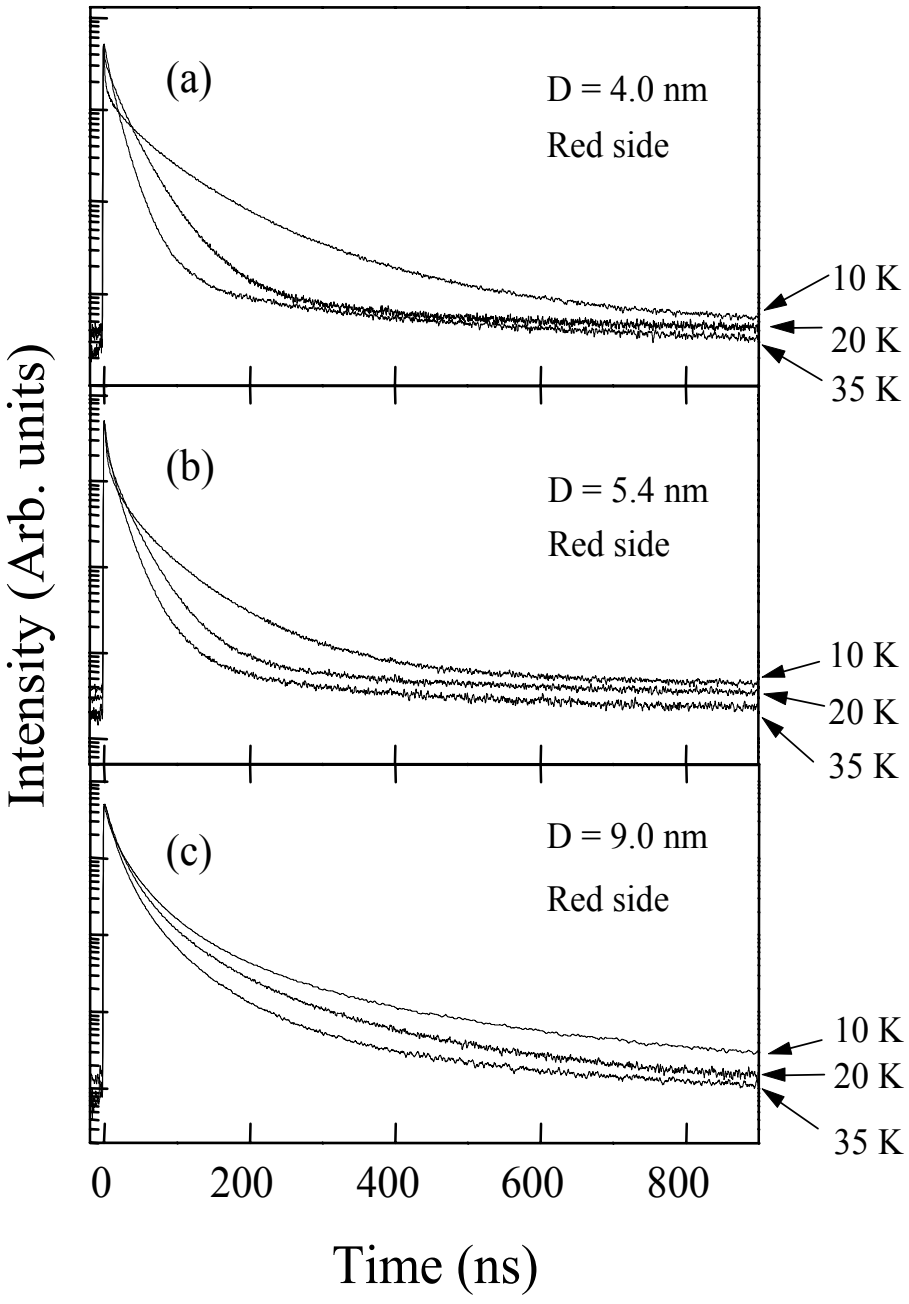

FIGURE 47. Temperature dependence of time-resolved photoluminescence in 1 μs scale. (a): NC1. (b): NC2. (c): NC3. Temperatures are T = 10 K, T = 20 K, and T = 35 K, respectively. The wavelength is centered approximately a half-width higher than the respective photoluminescence spectrum center.

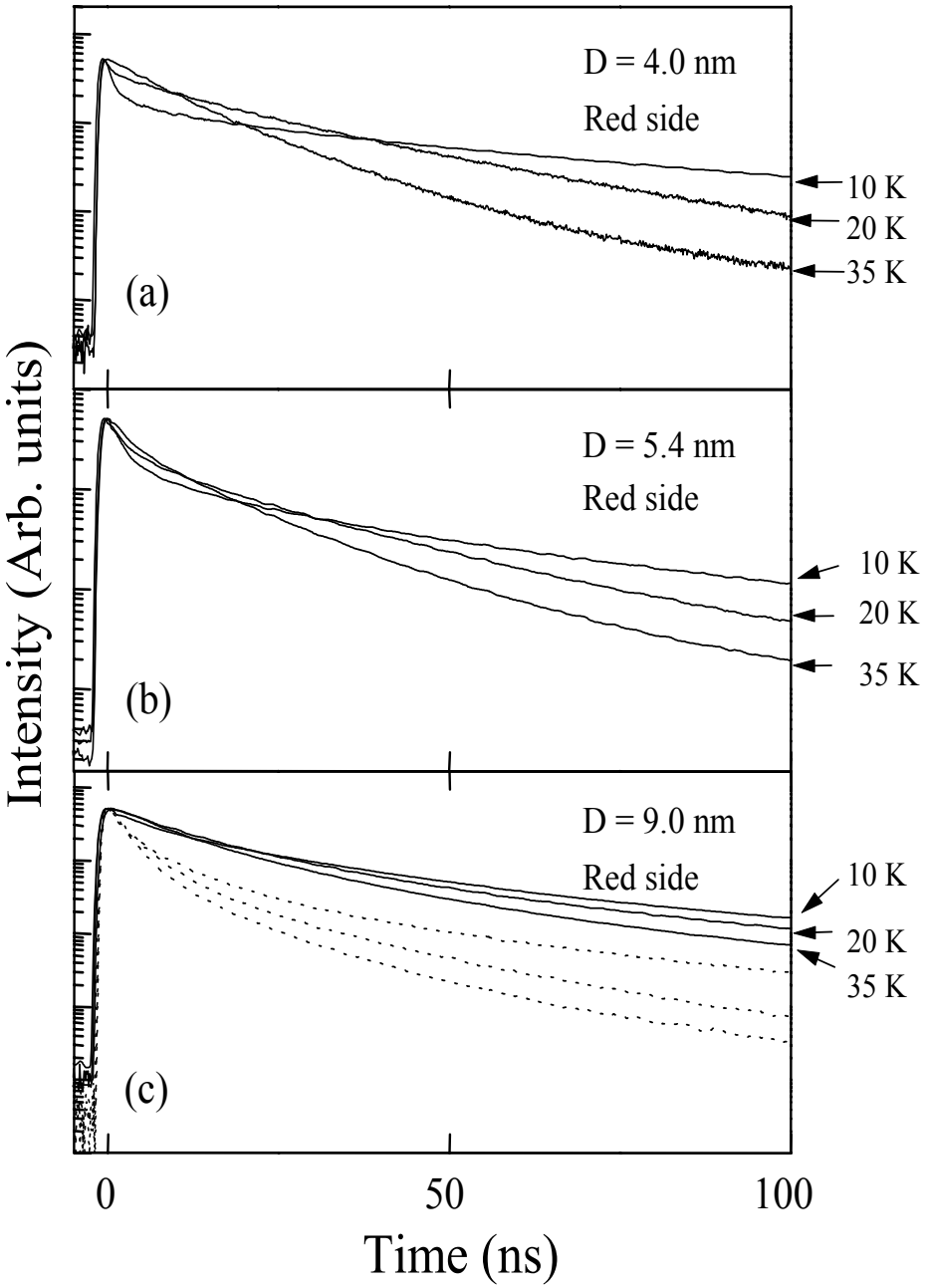

FIGURE 48. Temperature dependence of time-resolved photoluminescence of CdSe/ZnS nanocrystals for the first 100 ns clearly shows the different decay dynamics in the nanocrystals with different sizes. (a): NC1. (b): NC2. (c): NC3. Temperatures are T = 10 K, T = 20 K, and T = 35 K, respectively. The wavelength is centered approximately a half-width higher than the photoluminescence spectrum center (red side). Dotted lines are taken at the wavelength a half-width lower than the photoluminescence spectrum center (blue side).

of the change in nanocrystal temporal behavior as temperature varies. While it becomes negligible in NC3, the initial fast component of approximately 1 ns is easily observed at T = 10 K in both NC1 and NC2, showing the initial fast relaxation processes. However, at elevated temperatures, this component disappears, which was also previously observed by other groups [108]. This temperature dependence of the initial decay can be understood by considering the repopulation of the upper level state in a three-level system due to the thermal activation.

Cavity-QED Studies of CdSe/ZnS Nanocrystals

As shown in the previous section, the time-resolved photoluminescence of CdSe nanocrystals features extremely strong temperature, wavelength, and nanocrystal size dependence, making it extremely difficult to extract any information on radiative recombination in nanocrystals. In this section, we use an approach based on the cavity-QED effect that only radiative processes can be affected by the presence of a resonant cavity to single out radiative recombination from the complicated decay dynamics in semiconductor nanocrystals.

For cavity-QED studies, the nanocrystals are embedded within 1 μm of the interior surface of a polystyrene sphere as shown in Figure 49. This shell-like doping ensures the maximum spatial overlap between the nanocrystals and the lowest radial whispering gallery modes, thus considerably simplifying the photoluminescence spectra and data analysis. We have performed a series of time-resolved photoluminescence measurements to compare the temporal behavior of nanocrystals before and after the doping process. No indications of degradation have been observed.

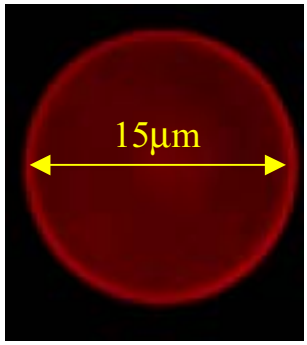

FIGURE 49. The image of a typical nanocrystal-doped polystyrene microsphere. The thickness of the doping shell is less than 1 μm. The red bright ring is due to the embedded nanocrystals with the average diameter of 5.4 nm. The whole sphere is UV illuminated.

For low temperature experiments, polystyrene spheres are spin-coated on a sapphire disk held to a cold finger. The time-correlated single photon counting setup is identical to what we have described in the previous section. The excitation laser beam is focused on the sphere and the whispering gallery modes are collected 90° off the incident direction, as shown in Figure 14.

Figure 50 shows, as an example, the photoluminescence spectrum obtained at 10 K from NC2 embedded in a polystyrene sphere. As discussed in Chapter III, for a polystyrene sphere, the surface scattering is the dominant factor that limits the Q-factor to $10^3 \sim 10^4$. The best Q-factor is obtained with a 15 μm diameter polystyrene sphere, as shown in the inset where the linewidth of the narrowest whispering gallery modes is 0.2 nm, corresponding to a Q-factor of 3000. Similar Q-factors are also obtained when the polystyrene microspheres are doped with the other two nanocrystal samples, NC1 and NC3.

At low temperature, the homogeneous linewidth of CdSe/ZnS nanocrystals

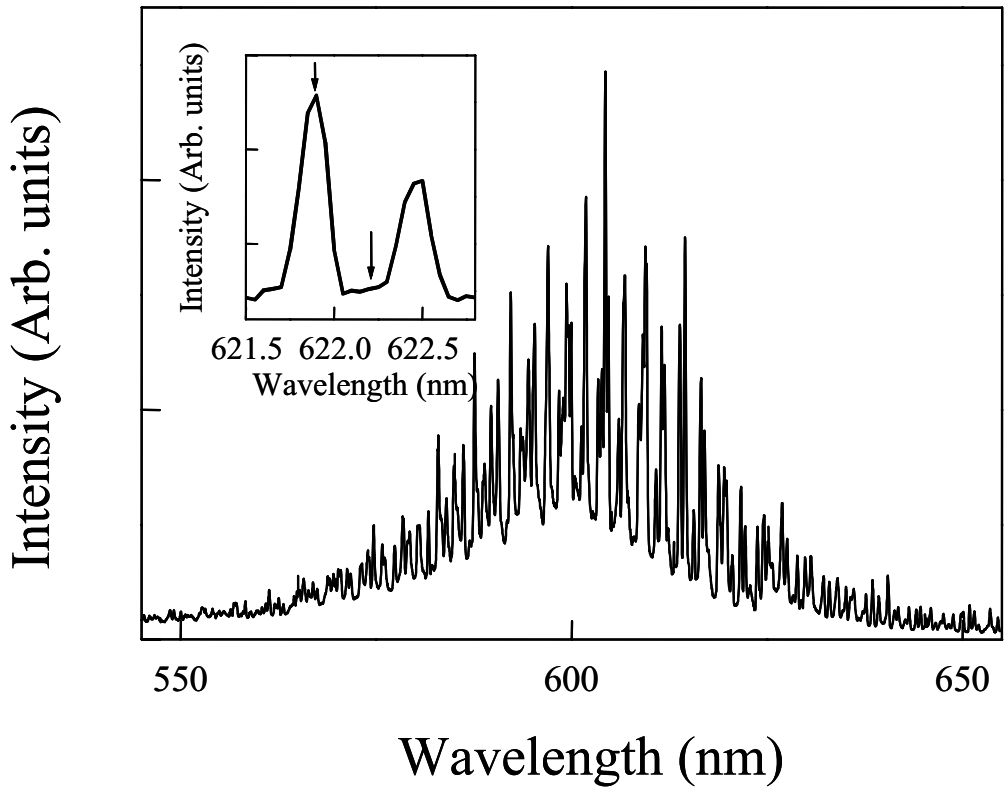

FIGURE 50. Photoluminescence spectrum of CdSe/ZnS nanocrystal doped in the interior surface of a polystyrene sphere shows pronounced whispering gallery mode resonances. Arrows in the inset show the spectral positions used for time-resolved photoluminescence. Spectral resolution is 0.1 nm for the main figure and 0.01 nm for the inset.

is less than 0.02 nm [100, 94], much narrower than the whispering gallery mode linewidth. This brings the composite nanocrystal and polystyrene microsphere into the low-Q regime where $\kappa \gg \gamma$. In this regime, the spontaneous emission rate from the exciton resonant with the cavity mode is enhanced and the enhancement is described by the Purcell factor:

$$F_p = \Gamma_c/\Gamma_r = QD\lambda^3/4\pi^2 n^3 V \tag{6.46}$$

where Γ_c is the spontaneous emission rate into the cavity mode and Γ_r is the spontaneous emission rate in a homogeneous medium. Q is the quality factor of the cavity mode, n is the refractive index of the medium, λ is the wavelength in vacuum, D is the mode degeneracy, and V is the effective mode volume. Note that we have assumed the optical dipoles resonant with the cavity mode have a random orientation and are positioned at the maximum of the vacuum electric field. For a 15 μm sphere, a Purcell factor of $F_p = 0.3$ is expected from Eq. (6.46), where we have used $Q = 3000$, $\lambda = 620$ nm, $n = 1.5, D = 2$, and an average effective mode volume $V = 35\ \mu\text{m}^3$ for lower order whispering gallery modes [31]. In our experiments, we also use polystyrene spheres with 5 μm, 7.5 μm, and 10 μm diameters. Although these smaller spheres feature smaller effective mode volumes, they do not lead to a significantly greater F_p due to the increased diffraction and scattering loss.

It should be noted that as long as the homogeneous linewidth is small compared with the cavity linewidth, the Purcell factor is determined by the properties of the cavity and remains nearly the same for all measurements for a given cavity. The actual observed relative change in the total decay rate, however, depends on

the relative contribution of the radiative decay rate Γ_r and the nonradiative decay rate Γ_{nonr}, since only Γ_r is enhanced by the presence of a resonant cavity. The relative change in the total decay rate, $\Gamma_t = \Gamma_{nonr} + \Gamma_r$, is given by

$$\varepsilon = \frac{\Gamma_{nonr} + (1 + F_p)\Gamma_r}{\Gamma_{nonr} + \Gamma_r} - 1 = F_p \frac{1}{1 + \Gamma_{nonr}/\Gamma_r}. \tag{6.47}$$

The manifestation of cavity-QED effects thus depends sensitively on the ratio Γ_{nonr}/Γ_r. For a relatively small F_p (< 1), clear signatures of changes in the total decay rate can be observed only when Γ_r is greater than or at least comparable to Γ_{nonr}. To suppress the temperature dependent nonradiative relaxations as discussed in the previous section, we first perform the experiment at 10 K. To further reduce the nonradiative relaxation and complications due to optical emissions from higher excited states, we have focused on measurements at the lower energy part of the nanocrystal photoluminescence spectrum.

Figures 51, 52, and 53 show the time-resolved photoluminescence of NC1, NC2, and NC3 nanocrystals embedded in polystyrene spheres. The photoluminescence is collected at the respective red side of the photoluminescence spectrum center. In each sub-figure, the lower curve is obtained at a wavelength resonant with a whispering gallery mode while the upper curve is obtained at a wavelength near but off-resonant ($\sim$ 0.3 nm away) with the given whispering gallery mode. An example of the relevant wavelength positions is shown in the inset in Figure 50. A spectral bandwidth of 0.1 nm is used for these studies in order to separate the resonant and off-resonant contributions. Note that in free space, the behavior of the time-resolved photoluminescence within a narrow spectral range of 5 nm is nearly identical. As shown in Figures 51, 52 and 53 as well as in their free space

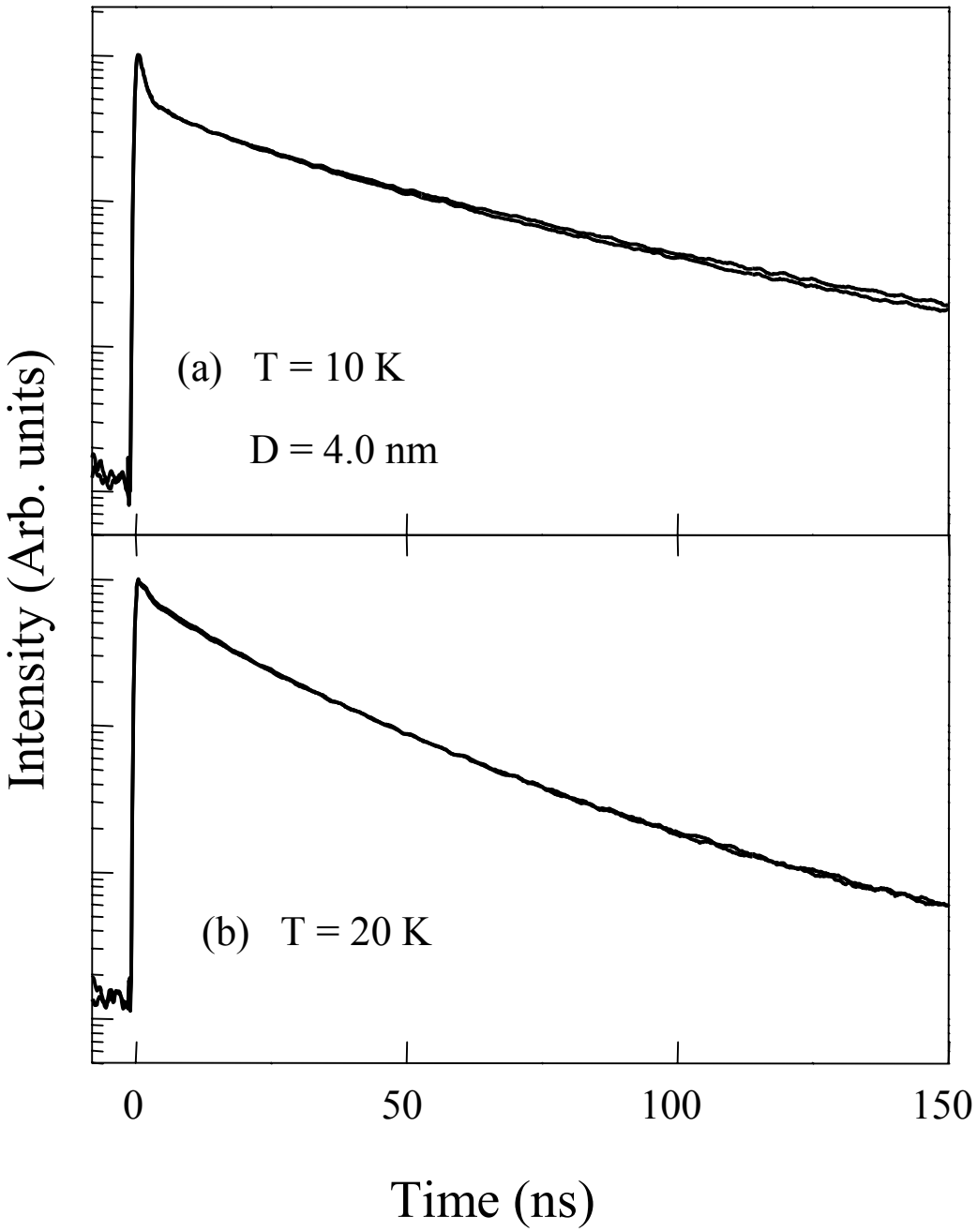

FIGURE 51. Enhanced spontaneous emission from 4.0 nm diameter CdSe/ZnS nanocrystals. Time-resolved photoluminescence from 4.0 nm diameter CdSe/ZnS nanocrystals doped in a d = 15 μm polystyrene sphere at spectral positions resonant (the lower curve in each figure) or off-resonant (the upper curve in each figure) with given whispering gallery modes. For each figure, the amplitude is normalized to the same peak intensity. (a): 10 K. (b): 20 K.

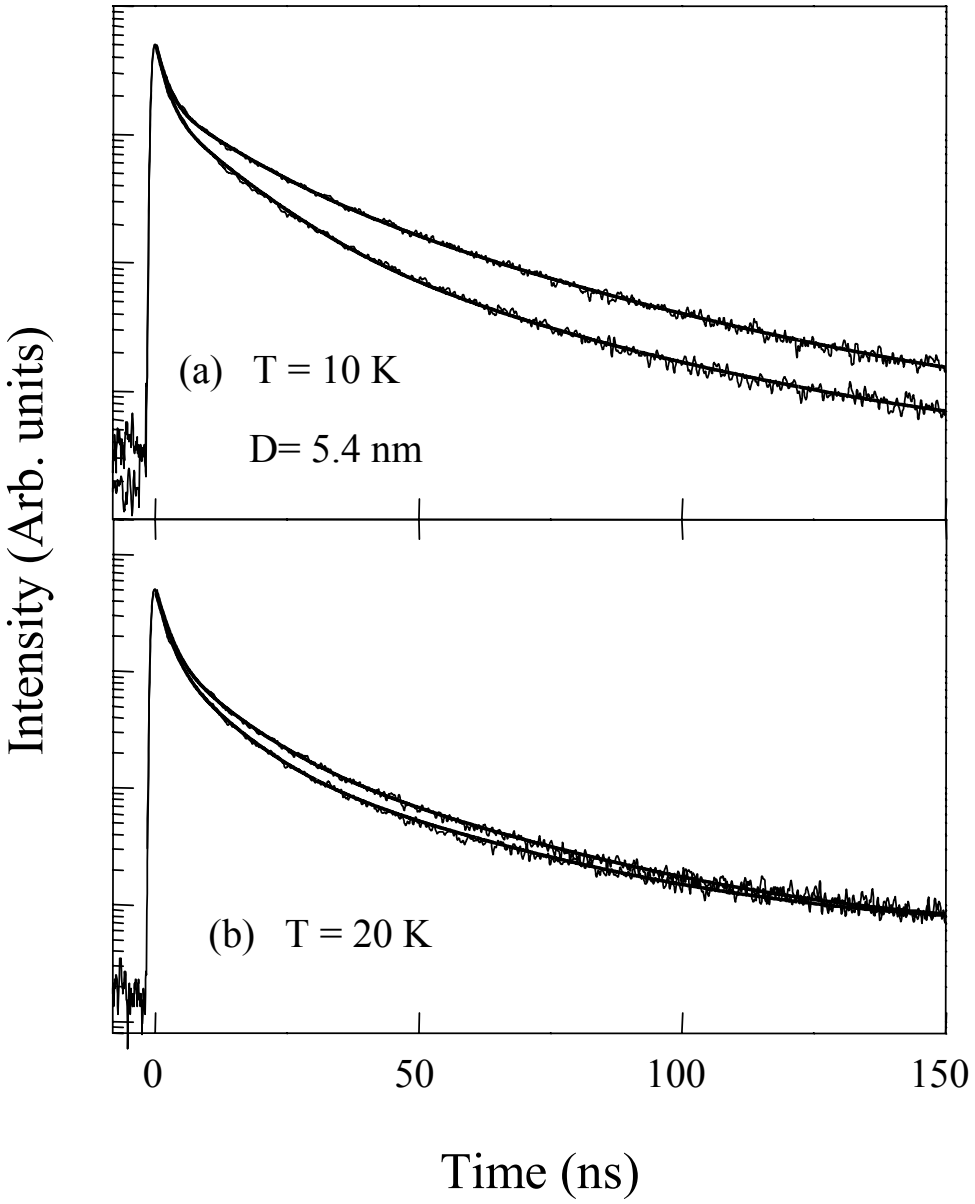

FIGURE 52. Enhanced spontaneous emission from 5.4 nm diameter CdSe/ZnS nanocrystals. Time-resolved photoluminescence from 5.4 nm diameter CdSe/ZnS nanocrystals embedded in d = 15 μm polystyrene sphere at spectral positions resonant (the lower curve in each figure) or off-resonant (the upper curve in each figure) with given whispering gallery modes (see the inset of Figure 50). For each figure, the amplitude is normalized to the same peak intensity. (a): 10 K. (b): 20 K. Curve fits are also plotted with the decay times given in Table 3 and Table 4.

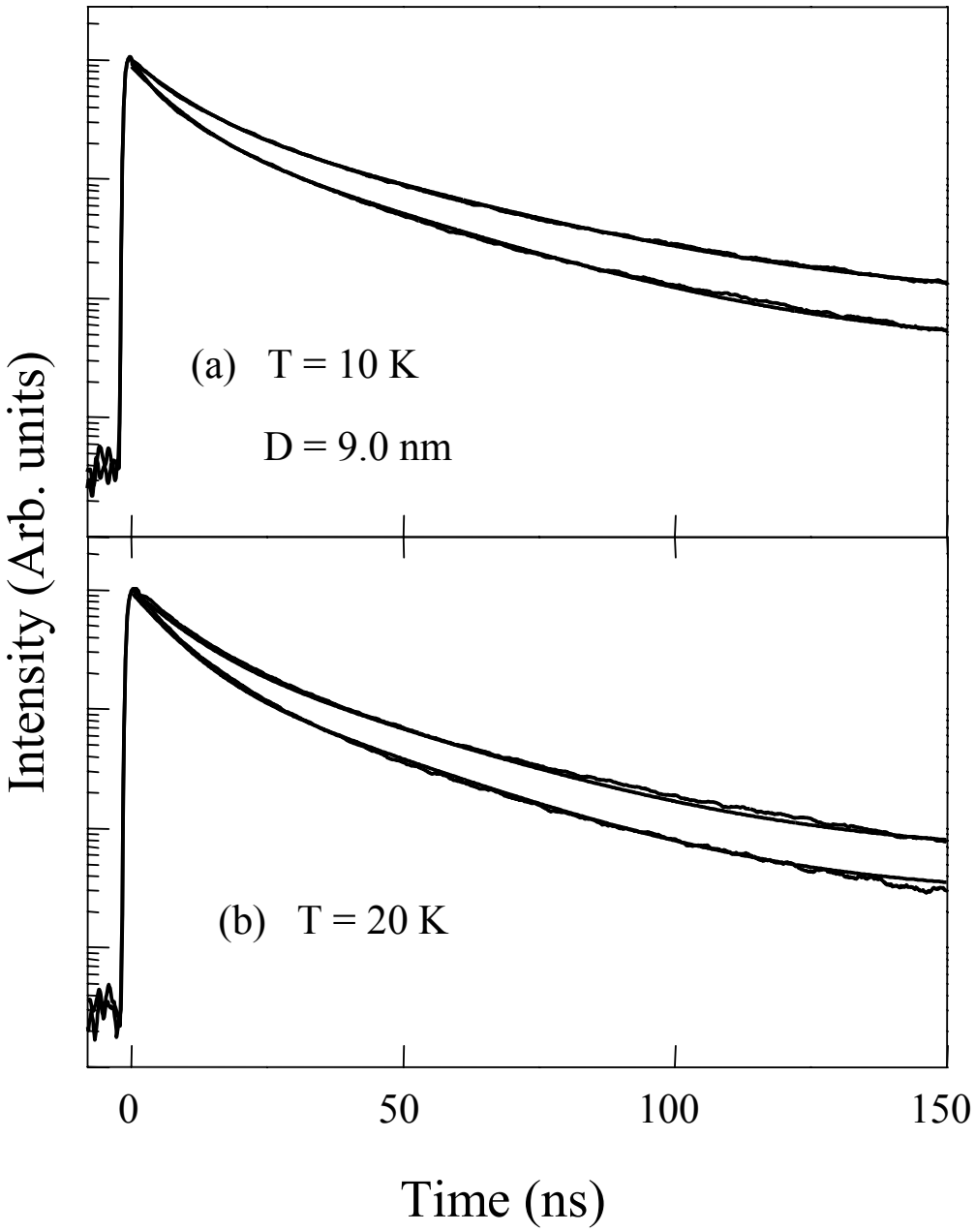

FIGURE 53. Enhanced spontaneous emission from 9.0 nm diameter CdSe/ZnS nanocrystals. Time-resolved photoluminescence from 9.0 nm diameter CdSe/ZnS nanocrystals embedded in d = 15 μm polystyrene sphere at spectral positions resonant (the lower curve in each figure) or off-resonant (the upper curve in each figure) with given whispering gallery modes. For each figure, the amplitude is normalized to the same peak intensity. (a): 10 K. (b): 20 K. Curve fits are also plotted with the decay times given in Table 5 and Table 6.

counterpart in Figure 48, in the first 150 ns, time-resolved photoluminescence can be characterized by three components. While the initial fast decay with a decay time of order 1 ns (negligible in NC3 but can still be seen in plots with a linear scale), and the third component with a much longer decay time are mostly from nonradiative relaxation processes, the second component (referred to as the cavity-QED component) is dominantly radiative for large nanocrystals (NC2 and NC3), featuring significant cavity-QED effects. A direct comparison between the photoluminescence on and off resonance with the corresponding whispering gallery modes clearly reveals an increase in the decay rate in this component for relatively large nanocrystals (NC2 and NC3). This enhancement in the spontaneous emission rate enables us to single out from the complex time-resolved photoluminescence a component whose decay is governed primarily by radiative processes.

To further verify the origin of the enhancement in the spontaneous emission, we perform the same time-resolved photoluminescence measurement with a 100 μm diameter polystyrene sphere as a control experiment, where the effective mode volume is over 30 times larger than that of a 15 μm diameter sphere. No indication of enhancement is observed as expected. The power dependence measurement of the decay also confirms that no significant stimulated emission occurs at the power level that we are using. Therefore, this enhancement in the spontaneous emission rate is solely due to the cavity-QED effects.

Figures 52 and 53 also show the numerical fits at T = 10 K and T = 20 K with the corresponding decay times given in Tables 3, 4, 5, and 6. To highlight the cavity-QED component, Figure 54 also plots the result of the numerical fit where we subtracted from the on and off resonance data shown in Figure 52(a) the first

TABLE 3. Decay times of 5.4 nm diameter CdSe/ZnS nanocrystals at 10 K. The numbers in boldface correspond to the cavity-QED components described in text.

	τ_1	$\tau_\mathbf{2}$	τ_3
Off resonance	1.9 ns	**12.4** ns	34.0 ns
On resonance	1.9 ns	**10.7** ns	32.0 ns

TABLE 4. Decay times of 5.4 nm diameter CdSe/ZnS nanocrystals at 20 K. The numbers in boldface correspond to the cavity-QED components described in text.

	τ_1	$\tau_\mathbf{2}$	τ_3
Off resonance	1.9 ns	**9.3** ns	31.0 ns
On resonance	1.9 ns	**8.4** ns	31.0 ns

and the third decay components. The relative contribution of the three photoluminescence components depends on whether the photoluminescence is resonant or off-resonant with the whispering gallery modes. The numerical fits for the upper and lower curves of NC3 in Figure 53(a) show an increase from 30% to 40% in the relative contributions of the cavity-QED component due to the enhancement effects. Similarly, for 5.4 nm diameter nanocrystals NC2, the relative contribution of the cavity-QED component is increased from 38% to 47%.

In addition to the radiative decay, nonradiative processes such as electron-phonon interactions also represent a significant contribution to the decay of the

TABLE 5. Decay times of 9.0 nm diameter CdSe/ZnS nanocrystals at 10 K. The numbers in boldface correspond to the cavity-QED components described in text.

	τ_1	$\tau_\mathbf{2}$
Off resonance	**8.7** ns	30.0 ns
On resonance	**7.2** ns	30.0 ns

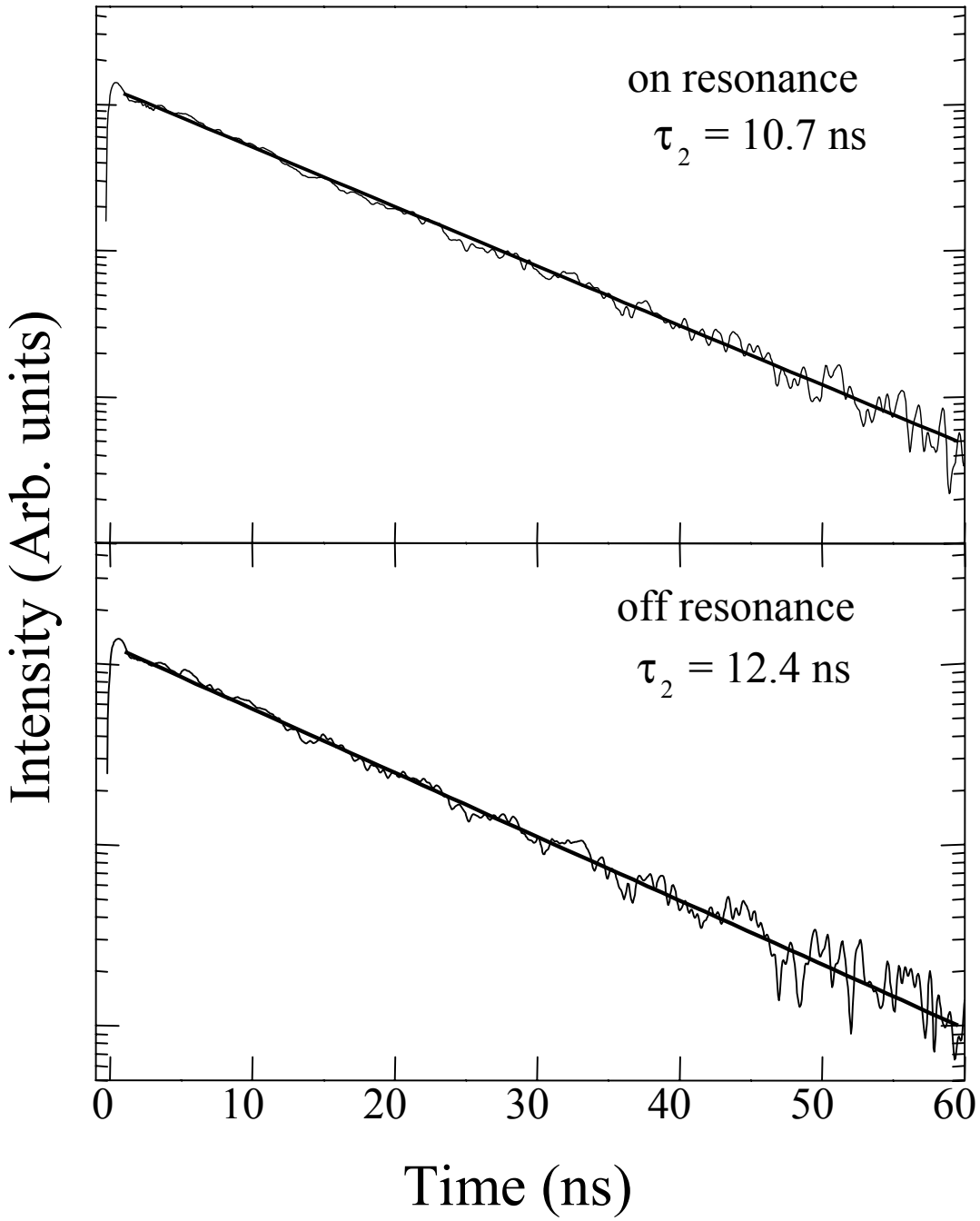

FIGURE 54. Cavity-QED components of time-resolved photoluminescence from 5.4 nm diameter CdSe/ZnS nanocrystals are obtained after substracting the first and the third decay components from the relevant time-resolved photoluminescence in Figure 52.

TABLE 6. Decay times of 9.0 nm diameter CdSe/ZnS nanocrystals at 20 K. The numbers in boldface correspond to the cavity-QED components described in text.

	τ_1	τ_2
Off resonance	**8.1** ns	28.0 ns
On resonance	**6.8** ns	28.0 ns

cavity-QED component, especially at elevated temperatures, leading to a further reduction in the relative increase in the overall decay rate, since modifications in vacuum fluctuations do not affect nonradiative decay rates. Figure 52(b) and Figure 53(b) show the time-resolved photoluminescence for NC2 and NC3, obtained at 20 K and under otherwise nearly identical experimental conditions as in Figure 52(a) and Figure 53(a). The relative increase in the overall decay rate in NC2, however, is considerably smaller due to greater contributions from the temperature dependent nonradiative processes. Note that at much higher temperatures, the homogeneous linewidth of the nanocrystal transition can become much greater than the cavity linewidth and the nonradiative relaxation becomes dominant, leading to a vanishing Purcell factor, as evidenced in Figure 55(a) where T = 30 K and the lowest curve in Figure 55(b) where T = 40 K.

As discussed previously, contributions from the rapid nonradiative relaxation processes such as spectral relaxation and higher excited states relaxation become dominant when the photoluminescence is collected at the higher energy. Consequently, the enhancement in the spontaneous emission rate due to the cavity-QED effects is completely obscured by the much faster overall decays, even at the center of the photoluminescence spectrum, as shown in Figure 56.

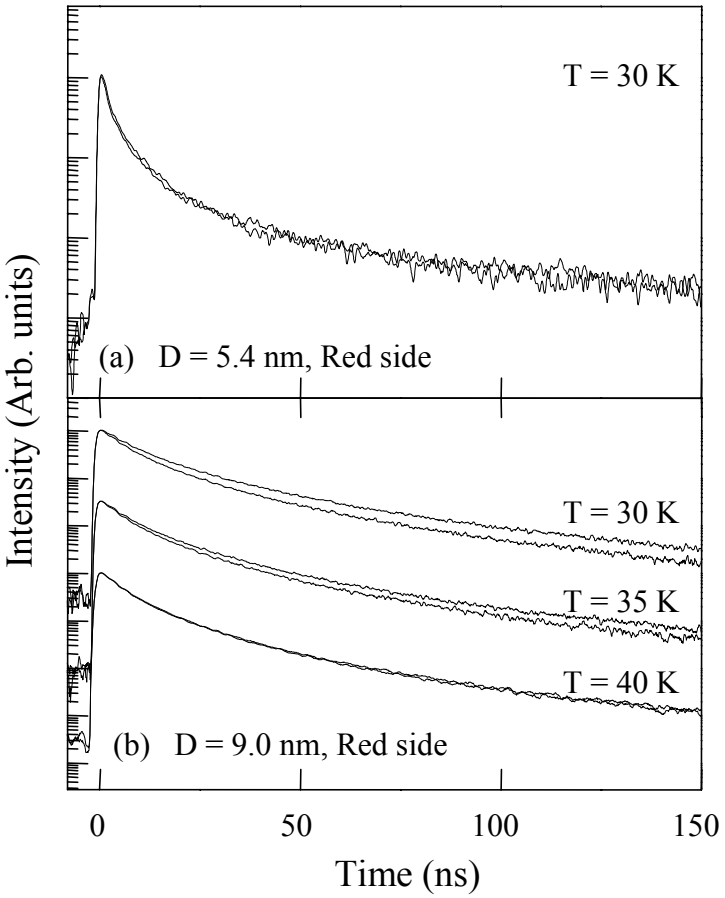

FIGURE 55. Enhanced spontaneous emission from CdSe/ZnS nanocrystals at elevated temperature. (a): Time-resolved photoluminescence from 5.4 nm diameter CdSe/ZnS nanocrystals at T = 30 K. (b): Time-resolved photoluminescence from 9.0 nm diameter CdSe/ZnS nanocrystals at T = 30 K, 35 K, 40 K. The curves are vertically shifted for clarity.

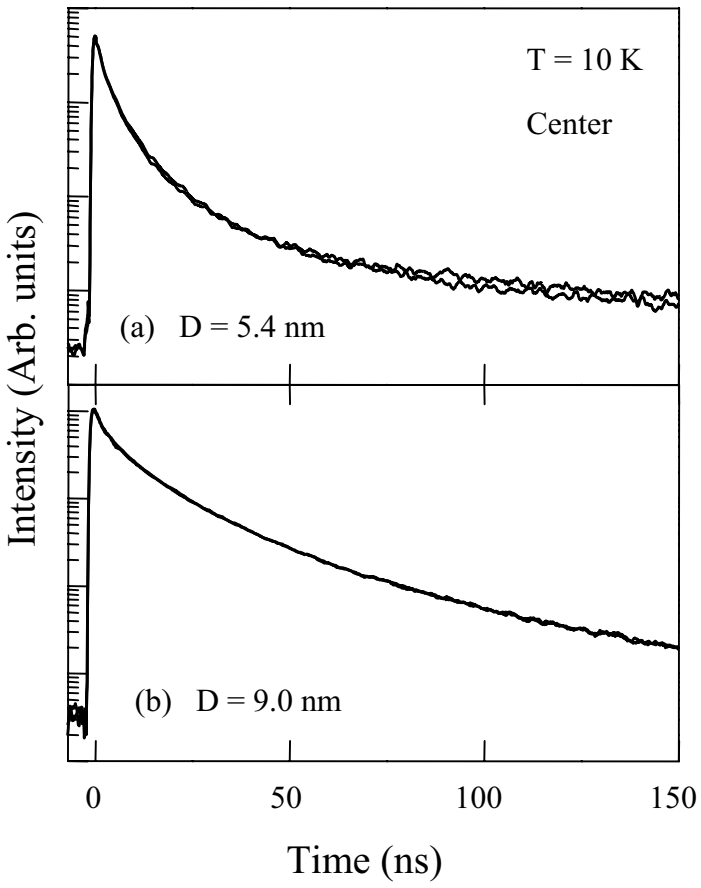

FIGURE 56. Enhanced spontaneous emission from CdSe/ZnS nanocrystals at the center of the photoluminescence spectrum at T = 10 K. (a): NC2. (b): NC3.

Discussion

Now we discuss the origin of the cavity-QED component. The manifestation of the cavity-QED effects on the spontaneous emission rate also features strong nanocrystal size dependence as shown in Figures 51, 52, and 53, providing additional information on the physical origin of the underlying decay processes, which is otherwise difficult to obtain.

As shown in Figures 57, for $\pm 1^L$ states, which are the lowest dipole-allowed transitions, Γ_{nonr} includes contributions from thermal activation to higher excited states and relaxation into the lowest excited states, which are ± 2 states (dark states). The relaxation into these dark states requires spin flipping of excitons and is shown to be extremely slow in recent studies based on time-resolved Faraday rotation [109]. At low temperature, thermal activation from the $\pm 1^L$ to $\pm 1^U$ states is also slow because of the large energy separation (> 10 meV) between these states as shown in Figure 40. In comparison, for excitonic states $\pm 1^U$ with energies higher than the $\pm 1^L$ states, rapid relaxation into lower energy states are expected since in this case the relaxation does not require spin flipping. For these states, Γ_{nonr} is much greater than Γ_r. Photoluminescence from these states contributes to the initial decay component in time-resolved photoluminescence.

The temporal behavior of photoluminescence and the manifestation of cavity-QED effects also depend on details of exciton thermalization. While extremely slow spin relaxation prevents thermalization between the $\pm 1^L$ and ± 2 states, the 0^U state can be repopulated by rapid thermalization with the 0^L dark state. For very large nanocrystals such as NC3, the energy spacing between these two states approaches 1 meV or smaller. This thermal repopulation, however, does not lead

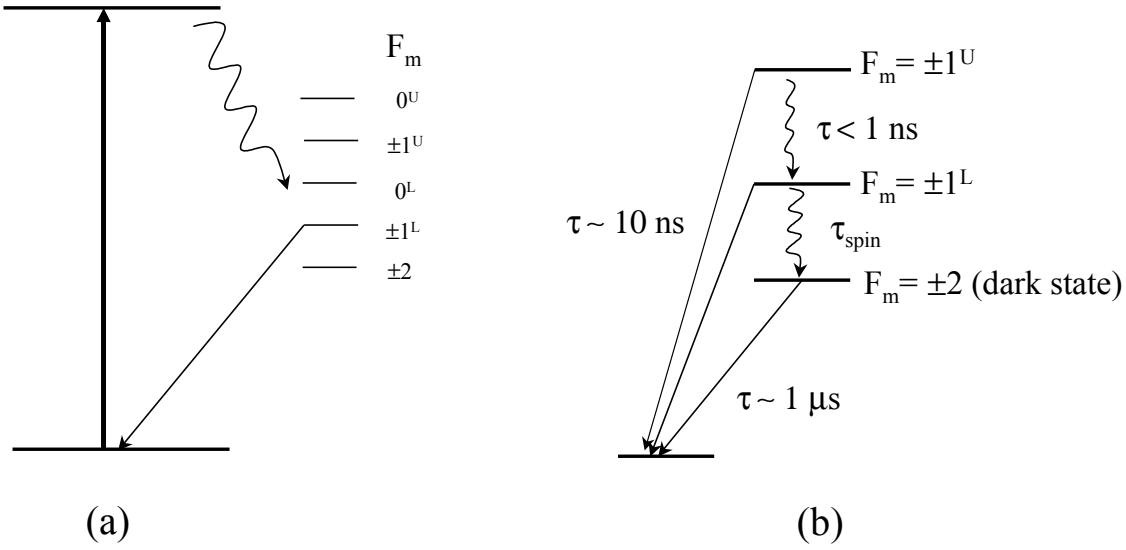

FIGURE 57. Decay dynamics of the exciton in CdSe nanocrystals. (a): Off-resonant pump, relaxation and recombination processes. (b): Detailed decay dynamics of the exciton at the band edge.

to a significant contribution to photoluminescence in Figures 51, 52, and 53 since as we discussed earlier, the data in these figures are obtained at the lower energy end of the photoluminescence spectra to minimize contributions from higher excited states. Theoretically, the 0^U state is nearly 20 meV or more above the bright states $F_m = \pm 1^L$ (see Figure 40) [101]. As shown in Figure 56, for all the nanocrystals that we have used, no cavity-QED effects were observed for photoluminescence obtained at the center or at the higher energy side of the photoluminescence spectra where contributions from higher excited states become much more important.

The above analysis leads us to conclude that the cavity-QED component in Figures 51, 52, and 53 arises from the lowest dipole-allowed transition, *i.e.*, from the $\pm 1^L$ states. This is further supported by the temperature and especially the nanocrystal size dependence of the cavity-QED effects, as we discuss in detail

below.

While the temperature and spectral position are responsible for Γ_{nonr} in Equation (6.47), Γ_r is solely determined by the size of the nanocrystals. As discussed in the theory section, a calculation based on EMA has shown that the oscillator strength of the $\pm 1^L$ states increases with increasing nanocrystal size [101]. When the nanocrystal size increases from less than 3 nm to more than 6 nm in diameter, the radiative lifetime $1/\Gamma_r$ decreases from of order 100 ns to of order 10 ns [101, 105]. The ratio Γ_{nonr}/Γ_r for the $\pm 1^L$ states is thus expected to increase with decreasing nanocrystal size. Hence, smaller nanocrystals should feature a smaller ε as well as a smaller relative contribution from the $\pm 1^L$ states to the overall photoluminescence, leading to negligible cavity-QED effects, as observed in NC1 (see Figure 51), in sharp contrast to the large nanocrystals where pronounced cavity-QED effects are observed. This size dependence of the oscillator strength is also reflected in the time-resolved photoluminescence from nanocrystals in free space. While it is obvious in NC1 and NC2, as shown in Figure 48, the fast initial decay disappears in larger nanocrystals NC3. This is due to the increased decay rate of $\pm 1^L$ with the increased nanocrystal size. In this case, the decay is overwhelmingly represented by the decay from $\pm 1^L$.

In addition, the decay of the cavity-QED component in Figure 48(c) exhibits very week temperature dependence in the first 20 ns due to the large ratio of Γ_r/Γ_{nonr}. This is in contrast to the results taken at the blue side of the photoluminescence spectrum as plotted in the dotted lines in Figure 48(c) and to the results taken with smaller nanocrystals in Figure 48(b). In both cases, the nonradiative relaxation becomes important and therefore the decay features strong temperature

dependence. The manifestation of cavity-QED effects at elevated temperatures also varies as nanocrystal size increases. While the cavity-QED effects nearly vanish at T = 30K for NC2, Figure 55(b) shows that the cavity-QED enhancement effects can still be observed even at T = 35 K for NC3 due to larger Γ_r/Γ_{nonr}.

The decay times of the cavity-QED components of NC2 and NC3, or generally, the lifetime of $\pm 1^L$ can be extracted by comparing the on and off-resonant curves. While the total decay obtained when the photoluminescence is off-resonant with the relevant whispering gallery mode is:

$$\Gamma_t = \Gamma_r + \Gamma_{nonr} = \frac{1}{\tau^{off}_{cavity-QED}}, \tag{6.48}$$

the total decay for the photoluminescence resonant with the whispering gallery mode is:

$$\Gamma_t = \Gamma_r(1 + F_p) + \Gamma_{nonr} = \frac{1}{\tau^{on}_{cavity-QED}} \tag{6.49}$$

where $\tau^{on}_{cavity-QED}$ and $\tau^{off}_{cavity-QED}$ are referred to as the respective decay times of the cavity-QED component when the photoluminescence is on and off-resonant with the relevant whispering gallery mode. Therefore, the enhanced spontaneous emission rate or the spontaneous emission rate into the resonant whispering gallery modes can be derived as follows:

$$\Gamma_c = \Gamma_r F_p = \frac{1}{\tau^{on}_{cavity-QED}} - \frac{1}{\tau^{off}_{cavity-QED}}. \tag{6.50}$$

According to Tables 3 and 5, Γ_t and Γ_c are 8.06×10^7/s and 1.3×10^7/s for

NC2, and 1.15×10^8/s and 2.4×10^7/s for NC3. These enhancements correspond to a 16% and 20% increase in the overall decay rate, compared with the Purcell factor of 0.3 expected from Equation (6.46). This difference can be accounted for by considering the spatial and spectral distribution of nanocrystals as illustrated in Figure 58. Even with surface doping, most of the nanocrystals are positioned near but not exactly at the peak of the vacuum electric field of the whispering gallery modes. Moreover, the spectral bandwidth of the spectrometer is still comparable to the cavity linewidth. Therefore, a significant fraction of the photoluminescence involved is slightly detuned from the cavity resonance center. The Purcell factor is thus given by [30]:

$$F_p(r,\omega) = F_p^{max} \frac{|\mathbf{E}(r)|^2}{|\mathbf{E}|^2_{max}} \frac{\Delta\lambda_c^2}{\Delta\lambda_c^2 + 4\omega^2} \tag{6.51}$$

where $\Delta\lambda_c^2$ is the cavity linewidth and ω is the detuning. F_p^{max} is the Purcell factor obtained when the photoluminescence is at the center of the cavity and the nanocrystal is positioned at the maximum of the electric field in the microsphere. Consequently, nanocrystals at different spatial and spectral positions should experience different enhancement and hence a different decay rate. The time-resolved photoluminescence of the nanocrystals in a microsphere can be expressed as:

$$I(t) \propto \int D(r)C(r)e^{-(\Gamma(r,\omega)+\Gamma')t} dr d\omega \tag{6.52}$$

where $D(r)$ is nanocrystal distribution function. $C(r)$ gives the coupling efficiency of the photoluminescence into the whispering gallery mode. Γ' represents the total decay rate that is not affected by the presence of the cavity. The decay rate into

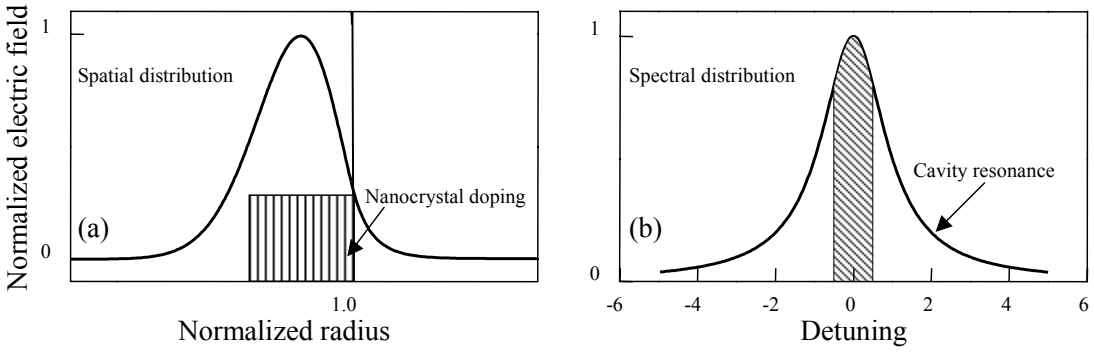

FIGURE 58. Spatial and spectral distribution of the Purcell factor. (a): Spatial distribution of the Purcell factor. Nanocrystals are uniformly doped in the shaded area. (b): Spectral distribution of the Purcell factor. Shaded area shows the bandwidth of the spectrometer.

the cavity-mode for a nanocrystal at a particular spatial and spectral position (r, ω) is given by $\Gamma(r,\omega)$, which should be proportional to the Purcell factor:

$$\Gamma(r,\omega) \propto \frac{|\mathbf{E}(r)|^2}{|\mathbf{E}|^2_{max}} \frac{\Delta\lambda_c^2}{\Delta\lambda_c^2 + 4\omega^2}. \tag{6.53}$$

We first discuss the effects of the spectral distribution of the Purcell factor. For the purpose of illustration, we only plot the decay associated with cavity-modified decay rate $\Gamma(r,\omega)$. The data marked as squares in Figure 59(a) shows the simulated decay using Equation (6.52) where we only consider the spectral detuning effects. In this simulation, the bandwidth of the spectrometer and the linewidth of the whispering gallery mode are 0.1 nm and 0.2 nm, respectively, as obtained from the experiment. While the actual dynamics should feature a deviation from the single exponential decay, this decay can still be reasonably fit using a single exponential component with an averaged Purcell factor as shown by

the solid line in Figure 59(a). Detailed calculation shows that due to the spectral distribution, the effective Purcell factor is reduced to 92% of the Purcell factor obtained when the nanocrystal photoluminescence is at the peak of the resonance.

Although the detailed information of the nanocrystal distribution along the radial direction is virtually impossible to obtain, from the confocal microscope image in Figure 49 we estimate that the nanocrystals are doped in the interior surface within a few percent of the radius. The decay marked as squares in Figure 59(b) is obtained using Equation (6.52) and the electric field of the mode with $l = 40$ and $p = 1$ (see Figure 11(a)) where we only consider the spatial distribution effects. In this simulation, we have assumed that the coupling efficiency $C(r)$ is proportional to the intensity of the electric field, *i.e.*, $C(r) \propto E^2(r)$. We have also assumed that the nanocrystals are uniformly doped within ten percent of the sphere radius. Likewise, the overall decay can still be fit using a single exponential component with an averaged Purcell factor, as shown in the solid line in Figure 59(b). The average Purcell factor is calculated to be 83% of the Purcell factor obtained when the nanocrystal is positioned at the peak of the electric field. For the actual sphere with $l > 100$, the electric field is more concentrated, as shown in Figure 11(b). Consequently, the reduction of the Purcell factor is expected to be even smaller.

Taken together, as a result of a statistical average over the spatial and spectral distribution of nanocrystals, the Purcell factor is reduced to 0.23, consistent with the experimental results. In addition, the cavity-QED component can still be reasonably fit using a single exponential component with an averaged Purcell factor. This justifies the curve fit that we used previously to obtain the decay rate

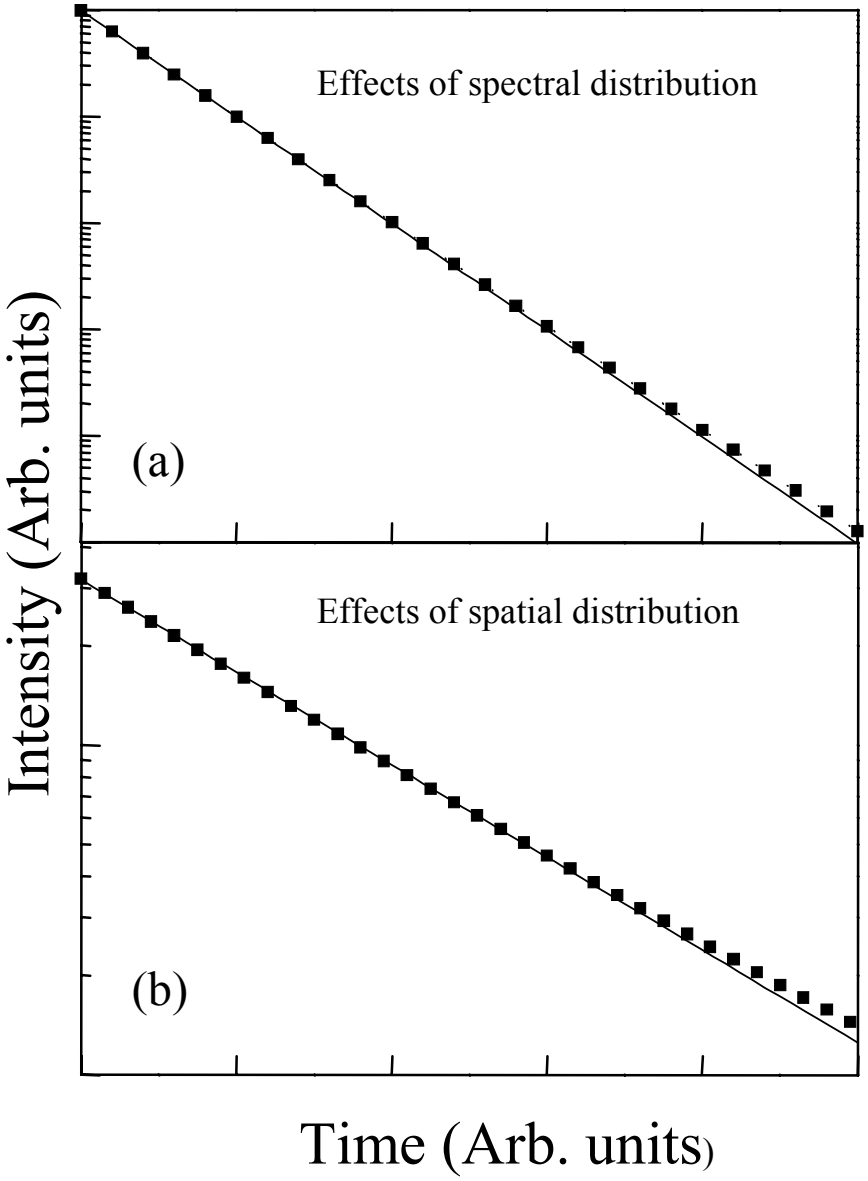

FIGURE 59. Effects of spatial and spectral distribution of the Purcell factor on time-resolved photoluminescence. (a): Effects of the spectral distribution of the Purcell factor on the time-resolved photoluminescence. The bandwidth of the spectrometer is 0.1 nm and the linewidth of the whispering gallery mode is 0.2 nm. (b): Effects of the spatial distribution of the Purcell factor on the time-resolved photoluminescence. We have assumed that the nanocrystals are uniformed doped within ten percent of the sphere radius. Simulated decays obtained using Equation (6.52) are shown as squares, whereas curve fits using a single exponential decay are drawn as solid lines.

of the cavity-QED component. It is noted that at T = 20 K, the relative change ε becomes smaller ($\sim$ 11%) due to the increased Γ_{nonr}. However, the respective enhanced spontaneous emission rates 1.2×10^7/s and 2.4×10^7/s, obtained from Tables 4 and 6, remain nearly unchanged for NC2 and NC3, indicating the same effective Purcell factor as expected.

Quantitative analysis using Eq. (6.46) and $F_p = 0.23$ yields a decay time $1/\Gamma_r$ for NC2 and NC3 of order 10 ns, in agreement with the theoretical expectation [105]. While there are considerable error bars ($\pm$20%) in the numerical analysis, the observation of the pronounced cavity-QED effects by itself indicates that Γ_r is considerably greater than Γ_{nonr} since otherwise ε would be too small to have a significant effect. Additionally, it should be noted that while the estimation of the decay time of $\pm 1^L$ is determined by the Purcell factor that we estimate, using the theoretical F_p, which is 0.3 for a 15 μm diameter microsphere, we arrive at the decay time of 23 ns for NC2 and 13 ns for NC3, which can be viewed as the upper limit of the lifetime of $\pm 1^L$ in these nanocrystals.

For many cavity-QED phenomena, especially in applications such as quantum logic gates, it is essential that the optical transition involved is dominated by radiative recombination. The nonradiative decay rate for the $\pm 1^L$ states of core/shell CdSe/ZnS nanocrystals can be derived using Equations (6.48) and (6.50). This results in the ratio of the radiative to nonradiative decay rates for the $\pm 1^L$ states in the range of $1:1-2:1$ for NC2 and of $2:1-9:1$ for NC3. The large variation in the ratio is due to the Purcell factor range (from the averaged Purcell factor of 0.23 to the maximum of the Purcell factor, *i.e.*, 0.3) that we have used in the estimation.

Conclusion

Using cavity-QED in the low-Q regime, we have demonstrated enhanced spontaneous emission from semiconductor CdSe/ZnS nanocrystals. We have also developed a spectroscopic technique based on cavity-QED effects to probe the radiative dynamics of dipole-allowed excitonic states in these semiconductor nanocrystals. By comparing the time-resolved photoluminescence resonant with and off-resonant with the relevant whispering gallery mode, we have singled out the radiative decay component from the complicated decay dynamics, which is attributed to the lowest dipole-allowed transition in the nanocrystals. Further analysis shows that the decay time of this radiative component is of order 10 ns. In addition, we have investigated the effects of nanocrystal size on the enhanced spontaneous emission. It is found that in the large nanocrystals radiative recombination is dominant due to the stronger oscillator strength, in contrast to the earlier belief that emissions from dark states dominate the photoluminescence process. With 9.0 nm diameter CdSe/ZnS nanocrystals, the ratio between the radiative to nonradiative rate can be nearly 10:1, thus opening the door to future cavity-QED studies in nanocrystals.

It should be noted that the experimental studies discussed above have focused on photoluminescence in the first tens of ns and on direct radiative recombination because of the additional information provided by the cavity-QED effects. Experimental studies that can provide detailed information on relatively slow phonon-assisted transitions, for example by probing decay of individual one or two LO-phonon lines, are still needed in order to achieve a complete understanding of photoluminescence in nanocrystals.

CHAPTER VII

CAVITY-QED STUDIES OF COMPOSITE NANOCRYSTAL AND MICROSPHERE SYSTEM IN THE HIGH-Q REGIME

Introduction

In the previous chapter we have discussed cavity-QED studies of a nanocrystal-based composite system in the low-Q regime. As discussed in Chapter I, one of the challenges of semiconductor cavity-QED is the realization of the strong coupling regime. It is natural to move one step forward from the low-Q regime to the high-Q regime by incorporating these semiconductor nanocrystals with a fused silica microsphere, as shown in Figure 60(a). Comparing with the composite system based on epitaxially grown samples, the excitons in these core/shell nanocrystals are much closer to the maxima of the electric field of the whispering gallery modes. As we will discuss later in this chapter, this composite system of nanocrystal and fused silica microsphere can be used as a model system to perform cavity-QED studies in the high-Q regime with the possibility of achieving strong coupling between an exciton in the nanocrystal and a photon in the cavity.

Two approaches can be used to attach nanocrystals onto the fused silica microsphere surface. As discussed in Chapter II, surrounding the outside of the core/shell nanocrystals is TOPO, which is readily replaced through ligand exchange. Therefore, self-assembled bifunctional organic monolayers can be used as bridge compounds to bind nanocrystals with the fused silica microsphere sur-

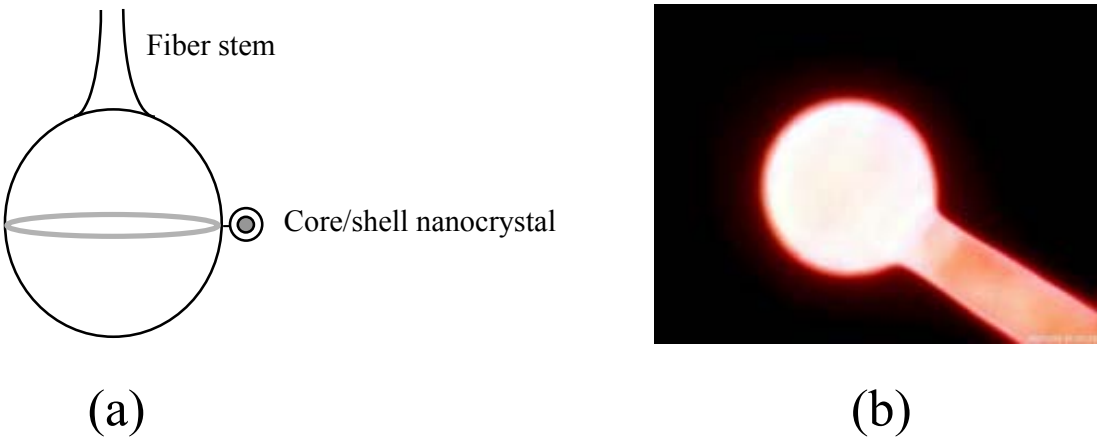

FIGURE 60. (a): A composite nanocrystal and fused silica microsphere system is constructed by attaching nanocrystals to the microsphere surface. (b): 5 nm diameter CdSe/ZnS nanocrystals are solution deposited on a 100 μm diameter fused silica microsphere. The picture is taken under UV illumination.

face [91, 110, 111]. This method, though complicated, allows us to position the nanocrystals in a more controllable way and, in addition, provides an easy way to estimate the nanocrystal density on the surface. In the experiments throughout this chapter, we employ a simpler way to combine the nanocrystals with a fused silica microsphere. We deposit nanocrystals onto the surface of a fused silica microsphere by using solution deposition, *i.e.*, simply dipping the microsphere in a core/shell nanocrystal solution. The nanocrystals are initially suspended in chloroform. After the rapid evaporation of the chloroform, the nanocrystals are weakly bonded to the sphere surface. As a demonstration, Figure 60 shows a picture of the composite nanocrystal and fused silica microsphere system prepared using solution deposition. The red ring on the sphere surface arises from the photoluminescence of nanocrystals under UV illumination. It should be noted that

at very high nanocrystal concentration, aggregation of nanocrystals on the sphere surface may lead to the degradation of the Q-factor due to surface scattering (see Equation 3.36). However, this is not the case at the concentration level used in our measurement, as discussed later in this chapter.

Figure 61 shows schematically the experimental setup for photoluminescence and resonant scattering measurements. A high refractive index prism is used to couple out the light from the whispering gallery modes. A gap between the prism and the microsphere is introduced by a piezoelectric translation stage to minimize the output coupling loss through the prism. Nanocrystals are excited either directly by an excitation laser beam or through the excitation of the whispering gallery modes.

Photoluminescence From the Composite System

Figure 62 shows the spectra of nanocrystal photoluminescence obtained at room temperature. While Figure 62(a) gives the photoluminescence from nanocrystals in free space as a reference, Figure 62(b) shows a portion of the photoluminescence spectrum of a composite nanocrystal-microsphere system. The nanocrystals used in the free space measurement and in the composite system have a mean core diameter of 4.5 nm. The composite system is excited above the bandgap of CdSe nanocrystals with an excitation wavelength of 532 nm. The free spectral range (FSR) of the whispering gallery modes is 0.7 nm and is determined by $\lambda^2/\pi nD$, where λ, n, and D are the wavelength in vacuum, index of refraction ($n = 1.452$), and the diameter (100 μm) of the sphere, respectively.

Whispering gallery modes in a sphere can be characterized by a radial mode

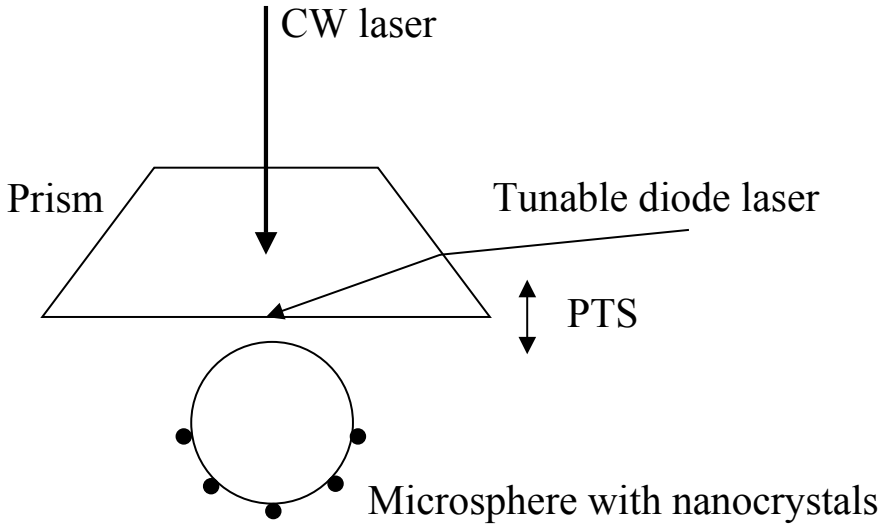

FIGURE 61. Experimental setup for cavity-QED studies of a composite nanocrystal and fused silica microsphere system. Nanocrystals are excited either directly by an excitation laser beam or through the excitation of the whispering gallery modes. In the resonant scattering experiment, the whispering gallery modes are launched via a tunable diode laser. A high refractive index prism acts as an optical output coupler. A piezoelectric translation stage (PTS) is used to generate a gap between the prism and the sphere.

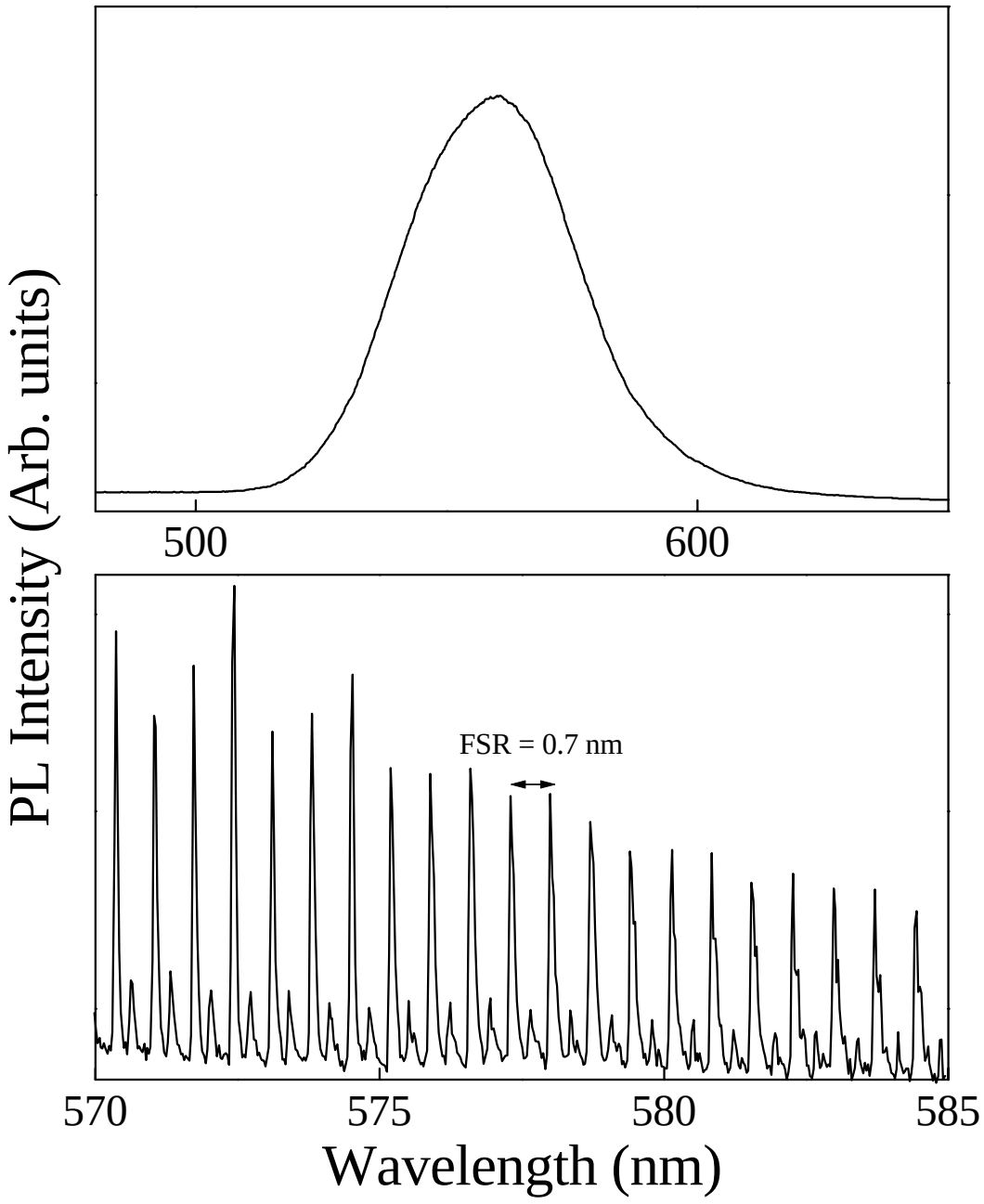

FIGURE 62. Photoluminescence from a composite nanocrystal and fused silica microsphere system. (a): Photoluminescence from 4.5 nm diameter nanocrystals in free space. (b): A portion of photoluminescence from composite nanocrystals and a fused silica microsphere. The free spectral range is 0.7 nm, corresponding the sphere diameter of 100 μm. Doublets in spectrum arise from the first two radial modes with the linewidth of 0.08 nm, limited by the spectrometer resolution. All data are obtained at room temperature.

number p, orbital mode number l, and azimuthal mode number m. There are two peaks within one FSR in Figure 62(b), corresponding to whispering gallery modes with THE same l but different p or different radial distribution. We assign the stronger peak to the p=1 mode since this mode has the best mode matching with nanocrystals on the sphere surface. Note that the slight ellipticity of the sphere removes the azimuthal degeneracy, which provides a convenient mechanism to select a single whispering gallery mode. Each peak in Figure 62(b) contains several whispering gallery modes with different azimuthal mode number m. These modes, however, are not resolved in the figure due to the limited instrument resolution.

Q-Factor of the Composite System

To characterize the intrinsic Q-factor of the composite nanocrystal-microsphere system, we have used a resonant light scattering technique. In these measurements, whispering gallery modes are launched by using frustrated total internal reflection via a high index prism. Emissions from these whispering gallery modes are collected along a direction away from the reflected laser beam and are measured as a function of the excitation wavelength. To avoid nanocrystal absorption, we performed the experiment at energies below the energy gap of the CdSe nanocrystals. Figure 63(a) shows the resonant scattering spectrum of a composite nanocrystal-microsphere system in overcoupling and undercoupling cases. The mode spacing in Figure 63(b) corresponds to the separation between two adjacent azimuthal modes and can be varied by changing the ellipticity of the sphere. The spectral linewidth of the whispering gallery modes shown in Figure 63(b) is 0.0001 nm, corresponding to a Q-factor of 8×10^6. The actual spectral linewidth is much smaller as we

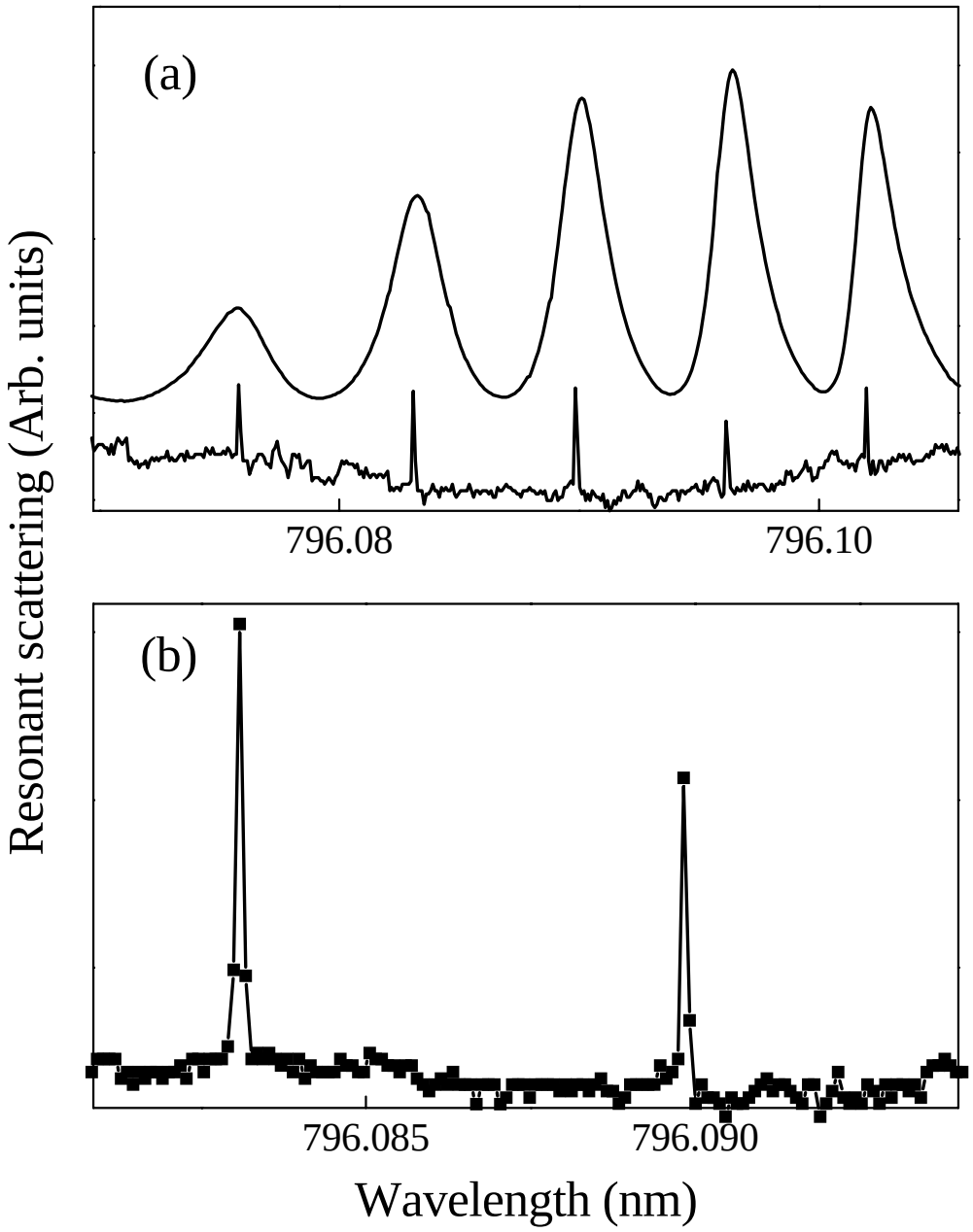

FIGURE 63. Resonant scattering spectrum of the composite nanocrystal and fused silica microsphere system. (a): Loading effects from the prism. Overcoupling in the upper curve and undercoupling in the lower curve. (b): Expanded portion of the resonant scattering spectrum of the lower curve in (a) shows that the linewidth of the resonance is 0.0001 nm, corresponding to a Q-factor of this system exceeding 8×10^6. This measured Q-factor is limited by the laser scanning step size.

discuss below since the measured spectral linewidth is limited by the scanning step size of the tunable diode laser (New Focus 6300) used in the measurement.

It should be noted that the nanocrystals are randomly deposited on the microsphere surface and form islandlike aggregates. As a consequence, both the surface contaminants and the nanocrystals can scatter light from the whispering gallery modes and lead to Q-spoiling. In contrast to a high concentration nanocrystal solution, no significant Q-spoiling effect from the nanocrystal scattering is observed at the solution concentration used in our experiments. In particular, when we perform the cavity-QED studies at the level of a single nanocrystal, the scattering arising from a small number of nanocrystals should be negligible. However, the intrinsic Q-factor, or the bare cavity photon lifetime, of the composite nanocrystal-microcavity system is limited by the deposition process which leaves residual chloroform on the sphere surface, as shown in the following measurement.

For a more accurate measurement of Q-factors, we have used time-domain ring-down spectroscopy [112, 113]. A tunable diode laser is tuned to be resonant with the whispering gallery mode of interest and gated with an acoustooptic modulator to generate 1 ns pulses. A cooled PMT in conjunction with an oscilloscope is used to count the photon number from the microsphere after the excitation. The decay of the excited whispering gallery mode directly reflects the photon storage lifetime.

Figure 64 compares the photon storage lifetime obtained after the solution deposition process with the photon storage lifetime obtained after removal of residual chloroform on the sphere surface by heating the sphere with a CO_2 laser. For this measurement, we have chosen to use a chloroform solution containing no nanocrys-

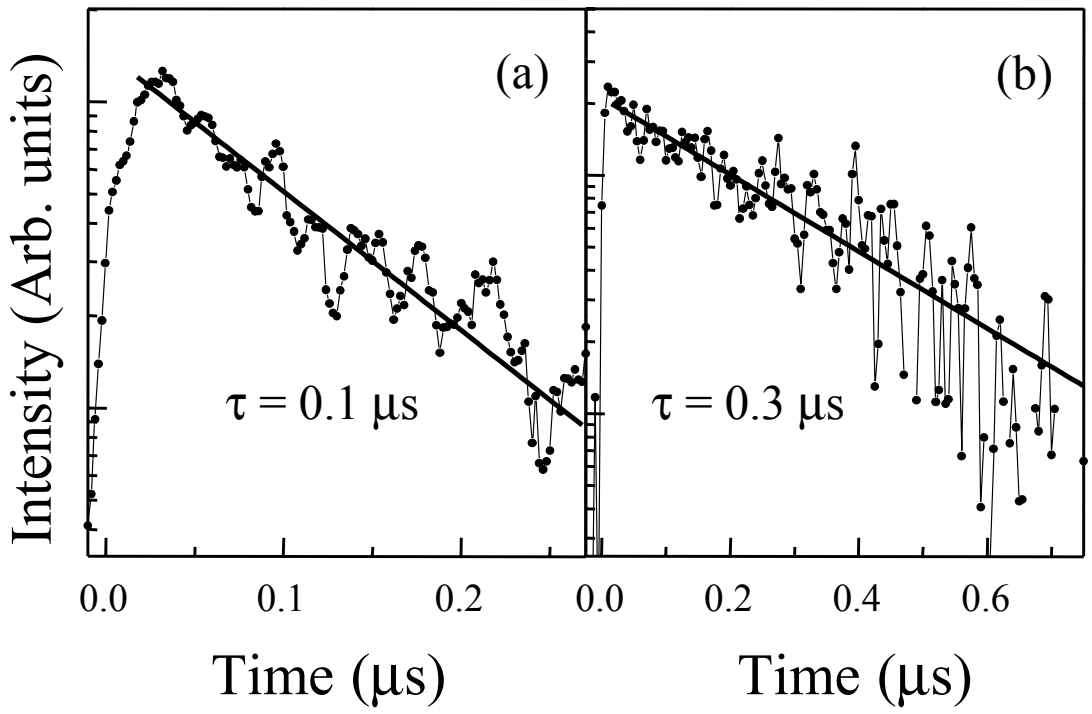

FIGURE 64. Measurement of photon lifetime in a whispering gallery mode. (a): After the solution deposition. (b): After reheating the microsphere. The diameter of the fused silica microsphere is 100 μm.

tals instead of a dilute solution of nanocrystals, since it is difficult to determine accurately the actual number or density of nanocrystals on the sphere surface and also since non-absorptive scattering loss from a small number of nanocrystals on the sphere surface should be negligible, as discussed above. As shown in Figure 64, after the deposition process a photon storage lifetime of 0.1 μs is obtained, corresponding to a Q-factor of 2.4×10^8, is obtained. After the removal of the residual chloroform, the photon storage lifetime is increased to 0.3 μs, corresponding to a Q-factor of 7×10^8. The above result shows that a Q-factor exceeding 10^8 can be achieved for the composite nanocrystal-microsphere system in spite of Q-spoiling due to the deposition process.

Discussion

As discussed previously, the composite nanocrystals and fused silica microsphere system features a Q-factor exceeding 10^8, at least four orders of magnitude higher than other existing semiconductor microcavities. The extremely high Q-factor along with the very small effective mode volume of lower order whispering gallery modes should enable us to enter the high-Q regime where $\kappa \ll \gamma$.

For such a high Q-factor, the absorption from nanocrystals is expected to have significant effects on the cavity linewidth. According to Equation (2.13), in the high-Q regime, the spectral linewidth of a whispering gallery mode coupling to a single resonant nanocrystal in its ground state is given by:

$$\kappa' = (\kappa + \frac{g^2}{\gamma})$$

where g is the dipole coupling rate between a nanocrystal and a resonant cavity

mode. The spectral broadening of the whispering gallery modes due to nanocrystal absorption is thus given by g^2/γ. As discussed above, for the composite nanocrystal and fused silica microsphere system, $\kappa/2\pi$ is of order 1 MHz and is limited by the residual chloroform on the sphere surface. We conservatively take $\kappa/2\pi = 2.5$ MHz, corresponding to a Q-factor of 1×10^8. While the homogeneous linewidth of nanocrystals still remains unknown, studies of photoluminescence from a single nanocrystal have shown a resolution-limited linewidth of 100 μeV [100]. Recently, our experiment using spectral-hole burning technique shows that the homogeneous linewidth is less than 40 μeV [94], corresponding to $\gamma/2\pi < 5$ GHz. For a microsphere with a diameter of 50 μm and for whispering gallery modes with $p = 1$ and $l = m$, the effective mode volume at 600 nm is of order 250 μm^3. Using a dipole moment of $3 \times 10^{-19} C \cdot \mathring{A}$ for relevant optical transitions in nanocrystals, we arrive at an estimated dipole coupling rate $g/2\pi$ of order 200 MHz for a nanocrystal on the sphere surface. The increase in the whispering gallery mode spectral linewidth due to absorption from a single nanocrystal is then $(g^2/\gamma)/2\pi = 8$ MHz. In this case, absorption from a single nanocrystal can lead to over 300% broadening of the resonant whispering gallery mode. This type of measurement can provide important information of the coupling strength between a single nanocrystal and a resonant whispering gallery mode and also potentially allows us to build a spectrometer with high sensitivity and spectral resolution to directly probe the absorption spectrum of a single nanocrystal, something that is extremely difficult to obtain with conventional grating-based spectrometers.

To demonstrate the Q-spoiling from the absorption of nanocrystals, we first perform resonant scattering spectroscopy at room temperature. Figure 65 shows

the resonant scattering spectra when the tunable diode laser is on or off resonance with the nanocrystal absorption. When the laser is far below the nanocrystals bandgap, the linewidth of the whispering gallery mode is 5×10^{-6} nm, corresponding to a Q-factor of 1.6×10^{8}. However, when the laser is on resonance with the nanocrystals, the linewidth is broadened to 4×10^{-4} nm, corresponding to a Q-factor of 1.4×10^{6}. The difference in the Q-factor is primarily due to the absorption of resonant nanocrystals. Using Equation 2.14, we estimate that the number of nanocrystals on resonance is approximately on the order of 10^{4} where we have assumed a homogeneous linewidth of order 10 meV for CdSe nanocrystals at room temperature.

With the Q-factor exceeding 10^{8}, it also becomes possible for this composite nanocrystal and fused silica microsphere system to achieve laser emission at the level of a single nanocrystal, thus providing a very unique system to investigate laser emission where the conventional description of the thermodynamic limit is no longer valid. In this system, we cannot use the conventional definition of lasing threshold that the optical gain equals the cavity loss, but rather we define the threshold as the pump power needed to bring the mean intracavity photon number to unity. At this point, stimulated emission becomes dominant [63, 114]. The mean photon number in the cavity at the lasing threshold can be expressed as:

$$n_{th} = \frac{\beta \tau_{photon} N_A}{\tau_{sp}} \geq 1 \tag{7.54}$$

where τ_{sp} and $\tau_{photon}$are the spontaneous emission lifetimes of the exciton and the photon in the cavity, respectively. β is the fraction of the total spontaneous emission into the cavity mode of interest and N_A is the number of atoms or nanocrystals

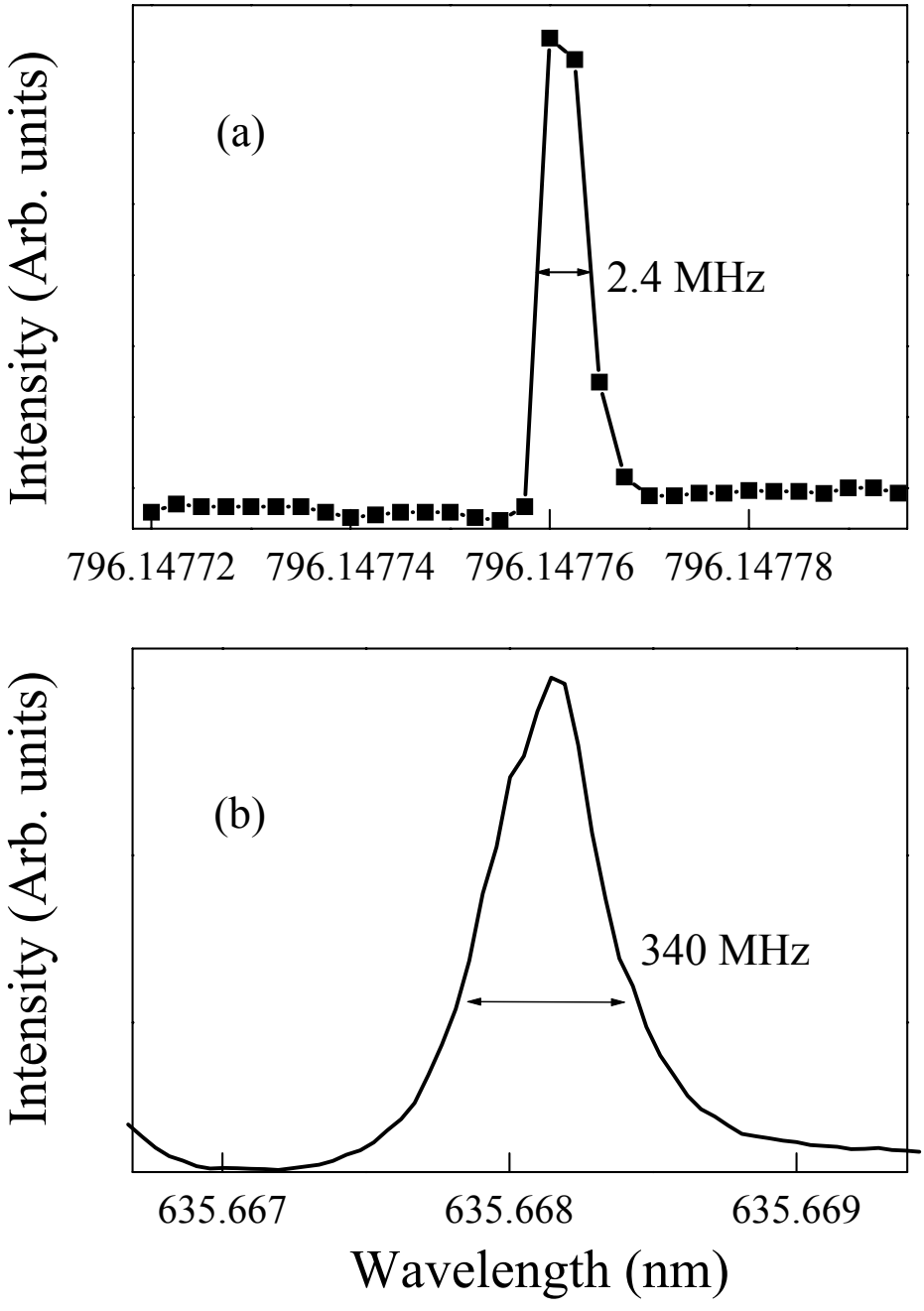

FIGURE 65. Q-spoiling effects of nanocrystal absorption. (a): In the absence of absorption from nanocrystals, the linewidth of the whispering gallery mode is 5×10^{-6} nm, corresponding to a Q-factor of 1.6×10^{8}. The data is limited by the scanning step size of the tunable diode laser. (b): The linewidth of the resonant whispering gallery mode is broadened due to the optical absorption from nanocrystals. The linewidth of 4×10^{-4} corresponds to a Q-factor of 1.4×10^{6}. The total number of nanocrystals on resonance is estimated to be of order 10^{4}.

needed at the lasing threshold. As a result, the minimum number of nanocrystals needed to reach the threshold is:

$$N_A^{min} = \tau_{sp}/\beta\tau_{photon} \tag{7.55}$$

As we have shown earlier, the spontaneous emission lifetime for CdSe/ZnS nanocrystals, is of order 10 ns and β is of order 10% for a 100 μm diameter microsphere. Therefore, with a Q-factor of 2.4×10^8 at $\lambda = 0.8$ μm, which corresponds to the photon lifetime exceeding 100 ns, it is possible to achieve the lasing emission with $N_A < 1$.

Summary

We have demonstrated a nanocrystal-based microcavity system by coupling core/shell nanocrystals to whispering gallery modes of a fused silica microsphere. We showed that this composite system can feature a Q-factor in excess of 10^8. The Q-factor is only limited by surface adsorption occurring during the solution deposition process, thus making this semiconductor microcavity system a model system for cavity-QED studies in the high-Q regime (or good cavity limit). Under the parameters that $(g, \gamma, \kappa)/2\pi = (200 \text{ MHz}, 5 \text{ GHz}, 2.5 \text{ MHz})$, we arrive at "critical atom number" $N_0 = 2\kappa\gamma/g^2 \sim 0.6 < 1$. This is the first time to achieve the "critical atom number" smaller than one in a semiconductor system. Consequently, a single nanocrystal can have considerable effects on the dynamics of the cavity-exciton system. Another interesting parameter is "critical photon number" $n_{sat} = \gamma^2/2g^2$. For the system discussed above, we have $n_{sat} \sim 300$.

As discussed before, a primary challenge in cavity-QED is the achievement of

strong coupling between a single exciton in a nanocrystal and a single photon in a whispering gallery mode. However, the homogeneous linewidth of these core/shell nanocrystals still remains an open question, which has been an obstacle to achieving the strong coupling regime. Further discussion in this regard will be presented in the next chapter.

CHAPTER VIII

SUMMARY AND FUTURE WORK

Summary

In this dissertation, I have presented experimental studies aimed at controlling the spontaneous emission process in semiconductor quantum dots. In order to achieve this goal, we have developed a composite semiconductor microcavity system by attaching colloidal semiconductor core/shell nanocrystals on the surface of a dielectric microsphere, thus effectively coupling these nanocrystals to the whispering galley mode of a dielectric microsphere.

A distinct feature of these composite systems is that a high Q-factor can be achieved. Particularly, we have shown that in a composite system based on semiconductor nanocrystal and fused silica microsphere, the Q-factor exceeds 10^8. Another feature of these composite systems is the separate engineering of the electronic and photonic confinement. The electronic confinement is provided by the semiconductor nanostructures whereas three-dimensional photonic confinement can be achieved using whispering gallery modes in a dielectric microsphere. Furthermore, the nanocrystals can be individually located and addressed. This scheme makes the whole system much more versatile than monolithic semiconductor microcavities where any manipulation of electronic confinement will have significant effects on the photonic confinement or vice versa.

In the first part of this dissertation, I have discussed the characterization of

the whispering gallery modes in a dielectric microsphere. I have also discussed the chemical synthesis of semiconductor core/shell CdSe/ZnS nanocrystals with the size ranging from 3 nm to 9 nm in diameter, which allows us to construct a nanocrystal-based microcavity system and also makes it possible for us to study the nanocrystal size dependence of the relevant physical phenomena.

In the second part of this dissertation, I have presented cavity-QED studies in both the low-Q and high-Q regimes. For studies in the low-Q regime, we have doped CdSe/ZnS nanocrystals in the interior surface of a polystyrene sphere and demonstrated pronounced enhancement in spontaneous emission rates when the nanocrystals are resonant with a whispering gallery mode. These studies were also aimed at understanding the radiative processes in these nanocrystals since these processes reflect the fundamental dynamical interactions between the nanocrystals and the vacuum electric field. By comparing the time-resolved photoluminescence resonant with and off-resonant with the relevant whispering gallery mode, we are able to single out from the complex decay dynamics the decay component dominated by radiative recombination. The studies of the temperature, spectral and nanocrystal size dependence of the time-resolved photoluminescence from the nanocrystals doped in a polystyrene sphere lead us to attribute the radiative recombination to the lowest dipole-allowed excitonic transition in the nanocrystals. We have found that for large core/shell nanocrystals (D $>$ 6 nm), dipole-allowed excitonic states can represent a predominant contribution to the overall photoluminescence, in contrast to the widespread belief that these states play no significant role in the optical emission processes. Our results also provide very important information for using these nanocrystals as artificial atoms in many applications

such as quantum logic gates in which the optical transition involved is required to have nearly unity quantum yield.

For studies in the high-Q regime, we constructed the composite nanocrystal and fused silica microsphere system by depositing the nanocrystals onto the sphere surface. We have demonstrated that the Q-factor of this composite system is in excess of 10^8, at least four orders of magnitude higher than that of conventional monolithic semiconductor microcavities. The Q-factor is primarily limited by surface adsorption of chloroform solution used in the deposition process. With the extremely high Q-factor, we have achieved for the first time in a semiconductor system the regime where the "critical atom number" is smaller than one, which allows us to further pursue cavity-QED studies at the level of a single nanocrystal. This composite nanocrystal-fused silica microsphere system should open up a new avenue to a variety of physical phenomena including single-quantum-dot lasers, vacuum Rabi oscillation of nanocrystals, and nanocrystal-based quantum information processing.

Future Work

The experimental studies presented in this dissertation provide an important step for cavity-QED studies using the composite system of nanostructure and dielectric microsphere. The next step is naturally aimed at achieving the strong coupling between a nanocrystal and a cavity mode. We have shown that in the composite nanocrystal and fused silica microsphere system, a Q-factor of nearly 2.4×10^8 is achieved, corresponding to $\kappa/2\pi = 1$ MHz at 600 nm. For a $d = 15$ μm fused silica microsphere, the dipole coupling rate $g/2\pi = 1.8$ GHz. However, the

dephasing time as well as dephasing mechanisms of the nanocrystals is still an open question. While it is expected that in these core/shell nanocrystals the pure dephasing rate resulting from electron-phonon interaction may be much smaller than in embedded quantum dots, due to quantization in phonon energy [1] [115], further detailed studies are needed to probe the dephasing time. Earlier studies on single nanocrystals at helium temperature give a resolution-limited homogeneous linewidth of order 100 μeV, corresponding to a dephasing rate $\gamma/2\pi = 12$ GHz [100]. The preliminary results obtained by Phedon Palinginis in our group using spectral hole-burning further reduce the linewidth down to $\gamma/2\pi = 5$ GHz [94]. According to the results obtained from the cavity-QED studies of the nanocrystals presented in Chapter VI, the transitions of the $F = \pm 1^L$ states are dominantly radiative with the decay rate of order 10 ns. Therefore, much narrower spectral linewidth is expected.

Because of the high Q-factor achieved in the composite nanocrystal and fused silica microsphere system, it also becomes possible to realize laser emission at the level of a single nanocrystal. This type of laser features extremely low lasing threshold and qualitatively different dynamics from conventional lasers and therefore can be used for fundamental research as well as for a variety of applications.

The effects of the absorption due to a single nanocrystal can also be an interesting future subject. The results at room temperature presented in Chapter VII have clearly demonstrated the Q-spoiling effects due to the nanocrystal absorption with estimated number of nanocrystals of order 10^4. Further experiment is aimed at performing cavity-QED studies of this composite system at helium

[1] See Appendix D.

temperature where the large inhomogeneous broadening of nanocrystals provides a convenient way for us to select a single nanocrystal resonant with the whispering gallery mode of interest [2]. These results can lead to the construction of a spectrometer with extremely high sensitivity to measure the homogeneous linewidth of a single nanocrystal and the coupling strength between the nanocrystals and the whispering gallery mode. Furthermore, it also allows us to build sensitive detectors for the monitoring of biological or chemical agents.

In this dissertation, I have also presented the studies of the whispering gallery modes in bare fused silica microspheres. These studies not only provide us important information for cavity-QED studies of composite systems, but also make feasible a number of immediate applications such as optical filters, ultra-low threshold lasers and various optical devices in telecommunications. Deformed spheres that feature directional emission are also of interest in many applications such as microsphere lasers.

Finally, I would like to emphasize the importance of the collaboration between physicists and chemists in the studies of nanocrystals that have long been the territory owned by chemists. Despite the success in fabrication and characterization, there are still many challenges such as blinking and spectral diffusion of these semiconductor nanocrystals [116, 117, 103, 118]. Chemistry techniques combined with physics techniques such as cavity-QED can tackle these problems from a new perspective, which may lead to a better understanding of the properties of semiconductor nanocrystals.

---

[2]The inhomogeneous linewidth of CdSe nanocrystals is nearly 30 nm at helium temperature. For a comparison, in the similar experiment performed in Chapter IV where a quantum well is used, the exciton inhomogeneous linewidth is of order 0.3 nm, making it very difficult to fabricate the microsphere with a resonant whispering galley mode.

APPENDIX A

LASER EMISSION FROM SEMICONDUCTOR MICROCAVITIES: THE ROLE OF CAVITY POLARITONS

Xudong Fan, Hailin Wang, H. Q. Hou, and B. E. Hammons

Physical Review A, Volume 56, 1997, page 3233-3236

Copyright (1997) by the American Physical Society

Reprint permission granted by the American Physical Society

PHYSICAL REVIEW A VOLUME 56, NUMBER 4 OCTOBER 1997

Laser emission from semiconductor microcavities: The role of cavity polaritons

Xudong Fan and Hailin Wang
Department of Physics and Oregon Center for Optics, University of Oregon, Eugene, Oregon 97403

H. Q. Hou and B. E. Hammons
Sandia National Laboratories, Albuquerque, New Mexico 87185

(Received 3 March 1997)

We present an experimental study on the role of cavity polaritons in laser emissions from a GaAs quantum-well microcavity. We show that cavity polaritons play no role in the laser emission process when the cavity is nearly resonant with the excitons. The laser emissions emerge from the bare cavity mode instead of from a cavity-polariton branch and the threshold density is much higher than the saturation density at which cavity polaritons vanish. We also show that the presence of emission doublets near the lasing threshold, which was previously taken as an evidence for laser emission from cavity polaritons, is primarily the result of spatial and/or temporal variations of exciton densities within the excitation volume. [S1050-2947(97)05010-5]

PACS number(s): 42.55.−f

Nonequilibrium condensation of exciton polaritons (coupled exciton-photon modes) was first discussed for bulk crystals with dipole-allowed interband optical transitions [1]. In such systems, the presence of a relaxation bottleneck near the turning point of the lower polariton dispersion leads to accumulation of polaritons. Stimulated transitions of polaritons into the bottleneck region become important when the occupation number of polaritons in this region exceeds 1. This stimulated transition process is very similar to stimulated emission of photons in a laser and could similarly lead to non-equilibrium condensation of polaritons in the bottleneck region.

Coupled exciton-photon modes are qualitatively modified near $k=0$ in a semiconductor microcavity due to the quantization of photon wave vectors and are referred to as cavity-polaritons [2–3]. Nonequilibrium condensation of cavity polaritons can in principle occur at $k=0$ instead of at the bottleneck region. In the limit excitons couple strongly to the cavity mode, the mass of cavity polaritons near $k=0$ can become much smaller than the mass of bare excitons. For GaAs quantum-well (QW) microcavity structures, the polariton mass corresponds to a thermal de Broglie wavelength of 7 μm at 4 K, far greater than the exciton Bohr radius (of order 0.01 μm). It was argued that because of this extremely large thermal de Broglie wavelength, nonequilibrium condensation of cavity polaritons could occur at a density far below the exciton Mott density and therefore could be realized experimentally [4,5]. Optical emissions from such a condensate are shown theoretically to be approximately in a coherent state, providing a mechanism for generating coherent laserlike emissions [5].

Evidence of nonequilibrium condensation of cavity-polaritons has been reported recently in a GaAs QW microcavity [4]. A doublet was observed in emission spectra with one of the emission resonance exhibiting laserlike threshold behaviors. It was argued that this doublet is due to emissions from two branches of cavity polaritons and the laserlike resonance is due to emissions from a nonequilibrium condensate of cavity polaritons. The physical origin of the emission doublet, especially, the role of cavity polaritons in the lasing process has been a subject of considerable debate.

In this paper we present an experimental study on the role of cavity polaritons in laser emission from a GaAs QW microcavity. We show that laser emissions emerge from the bare cavity mode instead of from a cavity-polariton branch and that cavity polaritons vanish at densities far below the lasing threshold. Physically, the lasing process is due to stimulated emission of photons rather than condensation of cavity polaritons. Measurements using a pinhole aperture to probe a small region within the excitation volume also reveal that emission doublets observed near the lasing threshold are the result of spatial and/or temporal variations of exciton densities within the excitation volume and cannot be taken as an evidence of persistence of cavity polaritons at the lasing threshold. In addition, exciton localization due to interface fluctuations is suggested as a major obstacle for achieving the elusive nonequilibrium condensation of cavity polaritons.

The GaAs QW microcavity used in our study has four 13 nm GaAs QW's placed at the center of a wavelength-long cavity and uses 16 (22) pairs of $Al_{0.11}Ga_{0.89}As$/AlAs Bragg reflectors as the top (bottom) mirror. The cavity length is tapered such that the cavity resonance varies slightly across the sample while the energy of excitons remains nearly constant. All measurements were performed at 10 K unless otherwise noted.

Figure 1(a) shows reflection spectra of the sample when the cavity is tuned slightly above the heavy-hole exciton absorption line center. At low excitation limit, the reflection spectrum is characterized by two well-resolved cavity-polariton resonances (the minimum normal mode splitting of the sample is 2.6 nm). At high excitation limit, the normal mode splitting collapses and cavity-polaritons disappear [6–8]. In this limit, reflectivity spectra are characterized by the bare cavity resonance as shown by the dashed curve in Fig. 1(a). The collapse of the normal splitting was shown to be due to ionization of excitons in an earlier study [8]. With a further increase in excitation levels the bare cavity resonance moves toward lower wavelength due to mode pulling of the cavity resonance (not shown).

 © 1997 The American Physical Society

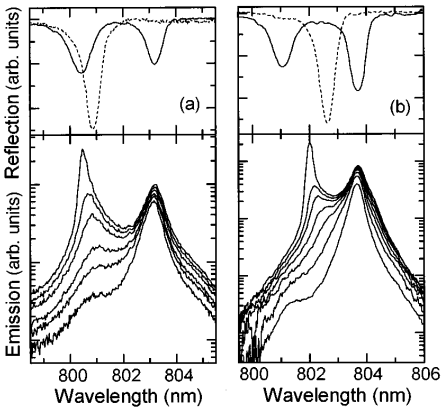

FIG. 1. Reflection and emission spectra with pulsed excitation at two different exciton-cavity detunings. The solid and dashed reflection spectra are obtained at low and high excitation limits, respectively. Emission spectra are obtained at input intensities of 80, 120, 150, 230, 290, 360 W/cm^2 for (a) and of 40, 80, 120, 160, 200, 240, 280 W/cm^2 for (b). The top emission spectrum is obtained at the threshold pumping intensity.

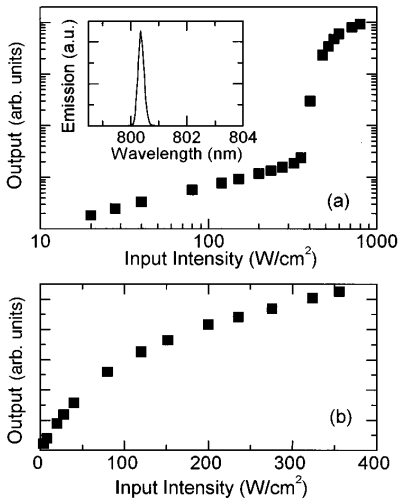

FIG. 2. (a) Total output intensity as a function of the input intensity. (b) Output intensity from the lower energy emission resonance as a function of the input intensity. The exciton-cavity detuning is the same as in Fig. 1(a). The inset shows an emission spectrum above the lasing threshold.

Corresponding emission spectra at various excitation levels are shown in Fig. 1(a). For the emission measurement, the sample is excited off resonantly at a reflection minimum near 755 nm with output from a mode-locked Ti:Sapphire laser. A doublet is observed in emission spectra. At lowest input intensities, the doublet corresponds to the two cavity-polariton resonances in the reflection spectrum and is due to emissions from the two branches of cavity polaritons. Emissions from upper (higher energy) cavity polaritons are much weaker because of the very low temperature.

With increasing excitation levels, the total emission intensity (spectrally integrated) increases rapidly while the intensity of the lower energy resonance in the doublet saturates. Figure 2(a) shows the threshold behavior of the total emission intensity as a function of the input intensity. Figure 2(b) shows saturation of the intensity of the lower energy resonance as a function of the input intensity. An emission spectrum above the lasing threshold is also shown as an inset in Fig. 2(a) and is completely dominated by the higher energy resonance. Behaviors qualitatively similar to those shown in Fig. 2 are also observed at other exciton-cavity detunings as long as the cavity is resonant or nearly resonant with the excitons.

Emission spectra shown in Fig. 1(a) along with the threshold behavior shown in Fig. 2(a) might lead to an assignment that the doublet in Fig. 1(a) is due to emissions from two cavity-polariton branches at all input intensities with the upper polariton going above the threshold with increasing input intensities. This assignment would imply that emissions from the lower (lower energy) polariton branch should saturate at an input intensity near the lasing threshold. Figure 2(b), however, shows that the output from the lower energy resonance saturates at an input intensity near 50 W/cm^2 much lower than the threshold intensity of 360 W/cm^2.

Problems associated with the above assignment become more evident when we examine emission spectra obtained with the cavity tuned slightly below the exciton resonance [see Fig. 1(b)]. At lowest input intensities, the emission spectra feature a doublet that corresponds to the two cavity-polariton resonances in the reflection spectrum. With increasing input intensities, however, the emission resonance from the upper cavity polariton disappears and a new resonance emerges from between the two cavity-polariton resonances. The energy position of the new resonance agrees with that of the bare cavity resonance and moves toward higher energy with increasing input intensities. We emphasize that the same behavior is also observed when we tune the cavity resonance above the exciton resonance. The approximate agreement in energy position between the upper cavity polariton and the higher energy emission resonance near the lasing threshold shown in Fig. 1(a) is coincidental since in this case the bare cavity resonance is close to the upper cavity polariton.

The main issue in understanding the above experimental result is whether near the lasing threshold cavity polaritons still remain a valid description for optical excitations in the microcavity. The observation of optical emissions from the bare cavity resonance far below the lasing threshold clearly indicates that the threshold density n_{th} is much greater than the saturation exciton density n_s at which normal mode splitting collapses and cavity polaritons vanish [9]. This is also supported by the saturation of the lower energy emission resonance at densities much smaller than n_{th} [see Fig. 2(b)] since optical emissions from the lower cavity polaritons are expected to saturate at n_s. We therefore conclude that cavity polaritons play no roles in the lasing process and that the laser emission is due to stimulated optical transitions rather than condensation of polaritons.

The above model satisfactorily explains the behavior of laser emission and the saturation of optical emission from

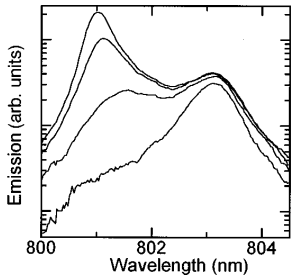

FIG. 3. Emission spectra collected from the center of the excitation volume. Input intensities used are 80, 160, 240, 280 W/cm^2. Other experimental conditions are similar to that of Fig. 1(a).

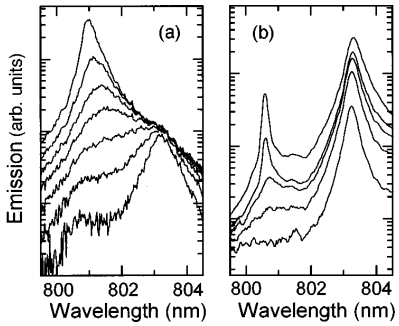

FIG. 4. Emission spectra with cw exciton and collected from the center of the excitation volume (a) and near the edge of the excitation volume (b). Input intensities used are $0.05I_0$, $0.1I_0$, $0.15I_0$, $0.2I_0$, $0.3I_0$, $0.45I_0$, $0.65I_0$ for (a) and $0.15I_0$, $0.5I_0$, $0.85I_0$, I_0, $1.5I_0$ for (b) where I_0 is the threshold pumping intensity. Other experimental conditions are similar to that of Fig. 1(a).

lower cavity polaritons but does not account for the persistence of emission doublets at or near the lasing threshold. As shown in Fig. 1, the energy position of the lower energy emission resonance follows that of the lower cavity polariton and remains nearly independent of the input intensities. The lower energy emission resonance is therefore associated with the lower cavity polaritons at all input intensities. In contrast, the higher energy emission resonance is due to emissions from the upper cavity polaritons only at very low input intensities and switches to the bare cavity resonance approaching the lasing threshold, as shown earlier. This raises the question that if $n_{\rm th} > n_s$, why strong optical emissions from the lower cavity-polariton can still be observed at the threshold pumping intensity. In fact, the presence of a doublet near the lasing threshold was taken to be a crucial evidence for the role of cavity polaritons in the lasing process.

Properties of optical excitations in a microcavity depend critically on the density of excitons when the exciton density is near n_s. The persistence of lower cavity-polariton emissions near the lasing threshold reflects important effects of spatial and/or temporal variations of exciton densities within the excitation volume. In a typical optical measurement and at a given pumping intensity, the exciton (or carrier) density varies greatly from the center to the edge. There are always outer regions where the density of excitons falls below n_s even when the density of excitons exceeds n_s at the center. Optical emissions from these outer regions are characterized by emissions from two branches of cavity polaritons. As a result, emission spectra can feature simultaneously contributions from the bare cavity resonance as well as the cavity polaritons. Note that emissions from the upper-cavity polaritons are more than one order of magnitude smaller than that of the lower cavity polaritons and can be overwhelmed by emissions emerging from the bare cavity resonance near the threshold pumping intensity.

Figure 3 shows emission spectra obtained by collecting emissions from only the center region of the excitation volume to eliminate effects of spatial variation of exciton densities. The measurement was done under experimental conditions similar to that of Fig. 1(a) but with a 5 μm aperture placed at the center of *the image* of the excitation spot (the laser spot size is estimated to be 130 μm). As shown in Fig. 3, just below the threshold pumping intensity lower cavity-polariton emissions are one order of magnitude smaller than emissions from the bare cavity resonance. In comparison, at similar pumping intensities emission spectra for the whole excitation volume feature nearly equal contributions from the lower cavity-polaritons and the bare cavity resonance [see Fig. 1(a)]. The residual emission from the lower cavity-polaritons near the threshold pumping intensity shown in Fig. 3 is due to temporal variation of exciton densities as we discuss below.

Measurements discussed so far have used output from a mode-locked Ti:Sapphire laser and the time interval between successive pulses (13 ns) is large compared with the exciton or carrier recombination time (of order 1 ns). Under these conditions, both the density and the distribution of electronic excitations in the sample are a function of the time. In particular, there are temporal regions where the density of excitons falls below n_s even when the peak exciton density is above n_s. This is especially true for sufficiently long delays after an excitation pulse. Therefore, emission spectra obtained with pulsed excitations can still feature contributions from both bare cavity resonance and cavity polaritons even when exciton densities are spatially uniform.

Figure 4(a) shows emission spectra obtained with off-resonant cw excitation and with a 5 μm aperture at the center of the image of the excitation spot to eliminate both spatial and temporal variations of excitation densities. Emerging of the bare cavity resonance and correspondingly the saturation of the lower cavity-polariton emission at densities far below $n_{\rm th}$ is clearly observed. Near and below the threshold pumping intensity, emissions from the lower cavity polaritons are now reduced to more than two orders of magnitude smaller than emissions from the bare cavity resonance. Note that, experimentally, it is difficult to compare excitation levels of cw and pulsed pumping and we have used the threshold input intensity as a reference. To further illustrate effects of spatial variations of exciton densities, Fig. 4(b) also shows emission spectra obtained by placing a 25 μm aperture at the edge of the image of the excitation spot. In this case, the persistence and a continued linear increase of the lower cavity-polariton emission even at intensities above the threshold pumping intensity is observed. These results clearly demonstrate that cavity polaritons vanish at a density far below $n_{\rm th}$ and that the persistence of lower cavity-polariton emissions at the threshold pumping intensity shown

in Fig. 1 is due to emissions from spatial or temporal regions where the exciton density is below n_s.

Finally, we discuss briefly mechanisms that prevent the realization of nonequilibrium condensation of cavity polaritons. Theoretically, quantum statistical effects of polaritons were predicted to be effective when the interparticle distance is small compared with the polariton thermal de Broglie wavelength, which implies that at very low temperature bosonic effects can become important at exciton densities as low as $10^7/\mathrm{cm}^2$ in GaAs QW microcavities. Significant buildup of cavity-polaritons near $k=0$, however, can be prevented by the extremely short polariton life time (of order 1 ps) along with the long polariton-acoustic phonon scattering time (of order 100 ps or longer [10]). Another mechanism that can prevent the condensation from occurring is exciton localization. For typical QW structures, interface fluctuations can localize excitons in local minima of the confinement potential [11–13]. These localized excitons behave as fermions rather than bosons. Experimental realization of nonequilibrium condensation of cavity polaritons therefore requires the use of nearly perfect quantum heterostructures where effects of exciton localization are negligible even at extremely low exciton densities.

In conclusion, we have shown that cavity polaritons play no role in laser emission from GaAs QW microcavities at low temperature when the cavity is nearly resonant with the excitons. The threshold density is much higher than the saturation density at which normal mode splitting collapses and cavity polaritons vanish. The presence of emission doublets near the lasing threshold, which was previously taken as an evidence for laser emission from cavity polaritons, is the result of spatial and/or temporal variations of exciton densities within the excitation volume.

We wish to acknowledge helpful and stimulating discussions with Y. Yamamoto, S. W. Koch, G. Khitrova, and H. Gibbs. The work performed at the University of Oregon is supported by AFOSR.

[1] For a recent review, see, L. V. Keldysh, in *Bose-Einstein Condensations*, edited by A. Griffin, D. W. Snoke, and S. Stringari (Cambridge University Press, New York, 1995).

[2] C. Weisbuch *et al.*, Phys. Rev. Lett. **69**, 3314 (1992); T. Norris *et al.*, Phys. Rev. B **50**, 14 663 (1994); J. Jacobson *et al.*, Phys. Rev. A **51**, 2542 (1995); H. Wang *et al.*, Phys. Rev. B **51**, 14 713 (1995).

[3] R. Houdre *et al.*, Phys. Rev. Lett. **73**, 2043 (1994); R. Stanley *et al.*, Phys. Rev. B **53**, 10 995 (1996).

[4] S. Pau *et al.*, Phys. Rev. A **54**, R1789 (1996).

[5] A. Imamoglu and R. J. Ram, Phys. Lett. A **214**, 193 (1996); A. Imamoglu *et al.*, Phys. Rev. A **53**, 4250 (1996).

[6] R. Houdre *et al.*, Phys. Rev. B **52**, 7810 (1995).

[7] J.-K. Rhee *et al.*, Solid State Commun. **97**, 941 (1996).

[8] F. Jahnke *et al.*, Phys. Rev. Lett. **77**, 5257 (1996).

[9] Although it is difficult to determine the density of excitons with desired accuracy, we estimate that the threshold intensity ($380\ \mathrm{W/cm}^2$) corresponds to an exciton (or electron-hole pair) density above $10^{11}/\mathrm{cm}^2$.

[10] S. Pau *et al.*, Phys. Rev. B **51**, 7090 (1995).

[11] J. Hegarty and M. D. Sturge, J. Opt. Soc. Am. B **2**, 1143 (1985).

[12] H. Wang, M. Jiang, and D. G. Steel, Phys. Rev. Lett. **65**, 1255 (1990).

[13] Emission measurements by tuning the cavity resonance far away from the exciton line center give a Stokes shift of 1.5 nm.

APPENDIX B

LASER EMISSION FROM SEMICONDUCTOR MICROCAVITIES: TRANSITION FROM NONPERTURBATIVE TO PERTURBATIVE REGIMES

Xudong Fan, Hailin Wang, H. Q. Hou, and B. E. Hammons

Physical Review B, Volume 56, 1997, page 15256-15260

Copyright (1997) by the American Physical Society

Reprint permission granted by the American Physical Society

PHYSICAL REVIEW B VOLUME 56, NUMBER 23 15 DECEMBER 1997-I

Laser emission from semiconductor microcavities: Transition from nonperturbative to perturbative regimes

Xudong Fan and Hailin Wang
Department of Physics and Oregon Center for Optics, University of Oregon, Eugene, Oregon 97403

H. Q. Hou and B. E. Hammons
Sandia National Laboratories, Albuquerque, New Mexico 87185

(Received 14 August 1997)

We have demonstrated laser emission at densities below the saturation exciton density in a semiconductor microcavity by tuning the cavity resonance to the low-energy side of the inhomogeneously broadened exciton distribution. Laser emission in this regime arises from population inversion of localized excitons at the low-energy tail of the inhomogeneous distribution. Distinct spectral line shapes of laser emission and especially a large and abrupt change in the lasing threshold are observed when the composite system undergoes a transition from the nonperturbative to the perturbative regimes. The abrupt threshold change is attributed to ionization of excitons occurring in the transition region. [S0163-1829(97)00148-3]

Semiconductor quantum well (QW) microcavities as a composite exciton-cavity system have provided a unique system for investigating optical and excitonic many-body interactions in a nonperturbative regime. In this regime, coherent dipole coupling rates between the exciton and the cavity mode are large compared with relevant damping rates, leading to the formation of coupled exciton-cavity modes, or cavity polaritons. Effects of cavity polaritons have been observed in various measurements including normal-mode splitting in emission or reflection spectra[1,2] and normal-mode oscillations in transient optical responses.[3,4]

Whether laser emission can occur in the nonperturbative regime of semiconductor microcavities has thus far remained an open question. In order to achieve laser emission in the nonperturbative regime, the threshold density n_{th} has to be small compared with the saturation exciton density n_{sat}, at which cavity polaritons start to vanish due to bleaching of the excitonic resonance.[5,6] For typical microcavity configuration, this is not the case and excitonic resonance bleaches at densities far below n_{th}.[7,8]

The difficulty in reaching the lasing threshold in the nonperturbative regime stems from the fact that *population inversion of excitons cannot be achieved for a homogeneously broadened system without bleaching the excitonic resonance*.[9] In order to achieve laser emission from an excitonic system, optical transitions have to involve other processes such as biexcitonic transition, phonon-assisted transition, bosonic condensation of excitons, or exciton localization.[9] Laser emission due to biexcitonic transition and exciton localization has been observed in semiconductors such as II-VI QW's that have a relatively large exciton binding energy.[10] Laser emission from excitons in II-VI QW microcavities has also been observed recently.[11]

In this paper we present experimental studies of laser emission in the nonperturbative regime in a composite system of high-Q cavity and inhomogeneously broadened excitons. By tuning the cavity resonance to the low-energy side of the inhomogeneous exciton distribution we are able to achieve laser emission at exciton densities considerably below n_{sat}. Laser emissions at these low densities are shown to arise from population inversion of localized excitons. Distinct spectral line shapes of laser emission and especially a large and abrupt change in the lasing threshold are also observed when the composite system undergoes a transition from the nonperturbative to the perturbative regimes. The abrupt threshold change is attributed to ionization of excitons occurring in the transition region.

The sample used for our study is a GaAs QW microcavity that has four 13-nm GaAs QW's placed at the center of a wavelength-long cavity and uses 16 (22) pairs of $Al_{0.11}Ga_{0.89}As/AlAs$ Bragg reflectors as the top (bottom) mirror. The microcavity is held at 10 K by using a cold-finger cryostat. The cavity thickness is tapered such that the cavity resonance varies across the sample while the energy of excitons remains nearly constant. Figure 1(a) shows the energy position of two cavity-polariton branches associated with the heavy-hole (hh) exciton as we tune the cavity resonance by moving the laser spot across the sample. The minimum normal-mode splitting observed is 2.6 nm. The exciton linewidth is estimated to be 1 nm and the empty cavity linewidth is 0.2 nm, reflecting the high Q factor of the cavity.

The threshold pumping intensity I_{th} as a function of the emission wavelength at the lasing threshold is shown in Fig. 1(b) (the laser spot size is estimated to be 2.5×10^{-4} cm^2). The threshold is identified from the onset of a rapid increase in the output power and a spectral narrowing in the corresponding emission spectrum (the threshold behavior will be discussed in detail later). The sample is excited off-resonantly at a reflection minimum near 755 nm with output from a mode-locked Ti:sapphire laser with a 80-MHz repetition rate. The wavelength dependence of I_{th} is obtained by tuning the cavity resonance within the hh exciton absorption profile.

As shown in Fig. 1(b), I_{th} decreases significantly below the exciton absorption line center, especially at the low-energy tail of the exciton absorption before increasing again when the cavity is tuned far below the line center. The mini-

 © 1997 The American Physical Society

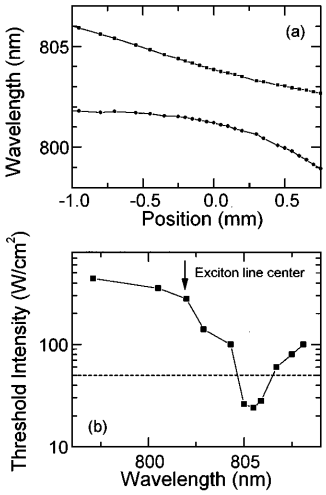

FIG. 1. (a) The wavelength of cavity polaritons at different sample positions. (b) Threshold pumping intensity as a function of the emission wavelength at the lasing threshold. The exciton line center is determined from reflection and emission spectra when the cavity is far detuned from the exciton resonance. The dashed line in (b) indicates the level of saturation pumping intensity.

mum I_{th} is more than one order of magnitude smaller than I_{th} at the line center. Note that the observed wavelength dependence cannot be accounted for by band-gap renormalization. For GaAs QW's, energy shifts of exciton resonance due to band-gap renormalization are nearly canceled by the decrease in the exciton binding energy and the energy position of the excitonic resonance remains nearly independent of the excitation level.[6,12] The drastic decrease in I_{th} results from effects of exciton localization in QW's, as we will discuss in detail later.[13,14]

The dashed line in Fig. 1(b) also indicates the level of saturation pumping intensity at which cavity polaritons start to vanish due to bleaching of the excitonic resonance. I_{sat} is measured when the cavity is tuned to near the exciton absorption line center since I_{sat} is independent of the exciton-cavity detuning. Experimentally, we determine I_{sat} by measuring the pumping intensity at which optical emissions from the lower (energy) cavity-polariton branch start to saturate. Note that I_{sat} can also be determined by measuring the pumping intensity at which normal-mode splitting starts to collapse although spatial and temporal variation of exciton densities within the excitation region can significantly complicate the measurement as shown in an earlier study (see Ref. 7 for a detailed discussion on measurements of I_{sat}).

The minimum I_{th} (24 W/cm^2), which is achieved in a spectral region 3 nm below the exciton absorption line center, is considerably below the saturation pumping intensity $I_{sat}=50$ W/cm^2, suggesting that laser emission at very low pumping intensities occurs in the nonperturbative regime. Although it is difficult to determine precisely exciton densities in our study, we estimate that the minimum I_{th} corresponds to an exciton density of 4×10^{10}/cm^2, which is well below the exciton Mott density. The very small I_{th} is also in part due to the small loss or high Q factor of the microcavity since in order to achieve lasing actions gain has to be greater than the loss.

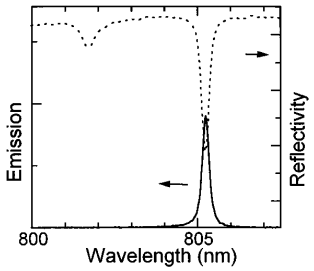

FIG. 2. Emission and reflection spectra at low excitation limit and at a sample position where I_{th} is below I_{sat}.

We now examine emission spectra when the cavity is tuned to below the exciton absorption line center for signatures of cavity polaritons near the lasing threshold. Figure 2 shows as a reference both reflection and emission spectra obtained at low excitation limit and with the cavity tuned to the spectral region where very low I_{th} is obtained. Two pronounced cavity-polariton resonances are observed in the reflection spectrum, indicating that the composite system is still in the nonperturbative regime,[15] although the energy separation between the bare mode and the corresponding coupled mode is now smaller than that when the cavity is at the exciton line center. A direct comparison of the reflection and emission spectra shows that the emission resonance is due to lower cavity polaritons. The spectral linewidth of the polariton emission is 0.25 nm.

Emission spectra obtained with increasing pumping intensities are shown in Fig. 3. Below a pumping intensity of 12 W/cm^2, the emission is due to spontaneous emission from lower cavity polaritons. Approaching I_{th}, a laser emission emerges directly from the lower cavity-polariton branch as shown in Fig. 3(a), in an agreement with $I_{th}<I_{sat}$. At the threshold pumping intensity of 26 W/cm^2, a rapid increase of the emission intensity [see the inset of Fig. 3(a)] is clearly observed and the emission linewidth is also reduced from 0.25 to 0.1 nm. With further increase in pumping intensities, the laser emission shifts gradually to lower wavelength as shown in Fig. 3(b). This blueshift is the result of mode pulling of the cavity resonance.

Figure 3(a) also shows that the laser emission is accompanied by a *broad resonance* at the lower cavity-polariton resonance even when the pumping intensity is above I_{th}. For the pulsed excitation we have used, the duration between successive pulses (13 ns) is long compared with the exciton lifetime, which means that laser emission is a transient process and the density of excitons or carriers varies as a function of the time. Hence, even if the pumping intensity is above I_{th}, spontaneous emissions from lower cavity polaritons will eventually become important when the exciton density falls below n_{th}.[16] The ratio $\alpha=A_L/A_B$, where A_L and A_B are the spectrally integrated intensity of the laser emission and the broad resonance, respectively, also reflects directly relative pumping intensity $(I-I_{th})/I_{th}$ as we will discuss further later.

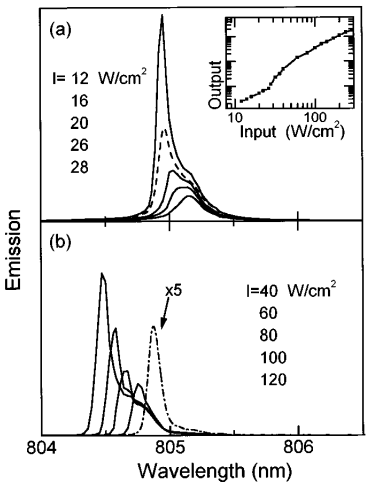

FIG. 3. Emission spectra at various pumping intensities as indicated in the figure. The data are obtained at the sample position used for Fig. 2. The dashed curve in (a) is the emission spectrum at the lasing threshold and the dotted curve in (b) is the emission spectrum just below the saturation pumping intensity. The inset shows the threshold behavior in the input-output relation.

When the pumping intensity exceeds I_{sat}, *an additional and pronounced broad resonance appears* at 804.75 nm as shown in Fig. 3(b) while the broad resonance at the lower cavity-polariton resonance can still be observed (see the log-scale plot in the inset of Fig. 4). When exciton densities exceed n_{sat}, both reflection and emission spectra of the composite system should be characterized by the bare-cavity resonance. The position of the additional broad emission resonance, which is independent of the pumping intensity and is 0.4 nm away from the lower cavity polariton, agrees well with that of the bare-cavity resonance deduced from the dispersion shown in Fig. 1(a). This additional broad emission resonance is due to spontaneous emission coming out of the bare-cavity mode and occurs when the exciton density exceeds n_{sat} but is still below the threshold density for laser emission in the perturbative regime where cavity polaritons vanish.

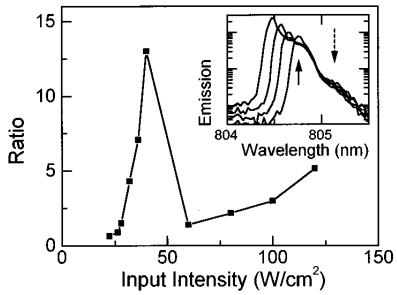

FIG. 4. The ratio of spectrally integrated intensities of the laser emission and the broad emission resonance shown in Fig. 3. The inset is a log-scale plot of the emission spectra in Fig. 3 when the pumping intensity is above the saturation intensity. The two arrows in the inset indicates positions of spectrally broad emissions at the lower cavity-polariton resonance (dashed arrows) and the bare-cavity resonance, respectively.

Emission spectra obtained near I_{sat} further reveal a striking change in the effective threshold pumping intensity when the composite exciton-cavity system undergoes a transition from the nonperturbative regime to the perturbative regime. As discussed earlier, the ratio $\alpha = A_L/A_B$ (where A_B is now the spectrally integrated intensity of both broad resonances) as a function of the pumping intensity can be used as a measure of $(I-I_{th})/I_{th}$. For pumping intensities just below I_{sat}, a very large ratio is observed as shown in Fig. 4, indicating a relatively large $(I-I_{th})/I_{th}$. In comparison, when the pumping intensity reaches just above I_{sat}, the ratio drops drastically, reflecting a small $(I-I_{th})/I_{th}$ and correspondingly *an abrupt increase in the lasing threshold*. These results indicate that I_{th} in the perturbative regime is considerably higher than I_{th} in the nonperturbative regime. Similar behaviors have also been observed at other sample positions where I_{th} can be smaller than I_{sat}. As we tune the cavity resonance, the abrupt threshold change always occurs near I_{sat} and at the wavelength of the bare-cavity resonance. This rules out the possibility that the abrupt change in $(I-I_{th})/I_{th}$ is the result of a slight change in the laser gain and the lasing threshold as the laser emission shifts gradually toward lower wavelength.

We also note that when the exciton density falls from above n_{sat} to below n_{sat} but is still above the threshold density for laser emission in the nonperturbative regime, we expect an additional laser emission near the lower cavity-polariton resonance. The emission spectra obtained when the pumping intensity is greater than I_{sat}, however, show no second laser emission resonance, suggesting that n_{sat} is bistable, i.e., n_{sat} occurring with decreasing densities is smaller than that with increasing densities. Such bistable behaviors have been predicated and observed for composite atom-cavity systems.[17] A detail discussion is beyond the scope of this paper.

For comparison, Fig. 5 also shows the threshold behavior at a sample position where I_{th} is just above I_{sat}. At low excitation limit, the emission resonance from the lower cavity polariton is at 804.8 nm. For pumping intensities above 30 W/cm^2, the output power increases superlinearly as shown in the inset. Signatures of spectral narrowing are also evidenced at a pumping intensity of 50 W/cm^2 [see the dotted curve in Fig. 5(a)], indicating that the composite system is close to the lasing threshold. The emission spectrum, however, broadens again with further increase in the pumping intensity, reflecting a large increase in the effective threshold intensity when the pumping intensity exceeds I_{sat} as we have discussed earlier. The lasing threshold is eventually reached at a pumping intensity of 100 W/cm^2 with laser emission wavelength at 804.3 nm. Note that when the cavity resonance is tuned further toward the exciton line center, cavity polaritons vanish far below the threshold and play no roles in the lasing process.[7]

Experimental results discussed above show that at the low-energy tail of the exciton inhomogeneous distribution, I_{th} can become considerably smaller than I_{sat} and that lasing threshold increases abruptly when the pumping intensity is increased from below to above I_{sat}, reflecting qualitative dif-

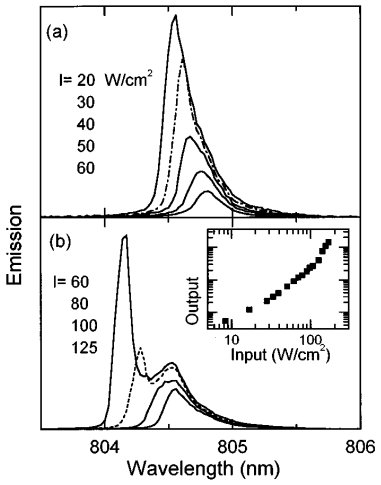

FIG. 5. Emission spectra at various pumping intensities as indicated in the figure. The data are obtained at a sample position where I_{th} is just above I_{sat}. The dotted curve in (a) shows spectral narrowing. The dashed curve in (b) is the emission spectrum at the lasing threshold. The inset in (b) shows the threshold behavior in the input-output relation.

ferences in laser emission in the perturbative and the nonperturbative regimes. Similar results have also been observed with cw excitations. The significant broad resonance in emission spectra obtained with pulsed excitations, however, allows us to obtain a quantitative measure of the threshold change across I_{sat}.

To understand the physical origin of laser emission at pumping intensities below I_{sat} we first turn to the drastic decrease in I_{th} below the absorption line center shown in Fig. 1(b). The decrease in I_{th} below the line center can be explained by effects of exciton localization. For a typical QW, there always exist monatomic layer fluctuations at the interface. At low temperature, these interface fluctuations localize excitons at local potential minimum. As a result, exciton energy depends on the local environment and the excitonic system is inhomogeneously broadened. After an off-resonant excitation, excitons at higher energies will relax toward the bottom of the inhomogeneous distribution through emission of phonons and will accumulate at the low-energy tail of the distribution, leading to a Stokes shift of the emission with respect to the absorption line center.[13] Note that the spectral relaxation time of localized excitons is short compared with the exciton recombination time.[14]

When a given localization site is occupied by an exciton, population inversion is achieved for this site. In this regard, localized excitons behave just like an inhomogeneously broadened atomic system but with spectral relaxation. For localized excitons at a given energy, the pumping intensity for achieving population inversion depends on the *total number of available localization sites at this energy* and also on details of spectral relaxation. Pumping intensities for achieving population inversion of excitons at very low energies can be much smaller than those at higher energies since states at very low energies are more likely to be occupied and also because the total number of available localization sites at these energies is relatively small. In principle, population inversion at the low-energy tail of the inhomogeneous distribution can be achieved at extremely low exciton densities and *without significant reduction in the overall coupling strength between the excitonic system and the cavity*.

Although a detailed understanding of laser emission in the nonperturbative regime still awaits further theoretical development, experimental results discussed above can be qualitatively understood by considering the linear dispersion model that has been used to describe coupled excitations in composite systems. In this model, the cavity-polariton resonance, especially the cavitylike polariton resonance, can be viewed as an effective cavity resonance with the frequency of the effective resonance modified by the dielectric response of the active media inside the cavity.[18] For a high-Q microcavity containing an inhomogeneously broadened excitonic system, a threshold density below the exciton saturation density (or the exciton Mott density) can be achieved by tuning the cavity resonance to the low-energy side of the inhomogeneous distribution. In this case, laser emission near the lower cavitylike polariton resonance such as that shown in Fig. 3(a) occurs in the nonperturbative regime in the sense that I_{th} is below I_{sat} and that cavity polaritons still persist at or near the lasing threshold. The laser emission, however, arises from population inversion of localized excitons at the low-energy tail of the inhomogeneous distribution.

It should be noted that laser emission in the nonperturbative regime discussed above does not imply that coherent energy exchange between excitons and cavity photons plays any direct role in the lasing process. Coherent normal-mode oscillations require the presence of a macroscopic polarization of excitons, or more specifically, a coherent superposition of two cavity-polariton branches. We also note that in principle normal-mode oscillations can contribute to optical emission processes even when incoherent excitations are used. For a composite atom-cavity system, strong optical interactions between the cavity and an initially inverted atomic system can lead to a macroscopic polarization through a super-radiant process and can result in oscillatory super-radiant emission. This ringing regime of super-radiance has been demonstrated by using Rydberg atoms in a high-Q resonant optical cavity.[19] The ability to achieve population inversion of excitons in a high-Q microcavity as shown in this paper suggests the possibility that with appropriate systems we might be able to observe this ringing regime of super-radiance in a semiconductor microcavity.

We attribute the large and abrupt change in I_{th} occurring near I_{sat} to ionization of excitons to continuum states. Recent studies have shown that for pumping intensities below I_{sat}, the reduction in the exciton oscillator strength is very small while the exciton linewidth can broaden significantly.[6] Theoretical calculations have further indicated that the bleaching of excitonic resonance and the corresponding vanishing of cavity polaritons occur quite abruptly when the normalized band edge approaches the $1s$ exciton resonance.[6] The estimated peak exciton density (of order $1\times10^{11}/\mathrm{cm}^2$) at I_{sat} is in general agreement with the theoretical prediction for the exciton Mott density. The abrupt threshold increase shown in Fig. 4 thus reflects directly this ionization of excitons into continuum states. Laser emission from localized excitons

features a considerably lower threshold pumping intensity while laser emission due to population inversion of an electron-hole plasma has a much higher threshold and occurs at the bare cavity resonance. In this respect, laser emission from microcavities near I_{sat} can also be used as a unique and extremely sensitive probe for important many-body processes such as the exciton to continuum transition.

In conclusion, we have demonstrated laser emission from a composite exciton-cavity system in the nonperturbative regime where the collective dipole coupling rate between the excitonic system and the cavity mode is large compared with relevant damping rates. Laser emission in this regime is shown to arise from population inversion of localized excitons. An abrupt change in the lasing threshold is also observed when the composite system undergoes a transition from the nonperturbative to the perturbative regime and is attributed to exciton ionization. These studies represent a significant step toward exploring and understanding lasing processes in the nonperturbative regime and should stimulate further theoretical and experimental efforts in understanding optical interactions in semiconductor microcavities.

We wish to acknowledge helpful discussions with H. Carmichael. The work performed at the University of Oregon was supported by AFOSR.

[1] C. Weisbuch *et al.*, Phys. Rev. Lett. **69**, 3314 (1992); R. Houdre *et al.*, *ibid.* **73**, 2043 (1994).

[2] R. Stanley *et al.*, Phys. Rev. B **53**, 10 995 (1996), and extensive references there.

[3] T. Norris *et al.*, Phys. Rev. B **50**, 14 663 (1994); J. Jacobson *et al.*, Phys. Rev. A **51**, 2542 (1995).

[4] H. Wang *et al.*, Phys. Rev. B **51**, 14 713 (1995).

[5] R. Houdre *et al.*, Phys. Rev. B **52**, 7810 (1995); J.-K. Rhee *et al.*, Solid State Commun. **97**, 941 (1996).

[6] F. Jahnke *et al.*, Phys. Rev. Lett. **77**, 5257 (1996).

[7] X. Fan *et al.*, Phys. Rev. A **56**, 3233 (1997).

[8] Y. Yamamoto (private communication); S. Pau *et al.*, Phys. Rev. A **54**, 1789 (1996).

[9] For a review, see E. Hanamura and H. Haug, Phys. Rep., Phys. Lett. **33C**, 209 (1977).

[10] J. Ding *et al.*, Phys. Rev. Lett. **69**, 1707 (1992); F. Keller *et al.*, *ibid.* **75**, 2420 (1995).

[11] P. V. Kelkar *et al.*, Phys. Rev. B **56**, 7564 (1997).

[12] S. Schmitt-Rink, D. S. Chemla, and D. A. B. Miller, Adv. Phys. **38**, 89 (1989).

[13] The Stokes shift measured by tuning the cavity far away from the exciton resonance is 1.5 nm.

[14] H. Wang, M. Jiang, and D. G. Steel, Phys. Rev. Lett. **65**, 1255 (1990).

[15] Normal-mode oscillations in transient nonlinear response similar to that shown in Ref. 4 have also been observed, confirming that the composite system is in the nonperturbative regime.

[16] Emissions from the outer region of the excitation spot where the exciton density is below n_{th} also contribute as a broad resonance.

[17] H. J. Carmichael *et al.*, in *Cavity Quantum Electrodynamics*, edited by P. R. Berman (Academic, Boston, 1994); J. Gripp *et al.*, Phys. Rev. A **54**, 3746 (1997).

[18] Y. Zhu *et al.*, Phys. Rev. Lett. **64**, 2499 (1990).

[19] Y. Kaluzny *et al.*, Phys. Rev. Lett. **51**, 1175 (1983).

APPENDIX C

BIEXCITONIC EFFECTS IN THE NONPERTURBATIVE REGIME OF SEMICONDUCTOR MICROCAVITIES

Xudong Fan, Hailin Wang, H. Q. Hou, and B. E. Hammons

Physical Review B, Volume 57, 1998, page R9451-9454

Copyright (1998) by the American Physical Society

Reprint permission granted by the American Physical Society

PHYSICAL REVIEW B VOLUME 57, NUMBER 16 15 APRIL 1998-II

Biexcitonic effects in the nonperturbative regime of semiconductor microcavities

Xudong Fan and Hailin Wang
Department of Physics and Oregon Center for Optics, University of Oregon, Eugene, Oregon 97403

H. Q. Hou and B. E. Hammons
Sandia National Laboratories, Albuquerque, New Mexico 87185

(Received 10 February 1998)

Polarization-dependent transient pump-probe spectroscopy reveals important effects of biexcitonic interactions on coupled optical excitations in semiconductor microcavities. We show that exciton-to-biexciton transitions can result in a significant increase in normal mode splitting of cavity-polaritons, in sharp contrast to effects of nonlinear optical interactions such as band filling that reduce the splitting. A phenomenological model based on Maxwell-Bloch equations is developed to elucidate how biexcitonic effects contribute to cavity-polaritons. [S0163-1829(98)50120-8]

Planar semiconductor microcavities embedded with quantum wells (QW) have been used as a composite exciton-cavity system to investigate excitonic optical interactions in a nonperturbative regime where collective dipole coupling rates between the exciton and the cavity mode are large compared with relevant cavity decay rates and exciton dephasing rates. Resonant optical excitations of the composite system in this regime are characterized by coupled exciton-cavity modes, or cavity polaritons. Extensive studies of semiconductor microcavities have shown normal mode splitting (NMS) of cavity polaritons in emission and reflection spectra and normal mode oscillation in transient optical responses.[1,2] Motional narrowing of cavity polaritons in a disordered potential has also been investigated recently.[3]

Strong coupling between the exciton and the cavity mode in the nonperturbative regime also leads to unusual manifestations of excitonic nonlinear optical interactions. Since NMS between two cavity-polariton branches reflects the collective dipole coupling strength between the exciton and the cavity mode, nonlinear optical processes such as phase space filling that saturate the excitonic transition reduce the magnitude of NMS,[4] while processes such as excitation-induced dephasing (EID) primarily broaden the cavity-polariton resonance.[5]

Biexcitonic interactions are also expected to affect optical excitations in the nonperturbative regime. Biexcitonic effects were shown to be important in understanding coherent nonlinear optical processes such as four-wave mixing of cavity polaritons.[6] A clear physical understanding of how biexcitons contribute to coupled excitations in semiconductor microcavities, however, is still lacking in part because biexcitonic effects cannot be easily incorporated into the widely used semiconductor Bloch equations.[7]

In this paper we present experimental and theoretical investigations on unique manifestations of biexcitonic effects in the nonperturbative regime in a microcavity embedded with GaAs QWs. Using polarization-dependent transient pump-probe spectroscopy, we found that biexcitonic interactions can result in a significant *increase* in NMS of cavity polaritons, in sharp contrast to effects of nonlinear optical interactions such as phase space filling that reduce the NMS. We attribute the observed increase in NMS to coupled excitations associated with the exciton-to-biexciton transition. A phenomenological model based on Maxwell-Bloch equations is also developed to elucidate how biexcitonic effects contribute to optical excitations in semiconductor microcavities. Our result underscores the necessity to include biexcitonic interactions in theoretical descriptions of optical interactions in the nonperturbative regime in semiconductor microcavities and should also impact interpretations of many other nonlinear optical studies in semiconductor microcavities.

The microcavity structure used in our study contains four 13-nm $GaAs/Al_{0.3}Ga_{0.7}As$ QWs placed at the center (antinode) of a wavelength long cavity. The two Bragg reflectors of the cavity consist of 16 and 22 pairs of $Al_{0.11}Ga_{0.89}As/AlAs$, respectively. The heavy-hole (hh) exciton absorption linewidth is estimated to be 1 nm, indicating that excitons are inhomogeneously broadened. The empty cavity linewidth is 0.25 nm. Additional information on the sample can also be found in earlier studies on laser emission from semiconductor microcavities.[8] Transient pump-probe studies were performed in the reflection geometry and with output from a mode-locked Ti:Sapphire laser with a pulse duration of 150 fs and a repetition rate of 82 MHz. All measurements were carried out at 10 K.

Figure 1 shows as dashed-lines reflection spectra of the sample obtained at low excitation limit. The NMS observed is 2.6 nm. Note that the linewidth for the upper (higher-energy) cavity polariton is considerably greater than that for the lower cavity polariton even though the cavity is at or very near the hh exciton absorption line center. The asymmetric linewidth, which has also been observed in numerous earlier studies, is likely the result of an asymmetric inhomogeneous line shape (or motional narrowing) in a QW with interface disorders.[3] Effects of light-hole excitons may also play an important role.

Reflection spectra when the sample is pre-excited by a resonant pump pulse are shown as solid lines in Fig. 1. When the pump-and-probe pulses have the same circular polarization, a large reduction in the NMS due to bleaching of the excitonic transition occurs as shown in Fig. 1(a). Significant broadening of the cavity-polariton resonance due to EID is

 © 1998 The American Physical Society

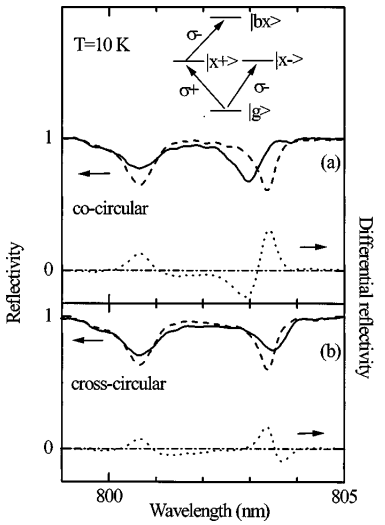

FIG. 1. Pump-probe reflection spectra. The dashed lines show as a reference spectra obtained in the absence of the pump beam. The solid lines are obtained when the sample is pre-excited with a resonant pump beam. The dotted lines represent the corresponding differential spectra. The pump-and-probe beams have the same and opposite circular polarization for (a) and (b), respectively. The inset shows the energy-level structure used to model the biexcitonic contribution.

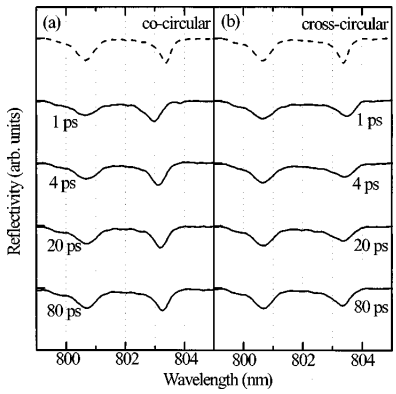

FIG. 2. Pump-probe reflection spectra as a function of the delay between the pump-and-probe beams as indicated in the figure. The dashed lines show as a reference reflection spectra obtained in the absence of the pump beam. The pump-and-probe beams have the same and opposite circular polarization for (a) and (b), respectively.

also evident. In comparison, when the pump-and-probe pulses have the *opposite* circular polarization (other experimental conditions remain the same) a significant *increase* of the NMS along with a broadening of the cavity-polariton resonance occurs, as shown in Fig. 1(b). Corresponding differential spectra plotted as dotted lines in Fig. 1 further confirm the above distinct polarization dependence. The average intensity of the pump beam used in these measurements is 30 W/cm^2, corresponding to an estimated exciton density of order 10^{10}/cm^2. The intensity of the probe beam used is less than 1% of that of the pump beam.

The observation of an increase in NMS is quite surprising since excitonic many body interactions are expected to lead to bleaching of the excitonic transition and consequently a decrease in NMS. An increase in NMS on the contrary corresponds to enhancement rather than bleaching of the underlying absorption process. Note that behaviors similar to that shown in Fig. 1(b) have also been observed at other pumping intensities where the NMS increases with the pumping intensity within the intensity range used in our measurements.

The polarization dependence of the pump-probe reflection spectra shown in Fig. 1 indicates that biexcitonic effects play an essential role.[9] The hh excitonic transition in a GaAs QW consists of both σ^+ and σ^- transitions associated with the excitation of σ^+ and σ^- excitons. Attractive interactions between two excitons with opposite spins (i.e., between σ^+ and σ^- excitons) can also lead to formation of biexcitons. The binding energy of biexcitons in GaAs QWs has been shown to range between 1 and 2 meV.[9] In the absence of spin relaxation, biexcitonic interactions become effective only when both σ^+ and σ^- excitons are excited.

When the microcavity structure is resonantly excited by a σ^+-polarized pulse, NMS of cavity polaritons associated with the σ^+ transition decreases due to absorption saturation. Cavity polaritons associated with the σ^- transition, however, can behave very differently. The presence of the σ^+ excitons does not lead to band filling for the σ^- excitonic transition. Furthermore, since biexcitons can be formed from two excitons with opposite spins, the presence of the σ^+ excitons induces an additional σ^- transition that results in creation of biexcitons (see the inset in Fig. 1). In the limit that the biexciton binding energy is comparable to the exciton inhomogeneous linewidth and an appreciable number of σ^+ excitons are excited, a significant increase in NMS associated with the σ^- transition is expected since the additional exciton-to-biexciton transition effectively increases the overall oscillator strength for the σ^- transition. In principle, strong coupling between the cavity mode and the additional exciton-to-biexciton transition can also lead to the formation of new cavity-polariton modes, as we will discuss in more detail later.

In addition to the unique polarization dependence discussed above, biexcitonic contribution to coupled optical excitations in semiconductor microcavities also exhibits distinctive temporal behaviors. Figure 2 compares results of pump-probe measurements at various delays between the pump and probe pulses. NMS shown in Fig. 2(a), where both the pump and probe beams have the same circular polarization, *increases* with increasing delay and recovers gradually the splitting observed at the low excitation limit. The recovery time is expected to be determined by the exciton recombination time.[4] In comparison, when the pump-and-probe beams have the opposite circular polarization, the NMS *decreases* initially with increasing delay, as shown in Fig. 2(b). In this case, spin relaxation of excitons excited by a circularly polarized pump beam reduces biexcitonic effects and leads to increasing effects of band filling. At a delay of 20 ps, the NMS observed is nearly the same as that at the low excitation limit although significant broadening still persists [see Fig. 2(b)].

When the exciton spins are randomized or when a linearly polarized pump beam is used (not shown), the reduction in NMS due to absorption saturation exceeds the increase due to biexcitonic effects (which can also be concluded from the polarization-dependent pump-probe measurements shown in Fig. 1). The absence of an increase in NMS, however, does not imply that biexcitonic effects play no roles in these measurements. The biexcitonic effects to some extent compensate the reduction in NMS due to absorption saturation, which may also be partially responsible for the nearly constant energy position of cavity polaritons below an ionization density shown in earlier steady-state pump-probe studies of cavity polaritons.

A satisfactory model of biexcitonic effects in semiconductor microcavities would require us to extend the semiconductor Bloch equations beyond the Hartree-Fock limit or to extend the recently developed diagrammatic theory of nonlinear optical interactions in semiconductors to the nonperturbative regime of semiconductor microcavities.[10] Considerable physical insight, however, can still be gained by using phenomenological optical Bloch equations (OBE) based on few-level systems along with the Maxwell equation. Earlier use of the phenomenological OBE has led to improved physical understanding of many-body processes such as biexcitons and local field effects in coherent nonlinear optical processes in semiconductors.[9,11]

To include effects of bound biexcitonic states, we have used a four level system shown in the inset of Fig. 1.[9] At a given exciton density, the Maxwell-Bloch equation describing the coupling between a σ^+ polarized cavity mode and excitons as well as biexcitons is given by

$$\dot{\alpha}_+ = -(i\omega_c + \kappa)\alpha_+ + \Omega\sqrt{1-2N_+/N_0}\beta_{x+} + \Omega\sqrt{N_-/N_0}\beta_{b+} + \kappa\varepsilon(t), \quad (1)$$

$$\dot{\beta}_{x+} = -(i\omega_x + \gamma)\beta_{x+} - \Omega\sqrt{1-2N_+/N_0}\alpha_+, \quad (2)$$

$$\dot{\beta}_{b+} = -(i\omega_b + \gamma)\beta_{b+} - \Omega\sqrt{N_-/N_0}\alpha_+, \quad (3)$$

where α_+ is the expectation value of the annihilation field operator for the cavity mode at the position of the QW inside the cavity; β_{x+} and β_{b+} is proportional to the σ^+ polarized optical polarization associated with the excitonic transition and the exciton-to-biexciton transition, respectively; $\varepsilon(t)$ represents a normalized external driving field; κ is the cavity decay rate; ω_c, ω_x, and ω_b are the resonant frequency of the cavity, the excitonic transition, and the exciton-to-biexciton transition, respectively; Ω is the collective dipole coupling rate for the σ^+ excitonic transition at the low excitation limit; N_0 is the equivalent of the total available number of σ^+ excitons; and N_+ and N_- are the density of σ^+ and σ^- excitons, respectively. For simplicity, we have assumed the same dephasing rate (denoted by γ) and dipole moment for both excitonic and the exciton-to-biexciton transitions. Effects of EID can be included by assuming a density-dependent dephasing rate. Note that saturation of the biexcitonic transition has been ignored in the above equations. We also emphasize that the very simple model presented above is aimed to illustrate how biexcitonic effects contribute to coupled excitations in the nonperturbative regime rather than to have a direct comparison between theory and experiment.

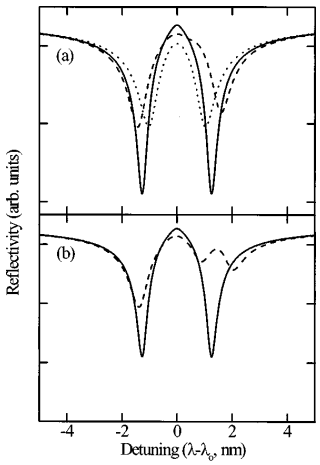

FIG. 3. Reflection spectra calculated based on the model discussed in the text. The solid lines show the reflection spectra in the low excitation limit. The dotted and dashed lines are reflection spectra at a given density of σ^+-excitons and are for σ^+ and σ^--polarized probes, respectively. The biexciton binding energy is assumed to be 1.2 meV in (a) and 3 meV in (b). λ_0 is the resonant wavelength of the cavity.

Equation (2) and the term proportional to β_{x+} in Eq. (1) describe coupling between the excitonic transition and the cavity mode and can lead to the formation of coupled exciton-photon modes. Equation (3) and the term proportional to β_{b+} in Eq. (1) describes coupling between the exciton-to-biexciton transition and the cavity mode and can lead to the formation of coupled excitations associated with the exciton-to-biexciton transition. This later coupling becomes effective only when there is a significant number of σ^- excitons present since the collective dipole coupling rate for the process is given by $\Omega\sqrt{N_-/N_0}$.

The calculated reflection spectrum at low excitation limit is shown as the solid line in Fig. 3 where we have assumed $\omega_c = \omega_x$, $\kappa = 0.75\ \mathrm{ps}^{-1}$, $\gamma = \kappa/2$, and $\Omega = 10\kappa$. Reflection spectra at a given density of σ^+ excitons are shown in Fig. 3(a) as the dotted line for a σ^+-polarized probe and the dashed line for a σ^--polarized probe where we have used an exciton dephasing rate of $1.2\ \mathrm{ps}^{-1}$ and an exciton density such that the collective dipole coupling rate is reduced to 0.8Ω for the σ^+ transition. For the σ^+-polarized probe, biexcitonic effects are absent and one expects a reduction in NMS and a broadening of the cavity-polariton resonance as shown in Fig. 3(a).

The σ^--polarized probe, however, is sensitive to the biexcitonic contribution. Along with a broadening of the cavity-polariton resonance, a significant increase in NMS is clearly shown in Fig. 3(a) where a biexciton binding energy of 1.2 meV is assumed. This increase in the NMS results directly from an increase in the overall absorption strength for the σ^- transition due to the induced exciton-to-biexcitons transition, as we have discussed earlier. The cavity-polariton resonance now involves both the excitonic and the exciton-to-biexciton transition. Note that the energy shift of the two cavity-polariton resonances is asymmetric. For the upper cavity-polariton resonance, a blueshift induced by the increase in

the oscillator strength is partially compensated by effects of a redshift in the center frequency of the overall σ^- transition.

In the limit that the biexciton binding energy is large compared with the exciton and cavity linewidth, new coupled excitations can arise from a strong coupling between the cavity mode and the exciton-to-biexciton transition. As a result, an additional cavity-polariton resonance can emerge in the reflection spectrum as shown in Fig. 3(b) where we have used a biexciton binding energy of 3 meV. It should be noted that in this case the strong coupling between the cavity mode and the exciton-to-biexciton transition affects strongly all cavity-polariton resonances.

Finally, we note that although Eqs. (1)–(3) can also be extended to include inhomogeneous broadening induced by interface disorders, as done in an earlier study,[12] a satisfactory description of the asymmetric cavity-polariton linewidth and especially the highly asymmetric reduction in NMS shown in Fig. 1(a) will require a microscopic understanding of effects of motional narrowing in disordered potentials on excitonic nonlinear optical processes.

In conclusion, using polarization-dependent pump-probe spectroscopy, we have shown important contribution of biexcitonic effects to coupled excitations in semiconductor microcavities. Biexcitonic interactions can lead to an increase in NMS and in the limit that the biexciton binding energy is large compared with relevant linewidth of the composite system can also result in an additional polariton resonance. The experimental results and the phenomenological model presented in this paper should stimulate further experimental and theoretical efforts in understanding optical interactions in the nonperturbative regime in semiconductors.

The work performed at the University of Oregon was supported in part by AFOSR.

[1] C. Weisbuch, M. Nishioka, A. Ishikawa, and Y. Arakawa, Phys. Rev. Lett. **69**, 3314 (1992).

[2] T. B. Norris, J. K. Rhee, C. Y. Sung, Y. Arakawa, M. Nishioka, and C. Weisbuch, Phys. Rev. B **50**, 14 663 (1994); J. Jacobson, S. Pau, H. Cao, G. Bjork, and Y. Yamamoto, Phys. Rev. A **51**, 2542 (1995); Hailin Wang, Jagdeep Shah, T. C. Damen, W. Y. Jan, J. E. Cunningham, M. H. Hong, and J. P. Mannaerts, Phys. Rev. B **51**, 14 713 (1995).

[3] D. M. Whittaker, P. Kinsler, T. A. Fisher, M. S. Skolnick, A. Armitage, A. M. Afshar, M. D. Sturge, and J. S. Roberts, Phys. Rev. Lett. **77**, 4792 (1996); V. Savona, C. Piermarocchi, A. Quattropani, F. Tassone, and P. Schwendimann, *ibid.* **78**, 4470 (1997).

[4] R. Houdre, J. L. Gibernon, P. Pellandini, R. P. Stanley, U. Oesterle, C. Weisbuch, J. O'Gorman, B. Roycroft, and M. Illegems, Phys. Rev. B **52**, 7810 (1995); J.-K. Rhee, D. S. Citrin, T. B. Norris, Y. Arakawa, and M. Nishioka, Solid State Commun. **97**, 941 (1996).

[5] F. Jahnke, M. Kira, S. W. Koch, G. Khitrova, E. K. Lindmark, T. R. Nelson, Jr., D. V. Wick, J. D. Berger, O. Lyngnes, H. M. Gibbs, and K. Tai, Phys. Rev. Lett. **77**, 5257 (1996).

[6] M. Kuwata-Gonokami, S. Inouye, H. Suzuura, M. Shirane, R. Shimano, T. Someya, and H. Sakaki, Phys. Rev. Lett. **79**, 1341 (1997).

[7] H. Haug and S. W. Koch, *Quantum Theory of the Optical and Electronic Properties of Semiconductors*, 2nd ed. (World Scientific, Singapore, 1993).

[8] Xudong Fan, Hailin Wang, H. Q. Hou, and B. E. Hammons, Phys. Rev. A **56**, 3233 (1997); Phys. Rev. B **56**, 15 256 (1997).

[9] K. Bott, O. Heller, D. Bennhardt, S. T. Cundiff, P. Thomas, E. J. Mayer, G. O. Smith, E. Eccleston, J. Kuhl, and K. Ploog, Phys. Rev. B **48**, 17 418 (1993); Hailin Wang, Jagdeep Shah, T. C. Damen, and L. N. Pfeiffer, Solid State Commun. **91**, 869 (1994), and references cited there.

[10] M. Z. Maialle and L. J. Sham, Phys. Rev. Lett. **73**, 3310 (1994).

[11] M. Wegener, D. S. Chemla, S. Schmitt-Rink, and W. Schaefer, Phys. Rev. A **42**, 5675 (1990).

[12] Hailin Wang, Y.-T. Chough, S. E. Palmer, and H. Carmichael, Opt. Express **1**, 370 (1997).

APPENDIX D

PURE DEPHASING INDUCED BY EXCITON-PHONON INTERACTIONS IN NARROW GaAs QUANTUM WELLS

Reprinted from

Solid State Communications, Volume 108

Xudong Fan, T. Takagahara, J. E. Cunningham, and Hailin Wang

"Pure Dephasing Induced by Exciton-phonon Interactions in Narrow Quantum Wells"

Page 857-861, Copyright (1998), with permission from Elsevier Science

Pergamon

Solid State Communications, Vol. 108, No. 11, pp. 857–861, 1998
© 1998 Elsevier Science Ltd. All rights reserved
0038–1098/98 $ - see front matter

PII: S0038–1098(98)00461-X

PURE DEPHASING INDUCED BY EXCITON–PHONON INTERACTIONS IN NARROW GaAs QUANTUM WELLS

Xudong Fan,[a] T. Takagahara,[b] J.E. Cunningham[c] and Hailin Wang[a,*]

[a]Department of Physics and Oregon Center for Optics, University of Oregon, OR 97403, U.S.A.
[b]NTT Basic Research Laboratories, Atsugi, Kanagawa, 243-01, Japan
[c]Bell Laboratories, Lucent Technologies, NJ 07733, U.S.A.

(*Received* 27 *May* 1998; *accepted* 31 *August* 1998 *by E.E. Mendez*)

We investigate both dephasing and population relaxation of excitons localized in quantum dot like islands in narrow GaAs quantum wells by using stimulated photon echoes. A direct comparison of these two closely related decay processes reveals a pure dephasing contribution that dominates excitonic dephasing at elevated temperatures but does not involve exciton population relaxation. The pure dephasing contribution arises from coupling of excitonic states with a continuum of acoustic phonons and is enhanced by 3D quantum confinement. Both the magnitude and the temperature dependence of the pure dephasing rate can be described by a theoretical model that generalizes the Huang–Rhys theory of *F*-centers. © 1998 Elsevier Science Ltd. All rights reserved

A resonant optical excitation creates an excited state population and also induces an optical polarization. Dynamics of this optical excitation are characterized by relaxation of the population as well as decay of the induced optical polarization (dephasing). In lower dimensional semiconductors, electronic confinement leads to qualitative changes in population relaxation including spontaneous emission and exciton–phonon scattering, as shown in extensive recent studies [1]. These population relaxation processes are expected to contribute to dephasing with a dephasing rate given by $\Gamma/2$ where Γ is the population decay rate. Pure dephasing processes that do not involve population or energy relaxation of excitons can also contribute to dephasing. Pure dephasing, which is a well-established concept for atomic systems, remains poorly understood in lower dimensional semiconductors due to a lack of direct comparison between dephasing and population relaxation and between theory and experiment. Understanding pure dephasing processes in lower dimensional semiconductors bridges our fundamental understanding of dephasing of atomic systems and of collective excitations in solids and is also essential for understanding a variety of physical processes that depend on the presence of optical coherence.

Narrow GaAs quantum wells (QWs) grown by molecular beam epitaxy (MBE) and with growth interruptions have provided a model system for investigating dephasing processes in lower dimensional semiconductors. In these narrow QWs, fluctuations at the interface between GaAs and AlGaAs lead to localization of excitons at monolayer-high islands. These strongly localized states have also been viewed effectively as weakly-confined quantum dot (QD)-like states [2–4]. One dimension of the confinement is defined by the width of the QW while the other two lateral dimensions are defined by the effective size of the islands. To avoid inhomogeneous broadening due to well-width and island-size fluctuations, earlier studies have used photoluminescence (PL) and PL excitation with high spatial resolution to probe excitons in individual islands [2–4]. Without additional information on population relaxation, it was suggested that at very low temperature dephasing of excitons in these structures is due to radiative recombination while at elevated temperature dephasing is mainly due to thermal activation of excitons to higher excited states [4].

* Corresponding author.

In this paper we report experimental and theoretical studies of dephasing and population relaxation, especially, pure dephasing processes of excitons in narrow GaAs QWs. Using stimulated photon echoes, we compared directly dephasing rates with population decay rates. This direct comparison reveals a pure dephasing process that dominates excitonic dephasing at elevated temperatures. The pure dephasing process arises from coupling of excitonic states with a continuum of acoustic phonons and is enhanced by 3D quantum confinement. The magnitude as well as the temperature dependence of the pure dephasing rate is described by a theoretical model that generalizes the Huang–Rhys theory of *F*-centers to include also mixing of excited electronic states through off-diagonal exciton–phonon interactions. The observed temperature dependence of the pure dephasing rate further underscores qualitative differences in dephasing of excitons with weak and strong 3D quantum confinement.

Two QW samples grown by MBE and with growth interruptions have been used in our study and qualitatively the same results have been obtained in both samples. Sample A (B) consists of 6 (60) periods of 2.8 (3.5) nm GaAs well and 10(15) nm $Al_{0.3}Ga_{0.7}As$ barrier. Sample A is grown under conditions similar to those of single QWs used in earlier studies of individual QD-like islands in narrow GaAs QWs [4, 5]. For brevity and for comparison with earlier studies in [4], we present in this paper only results obtained on sample A. To avoid complications due to direct excitation of excited states in QD-like islands, we have restricted our measurements to excitons at relatively low exciton energies.

The absorption spectrum of sample A can be found in [5]. The spectrum is characterized by two well-resolved heavy hole (*hh*) exciton resonances corresponding to *hh* excitons in islands that differ in sell width by one monolayer. The absorption linewidth of 2.7 nm indicates that the sample is of high quality but is inhomogeneously broadened. The PL spectrum also shows an additional emission resonance from islands that are one monolayer wider than those associated with the lower *hh* resonance in the absorption spectrum [5]. The Stokes shift is 1.2 nm.

Experimental configuration for stimulated phonon echo studies is shown as an inset in Fig. 1(a). In these studies, three nearly transform-limited pulses with 1 nm spectral width are incident on the sample at times t_1, t_2 and t_3, respectively. Optical polarization induced by the first pulse interacts with the second pulse, creating a spatial modulation of the excited state population. The third pulse scatters from this spatial grating and generates a background free four-wave-mixing (FWM) signal in the direction of $\mathbf{k}_1 - \mathbf{k}_2 + \mathbf{k}_3$. For inhomogeneously broadened systems, the signal is a photon echo and complications due to inhomogeneous broadening are avoided through the formation of a photon echoes. Intrinsic dephasing is probed by measuring the time-integrated FWM signal as a function of $t_1 - t_2$ while population relaxation is probed by measuring the decay of the signal as a function of $t_1 - t_2$ [6, 7].

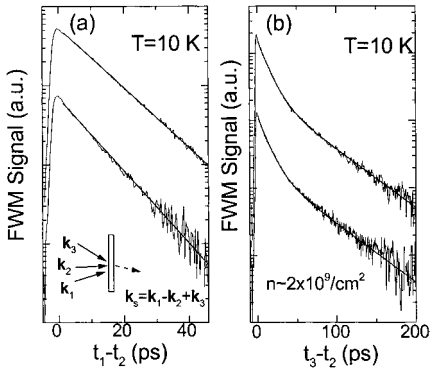

Fig. 1. FWM response at 10 K for excitons at 7173 Å (upper curve) and 7184 Å (lower curve). Solid lines show the exponential fit to the response. (a) As a function of $t_1 - t_2$ with $t_1 = t_3$. Dephasing rates derived are $0.023\ \mathrm{ps}^{-1}$ and $0.026\ \mathrm{ps}^{-1}$ for the upper and lower curves, respectively. (b) As a function of $t_3 - t_2$ with $t_1 = t_2$. Population decay rates derived are $0.04\ \mathrm{ps}^{-1}$ and $0.01\ \mathrm{ps}^{-1}$ for the fast and slow component, respectively (both curves). The inset in (a) shows the configuration for the stimulated photon echo measurement.

Figure 1 shows typical FWM responses at 10 K and at two different wavelengths. Figure 1(a) is obtained by measuring the FWM signal as a function of $t_1 - t_2$. Decay rate of the FWM response is 4γ where γ is the dephasing rate. Figure 1(b) is obtained by measuring the FWM signal as a function of $t_3 - t_2$ and reflects exciton population relaxation. The response in Fig. 1(b) features an initial fast decay followed by a relatively slow decay and will be discussed in detail later.

Figures 2(a) and 2(b) show the energy and density dependence of the dephasing and population decay rates (the fast component), respectively. The dephasing rate increases linearly with the exciton density while the population decay rate is nearly independent of the exciton density. To avoid complications due to exciton–exciton scattering, data shown in Fig. 2(a) and in Fig. 3 discussed later are obtained by extrapolating the decay rates to the zero density limit. The long dephasing time shown in Fig. 2(a) (of order 50 ps) corresponds to a homogeneous linewidth of $27\ \mu\mathrm{eV}$, in agreement with earlier studies [2–4]. At 10 K both dephasing and population decay rates are nearly independent of the exciton energy in the spectral range of our

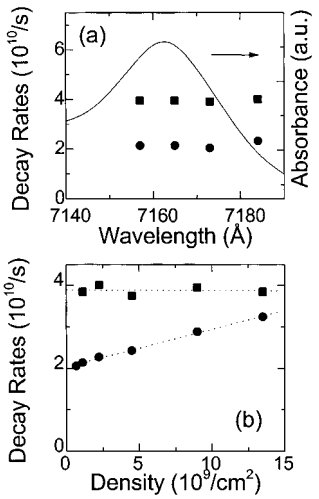

Fig. 2. Energy and density dependence of exciton dephasing rates (circles) and population decay rates (squares) at 10 K. The density dependence is obtained at $\lambda = 7173$ Å. Absorption spectrum of the lower energy *hh* exciton resonance is also plotted in (a).

measurements, in contrast to exciton dynamics in wider QWs where both decay rates increase rapidly across the absorption line center [8]. In narrow QWs, excitons near or above the absorption line center can be localized as also shown in earlier studies [2, 4]. Note that the density dependence shown in Fig. 2(b) is obtained by varying the

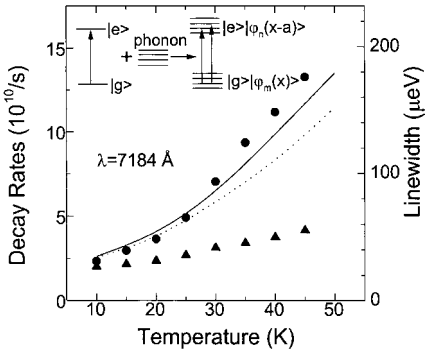

Fig. 3. Dephasing rates (circles) and half population decay rates $\Gamma/2$ (triangles) as a function of the temperature. The solid and dashed curves show theoretical results of dephasing rates for the exciton ground state with and without the contribution of off-diagonal electron–phonon interactions, respectively. The inset shows schematically pure dephasing arising from coupling of excitonic states with a phonon continuum where we have considered only effects of diagonal electron–phonon interactions. For simplicity the excited state manifold is ignored in the inset.

level of coherent excitations. Complications to FWM response arising from effects such as exciton–exciton interaction-induced dephasing have been discussed in detail in earlier studies [9].

Figure 3 shows the temperature dependence of the dephasing and population decay rates (the fast component) for excitons at an energy 2 nm below the absorption line center. Similar temperature dependence has also been observed within the spectral range of our measurements. The observed temperature dependence is in general agreement with an earlier study using PL with high spatial resolution [4]. Note that the earlier study was done at a lower exciton energy where islands with comparable energies are spaced far apart such that discrete energy structures of a single island can be probed by using PLE with a 1.5 μm diameter aperture. For the present study islands with comparable energies are spaced closer and as a result exciton migration among islands, which we will discuss below, becomes more important.

We first discuss population relaxation of excitons. The population relaxation involves exciton recombination as well as migration of excitons among different islands. At elevated temperatures, thermal activation also becomes important. The migration proceeds through tunneling between neighboring islands or through inter-island dipole–dipole interactions [10]. For excitons *at a given energy*, the total population decay rate is $\Gamma = \Gamma_m + \Gamma_t + \Gamma_{re}$ where Γ_m is the migration rate, Γ_t is the thermal activation rate and Γ_{re} is the recombination rate. This total population decay is represented by the initial fast decay of the FWM response shown in Fig. 1(b).

We attribute the slow decay component in Fig. 1(b) to exciton recombination. In the limit that migration is fast compared with exciton recombination, excitons can form a quasi-equilibrium distribution that also contributes to the FWM response [11]. The life time of this distribution is determined by the relatively long exciton recombination time.

We now discuss dephasing processes of excitons. Theoretically, contribution to dephasing from population relaxation is $\Gamma/2$. As shown in Fig. 3, at very low temperature the dephasing rate γ is very close to $\Gamma/2$ and dephasing is mainly due to population relaxation. With increasing temperature the dephasing rate increases much faster than the population decay rate. At elevated temperatures (>30 K), dephasing rates become much greater than $\Gamma/2$, indicating a dominant contribution of pure dephasing, i.e. decay of optically-induced dipole coherence without measurable change in the population of electronic states of the relevant optical transition. Note that for delocalized excitons in GaAs QWs, dephasing rates are much greater than those of localized excitons and increase linearly with temperature

(below 50 K), in contrast to the nonlinear temperature dependence shown in Fig. 3 [12].

The strong temperature dependence of the pure dephasing rate ($\Gamma - \Gamma/2$) signals that interactions between excitons and acoustic phonons play an essential role in the pure dephasing process. Dephasing (or equivalently, homogeneous linewidth) of impurity states in solids due to electron–phonon interactions has been treated theoretically by using models based on the Huang-Rhys theory of *F*-centers [13, 14]. These models, however, do not take into account the mixing of electronic states through off-diagonal electron–phonon interactions. To understand pure dephasing for excitons localized in QD-like islands, we have developed a model that generalizes the Huang–Rhys theory to also include effects of off-diagonal electron–phonon interactions. In this model, the Hamiltonian for the relevant ground and excited states can be written respectively, as

$$H_g = \sum_\alpha \hbar\omega_\alpha b_\alpha^+ b_\alpha \quad \text{and}$$
$$H_e = H_e^0 + H_g + \sum_\alpha M_\alpha (b_\alpha + b_\alpha^+) \tag{1}$$

where $b_\alpha(b_\alpha^+)$ is the annihilation (creation) operator of the acoustic phonon mode with index α, H_e^0 is the diagonal energy matrix of the excited state manifold for the QD-like island and matrix M_α has both diagonal and off-diagonal elements. The off-diagonal matrix elements induce mixing among the excited state manifold. Note that crystal momentum conservation needs to be satisfied in directions where translational invariance holds. The pure dephasing process becomes prominent in systems with 3D electronic confinement because the 3D confinement relaxes the crystal momentum conservation and also suppresses exciton population relaxation induced by exciton–phonon interactions.

Pure dephasing can arise from coupling of excitonic states with a continuum of acoustic phonons. To elucidate this, we show schematically in the inset of Fig. 3 eigenstates of a coupled exciton–phonon system. In the limit that off-diagonal elements in M_α can be ignored, the Hamiltonian in equation (1) can be diagonalized analytically. The main effects of the exciton–phonon coupling are then a shift in the equilibrium position of lattice vibrations and a temperature-independent polaron shift of the exciton energy [13, 14]. In this limit, the ground and excited states of the coupled exciton–phonon system can be described (in terms of eigenfunctions of the uncoupled system) by $|\phi_g\rangle|\varphi_m(x)\rangle$ and $|\phi_e\rangle|\varphi_n(x-a)\rangle$, where $\varphi_m(x)$ is the wave function for a phonon state with m phonons, x is the phonon coordinate with a being a relative shift in the equilibrium position induced by the exciton–phonon coupling and ϕ_g and ϕ_e are the wave functions of the electronic ground and excited states, respectively. The dipole matrix element between the ground and excited states of the coupled state is then $\langle\phi_g|\mathbf{r}|\phi_e\rangle\langle\varphi_m(x)|\varphi_n(x-a)\rangle$. The optical transition can now take place between states involving different phonon numbers since $\langle\varphi_m(x)|\varphi_n(x-a)\rangle \neq 0$ even when $m \neq n$ and can be viewed as *transitions between two quasi-continuous manifolds,* as shown in the inset of Fig. 3. The resulting spectral broadening of the optical transition depends on the relative strength of relevant transition *but does not involve population relaxation of the excitonic states*.

We calculate the homogeneous linewidth from the absorption spectrum given by

$$I(\omega) = \mathrm{Re}\left[\int_0^\infty \mathrm{d}t\, \mathrm{e}^{-i\omega t}\langle 0|\mathrm{e}^{iH_e t/\hbar}\mathrm{e}^{-iH_g t/\hbar}|0\rangle\right], \tag{2}$$

where $|0\rangle$ is the ground state of the system. The absorption spectrum can be estimated by a diagrammatic expansion and is given by

$$I(\omega) = \mathrm{Re}\; G(i\omega + \delta) \quad \text{with} \quad G(s) = \frac{1}{s - iH_e^0/\hbar - \Sigma(s)}, \tag{3}$$

where δ indicates half of the population decay rate caused by mechanisms other than phonon scattering. The self-energy $\Sigma(s)$ in (3) can be expanded in powers of M_α as

$$\Sigma(s) = \Sigma^{(2)}(s) + \Sigma^{(4)}(s) + \cdots. \tag{4}$$

In actual calculations, the self-energy is iteratively improved by replacing the propagators in Σ with Green's function G obtained in the last iteration and thus by summing an infinite series of a particular type of diagrams. We have employed a quantum disk model for the island structure whose height L_z is given by the thickness of the constituent QW and whose lateral size (an adjustable parameter) is chosen as 40 nm. These parameters reproduce reasonably well the exciton energy level structures in Ref. 4 [15].

Theoretical results for dephasing rates of the exciton ground state are shown as the solid curve in Fig. 3 and are in general agreement with the experimental result except for the high temperature region. For comparison, we also show as the dashed curve the result that takes into account only the exciton ground state in which only the diagonal electron–phonon interaction is relevant. We see that the pure dephasing processes arise mainly from the diagonal electron–phonon interaction but the contribution from the off-diagonal electron–phonon interaction is also substantial. The off-diagonal interaction is expected to be strongly enhanced when the thermal energy $k_B T$ approaches the relevant energy level spacing for the QD-like islands in narrow GaAs QWs. Note that

contributions to dephasing from interactions with optical phonons is also expected to become important when the thermal energy approaches the optical phonon energy.

It is important to point out that temperature dependence of dephasing rates can differ qualitatively for semiconductors with strong and weak 3D confinement. For QDs that have strong 3D confinement such as II–VI nanocrystals, a linear temperature dependence has been observed up to 200 K [16]. On the other hand, for CuCl nanocrystals belonging to the weak confinement regime, a temperature dependence similar to that in Fig. 3 was observed [17, 18], although strongly nonlinear temperature dependence occurs above a higher temperature (~50 K). These different temperature dependences can be accounted for by the above model if we consider the different energy structures involved. For GaAs islands the energy separation between the ground and first excited states is a few meV, whereas for CuCl nanocrystals with 4 nm radius the energy separation is about 10 meV. In CdSe nanocrystals with radii smaller than 2 nm, the relevant energy spacing is determined by the A- and B-exciton splitting (26 meV). In the limit of large energy level spacing, diagonal electron–phonon interactions associated with small energy acoustic phonons dominate the pure dephasing process and lead to a linear temperature dependence [15].

In conclusion, by comparing directly dephasing and population relaxation of excitons in narrow GaAs QWs we have identified a pure dephasing process that dominates excitonic dephasing at elevated temperatures. The magnitude and temperature dependence of the pure dephasing rate can be described by a model that generalized the Huang–Rhys theory of *F*-centers. The temperature dependence of the dephasing rate also points to important differences in pure dephasing for semiconductors with weak and strong 3D confinement. The pure dephasing process is enhanced by 3D confinement and can become a dominant contribution to dephasing in systems with 3D confinement.

Acknowledgements—We thank D. Gammon for providing one of the samples used for this study and for many helpful and stimulating discussions. The work performed at the University of Oregon is supported by AFOSR and by a NSF career award.

REFERENCES

1. See for example, Andreani, L.C., in *Confined electrons and photons, New physics and devices* (Edited by E. Burstein and C. Weisbuch). Plenum, New York, 1995; Citrin, D.S., *Phys. Rev*., **B47,** 1993, 3832; Benisty, H. *et al*., *Phys. Rev*., **B44,** 1991, 10945; Bockelmann, *et al*., *Phys. Rev*., **B48,** 1993, 17637.
2. Hess, H.F. *et al*., *Science*, **264,** 1994, 1740.
3. Brunner, K. *et al*., *Phys. Rev. Lett.*, **73,** 1994, 1138.
4. Gammon, D. *et al*., *Science*, **273,** 1996, 87; Gammon, D. *et al*., *Phys. Rev. Lett*., **76,** 1996, 3005.
5. The absorption spectrum of sample A is shown in Gammon, D. *et al*., *Phys. Rev*., **B51,** 1995, 16785. The PL spectrum of sample A is nearly the same as that of the 2.8 nm single QW grown under similar conditions shown in [4].
6. Mossberg, T.W. *et al*., *Phys. Rev. Lett.*, **42,** 1979, 1665.
7. Weiner, A.M., De Silvestri, S. and Ippen, E.P., *J. Opt. Soc. Am.*, **B2,** 1985, 654.
8. Hegarty, J. and Sturge, M.D., *J. Opt. Soc. Am*., **B2,** 1985, 1143; Webb, M.D., Cundiff, S.T. and Steel, D.G., *Phys. Rev*., **B43,** 1991, 12658.
9. Wang, H. *et al*., *Phys. Rev.*, **A49,** 1994, R1551.
10. Takagahara, T., *Phys. Rev*., **B32,** 1985, 7013; *J. Lumin*., **44,** 1989, 347.
11. Wang, H., Jiang, M. and Steel, D.G., *Phys. Rev. Lett*., **65,** 1990, 1255.
12. Schultheis, L. *et al*., *Phys. Rev.*, **B34,** 1986, 9027.
13. Huang, K. and Rhys, A., *Proc. Roy. Soc. (London)*, **A204,** 1950, 406.
14. Duke, C.B. and Mahan, G.D., *Phys. Rev.*, **139,** 1965, A1965.
15. Takagahara, T. *et al*., unpublished.
16. Shoenlein, R.W. *et al*., *Phys. Rev. Lett.*, **70,** 1993, 1014.
17. Itoh, T. and Furumiya, M., *J. Lumin.*, **48&49,** 1991, 704.
18. Inoue, K. *et al*., *OSA Tech. Digest Series (CLEO'98)*, **6,** 1998, 266.

BIBLIOGRAPHY

[1] P. R. Berman, editor, *Cavity Quantum Electrodynamics*, Academic, Boston, 1994.

[2] S. Haroche and D. Kleppner, Phys. Today **42**, 24 (1989).

[3] E. M. Purcell, Phys. Rev. **69**, 681 (1946).

[4] E. T. Jaynes and F. W. Cummings, Proc. IEEE **51**, 89 (1963).

[5] E. H. Drexhage, in *Progress in Optics XII*, E. Wolf, editor, North Holland, Amsterdam, 1974.

[6] R. G. Hulet, E. S. Hilfer, and D. Kleppner, Phys. Rev. Lett. **55**, 2137 (1985).

[7] R. J. Thompson, G. Rempe, and H. J. Kimble, Phys. Rev. Lett. **68**, 1132 (1992).

[8] H. J. Kimble, Phil. Trans. R. Soc. Lond. **355**, 2327 (1997).

[9] M. Brune, F. Schmidt-Kaler, A. Maali, J. Dreyer, E. Hagley, J. M. Raimond, and S. Haroche, Phys. Rev. Lett. **76**, 1800 (1996).

[10] P. Meystre, in *Progress in Optics XXX*, E. Wolf, editor, Elsevier Science Publishers B. V., 1992,

[11] D. Meschede, H. Walther, and G. Muller, Phys. Rev. Lett. **54**, 551 (1985).

[12] Y. Mu and C. M. Savage, Phys. Rev. A **46**, 5944 (1992).

[13] K. An, J. J. Childs, R. R. Dasari, and M. S. Feld, Phys. Rev. Lett. **73**, 3375 (1994).

[14] J. J. Childs, K. An, M. S. Otteson, R. R. Dasari, and M. S. Feld, Phys. Rev. Lett. **77**, 2901 (1996).

[15] K. An, R. R. Dasari, and M. S. Feld, Opt. Lett. **22**, 1501 (1997).

[16] S. Haroche, M. Brune, and J. M. Raimond, Europhys. Lett. **14**, 19 (1991).

[17] Q. A. Turchette, C. J. Hood, W. Lange, H. Mabuchi, and H. J. Kimble, Phys. Rev. Lett. **75**, 4710 (1995).

[18] J. I. Cirac and P. Zoller, Phys. Rev. Lett. **74**, 4091 (1995).

[19] T. Sleator and H. Weinfurter, Phys. Rev. Lett. **74**, 4087 (1995).

[20] J. I. Cirac, P. Zoller, H. J. Kimble, and H. Mabuchi, Phys. Rev. Lett. **78**, 3221 (1997).

[21] D. S. Chemla, Helvetica Physica Acta **56**, 607 (1983).

[22] Y. Yamamoto, editor, *Coherence, Amplification and Quantum Effects in Semiconductor Lasers*, John Wiley, New York, 1991.

[23] M. S. Sherwin, A. Imamoglu, and T. Montroy, e-print quant-ph/9903065.

[24] T. A. Brun and H. Wang, Phys. Rev. A **61**, 32307 (2000).

[25] D. Loss and D. P. DiVincenzo, Phys. Rev. A **57**, 120 (1998).

[26] J. D. Joannopoulos, R. D. Meade, and J. N. Winn, *Photonic crystals : molding the flow of light*, Princeton University Press, Princeton, 1995.

[27] C. Weisbuch, M. Nishioka, A. Ishikawa, and Y. Arakawa, Phys. Lett. **69**, 3314 (1992).

[28] A. Schülzgen, R. Binder, M. E. Donovan, M. Lindberg, K. Wundke, H. M. Gibbs, G. Khitrova, and N. Peyghambarian, Phys. Rev. Lett. **82**, 2346 (1992).

[29] Y. Yamamoto and R. Slusher, Phys. Today **46**, 66 (1993).

[30] J. M. Gérard, B. Sermage, B. Gayral, B. Legrand, E. Costard, and V. Thierry-Mieg, Phys. Rev. Lett. **81**, 1110 (1998).

[31] V. B. Brakinsky, M. L. Gorodetsky, and V. S. Ilchenko, Phys. Lett. A **137**, 393 (1989).

[32] L. Collot, V. Lefèvre-Seguin, M. Brune, J. M. Raimond, and S. Haroche, Europhy. Lett. **23**, 327 (1993).

[33] F. Treussart, J. Hare, L. Collot, V. Lefèvre, D. S. Weiss, V. Sandoghdar, J. M. Raimond, and S. Harche, Opt. Lett. **19**, 1651 (1994).

[34] D. W. Vernooy, A. Furusawa, N. P. Georgiades, V. S. Ilchenko, and H. J. Kimble, Phys. Rev. A **57**, R2293 (1998).

[35] D. J. Norris, M. Kuwata-Gonokami, and W. E. Moener, Appl. Phys. Lett. **71**, 297 (1997).

[36] H. B. Lin and A. J. Campillo, Phys. Rev. Lett. **73**, 2440 (1994).

[37] R. K. Chang and A. J. Campillo, editors, *Optical Processes in Microcavities*, World Scientific, Singapore, 1996.

[38] V. S. Ilchenko, P. S. Volikov, V. L. Velichansky, F. Treussart, V. Lefèvre-Seguin, J. M. Raimond, and S. Haroche, Opt. Commun. **145**, 86 (1998).

[39] M. Cai, private communications.

[40] D. Vernooy, private communications.

[41] G. Mie, Ann. Phys. **25**, 377 (1908).

[42] L. Rayleigh, Phil. Mag. **27**, 100 (1914).

[43] V. D. Hulst, *Light Scattering by Small Particles*, Wiley, New York, 1957.

[44] P. W. Barber and R. K. Chang, editors, *Optical Effects Associated with Small Particles*, World Scientific, Singapore, 1988.

[45] H. M. Nussenzveig, *Diffraction Effects in Semiclassical Scattering*, Cambridge University Press, Cambridge, 1992.

[46] B. R. Johnson, J. Opt. Soc. Am. A **10**, 343 (1993).

[47] H. M. Lai, P. T. Leung, K. Young, P. W. Barber, and S. C. Hill, Phys. Rev. A **41**, 5187 (1990).

[48] H. M. Lai, , C. C. Lam, P. T. Leung, and K. Young, J. Opt. Soc. Am. B **8**, 1962 (1991).

[49] M. L. Gorodetsky, A. A. Savchenkov, and V. S. Ilchenko, Opt. Lett. **21**, 453 (1996).

[50] D. W. Vernooy, V. S. Ilchenko, H. Mabuchi, E. W. Streed, and H. J. Kimble, Opt. Lett. **23**, 247 (1998).

[51] S. C. Hill and R. E. Benner, J. Opt. Soc. Am. B **3**, 1509 (1986).

[52] A. W. Adamson, *Physical Chemistry of Surfaces*, Wiley, New York, 1977.

[53] J. C. Knight, N. Dubreuil, V. Sandoghdar, J. Hare, V. Lefèvre-Seguin, J. M. Raimond, and S. Haroche, Opt. Lett. **20**, 1515 (1995).

[54] M. Cai, O. Painter, and K. Vahala, Phys. Rev. Lett. **85**, 74 (2000).

[55] J. C. Swindal, D. H. Leach, and R. K. Chang, Opt. Lett. **18**, 191 (1993).

[56] M. L. Gorodetsky and V. S. Ilchenko, Opt. Commun. **113**, 133 (1994).

[57] J. U. Nockel, A. D. Stone, G. Chen, H. L. Grossman, and R. K. Chang, Opt. Lett. **21**, 1609 (1996).

[58] J. U. Nockel and A. D. Stone, Nature **385**, 45 (1997).

[59] S. Lacey, private communications.

[60] M. Asada, Y. Miyamoto, and Y. Suematsu, IEEE J. Quantum Electron. **QE-22**, 1915 (1986).

[61] K. J. Vahala, IEEE J. Quantum Electron. **24**, 523 (1988).

[62] J. J. LePore, J. Appl. Phys. **51**, 6441 (1981).

[63] M. Pelton and Y. Yamamoto, Phys. Rev. A **59**, 2418 (1999).

[64] H. F. Hess, E. Betzig, T. D. Harris, L. N. Pfeiffer, and K. W. West, Science **264**, 1740 (1994).

[65] L. C. Andreani and A. Pasquarello, Phys. Rev. B **42**, 8928 (1990).

[66] M. Hines and P. Guyot-Sionnest, J. Phys. Chem. **100**, 468 (1996).

[67] A. P. Alivisatos, J. Phys. Chem. **100**, 13226 (1996).

[68] V. L. Colvin, M. C. Schlamp, and A. P. Alivisatos, Nature **370**, 354 (1994).

[69] B. Dabbousi, M. Bawendi, O. Onostsuka, and M. F. Rubner, Appl. Phys. Lett. **66**, 1316 (1995).

[70] M. B. Jr., M. Moronne, P. Gin, S. Weiss, and A. P. Alivisatos, Science **281**, 2013 (1998).

[71] W. C. Chan and S. Nie, Science **281**, 2016 (1998).

[72] L. E. Brus, App. Phys. **A53**, 465 (1991).

[73] H. Weller, Adv. Mater. **5**, 88 (1993).

[74] B. O. Dabbousi, J. Rodriguez-Viejo, F. V. Mikulec, J. R. Heine, H. Mattoussi, R. Ober, K. F. Jensen, and M. G. Bawendi, J. Phys. Chem. **101**, 9463 (1997).

[75] M. Kuno, J. K. Lee, B. O. Dabbousi, F. V. Mikulec, and M. G. Bawendi, J. Phys. Chem. **106**, 9869 (1997).

[76] X. Peng, M. C. Schlamp, A. V. Kadavanich, and A. P. Alivisatos, J. Am. Chem. Soc. **119**, 7019 (1997).

[77] K. A. Littau, P. J. Szajowski, A. J. Muller, A. R. Kortan, and L. E. Brus, J. Phys. Chem. **97**, 1224 (1993).

[78] L. E. Brus, J. Phys. Chem. **98**, 3575 (1994).

[79] M. A. Olshavsky, A. N. Goldstein, and A. P. Alivisatos, J. Am. Chem. Soc. **112**, 9438 (1990).

[80] A. A. Guzelian, U. Banin, A. V. Kadavanich, X. Peng, and A. P. Alivisatos, Appl. Phys. Lett. **69**, 1432 (1996).

[81] X. Peng, J. Wickham, and A. P. Alivisatos, J. Am. Chem. Soc. **120**, 5343 (1998).

[82] M. G. Bawendi, A. R. Kortan, M. L. Steigerwald, and L. E. Brus, J. Chem. Phys. **91**, 7282 (1989).

[83] S. H. Tolbert and A. P. Alivisatos, Annu. Rev. Phys. Chem **46**, 595 (1995).

[84] W. U. Huynh, X. Peng, and A. P. Alivisatos, Advanced Materials **11**, 923 (1999).

[85] X. Peng, L. Manna, W. Yang, J. Wickham, E. Scher, A. Kadavanich, and A. P. Alivisatos, Nature **404**, 59 (2000).

[86] M. G. Bawendi, P. J. Carroll, W. L. Wilson, and L. E. Brus, J. Chem. Phys. **96**, 946 (1989).

[87] C. H. Henry and K. Nassau, Phys. Rev. B **1**, 1628 (1970).

[88] C. B. Murray, D. J. Norris, and M. G. Bawendi, J. Phys. Chem. **115**, 8706 (1993).

[89] J. E. B. Katari, V. L. Colvin, and A. P. Alivisatos, J. Phys Chem. **98**, 4109 (1994).

[90] D. J. Norris, A. Sacra, C. B. Murray, and M. G. Bawendi, Phys. Rev. Lett. **72**, 2612 (1994).

[91] V. L. Colvin, A. N. Goldstein, and A. P. Alivisatos, J. Am. Chem. Soc. **114**, 5221 (1990).

[92] A. L. Smith, editor, *Particle Growth in Suspensions*, Academic Press, 1983.

[93] X. Peng, private communications.

[94] P. Palinginis, private communications.

[95] J. N. Demas and G. A. Crosby, Phys. Chem. **75**, 991 (1971).

[96] R. F. Kubin and A. N. Fletcher, J. Luminescence **27**, 455 (1982).

[97] M. Fischer and J. Georges, Chem. Phys. Lett. **260**, 115 (1996).

[98] X. Fan, A. Doran, and H. Wang, Appl. Phys. Lett. **73**, 3190 (1998).

[99] X. Fan, S. Lacey, and H. Wang, Opt. Lett. **24**, 771 (1999).

[100] S. A. Empedocles, D. J. Norris, and M. Bawendi, Phys. Rev. Lett. **77**, 3873 (1996).

[101] A. L. Efros and M. Rosen, Phys. Rev. B **54**, 4843 (1996).

[102] S. A. Empedocles and M. Bawendi, Science **278**, 2114 (1997).

[103] A. L. Efros and M. Rosen, Phys. Rev. Lett. **78**, 1110 (1997).

[104] M. Nirmal, D. J. Norris, M. Kubo, M. Bawendi, A. L. Efros, and M. Rosen, Phys. Rev. Lett. **75**, 3728 (1995).

[105] K. Leung, S. Pokrant, and K. B. Whaley, Phys. Rev. B **57**, 12291 (1998).

[106] J. M. Luttinger and W. Kohn, Phys. Rev. **97**, 869 (1955).

[107] W. Yang, private communications.

[108] M. Nirmal, C. B. Murray, and M. Bawendi, Phys. Rev. B **50**, 2293 (1994).

[109] J. A. Gupta, D. D. Awschalom, X. Peng, and A. P. Alivisatos, Phys. Rev. B, Rapid Communication **59**, R10421 (1999).

[110] C. A. Goss, D. H. Charych, and M. Majda, Anal. Chem. **63**, 85 (1991).

[111] M. A. Ansell, E. B. Cogan, G. A. Neff, R. von Roeschlaub, and C. J. Page, Supramolecular Science **4**, 21 (1997).

[112] B. A. Paldus, J. S. H. Jr., J. Martin, J. Xie, and R. N. Zare, J. Appl. Phys. **82**, 3199 (1997).

[113] R. A. Provencal, J. B. Paul, C. N. Chapo, and R. J. Saykally, Spectroscopy **14**, 24 (1999).

[114] G. Bjork, A. Karlsson, and Y. Yamamoto, Phys. Rev. A **50**, 1675 (1994).

[115] X. Fan, T. Takagahara, J. E. Cunningham, and H. Wang, Solid State Commun. **108**, 857 (1998).

[116] S. A. Blanton, M. A. Hines, and P. Guyot-Sionnest, Appl. Phys. Lett. **69**, 3905 (1996).

[117] M. Nirmal, B. O. Dabbousi, M. G. Bawendi, J. J. Macklin, J. K. Trautman, T. D. Harris, and L. E. Brus, Nature **383**, 802 (1996).

[118] U. Banin, M. Bruchez, and A. P. Alivisatos, J. Chem. Phys. **110**, 1195 (1999).